Practical and Theoretical Investigation of Underwater Laser Cutting for Decommissioning Applications

Chris Nyamayaro, MSc, BEng

A thesis submitted in fulfilment for the degree of Doctor of Philosophy at Lancaster University

Lancaster University

September 2021
Department of Engineering, Lancaster University, UK

Abstract

Energy Act 2008 requires that a large proportion of the North Sea infrastructure will need to be decommissioned in the next 30 years. To perform subsea decommissioning activities, technologies which are flexible (there is large heterogeneity in the structures), fast (deployment costs are significant), reliable (to minimise down-time) and deployable remotely (to avoid the use of divers) need to be developed. Underwater laser cutting provides an innovative cutting technology for decommissioning offshore infrastructures and nuclear waste which is cheaper, safer and relatively faster. In this research, three approaches were used to investigate underwater laser cutting of C-Mn steel using a 10 kW fibre laser. These approaches comprise of an experimental, theoretical, and numerical study of underwater laser cutting. The experimental work consisted of underwater laser cutting trials, conducted in a $1m^3$ tank and a high pressure vessel. The findings for both cutting trials were analysed for the influence of process parameters on performance and cut quality. The cut quality is assessed in terms of the attached dross height and kerf width because the key requirement in decommissioning applications is that the parts being cut must be separated with minimal secondary waste. A 50 mm thick C-Mn steel workpiece was adequately cut with a maximum cutting speed of 200 mm/min for hydrostatic pressure conditions of up to 20 bar, representing a water depth of ~200 m. The process performance and kerf width results predicted by the theoretical model are validated by underwater laser cutting trials carried out in a $1 m^3$ tank. A key finding in the numerical study of a 3-dimensional (3D) gas jet expansion model is that a mixed phase (water, water vapour (steam) and air) medium was observed at the exit of the virtual kerf along the path of the laser beam.

Declaration

I declare that this thesis is my own work and has not been submitted by me for the award of a higher degree elsewhere. No sections of this thesis have been published or submitted for a higher degree elsewhere.

Name: Chris Nyamayaro

Date: 29/09/21

Acknowledgements

Table of Contents

List of figures

List of tables

Nomenclature

b_c Cut kerf width

v_c Cutting velocity

ρ Density

c_p Specific heat capacity

z_r Rayleigh length

T_p Process temperature of the material

T_∞ The ambient temperature

T_{in} Inclination temperature

V Cutting speed

T_m Melting temperature of the material

T_v Vaporisation temperature

P_e Peclet number

t Cut thickness

H_m The specific enthalpy of fusion of the material

K Thermal conductivity of the material

κ Thermal diffusivity of the material

K_w Thermal conductivity of water

Pr_w Prandtl number of water

H_{FeO} The reaction enthalpy for the formation of FeO

n_d Nozzle diameter

A Absorption

A_{AVE} Average absorptivity

P_L Incident laser power

P_w Heat for heating of the liquid material

P Laser power

P_{in} Transmitted laser power

n Refractive index

k Extinction coefficient

M_w Molecular weight of the assisting gas (air)

ρ_g Density of air

β The fraction of the kerf width above the boiling temperature (Bolling coefficient)

R_P Reflection for parallel polarised laser radiation

R_S Reflection of perpendicular polarised laser radiation

R_{AVE}	Average value of the reflectivity
d_Z	Depth of focus
λ	Wavelength
v_1	Speed of propagation in medium 1
g	Gravitational constant
ΔT	Temperature rise from the initial temperature to the melting temperature
P_{hydro}	Hydrostatic pressure
M_t	Mach number at the nozzle throat
P_o	Stagnation pressure
P_b	Back pressure
P_*	Critical pressure
P	Pressure
U	Nozzle exit velocity
$d(z)$	Beam diameter along the beam propagation axis, z
Pe_d	Peclet number at diffusion velocity
u	Air flow speed (Mach 1.7) at 8 bar simulations in numerical model
d	Beam spot diameter on the surface of the material
d_{waist}	Beam waist diameter
d_{fibre}	Delivery optical fibre diameter
d_{focus}	Focusing lens focal length
$d_{collimator}$	Collimating lens focal length
z	Distance from the beam waist to the material surface
n	Constant term which depends on the temperature distribution in the radial direction
K_w	Thermal conductivity of water at 20 °C
Pr_w	Prandtl number of water at 20 °C
v_w	Dynamic viscosity of water at 20 °C
T_o	Initial temperature of the workpiece
T_i	Interaction time
ρ_w	Density of water
Re_w	Reynolds number of air/water mixture
P_{mw}	Melting and heating power expressed in terms of the Peclet number
X_{abbr}	Burn-off
δ_{df}	Thermal diffusion length

Re_w	Reynolds number of water
q_s	Rate of conduction loss to the base of the material
H_c	Forced convection heat transfer coefficient
q_w	The rate of convective heat loss from the surface of molten layer
P_{abs}	Absorbed power
v_{diff}	Diffusion velocity of mild steel
P_r	Reactive power gain due to oxidation
P_m	Heat for melting
$\propto$	Absorption coefficient of water
P_{hl}	Thermal leakage power/Conduction
f	Focal length
σ	Molecular diameter of air
P_g	Air pressure
φ_{in}	Angle of incidence
ψ	Angle of refraction
$\dot{V}$	Rate of penetration of the incident laser beam
D	Raw beam diameter on the focusing lens.
h	Water height
v_2	Speed of propagation in medium 2
L_m	Latent heat of melting
L_v	Latent heat of vaporization
d_f	Focused spot diameter
M	Mach number
M_e	Mach number at the nozzle exit
T	Temperature
T_o	Stagnation temperature
ρ_o	Stagnation density
γ	Specific heat ratio/adiabatic index
u	Axial velocity
U^*	Normalised axial-velocity
C-Mn	Carbon-Manganese
CO_2	Carbon dioxide
Yb	Ytterbium
O_2	Oxygen
ρ_m	Density of the mixture

$\bar{u}_i$ & $\bar{u}_j$	Filtered velocity components
x_i and x_j	Distance components
$\bar{p}$	Filtered pressure
τ_{ij}	Subgrid-scale stress
E_k	Kinetic energy
$\bar{S}_{ij}$	Rate-of-strain tensor
$\mathcal{E}_f$	Dissipation of kinetic energy of the filtered velocity field by viscous stress
$\prod$	Sub-filter scale dissipation of kinetic energy
t	Time
p	Gas pressure
F_i	Sum of the gravity and buoyancy forces
F_{CSF}	Surface tension force
a_g	Volume fraction of gas
a_w	Volume fraction of water
k_{eff}	Effective thermal conductivity
u_g	Velocity of the gas
k_t	Turbulent thermal conductivity
k	Thermal conductivity in multiphase flows
h_k	Enthalpy based on the specific heat capacity at constant pressure and temperature
v_k	Normal velocity
ϕ_m	Physical property of the mixture
R	Ideal gas constant.
k	Turbulence kinetic energy
ε	Rate of dissipation
μ_m	Dynamic viscosity of mixture
μ_t	Turbulent viscosity
G_k	Generation of turbulence kinetic energy due to the mean velocity gradients
G_b	Generation of turbulence kinetic energy due to buoyancy
Y_m	Contribution of the fluctuating dilatation in compressible turbulence to the overall dissipation rate
σ_k	Turbulent Prandtl numbers for kinetic energy
σ_ε	Turbulent Prandtl numbers for the rate of dissipation

List of abbreviations

1D	1-Dimensional
2D	2-Dimensional
3D	3-Dimensional
AWJ	Abrasive Water Jet
BLS	Boundary Layer Separation
BPP	Beam Parameter Product
CEA	Commissariat à l'Energie Atomique
CNC	Computer Numerical Control
CW	Continuous-Wave
DVD	Digital Versatile Disc
DWS	Diamond Wire Sawing
HLW	High Level Waste
ILW	Intermediate Level Waste
IPG	IRE-Polus Group
JAEA	Japan Atomic Energy Agency
LAS	Lasers and Sheet processes
LASER	Light Amplification by Stimulated Emission of Radiation
LASOX	Laser Assisted Oxygen Cutting
LBC	Laser Beam Cutting
LCU	Laser Control Unit
LE	Lifetime Extension
LED	Light-emitting Diode
LES	Large Eddy Simulation
MLN	Minimum Length Nozzle
PAC	Plasma Arch Cutting
PISO	Pressure-Implicit with Splitting of Operators
PRESTO!	PREssure STaggering Option
ROE-FDS	Roe Flux-difference Splitting
SCM	Subsea Cutting Methods
SGS	Sub-Grid Scale
SIMPLE	Semi-Implicit Method for Pressure Linked Equations
STS	Sub-Filter Scale
TWI	The Welding Institute
UKCS	United Kingdom Continental Shelf
VOF	Volume of Fluid

1   Introduction

1.1   Background of the Study

Decommissioning of offshore installations has been of concern to governments and industry for many years and will continue to be for years to come, considering the number of installations. In 2010, there were approximately 832 oil and gas structures in the North Sea [1, 2]. In 2013, 1340 offshore installations consisting of 735 sub-sea steel structures and 522 fixed steel installations were operational in the North Sea [3, 4]. Currently, there are more than 7000 registered drilling and production platforms located on the continental shelves of 53 countries and 1500 of these are in the North Sea [5]. This clearly shows the accelerated production of offshore structures.

Many of the structures producing oil and gas have a limited lifespan, often 25-40 years, and an increasing number are due to be taken out of service [6]. However, with certain processes and criteria, the lifespan of an ageing oil and gas infrastructure can be extended without compromising the safe working limits. This concept of increasing the life of an aging oil and gas facility without increasing the risk is termed as Lifetime Extension (LE). Factors such as oil reservoirs producing more oil than estimated can influence the decision to extend the operation of an offshore oil and gas infrastructure [7, 8].

An example of an oil and gas infrastructure is a jacket (see Figure 1), which is a common type of steel structure in UK waters [1].
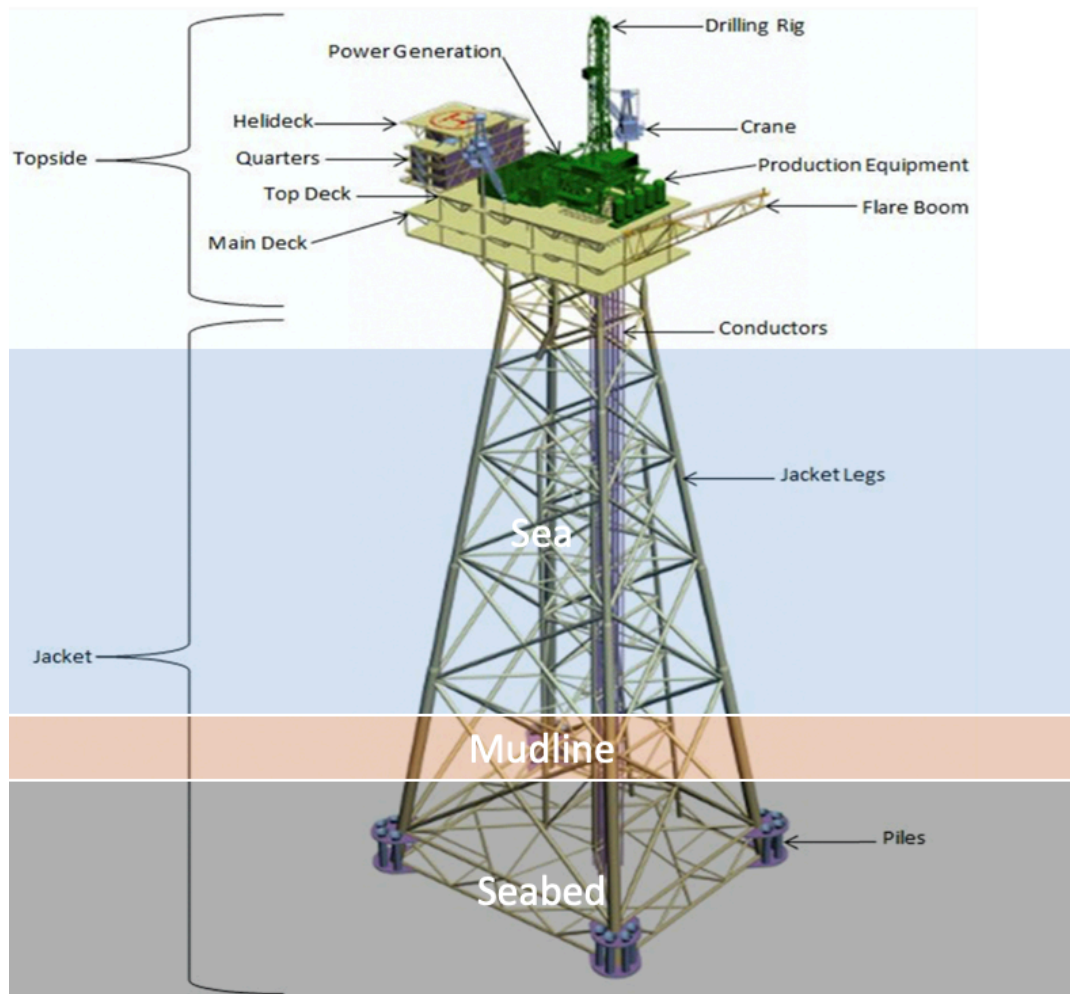
Figure 1: Schematic of a generalised offshore oil and gas platform [9]

An offshore platform comprises of the topside, splash-zone, jacket, and piles. Excluding the piles which secure the structure to the seabed, the vertical extent can be between 70 m and 300 m. The lowest deck of the topside is ~20 m above sea level. The zone between the topside and the sea is the splash zone, where it is difficult to undertake prolonged work due to wave action. The jacket is the steel or concrete structure that supports the topsides and includes the splash zone, hydrocarbon transporting pipes and conductors. The piles are thick walled pipes that are pile driven hundreds of metres into the seabed to secure the jacket to the seabed [10].

Driven by the legislation under the Energy Act 2008, a large proportion of the North Sea's oil and gas infrastructure will need to be decommissioned in the next 30 years [11]. So far in the UK continental shelf only 88 (12%) installations have been decommissioned to date, reflecting the nascent nature of the decommissioning market [12]. With more stringent environmental legislations related to global warming and the depletion of oil reserves due to rising demand, it's thought that decommissioning will become a priority for many companies. This will potentially provide substantial decommissioning opportunities for years to come.

Decommissioning costs and timings vary widely depending on factors such as water depth, type, size and weight of structure, complexity, age of the installation, the number of wells and so on [13]. Decommissioning typically takes several years of careful planning before execution starts. The physical removal of an offshore platform can take anywhere from weeks to months, depending on the complexity and size of the installations [14].

The oil and gas industry has managed its offshore decommissioning activities in the North Sea despite the Coronavirus pandemic; however, the future is still uncertain. Commodity prices remain volatile, particularly in the case of gas. Gas prices have increased by more than 400 per cent throughout the year, reaching record and prolonged high levels. While this may result in the deferral of some decommissioning activities, the impact will be fully assessed in the coming years [15].

The total spend on decommissioning in 2020 and 2021 was estimated at £1.07 and £1.46 billion, respectively [15, 16]. The British industry is looking to spend approximately £16.6 billion over the next decade for decommissioning projects on the UKCS (United Kingdom Continental Shelf) alone [15-17]. Projected North Sea decommissioning activity estimates vary, with the most conservative estimates predicting the market will require over £30 billion of expenditure before 2040 in the UKCS [12]. Globally, the offshore decommissioning market is estimated to be worth over £64 billion over the next ten years [17].

There is currently a selection of different Subsea Cutting Methods (SCMs) which could be effectively utilised for decommissioning offshore installations. The three main competing technologies for decommissioning subsea structures are abrasive water jet, diamond wire cutting and plasma arc cutting [1, 18]:

- Abrasive Water Jet (AWJ): This technology uses an industrial tool (water jet cutter) capable of cutting a wide variety of materials using an extremely high-pressure jet of water, or a mixture of water and an abrasive substance. This SCM can cut variety of materials, in varied depths and in thick-sections but it is inherently slow and produces significant secondary waste in the form of contaminated abrasive in a water sludge;
- Diamond Wire Sawing (DWS): DWS is a cutting technology which uses a wire of various diameters and lengths, impregnated with diamond dust of various sizes to cut through materials. This technology is frequently used by oil and gas industries for dismantling of large structures and can be used at extreme depths. However, such machines are large, heavy and contain complicated mechanisms for traversing the wire. The major limitation of this technology is the cost of deployment;
- Plasma Arc Cutting (PAC): This cutting method employs superheated, ionized gas funnelled through a plasma torch to heat, melt and, ultimately, cut the material. This technology has proven itself to be cheap and reliable in cutting metallic materials, but mostly on planner geometries and it is used by the oil

3

and gas sector as well as the nuclear industry. However, its use is inherently limited by standoff distance and electrically conductive and flat material geometries. Furthermore, due to considerably large kerf, the process produces a high level of secondary waste, and requires frequent nozzle changes, increasing operational time and costs.

In offshore decommissioning applications, a technology which cuts various geometries and thicknesses, provides flexible functionality to cut with a single tool (ease of remote deployment, operation and maintenance) and enable the capability to cut both from outside-in and inside-out would be considered highly desirable. Fibre delivered laser beam cutting has the potential to deliver these benefits by means of cutting safer, cheaper and relatively faster. This provides a great opportunity for development, deployment and the use of fibre laser technology, particularly for underwater cutting applications.

1.2   Motivation

Underwater laser cutting offers great potential to replace underwater cutting methods like AWJ, DWS and PAC for tasks such as dismantling offshore infrastructures. The main motivation for this research is to investigate underwater laser cutting in atmospheric pressure conditions and hyperbaric conditions that simulate offshore settings. This work is structured around the experimental investigation of underwater laser cutting of C-Mn steel, considering the application for the decommissioning of subsea installations. Therefore, this work provides the underlying data for theoretical analysis by developing and applying experiments relevant to the practical application of underwater laser cutting. The main objective of the theoretical work is to predict the process performance, in terms of the maximum cut thickness, and kerf width generated from the underwater laser cutting process at various laser powers. Moreover, this work examines an underwater gas jet expansion model for underwater laser cutting, an innovative study in this research field.

1.3   Aims and objectives

The aims and objectives of this study can be stated as follows:

- Scientific
  - To develop a scientific understanding of the underwater laser cutting process and influencing parameters up to a hydrostatic pressure of 20 bar on C-Mn steel structures up to 50 mm in thickness.

- Technical
  - To advance the state-of-the-art of an existing underwater laser cutting technology with the capability of cutting 50 mm thickness C-Mn steel at depths up to 200 m.

1.4   Structure of Thesis

There are seven chapters in this thesis. The first chapter is an introduction to the study that presents the background of the study, motivation, objectives of the study, and contribution of the thesis.

The influence of process parameters on cutting speed (performance) and cut quality (dross height and kerf width) in 1-micron lasers for both conventional and underwater laser cutting are explained in detail in Chapter 2. The influence of process parameters mostly focuses on fibre delivered laser systems because 10.6 μm CO_2 lasers cannot be delivered via a fibre [19]. This literature review also focuses on laser cutting C-Mn steel and stainless steel because most offshore structures are made from stainless steel and most non-contaminated offshore facilities are made from C-Mn steel [20]. Studies that use air or an inert cutting gas are investigated because the use of pure oxygen as an assist gas raises major safety issues in decommissioning applications [20].

The third and fourth chapter presents the experimental investigation of underwater laser cutting. Chapter 3 describes the equipment and experimental procedures used in this work. The experimental work in this project was organized into two sets of cutting trials, both conducted at The Welding Institute (TWI). The 1st set of underwater laser cutting trials were carried out in a 1 m^3 tank. The 2nd set of underwater laser cutting trials were conducted inside a high pressure vessel, designed and manufactured by TWI. Chapter 4 presents the results from the 1st and 2nd set of cutting trials. This addresses the influence of laser power, cutting speed, assist gas pressure, hydrostatic pressure and standoff distance on the corresponding maximum cut thickness, dross height and kerf width.

Chapter 5 describes the development of a power balance theoretical model for underwater laser cutting which was accomplished in two phases. The first phase comprises of modelling laser cutting and validating the theoretical results using experimental data of conventional laser cutting. The second phase concerns modifying the power balance equation in conventional laser cutting with conduction and convection heat losses that occur underwater. The theoretical findings are then validated by experimental results of underwater laser cutting in a 1 m^3 tank.

The sixth chapter presents the development and application of a gas jet expansion numerical model for underwater laser cutting. The development of an underwater gas jet expansion model for underwater laser cutting was accomplished in two key stages using ANSYS Fluent 18.2 [21]. The goal of this chapter is to investigate the effect of fluid flow on the underwater laser cutting process to identify a mixed phase (water,

water vapour (steam) and air) medium along the path of the laser beam. A mixed phase region at the laser-material processing zone can affect both the cutting performance and quality in underwater laser cutting. This research is required because an underwater gas jet expansion flow is unsteady and turbulent, making it difficult to quantify the volume fraction of air and velocity in the path of the laser beam using experimental visualisation [22, 23]. Finally, the conclusions of the study and recommendations for future work are given in Chapter 7.

1.5   Contribution of thesis

This thesis presents an analysis of underwater laser cutting of a 50 mm thick C-Mn steel workpiece in hydrostatic pressure conditions of up to 20 bar, corresponding to a water depth of ~200 m. A 10 kW IPG Ytterbium fibre laser system operating in continuous wave (CW) mode was used together with air as a cutting gas. The contributions of this thesis can be separated into three categories, which are an experimental study, a theoretical modelling study and the development of a 3D gas jet expansion numerical model for underwater laser cutting. The experimental work contributes to the study of underwater laser cutting by:

- Providing an approach of performing underwater laser cutting trials in increasing hydrostatic pressure conditions of up to 20 bar, representing a water depth of ~200 m;
- Showing that a 50 mm thick C-Mn steel workpiece can be adequately cut with a maximum cutting speed of 200 mm/min for hydrostatic pressure conditions of up to 20 bar, representing a water depth of ~200 m;
- Analysing the influence of water depth on the process performance (in terms of maximum cut thickness) and cut quality (dross height and kerf width) in increasing hydrostatic pressure conditions, which adds new knowledge in this research field.

The theoretical modelling work provides new knowledge to the study of underwater laser cutting by:

- Predicting the process performance and kerf width results in underwater laser cutting by theoretical formulation as analytical modelling literature in this research field could not be found. The lack of analytical modelling studies in underwater laser cutting can be attributed to the fact that research in this field is mainly experimental [1].

The development and application of a 3D underwater gas jet expansion numerical model aids to the study of underwater laser cutting by:

- Identifying a mixed phase (water, water vapour (steam) and air) medium along the path of the laser beam. This study is vital as it is difficult to quantify the

volume fraction of air and velocity in the path of the laser beam using experimental visualisation as an underwater gas jet expansion flow is unsteady and turbulent.

2 Literature review

2.1 Background of lasers

The concept of a laser began in 1917 when Albert Einstein theorised the principle of a laser as a stimulated emission [24]. The first theory of a LASER (an acronym for Light Amplification by Stimulated Emission of Radiation) was published in 1958 by Schawlow and Towns. However, Gould who also published the term LASER in his 1959 paper was later granted the patent for LASER and most laser processes after a 30-year patent war against Schawlow and Townes [25, 26]. In 1960, the first ruby laser was invented by Maiman [27] and Snitzer [28, 29] invented the first fibre laser in 1963. The Western Electric Engineering Research Centre designed the first production laser cutting machine in 1965 to drill holes in diamond dies for wire extrusion using a ruby laser which produced pulses of coherent visible light at a wavelength of 694.3 nm [24]. In May 1967, Sullivan and Houldcroft cut a millimetre thick steel sheet using a 300 W CO_2 laser at a TWI Laboratory [30, 31]. This was the start of oxygen assisted laser cutting of metals [24].

The first industrial use of a CO_2 laser started in 1971 and lasers for sheet metal cutting applications began to be adapted industrially in 1975 [32, 33]. Initially developed for the telecoms industry, the industrial use for fibre delivered laser beam sources became commercially available on the market in the late 1980s. Lasers have evolved since then as they are now used in many manufacturing processes, which include welding, cladding, marking, surface treatment, drilling, and cutting; the single largest application is metal cutting [24].

With recent developments in fibre laser technology in terms of higher wall plug efficiency, increased flexibility and automation control, the demand and use of fibre lasers in material processing has grown significantly. Fibre laser sources have also overtaken CO_2 laser sources in market share for 2-D flatbed cutting applications. This is particularly fuelled by China's growth in using fibre lasers over CO_2 lasers for material processing and the growing laser uses in the automotive sector mostly in the Asia Pacific region [24, 34].

2.1.1 Laser cutting process

The laser cutting process is a thermal, non-contact cutting method in which a high-power focused laser beam with required intensity is used to melt and possibly vaporise the workpiece at the focused region. A pressurised gas jet coaxially aligned with the laser beam is used to eject the molten or vaporised layer from the cut channel/kerf (see Figure 2). The laser cut kerf is created by the relative motion between the incident laser beam and the workpiece, together with the removal of molten material by an assist gas jet. The principal components of the laser cutting system include [1, 35, 36]:

- The laser source, which generates laser beam with a suitable cooling system to control temperature.
- The beam guidance system (i.e. fibre optics or free-space propagation using mirrors).
- The laser cutting head consisting of the collimation and focusing optics, the assist gas nozzle assembly and the workpiece handling equipment.

Laser Beam Cutting (LBC) process occurs when the laser power intensity is high enough to melt or vaporise the material and the laser power intensity is given as [24]:

$$Power\ intensity = \frac{Power}{Area} = \frac{4P}{\pi d^2} \qquad (1)$$

Where P is the laser power and d is the beam's diameter on the material surface. Figure 2 shows a schematic representation of a gas-assisted laser cutting process [37]:

| Laser beam |
| Nozzle |
| Gas jet |
| Workpiece |
| Kerf |
| Attached dross |
| Sedimented dross and aerosols |
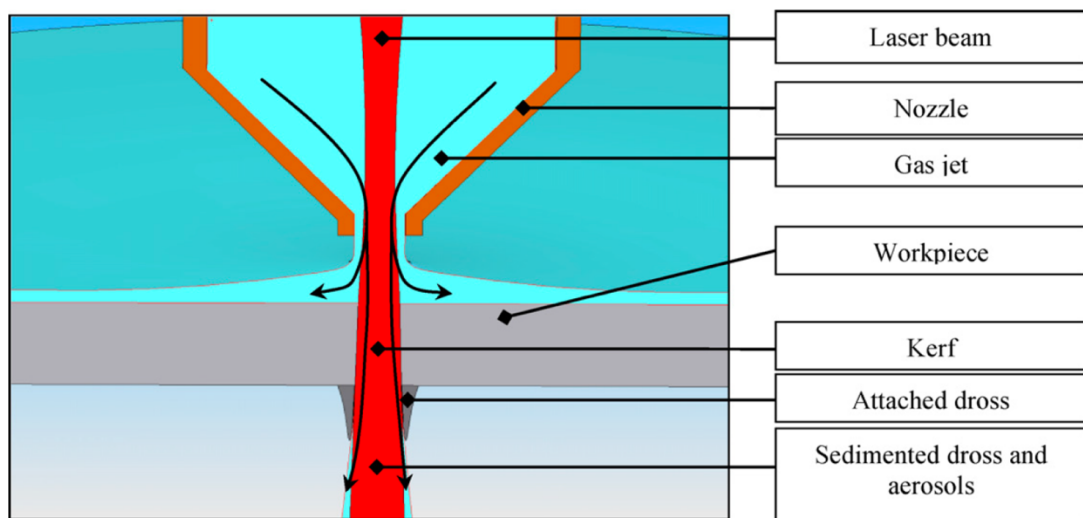
Figure 2: A schematic representation of the gas-assisted laser cutting process [37]

2.1.2   Laser-metal interaction

All materials either transmit, reflect or absorb laser radiation. For opaque materials [24]:

$$Reflectivity + \ Absorptivity = \ 1 \qquad (2)$$

For transparent materials:

$$Reflectivity + Absorptivity + \ Transmissivity = \ 1 \qquad (3)$$

This fundamental characteristic of laser radiation is dependent upon its wavelength and material properties such as refractive index, extinction coefficient and radiation absorption coefficient. Figure 3 schematically shows the reflection and absorption definition of an incident laser beam with the angle of incidence, φ_{in} [38].
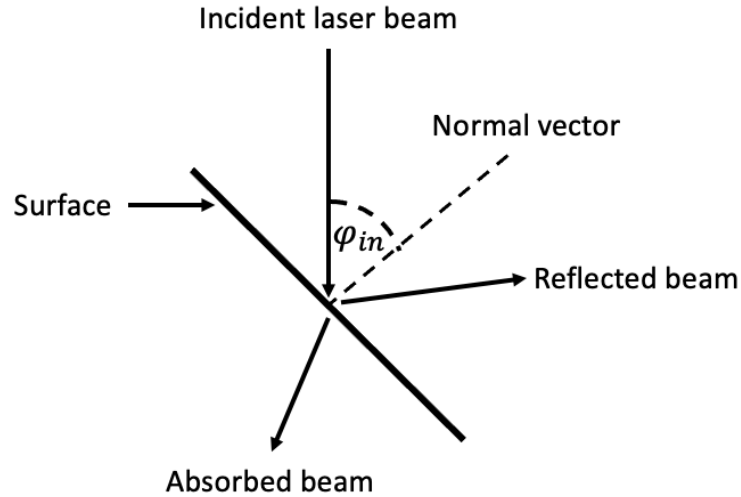
Figure 3: Diagram defining the reflection and absorption of a laser beam

The quantity of heat absorbed depends on the absorptivity of the workpiece surface to the laser radiation. Absorptivity is the ratio of the amount of heat absorbed to the incident laser power. In opaque metals; absorptivity A can be simplified as [24]:

$$A = 1 - Reflectivity\ of\ workpiece\ surface \qquad (4)$$

Equation (4) can be written as:

$$A = \frac{4n}{n^2 + k^2 + 2n + 1} \qquad (5)$$

Where n is the refractive index and k is the extinction coefficient. For iron at 25°C, Table 1 shows the values of n and k and A [39]:

Table 1: Properties of iron at 25 °C [39]

Wavelength (λ)	1.06 μm (≈YAG)	10.6 μm (≈CO$_2$)
Extinction coefficient (k)	4.7	29
Refraction coefficient (n)	3.2	6.4
Absorption coefficient (A) (calculated from equation (5))	0.322	0.029

The absorptivity depends on the angle of incidence, plane of polarisation of the light beam, material type, temperature of material, phase of the material and the wavelength of laser radiation [24]. When the angle of incidence is zero ($\varphi_{in} = 0$), the

beam component parallel to the incidence plane R_P and normal component R_S are absorbed equally. The reflectivity R_P and R_S in fibre lasers are given by Fresnel relations according to [36, 40]:

$$R_P = \frac{(n \cos \varphi_{in} - 1)^2 + (k \cos \varphi_{in})^2}{(n \cos \varphi_{in} + 1)^2 + (k \cos \varphi_{in})^2} \tag{6}$$

and

$$R_S = \frac{(n - \cos \varphi_{in})^2 + k^2}{(n + \cos \varphi_{in})^2 + k^2} \tag{7}$$

Where R_P is the reflection for parallel polarised laser radiation, R_S is the reflection of perpendicular polarised laser radiation and φ_{in} is the angle of incidence. In the case of un-polarised or circularly polarised radiation, the reflectivity R_{AVE} can be estimated as the average value of the reflectivity R_P and R_S according to [40]:

$$R_{AVE} = \frac{R_S + R_P}{2} \tag{8}$$

As a result, the average absorptivity A_{AVE} is given by [40]:

$$A_{AVE} = 1 - \left(\frac{R_S + R_P}{2} \right) \tag{9}$$

The index of reflection n and absorption k vary slightly with temperature but are strongly dependent on the wavelength [38]. Table 2 shows the indices of refraction and extinction coefficients of molten iron for different wavelengths and temperatures.

Table 2: Index of refraction and extinction coefficients of iron for different wavelengths and temperatures (melting point, boiling point and average) [40]

Temperature (K)	Wavelength = 1.07 µm		Wavelength = 10.6 µm	
	n	k	n	k
1800	5.46	3.96	15.5	15.1
3000	5.14	3.68	14.6	14.1
2400	**5.30**	**3.82**	**15.0**	**14.6**

Figure 4 illustrates the theoretical absorptivity for different un-polarised laser beam wavelengths of 10.6 µm (CO_2) and 1.06 µm (fibre/disk) as a function of the incident angle. The absorptivity reaches a maximum at a distinct angle of incidence which is known as the Brewster angle. The Brewster angle or polarisation angle is a special angle of incidence at which an unpolarised beam is reflected from the surface perfectly polarised (perpendicularly) while the absorbed ray is partially polarised. At Brewster angle, the angle of reflection is at right angles to the angle of refraction and, the

coefficient of reflection of perpendicularly polarised light (R_S) is at its lowest and the coefficient of reflection of parallel polarised light (R_P) is at its highest [24, 36].
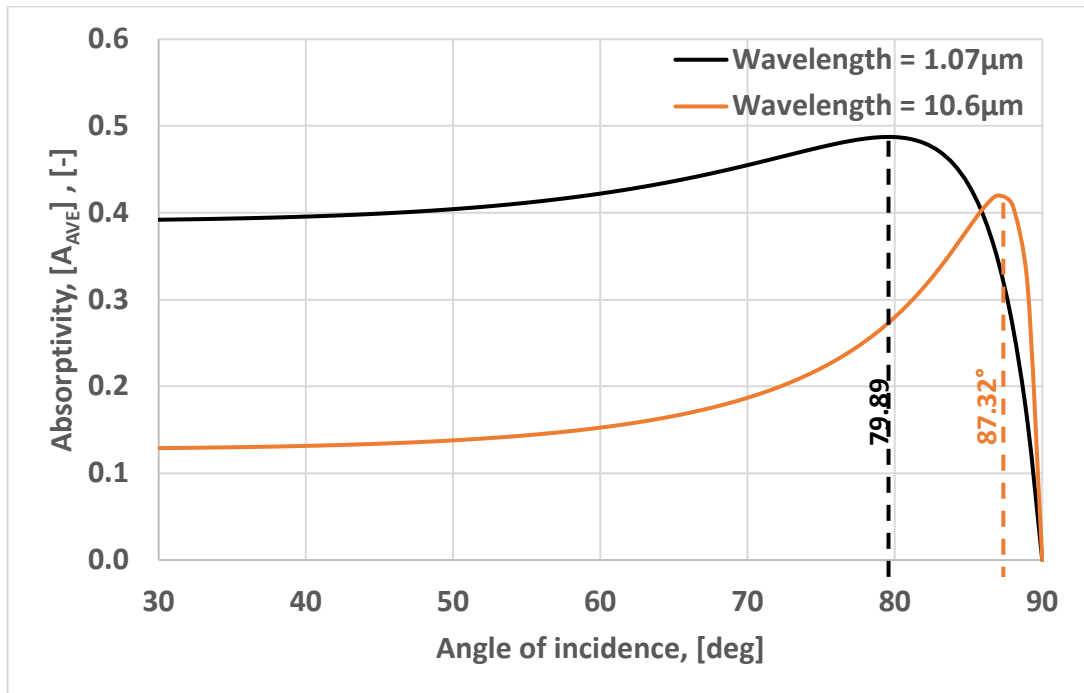
Figure 4: Absorptivity of molten iron for un-polarised laser radiation with different wavelengths

According to Figure 4, for a Ytterbium (Yb) fibre laser (wavelength of 1.07 μm), the Brewster angle is 79.89° and for a CO_2 laser (wavelength of 10.6 μm), the Brewster angle is 87.32°. After exceeding this angle, the absorptivity strongly diminishes with subsequent increased values of the inclination angle. The theoretical absorptivity is the same for both wavelengths at an angle of 85.9°. The absorptivity in metals generally increase with shorter wavelengths, as the material is being heated to its melting temperature during the laser cutting process [24, 36].

2.2   Laser cutting for manufacturing applications

Nearly all metals are greatly reflective of infrared energy (electromagnetic radiation with wavelengths longer than those of visible light) but focusing a laser of more than 1 MW/cm^2 can quickly initiate surface melting or vaporisation on the focused region. Convection and conduction in the molten material transfer heat to the solid material and increases the molten material volume. Therefore, laser cutting can be characterised by energy thresholds because a characteristic temperature must be reached in the material - i.e. melting, vaporisation and evaporation while energy is lost from the interaction zone by heat conduction to the substrate metal.

2.2.1 Laser vaporisation/ Sublimation cutting

The principle of vaporisation cutting depends on a high intensity focused laser beam to raise material surface temperature to its boiling point until a keyhole is created. The keyhole causes an increase in the absorption of the laser beam due to the multiple reflections within the cavity walls and the hole deepens quickly. The multiple reflections from the incident laser beam can destabilise the lower part of the cut zone and cause coarser striations [36, 41]. Assuming heat conduction is negligible, the rate of penetration $\dot{V}$ of the incident laser beam can be assumed to be [24]:

$$\dot{V} = \frac{AP_L}{\rho b_c t[L_m + L_V + c_p(T_v - T_o)]} \tag{10}$$

Where A is the absorptivity of the material, P_L is the incident laser power, ρ is the material density, b_c is the kerf width, t is the material thickness, L_m is the latent heat of melting, L_V is the latent heat of vaporisation, c_p is the specific heat capacity, T_v is the vaporisation temperature and T_o the initial temperature of the workpiece [24].

Vaporisation cutting uses a laser to evaporate the material with as little melting as possible [42]. Ion [43] characterises vaporisation cutting as a process in which both vapour and melt are formed and removed from the kerf by an assist gas jet, while Radovanovic [44] defines it as a process in which only the material vapour is exclusively removed by vaporisation as almost no melt occurs.

Vaporisation laser cutting requires very high-power intensities and is normally used with pulsed lasers [43]. This process is sufficient for cutting of non-metals and very thin-section (< 1.0 mm) metal workpieces such that conduction losses from the cutting zone to the substrate metal can be considered negligible [36]. In the cutting of thicker metal workpieces, a very high-power intensity would be required to vaporise all the melted kerf volume as well as compensate for the high conduction losses, therefore, laser melt cutting is sometimes applied.

2.2.2 Laser melt cutting/ Laser fusion cutting/ Melt and blow

The laser fusion cutting process uses a focused high intensity laser beam to melt material corresponding to the kerf volume and a high-pressure inert cutting gas jet to eject the molten material out of the cut kerf. The laser beam intensity is not high enough to vaporise the kerf volume, but sufficient to melt it, so that it can be removed by inert assist gasses, such as Argon or Nitrogen. Laser fusion cutting may be used for cutting mild steels up to 25 mm thick [45]. This process produces oxide free cut edges which do not require any cleaning operation but with lower cutting speeds compared to the use of an active (oxygen) assist gas [46].

Assuming that all the absorbed laser power is used in melting the kerf volume before significant conduction occurs, the lumped heat capacity equation for laser fusion cutting is given by [36]:

$$AP = b_c t v_c \rho [L_m + c_p \Delta T]$$ (11)

Where v_c is the cutting speed and ΔT is the temperature rise from the initial temperature to the melting temperature of the material. Rearranging Equation (11) gives:

$$\frac{P}{dV} = \frac{b_c \rho}{A} [L_m + c_p \Delta T]$$ (12)

Here, the width b_c (a function of the focused spot diameter and cutting speed) and absorption A are functions of the laser wavelength, whilst all the other parameters are constant thermophysical properties of the material. Therefore, in laser fusion cutting, it can be assumed that the energy per unit area $\frac{P}{dV}$ is constant for a given beam and material [24].

2.2.3 Laser oxygen cutting /Oxidation cutting/ Reactive fusion cutting

In reactive fusion cutting, an oxygen gas jet is used, which provides additional heat input to the process via an exothermic reaction. Laser oxygen cutting is often used for cutting alloy steel such as mild steel and thicknesses up to 40 mm at relatively fast processing speeds [45]. The exothermic reaction can potentially provide 60% to 90% of additional energy to the cutting process [1, 24]. The amount of energy supplied by the exothermic reaction varies with the material; with mild steel and stainless steel it is about 60% of the energy used for cutting, and with a reactive metal like titanium it is around 90% [24].

The drawback of this process is the presence of the oxide layer on the cut edge, which may influence the final quality, requiring further re-processing steps in manufacturing operations e.g. welding or painting. However, the advantage for laser oxygen cutting is the ability to cut thicker materials with the same laser power compared to fusion cutting. Also, metal oxidation increases melt removal by lowering the viscosity and surface tension of the molten material during the cutting process [47, 48].

Laser Assisted Oxygen Cutting (LASOX) is also another effective method which allows the cutting of thick steel with relatively low laser power [49]. With the full use of combustion heat from Fe-O reaction, LASOX can cut thick mild steel plates by a defocused laser of medium power using a supersonic nozzle. The LASOX technique relies on the laser beam heating the surface of the steel to the ignition point across the whole area of gas jet impingement. As a result, the laser power requirements are much reduced and the dynamics of the gas jet control the process result [50]. LASOX

was performed by O'Neill and Gabzdyl [50] when cutting a 50 mm thick 43A mild steel plate with an incident laser power level of 1 kW, cutting speeds in the range of 150 - 220 mm/min, a stand-off distance of 3 mm, a nozzle exit diameter of 2.5 mm and an oxygen gas pressure of 8 bar.

2.3 Laser cutting parameters and process performance

The quality of the laser cutting process – and consequently the resulting cut quality – is governed by a number of parameters related to the laser system, material, and the process [24] (see Figure 5). The material parameters consist of the material thickness and type; the laser system parameters include the laser beam quality, wavelength of the laser radiation and maximum output laser power; and the processing parameters comprise of the focal length of the focusing lens, pressure and type of assist gas, used laser power, nozzle diameter, focal point position relative to workpiece top surface, nozzle standoff distance and cutting speed [24].

For the cutting of a particular material and specimen thickness using a specific laser system, the processing parameters can be altered by the operator to optimise the cutting process and attain high cut quality at a high cutting speed for high productivity. The laser system parameters - which are characteristics of the laser system – cannot be modified by the operator [36].
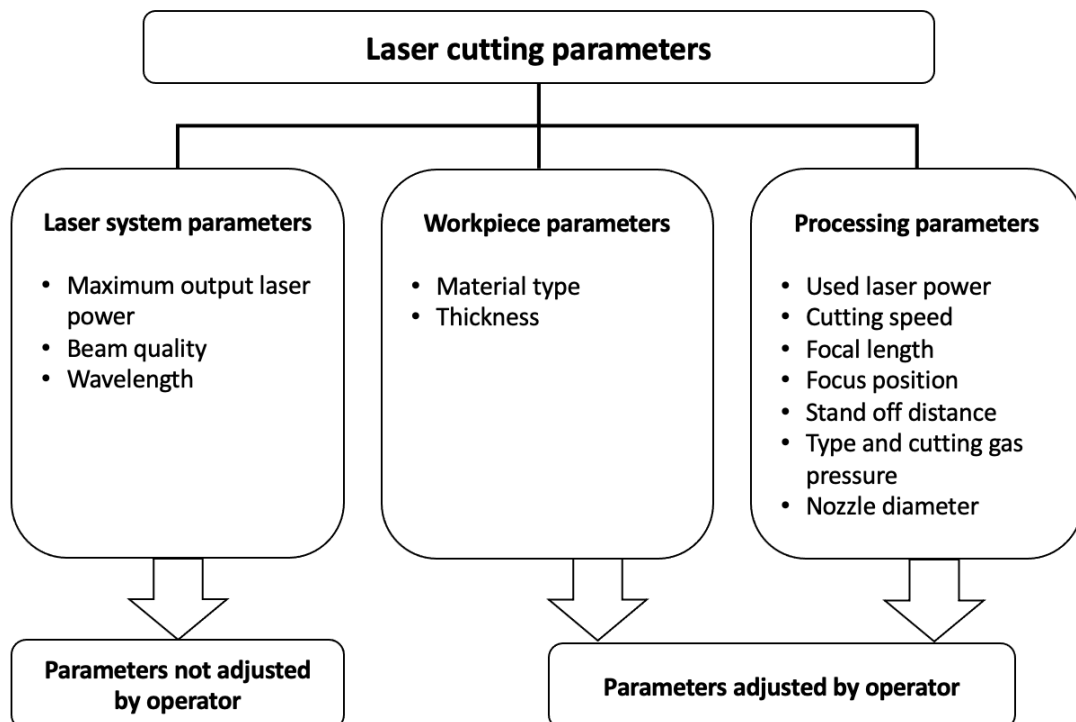
Figure 5: Laser cutting parameters [24]

2.3.1 Laser power

The laser power used for cutting determines the maximum cutting speed for a given workpiece thickness. The power balance at the cutting front is such that the sum of laser power absorbed to melt the kerf volume, reflected from the cut front and the power lost from the cutting zone through heat conduction to the substrate metal is equal to the total power used in the cutting process [36].

The overall effect of increasing the power is to allow cutting at faster speeds and/or greater thicknesses. The potential disadvantage of increasing the power is that the kerf width increases often resulting in poor cut edge quality [24]. Excessive power results in a wide kerf width, a thicker recast layer, and an increase in dross. With insufficient power, cutting cannot be initiated [43]. The effect of laser power on the cutting performance has been investigated by Chagnot et al. [37], Wandera et al. [48, 51] and Golnabi & Bahar [52]. Generally, the maximum possible cutting speed is proportional to laser power, provided the power intensity on the workpiece surface increases proportionally. However, the influence of laser power on maximum cutting speed is more significant when cutting low thicknesses in both inert [52] and reactive gas (air) cutting [37].

2.3.2 Gas pressure

The assist gas pressure is one of the most essential parameters in laser cutting. It provides the required shear and pressure gradient forces to eject the molten material from the cut kerf, protects the optical lenses from spatter, cools the cutting edge with forced convection, helps to produce oxide free cuts in inert gas cutting, protect the laser-material interaction region from the surrounding environment and contributes to 60-90% of the cutting process energy in reactive gas cutting [24].

The principal role of an inert assist gas jet - e.g. argon or nitrogen - during laser cutting of a metal specimen is to shield the cut zone from oxidation and expel the molten layer from the cut kerf. The use of an active assist gas jet (air or oxygen) for laser cutting of a metal specimen affects the energy balance at the cutting zone. The oxygen gas jet plays two major roles during the laser cutting process, firstly the oxygen gas reacts exothermically with the molten metal resulting into energy addition to the cutting zone, and secondly the oxygen gas jet exerts the necessary thrust required to eject the oxidised melt from the cut kerf [36].

The effect of gas pressure on the process performance has been investigated by Hilton & Khan [53] and Sparkes et al. [54]. Hilton & Khan [53] used a 5 kW fibre laser to cut 304L stainless steel tubes of diameter up to 170 mm and wall thickness up to 11 mm. In this study, the maximum possible cutting speed increased with increasing assist air pressures from 2-10 bar particularly in tubes with lower thicknesses. In contrast, Sparkes et al. [54] reported very little difference in maximum cutting speed with

changes in focal position, nozzle diameter and cutting gas pressure of 10-20 bar in inert gas laser cutting on 6–10 mm thick stainless steel plates using a 2.2 kW fibre laser.

2.3.3 Thickness/ Cut depth

The depth of cut in laser cutting refers to the maximum sheet thickness that can be cut using an employed laser cutting condition. In commercial laser reactive cutting, maximum depths of cut around 12-15 mm in mild steel with 2 kW lasers are achievable [50]. Power levels substantially above 2 kW are required to cut plates above 15 mm thick with process stability reducing with increasing section thickness [55]. The maximum cutting speed at which a through cut is possible generally decreases with increasing material thickness in both inert [56] and reactive gas cutting [52] of steel with a 1.06 µm wavelength laser light source.

2.3.4 Wavelength

The wavelength of a particular laser depends on the energy levels of atoms in the laser medium and transitions in the process of stimulated emission [43]. The shorter the wavelength, the higher the absorptivity, and the finer the focus for a given mode structure and optics train [24]. The maximum absorption of laser energy with lowest reflection can be obtained with a certain wavelength for a specific material type. The two most common commercial lasers are CO_2 lasers with a wavelength of 10.6 µm and fibre/disk with 1.06 µm, both of which are used in cutting and welding processes [38]. Due to the shorter wavelength, fibre lasers have some advantages over CO_2 lasers. Important advantages of the fibre laser which are of special interest to laser cutting include [57]:

- Depth of focus, capability to focus;
- High absorption for metallic materials;
- Possibility to use fibre delivery;
- High electric efficiency;
- Compact design and mobility.

A comparison of the cutting speed between fibre/disk and CO_2 lasers in cutting steels was investigated by Hilton [19], Petring et al. [41, 58], Stelzer et al. [56], Wandera et al. [59] and Seefeld & O'Neill [60]. The main message of these publications is that the benefits of high beam quality as well as a shorter wavelength (as compared to the 10.6 µm CO_2 laser) in terms of cutting speed are much more obvious for cutting thin rather than thicker steel sections [58]. The reasons for the different performances between fibre/disk and CO_2 laser cutting are not yet completely realised and there are debatable discussions in the literature [38].

17

2.3.5   Stand-off distance

Another important practical parameter in laser cutting is the distance between the nozzle and the workpiece top surface – the stand-off distance (see Figure 6). This distance influences the flow patterns in the gas, which have a direct bearing on cutting performance and cut quality. A short stand-off distance gives stable cutting conditions, although the risk of damage to the lens from spatter is increased. The stand-off distance is normally selected in the same range as the diameter of the cutting nozzle to minimise turbulence. The nozzle stand-off distance is optimised to maximise cutting speed and quality [61].

The nozzle delivers the assist gas jet to the cutting front and the design of the nozzle orifice determines the shape of the cutting gas jet at the cutting front and influences the efficiency of melt ejection. The nozzle stand-off distance influences the gas flow dynamics at the entrance of the cut kerf and consequently influences the gas flow patterns at the cutting front. The gas flow patterns at the cutting front have a strong bearing on the resulting cut edge quality especially during high pressure inert gas assisted laser cutting [62-64].
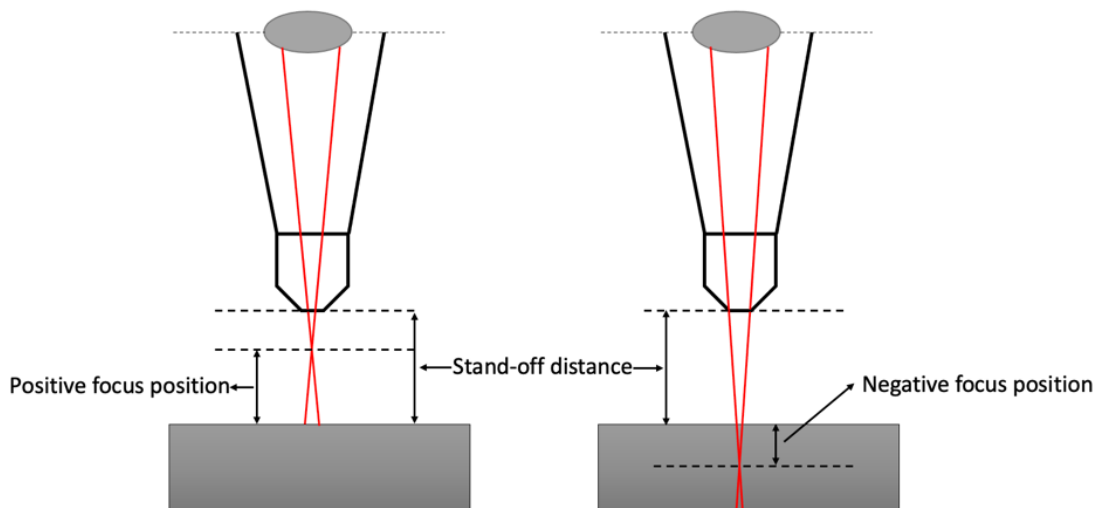
Figure 6: Definitions of stand-off distance and focus position distance (positive focus position - left and negative focus position - right)

2.3.6   Focus position

The focal point position is the location of the minimum focused spot size relative to the workpiece top surface and affects the laser power intensity on the workpiece [65]. The focus position can either be positive or negative depending on its location relative to the workpiece surface (see Figure 6). Generally, a positive focus position is located above the material surface and a negative focus position is located below the workpiece surface. In laser cutting processes, there is an optimum focal point position - for a particular workpiece thickness - which produces minimum cut edge surface roughness and minimum dross attachment on the lower cut edge. There are also focal

point positions where laser cutting through the material cannot be achieved because of the reduced power intensity on the workpiece [36].

The focus position controls the surface spot size which determines the surface power intensity and whether penetration will occur [24]. In reactive fusion cutting, the maximum cutting speed is achieved if the focal plane of the beam is positioned at the workpiece surface for thin metal sheets, or about one third of the plate thickness below the surface for thick metal plates [61]. In fusion laser cutting processes, however, the optimum position is closer to the lower surface of the plate, because a wider kerf is produced that allows a larger part of the gas flow to penetrate the kerf and eject molten material [61]. This was reported by Wandera and Kujanpaa [66] when conducting a series of inert cutting trials on 10 mm thick stainless steel using a 5 kW fibre laser.

2.3.7   Focal length

The focal length of the focusing lens determines the minimum focused spot size essential for high power intensity required for laser cutting of a metal workpiece. The relationship between the lens focal length and the focused spot diameter is defined as [67]:

$$d_f = \frac{4f}{D} BPP \tag{13}$$

Where d_f is the focused spot diameter, f is the focal length of the focusing lens, BPP is the Beam Parameter Product of the incident laser radiation and D is the raw beam diameter on the focusing lens.

The focal length also determines the depth of focus which is the effective distance over which the minimum focused beam diameter is maintained. The depth of focus is the distance over which satisfactory cutting can be achieved. The relationship between the lens focal length and the depth of focus is given as [67]:

$$d_Z = 4 \left(\frac{f}{D}\right)^2 BPP \tag{14}$$

Where d_Z is the depth of focus. The use of a shorter focal length lens for focusing of the incident laser beam gives a smaller focused spot size with high power intensity but with a smaller depth of focus, consequently a longer focal length may be necessary in some applications where a longer depth of focus is essential for good cut edge quality like in thick-section metal cutting [36].

2.4 Laser cut quality

Cut quality can be characterised in terms of perpendicularity or angularity of the cut edge, kerf width, surface roughness, dross height, cut edge surface roughness, boundary layer separation point and so on [24, 68]. These characteristics are explained in detail in the following sections.

2.4.1 Kerf width

The kerf is the cut slot that is formed during through-thickness cutting. It is normally narrower at the bottom of the workpiece than the top [61]. The cut kerf width is the distance separating the two cut surfaces of the cut slot and represents the amount of material removed during the laser cutting process [24]. In laser cutting processes, the diameter of the laser spot impinging the work piece defines the kerf width [37]. This is supported with many studies by Lopez [35], Chagnot et al. [37], Wandera & Kujanpää [69], Hashemzadeh et al. [70] and Himmer et al. [71]. Therefore, all cutting parameters that affect the beam spot size on the surface of the material affects the kerf width and that includes the focus position [72].

The cut kerf width also depends on the laser power and to some extent cutting speed [24]. Golnabi and Bahar [52] investigated the influence of cutting speed, laser power, thickness, material type and oxygen gas pressure on the average cut width using a Nd:YAG laser to cut stainless steel and mild steel workpieces. The average kerf width decreased with increasing cutting speed and increased with increasing laser power. The average kerf width was not greatly influenced by the assist gas pressure.

2.4.2 Dross height

Dross is the part of the melted material that is not completely ejected from the cut kerf but resolidifies and remains firmly attached to the lower cut edge (see Figure 7- the workpiece's shape is shown by the white lines provided.) [61]. The formation of adherent dross is closely related to the properties of the melt flow and the geometrical shape of the lower edge of the melting front [73]. Molten metals with high values of surface tension and viscosity are more difficult to eject from the cut kerf by the assist gas jet and can result in adherent dross on the lower cut edge.

Low gas pressure also increases the possibility of adherent dross [36, 66]. This was reported by Wandera [66] who investigated the effects of assist gas pressure, nozzle diameter, nozzle standoff, focal point position, and cutting speed in inert gas fibre laser cutting of 10 mm thick stainless steel workpieces. Dross attachment on the lower cut edge reduced with increasing assist gas pressure and cut kerf width. Overall, the assist gas pressure, nozzle diameter, and focal point position were found to significantly affect the efficiency of melt removal from the cut kerf and thereby minimise dross attachment [66].
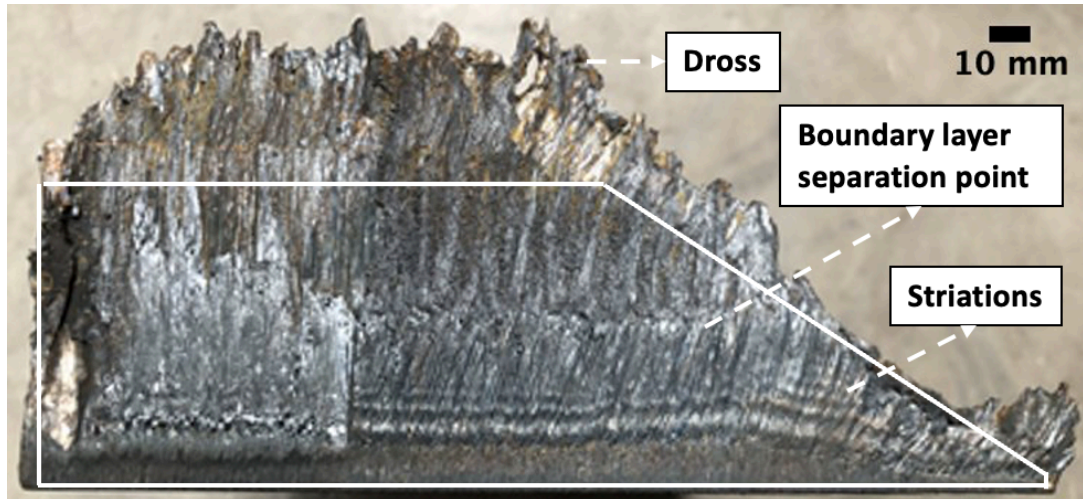
Figure 7: Dross attachment on the lower cut edge of a 5-50 mm thick C-Mn steel workpiece (10 kW laser power, 8 bar assist air pressure, 125 mm/min cutting speed, 4 mm stand-off distance and a focal point position 4 mm above the workpiece top surface underwater).

2.4.3 Surface roughness

The cut edge surface roughness is the unevenness or irregularity of the cut surface profile which is observed as striations on the cut edge. The dynamic behaviour of the laser cutting process affects the shape of the cutting front and the melt flow mechanism resulting in the formation of striations on the cut edge [73]. The mean height of the profile (average value of roughness), R_z, measured in micrometres is used in the quality classification [43]. The length of measurement is 15 mm, which is divided into five partial measuring lengths. The distance between the highest peak and the lowest trough is determined for each partial measuring length. Quality classes can be defined, based on those for thermal cutting techniques, which express roughness in terms of the material thickness, a. The classification of the mean height of the profile shown in Figure 8 are provided in the standard for thermal cuts (SFS-EN ISO 9013) [43, 74]. The lowest mean height of the profile (Class 1) gives the best cut quality in terms of the cut edge surface roughness.
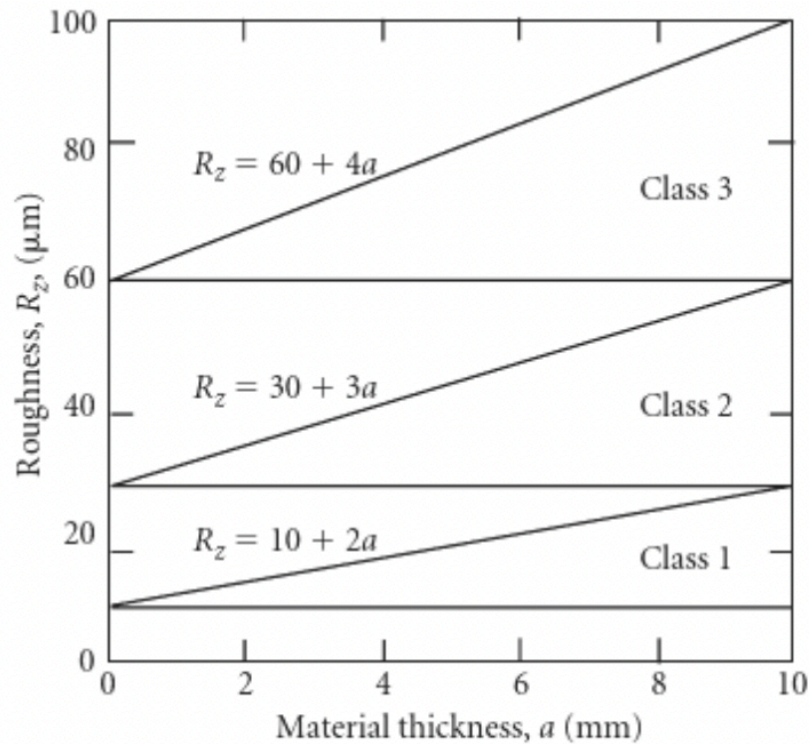
Figure 8: Quality classes for thermal cutting based on edge roughness [43, 74]

Generally, 1-micron fibre lasers give a better surface roughness when cutting thin materials, while CO_2 lasers give a better surface roughness when cutting thick materials. Hilton [19] compared the surface roughness of cutting stainless steel plate, from 0.6 to 6 mm in thickness, using an Yb:YAG disc laser and a CO_2 laser, both operating at 5 kW of power and using nitrogen assist gas. Using both lasers, cutting speeds were established for each material thickness which produced the best cut quality in terms of surface roughness. The disc laser could cut thin materials (0.6 and 1.2 mm thickness) at higher speeds and with lower edge roughness than the equivalent power CO_2 laser. However, for thicker stainless steel plates (3 and 6 mm thickness), the CO_2 laser produced better cut quality, particularly in terms of surface roughness [19]. Himmer et al. [57] and Wandera et al. [59], using both fibre and disc lasers, produced results that agree with the findings from this study at different cutting conditions.

2.4.4 Cut edge squareness (perpendicularity) deviation

The cut edge squareness (perpendicularity) deviation, u is the greatest perpendicular distance between the actual surface and the intended surface [43] (see Figure 9). The ranges for the classification of perpendicularity tolerances shown in Figure 10 are provided in the standard for thermal cuts (SFS-EN ISO 9013:2002) [43, 74]. The smallest perpendicularity tolerance - corresponding to Class 1 - is desired.
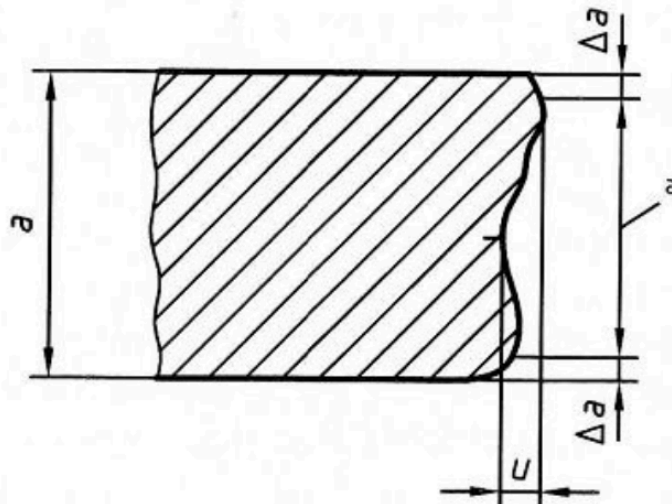
Figure 9: Squareness (perpendicularity) deviation, u of a vertical cut; a is the workpiece thickness and Δa is the thickness reduction for determination of perpendicularity tolerance [74]
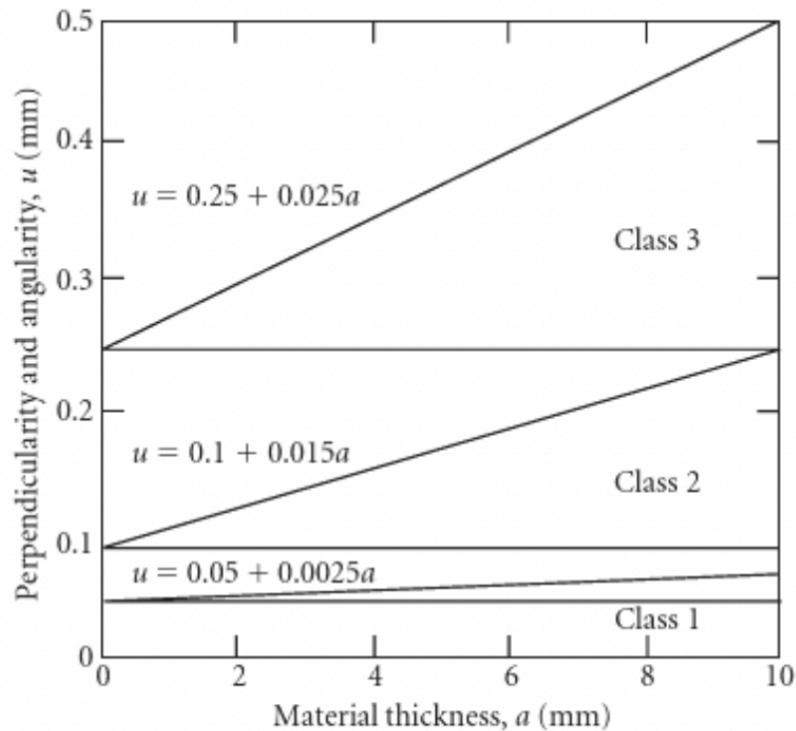
Figure 10: Quality classes for thermal cutting based on edge perpendicularity and angularity [43, 74]

2.4.5 Boundary layer separation point (BLS)

The boundary layer separation point (see Figure 7) is the depth where the flow separates from the solid kerf wall and the melt flow regime transitions from a laminar boundary layer flow to a turbulent boundary layer flow. The location where the melt flow separates from the solid kerf wall depends strongly on the velocity and thickness

23

of the melt [73]. Flow separation occurs when the mainstream flow decelerates in the flow direction and the static pressure in the mainstream increases in the flow direction according to the Bernoulli's equation (i.e. conservation of energy) [75, 76].

In laser cutting, more molten material is added to the melt layer as the melt flow progresses down the kerf; and the viscous shear in the boundary layer continuously retards the melt streamlines in the boundary layer, especially in the regions close to the solid kerf wall, causing a deformation of the velocity profile in the boundary layer. At some downstream location along the kerf wall (called separation point), the velocity of the streamlines close to the kerf wall becomes zero and the melt layer thickens rapidly to satisfy continuity within the layer. Downstream of the separation point, the fluid near the kerf wall starts moving in an upstream direction pushing the boundary layer and the mainstream flow away from the kerf wall (see Figure 7). The boundary layer separation point on the cut edge mostly appears in inert gas assisted laser cutting of thick-section metal depending on the process parameters [36].

2.5   Laser cutting for decommissioning applications

2.5.1   Background

The term "decommissioning'' refers to the safe end-of-life management of many different types of nuclear and offshore facilities [77]. In nuclear power plants, most Intermediate Level Waste (ILW) and High Level Waste (HLW) are stored underwater after service. Due to restrictions in storage space and increased risk of dose uptake during handling, the use of underwater cutting technology for dismantling or size reduction is often preferred [18]. For offshore facilities, as oil and gas fields reach the end of their lifespan, they must be decommissioned and the surrounding area returned to its natural condition. One feature that these two applications have in common is that the resulting cut quality is not a particular issue. In decommissioning, the key requirement is that the parts being cut must be separated with minimal secondary waste [20, 78].

The decision to decommission any facility is often based both on safety and on economics [77]. Therefore time, safety and cost are major drivers in decommissioning applications [78]. Compared to conventional cutting technologies, the cutting speed, remote deployment, automation, and flexibility offered by fibre lasers today is now being considered as a viable technology for dismantling large and complex structures in decommissioning applications. This is because compared to mechanical and other thermal cutting processes, laser cutting offers many benefits, which include [20, 78]:

- Light weight and small cutting head with flexibility offered by optical fibre beam delivery making remote deployment less difficult and costly;
- Minimal secondary waste which reduces risk to the operator and lower emissions on the environment;
- Ability to cut complex structural geometries with minimal reaction force on the part being cut;

- High degree of remote automation and large stand-off distance control;
- Low deployment input and maintenance, providing significant cost savings;
- Fibre laser systems are a high value asset that can be reused many times on multiple applications.

These benefits of lasers satisfy the major drivers in decommissioning applications. However, fire hazards and the laser beam effects on the structure below the cut raises major safety concerns in decommissioning applications [78]. In offshore decommissioning studies, oxygen should not be applied in underwater cutting applications [1] because oxygen that has not been used might create a fire or explosion hazard as the gas could be trapped underneath protrusions where it accumulates, as mentioned for hydrogen gas in underwater plasma cutting by Donaghy [79].In nuclear decommissioning studies, fusion laser cutting or reactive fusion cutting using air as an assist gas is normally used as the appropriate laser cutting method because the use of pure oxygen as a cutting gas is not allowed in a nuclear environment [20].

The best cutting performance in terms of speed and thickness for the same laser power among the reported results of thick steel fibre laser cutting for nuclear decommissioning applications were stated by Shin et al. [80, 81]. At a laser power of 6 kW and an assist air pressure of 10 bar, the maximum cutting speeds for a 60-mm thickness were 72 mm/min for the stainless-steel plates [80] and 35 mm/min for the carbon steel plates [81]. The high process performance achieved was attributed to the following [80, 82]:

- A developed cutting head for efficient cutting of thick steels;
- A small 0.1 mm process fibre diameter;
- A small spot size of 0.362 mm;
- A high focal length to give a high depth of focus;
- A small divergence angle of 39.372 mrad;
- A 1 mm stand–off distance;
- A step like increase of the cutting speed – a cutting technique which involves increasing the cutting speed gradually along the cut length to initiate the cut channel, couple the laser energy with the cut front and preheat the material.

Using a 10 kW fibre laser and air as an assist gas, this cutting technique was also used to cut 100 - 150 mm thick stainless steel plates and 100 mm thick carbon steel workpieces [81, 83]. For the thickness of 100 mm, both stainless steel and carbon steel plates were cut at maximum cutting speeds of approximately 30 mm/min. This group was also able to cut a 150-mm thick stainless-steel plate at a maximum possible cutting speed of 3 mm/min [83]. In the literature reviewed for laser cutting in decommissioning applications, this cut thickness is the highest among the published reports for fibre laser cutting using a laser power of 10 kW and air as an assist gas.

Shin et al. [81] also achieved the highest cutting capability of approximately 16.6 mm per kW. This means that their laser cutting system could cut a thickness of 16.6 mm per kW. A maximum cutting speed of 7 mm/min for stainless steel and 5 mm/min for carbon steel was achieved when a thickness of 100 mm was cut at a laser power of 6

kW [81]. The cutting capability of stainless steel was higher than that of carbon steel because the thermal conductivity of carbon steel is higher than that of stainless steel [81]. This process capability is much higher than that of other groups which are studying the use of high-power fibre lasers to cut thick steels using air as an assist gas for decommissioning applications. These groups include the Commissariat à l'Energie Atomique (CEA) [37], Japan Atomic Energy Agency (JAEA) [84], Hilton et. al. [78] and Chagnot et al. [37].

The advantages for in-air cutting for decommissioning applications is equally applicable for underwater decommissioning scenarios, and fibre lasers provided the transition platform from applications in-air to underwater. Recently, remote air and underwater fibre laser cutting for both nuclear and offshore decommissioning applications is being researched by many countries including the UK [10], Germany [85-87], China [88], India [89, 90] and South Korea [91-93].

2.5.2   Underwater laser cutting for subsea decommissioning applications

In the North Sea subsea industry, laser as a cutting tool is not yet established but the thought of its application has been around since the late 1970s [94]. In 1979, a patent for CO_2 subsea laser cutting was granted to Fenneman and Geres [95]. This patent is interesting since the presented arrangement incorporates many ideas used in the modern concept for underwater laser cutting for subsea decommissioning. The modern concept of underwater laser cutting when cutting from outside in was presented by Meinecke [1] (see Figure 11):

- The laser source on a vessel i.e. above the water;
- The laser beam guided from the vessel to the working location underwater via a fibre (in the patent guided by a light beam guide);
- The cutting location, protected by the means of a dry cavity created by the cutting gas (in the patent created by the means of a solid chamber).
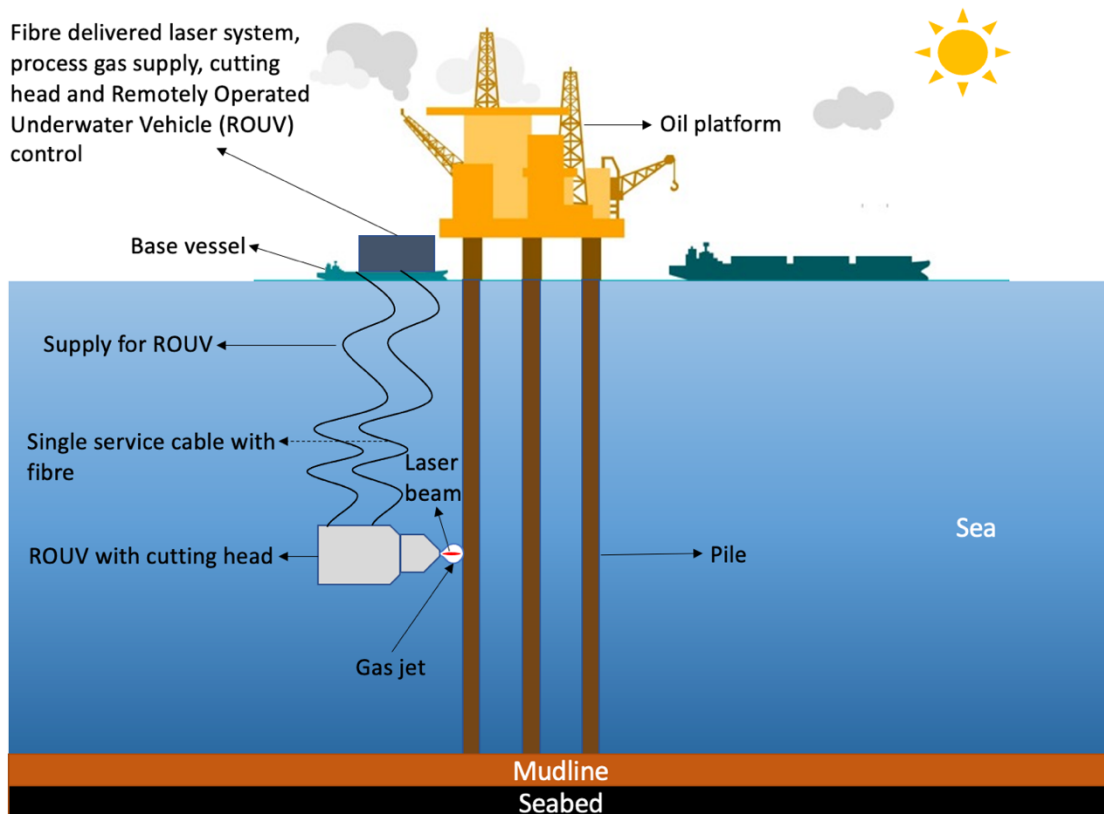
Figure 11: Modern concept of underwater laser cutting concept (from outside in) [1]

The modern concept differs technically from the US Navy patent insofar as the development in fibre laser technology has made underwater laser cutting more practical. With the developments in the fibre laser technology in terms of higher wall plug efficiency, increased flexibility and automation control, fibre lasers are now compact, almost plug and play devices of a robustness that allows for transportable, e.g. containerised, high power laser units [1, 96].

Underwater fibre delivered laser cutting has the potential to offer many benefits, which include [20, 78, 97]:

- Underwater laser cutting at extreme water depths without geometry limitations;
- The use of a non-contact laser process will eliminate the risk of mechanical jamming, thereby minimising down-time;
- Low deployment input and maintenance, providing significant cost savings and the need for divers;
- Fibre laser systems are a high value asset that can be reused many times on multiple applications;
- A safer subsea cutting method for workers as it does not require the use of chemicals, flammables, or explosives;
- Minimal secondary wastes which lower water pollution.

Having described the modern concept and potential benefits of underwater laser cutting, the technical aspects of the underwater laser cutting process will be discussed

in their technical chronology, one at a time with a comparison between conventional and underwater laser cutting at the end. This starts with the effect of water in laser material processing.

2.5.3   Laser-water interaction

The effect of water in laser material processing mostly consists of conversion of part of the light energy into a mechanical impulse (via vaporisation and plasma formation), which transports material (debris, particles on surface) and induces shock waves [94]. The sudden release of energy delivered by a pulsed laser beam on a material (solid, liquid or gaseous) may produce a small (but strong) explosion, which is associated, together with other effects (ablation of material, plasma formation and excitation), with a violent displacement of the surrounding material and the production of a shock wave [98].

When water/water vapour interacts with the light beam, it will either transmit, reflect or absorb laser radiation [24, 99]. One of the main issues of using lasers underwater is the energy absorption by the water environment [10]. The absorption coefficient can be calculated using Beer–Lambert law for transmitted laser power in equation (15) [94]:

$$P_L = P_{in} exp(-\propto h)$$
(15)

Here, P_L is the incident laser power, P_{in} is the transmitted laser power, $\propto$ is the absorption coefficient and h is the water column height. The absorption coefficient of water at 1.06 μm /1.07 μm wavelengths is ~0.135 cm^{-1} [100, 101].

For water, the relation between absorption coefficient, $\propto$, and the imaginary part of complex index of refraction, n, is [99]:

$$\propto= \frac{4\pi n}{\lambda}$$
(16)

The infrared reflection coefficient from water is nearly zero. Therefore, in most cases one could neglect the reflection coefficient in comparison to the absorption and transmission coefficients [99].

On transmission, the ray undergoes refraction described by Snell's law. The refractive index can be expressed as:

$$n = \frac{sin\varphi_{in}}{sin\psi_{in}} = \frac{v_1}{v_2}$$
(17)

Where ψ is the angle of refraction, v_1 is the apparent speed of propagation in medium 1 and v_2 is the apparent speed of propagation in medium 2. The apparent change in the velocity of light as it passes through a medium is the result of scattering by the individual molecules [24].

Scattering of light can be described as the phenomenon in which light rays deviate from their straight path when it hits an obstacle such as molecules of gas or dust, water vapours, etc [24]. Scattering of light depends upon various factors like the size of the particles causing the scattering, the wavelength of the light being scattered, and the density of the medium containing the particles. Rayleigh scattering occurs when particles much smaller than the wavelength of the incident light (for example, molecular clusters or imperfections in the silica lattice of a fibre) scatter the radiation in the form of a spherical wave. The extent of this power loss depends on the number of particles and the wavelength. Mie scattering occurs when the diameter of the particles is approximately the size of the incident wavelength. The scattering is less dependent on the wavelength. Bulk scattering occurs for particles much greater than the wavelength of incident radiation. The scattered laser intensity is almost independent of the wavelength [24].

Laser absorption in water is influenced by many parameters which include water height, salinity, water temperature and wavelength. Mullick et al. [102] investigated the effects of water column height, temperature, and laser intensity on the absorption coefficient for an unfocussed beam from a 2 kW CW Yb-fibre laser operating at 1.07 wavelength. The absorption coefficient was estimated to be 0.135 cm^{-1} at 25 °C water temperature, and this was found to decrease with temperature at a rate of 5.7×10^{-4} cm^{-1} °C^{-1}. Focussing the beam 5 mm below the water surface increased the absorptivity significantly. This increase in absorptivity was attributed to the absorption and scattering losses of laser radiation in a cavity formed underwater [102].

Laser propagation underwater was also studied in 1-micron lasers by Glova and Lysikov [103]. These authors conducted underwater laser cutting experiments on 0.15 mm thick titanium and stainless steel plates without an assist gas using a Nd:YAG laser at a water depth of 2 mm. During the underwater cutting process, the boiling process in the water volume adjacent to the focal spot was observed vividly. This was followed by gas bubbles produced by boiling emerging on the water surface and their symmetric propagation in water in the radial direction off the beam axis [103].

2.6 Underwater gas jet expansion numerical model

Before generating an underwater gas jet expansion model, an axisymmetric gas jet expansion model in air was simulated. A gas jet expansion model in air is necessary to understand the expansion and characteristics of compressible fluid flow with convergent nozzles. This model was simulated at different inlet pressure conditions and validated by the table of isentropic flow of perfect gases at approximately the same pressure ratios. The gas jet expansion model was simulated using the same

nozzle geometry specification and inlet pressure conditions used in the underwater laser cutting trials.

2.6.1 Gas jet expansion model in air

A flow is considered compressible when changes in the fluid's (gas or liquid) momentum produce significant variations in pressure and density, and the fluid's thermodynamic characteristics play a direct role in the flow's development [104]. Flows are usually treated as being incompressible when the Mach number (the ratio of the speed of the flow to the speed of sound) is smaller than 0.3 (since the density change due to velocity is about 5% in that case) [105]. Using the Mach number, M, compressible flows in converging nozzles can be nominally classified as follows [104]:

- Incompressible flow: $M = 0$. Fluid density does not vary with pressure in the flow field. The flowing fluid may be a compressible gas, but its density may be regarded as constant;
- Subsonic flow: $0 < M < 1$. The Mach number does not exceed unity anywhere in the flow field. Shock waves do not appear in the flow and subsonic flows for which $M < 0.3$ are often treated as being incompressible;
- Transonic flow: $0.8 < M < 1.2$. Shock waves may appear. Analysis of transonic flows is difficult because the governing equations are inherently nonlinear, and because a separation of the inviscid and viscous aspects of the flow is often impossible;
- Supersonic flow: $M > 1$. Shock waves are generally present. In many ways analysis of a flow that is supersonic everywhere is easier than analysis of a subsonic or incompressible flow. This is because information propagates along certain directions, called characteristics, and a determination of these directions greatly facilitates the computation of the flow field;
- Hypersonic flow: $M > 3$. Very high flow speeds combined with friction or shock waves may lead to sufficiently large increases in a fluid's temperature so that molecular dissociation and other chemical effects occur.

A compressible flow of a gas jet expanding in air was modelled using ANSYS Fluent 18.2 [21]. The flow conditions in a converging nozzle depend on the stagnation pressure, P_o and the back pressure, P_b (see Figure 12). At $P_b = P_o$, there is no flow in the nozzle. If the back pressure is reduced, a subsonic flow develops inside the nozzle. When the back pressure is further reduced, a subsonic flow develops until the gas reaches a critical pressure $P_* = 0.528P_o$ (for gasses with an adiabatic index, γ, of 1.4), where the Mach number at the throat of the nozzle, $M_t = 1$. This is when the condition of choked flow occurs, where mass flow rate is at a maximum and a further decrease of the back pressure, P_b has no effect in the nozzle flow. As a result, supersonic expansion waves appear at the nozzle exit to accommodate the nozzle exit pressure, P_e to back pressure, P_b [106].
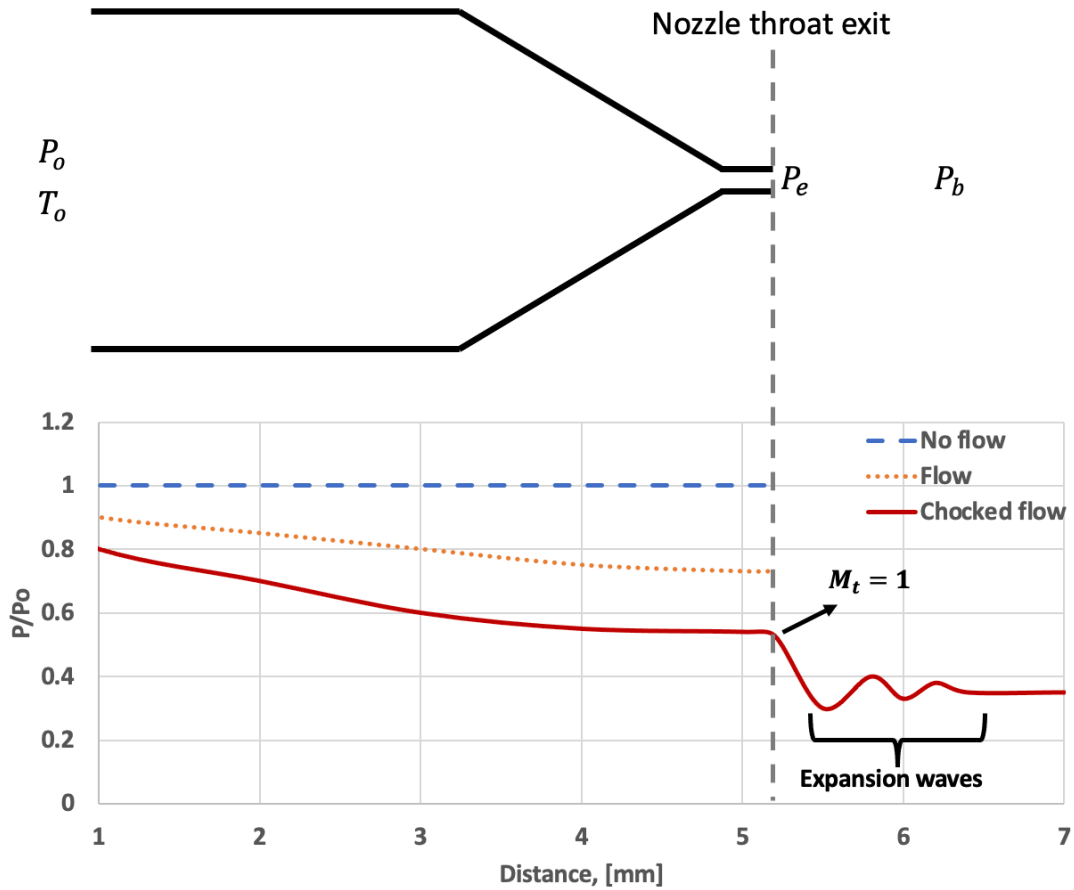
Figure 12: Illustration of isentropic compressible flow in a converging nozzle in air [106]

The set of governing equations consist of the mass conservation equation, momentum conservation equation, energy conservation equation and the original k-ε two-equation turbulence closure. The governing equations of compressible steady flow can be listed as follows [107]:

Continuity conservation equation:

$$\frac{\partial \rho}{\rho} + \frac{\partial u}{u} + \frac{\partial A}{A} = 0 \tag{18}$$

Momentum conservation equation:

$$-\frac{\partial p}{\partial x} = \rho u \frac{\partial u}{\partial x} \tag{19}$$

Energy conservation equation:

$$\frac{\partial u}{u}(M^2 - 1) = \frac{\partial A}{A} \tag{20}$$

Where ρ is the density, u is the velocity, A is the area, p is the pressure, u is the velocity, x is the distance and M is the Mach number [107].

2.6.2 Geometry and boundary conditions

The geometry of the numerical model was designed using SOLIDWORKS 2017 [108] and imported into ANSYS Fluent 18.2 [21]. This axisymmetric geometry was simulated using the same nozzle geometry specification and inlet pressure conditions used in the underwater laser cutting trials to investigate the characteristics of gas jet expansion using a convergent nozzle in air. Figure 13 shows the geometry and boundary conditions.

Figure 13: 2D geometry and boundary conditions in air

The design parameters of the nozzle geometry are as follows: length of nozzle throat is 2 mm; width of the nozzle throat is 2 mm; vertical height of the nozzle inlet is 20 mm; total length of the nozzle is 52 mm; length of the converging part of the nozzle is 20 mm; depth of nozzle from the outlet is 400 mm. The throat size is chosen to choke the flow and set the mass flow rate through the nozzle. The flow in the throat is sonic which means the Mach number is equal to one in the throat [107]. The inlet, outlet, symmetry, and wall boundary conditions are indicated by A, B, C and D, respectively (see Figure 13).

A pressure boundary type was set at the inlet and outlet. For the inlet, various inlet pressure conditions of 2, 4, 8, 16 and 32 bar were specified together with a temperature of 300 K. For the outlet, ambient pressure conditions (1 atmospheric pressure) and other flow variables are extrapolated. On the walls, the field wall boundary is under a stationary wall condition, no-slip and adiabatic rules pertain. The concerned flow field of the geometry is the external region of the nozzle along the symmetry boundary condition as this is the expansion region of the gas jet. Therefore, edge sizing with a maximum face size of 0.0001 m was specified at the symmetry boundary condition to set a finer mesh (see Figure 14).
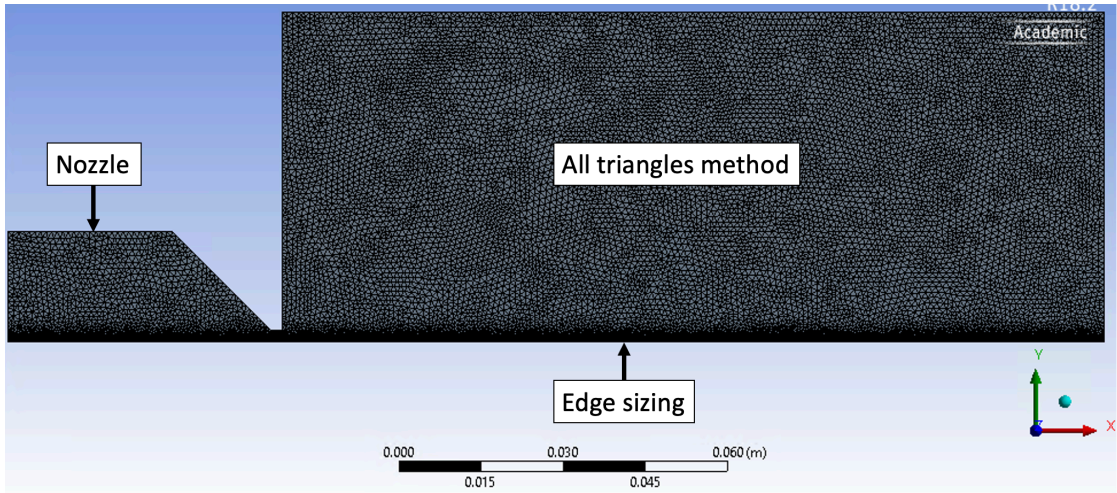
Figure 14: Mesh configuration

The all-triangle method was used to generate the computational mesh. For the grid independence study, air was taken as the working fluid and the simulation was run at an inlet pressure of 8 bar. A grid independence study was performed to make sure the solution is independent of the mesh resolution and to discover the optimum grid size for the present study [109]. Three different grid resolutions (course, medium and fine) were tested to find out the effect on the Mach number calculated at the nozzle exit Table 3 shows the mesh variables in the independence study.

Table 3: Grid independence study

Mesh Type	Number of elements	Number of nodes	Mach number at the nozzle exit
Course	11828	24747	2.01
Medium	20524	42793	2.03
Fine	42054	86475	2.05

According to Richardson extrapolation theory, for a grid refinement ratio greater than 1.3, the solution is independent of mesh resolution if it remains relatively constant [110]. The refinement ratio is given by [111]:

$$Refinement\ ratio\ 1 = \frac{Number\ of\ fine\ mesh\ elements}{Number\ of\ medium\ mesh\ elements} = \frac{42054}{20524} = 2.05 \quad (21)$$

$$Refinement\ ratio\ 2 = \frac{Number\ of\ medium\ mesh\ elements}{Number\ of\ course\ mesh\ elements} = \frac{20524}{11828} = 1.74 \quad (22)$$

Therefore, the Mach number is independent of the mesh resolution as there is no significant change in Mach number at all mesh types. As a result, a fine mesh of 86 475 nodes and 42 054 elements has been used to perform all the simulations for this model [112]. After setting up the geometry, mesh and boundary conditions, the setup of the model was configured.

2.6.3   Setup and solution procedure

At the beginning of the setup, a 2D serial analysis type solver was adapted. For the general settings of the setup, a density based steady axisymmetric model was specified. Air is assumed to be an ideal compressible gas with a density that conforms to the ideal gas law. The viscosity of air was assumed to follow Sutherland's Law and the whole flow field is axisymmetric. Table 4 shows the default air properties adapted in this model.

Table 4: Air properties [21]

Properties	Value
Operating pressure (Bar)	1
Reference temperature (K)	288.16
Ratio of specific heats of gas	1.4
Density (kg/m^3)	1.225
Thermal conductivity (W/m·K)	0.0242
Specific heat capacity (kJ/kg·K)	1.00643
Molecular weight (kg/kmol)	28.966

In reference to the solution method, a first upwind scheme was selected for the equations of turbulent kinetic energy, turbulent dissipation energy and flow. The first-order scheme was adapted because the second-order scheme is computationally expensive. An implicit formulation was also set [113]. Due to the broader stability characteristics of the implicit formulation, a converged steady-state solution can be obtained much faster than the explicit formulation. However, the implicit formulation requires more memory than explicit formulation [114].

The finite volume method (Fluent) computes fluxes across cell boundaries. This process can be separated into two steps: evaluating the face values on either side, and evaluating the flux given the two side values [115]. ANSYS Fluent 18.2 [21] provides spatial discretisation scheme options which refer to the first step, while the flux types refer to the second step. The Least Squares Cell-Based method was selected for the first step to compute the gradients needed not only for constructing values of a scalar at the cell faces, but also for computing secondary diffusion terms and velocity derivatives. This method was adapted as it has less computational cost than other node-based gradient methods [116]. The default Roe flux-difference splitting (ROE-FDS) convective flux type was adapted for the second step to solve for flux. The ROE-FDS convective flux type was specified as there is discontinuity at some of the cell boundaries (shocks) that need to be captured [113].

In regards to the solution formulation controls, the default courant number (a dimensionless value representing the time a particle stays in one cell of the mesh) and under-relaxation factors (factors of turbulent kinetic energy, turbulent dissipation rate and turbulent viscosity which ensure that the solution from one step to the next does not change too much as it then might get unstable) were set [117, 118]. Table 5 shows the default solution controls.

Table 5: Solution controls

Control factor	Courant number	Turbulent kinetic energy (J/kg)	Turbulent dissipation rate (J/kg.s)	Turbulent viscosity (kg/m.s)
Value	1	0.8	0.8	1

The solution calculation settings of the model were initialised from the inlet with the specified initial values of temperature and pressure. The solution was calculated until convergence was reached. At convergence, the following conditions were satisfied:

- All discrete conservation equations (mass, momentum, energy, etc.) are obeyed in all cells to a specified tolerance or the solution no longer changes with subsequent iterations;
- Overall mass (equation (18)), momentum (equation (19)), energy (equation (20)), and scalar balances are achieved for the generated Mach number distribution.

2.6.4 Mach number distribution

The Mach number contours were generated at different inlet pressure conditions. The same inlet pressure conditions of 2, 4 and 8 bar used in the underwater laser cutting trials in a $1m^3$ tank were specified, together with additional inlet pressure conditions of 16 and 32 bar to provide a wider range of inlet pressure settings. Figure 15 shows a gas jet expansion model at increasing inlet pressure conditions of (a) 2, (b) 4, (c) 8, (d) 16 and (e) 32 bar.
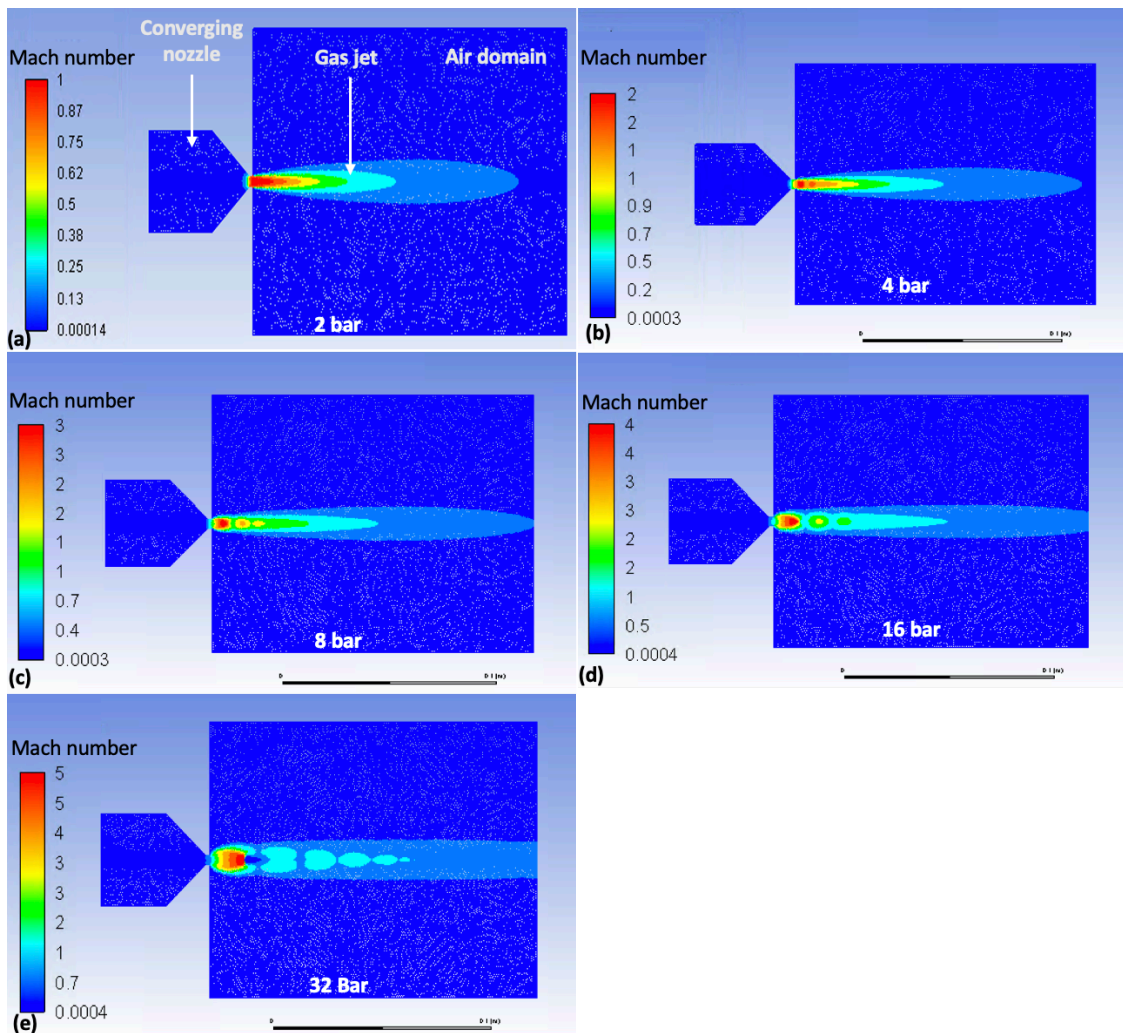
Figure 15: Mach number contour at an inlet pressure of (a) 2, (b) 4, (c) 8, (d) 16 and (e) 32 bar

At all inlet pressure conditions, near sonic conditions are reached at the throat of the nozzle ($M_t = 1$). Therefore, a fan of expansion waves appears at the nozzle exit to accommodate the nozzle exit pressure to back pressure. As the inlet pressure increases from 2 to 32 bar, the flow inside the nozzle is unaltered. This is because air is already travelling at the speed of sound at the nozzle exit at 2 bar, therefore, increasing the inlet pressure has no effect on the flow inside the nozzle as the maximum mass flow rate inside the nozzle has already been reached (choked flow). Consequently, the flow detects the increase in the inlet pressure only after it reaches the nozzle exit.

Outside the nozzle exit, air expands further and equilibrates with the ambient conditions downstream. This is accomplished by supersonic expansion waves centred at the centreline of the nozzle. The jet swells initially as it comes out of the nozzle and expands, but shrinks afterwards due to entrainment of the ambient air and equalisation of static pressure (see Figure 15) [107].

2.6.5 Validation of gas jet expansion model in air

The simulated gas jet expansion model in air is validated by one-dimensional (1D) mathematical equations of compressible flow in convergent nozzles. The mathematical equations for such a problem are well solved and have theoretical solutions. To validate the numerical method, the numerical findings were compared to theoretical solutions. The temperature, pressure and density ratios of isentropic flow can be calculated by the following equation (23), equation (24) and equation (25), respectively [104].

$$\frac{T_o}{T} = \left(1 + \frac{\gamma - 1}{2} M^2\right) \tag{23}$$

$$\frac{P_o}{P} = \frac{T_o}{T}^{\gamma/(\gamma-1)} = \left(1 + \frac{\gamma - 1}{2} M^2\right)^{\gamma/(\gamma-1)} \tag{24}$$

$$\frac{\rho_o}{\rho} = \frac{T_o}{T}^{1/(\gamma-1)} = \left(1 + \frac{\gamma - 1}{2} M^2\right)^{1/(\gamma-1)} \tag{25}$$

Where T_o, P_o and ρ_o are the stagnation temperature, pressure and density, respectively [106]. The table of isentropic flow provides the temperature, pressure, and density ratios for a given Mach number. As a result, the pressure ratios in the table of isentropic flow of a perfect gas can be used to validate an air jet expansion model of a convergent nozzle, assuming the flow through the nozzle is steady quasi-1D isentropic flow [106]. The Mach number values along the symmetry boundary condition of the gas jet expansion numerical model were plotted with the corresponding x-value location at an inlet pressure of 2, 4, 8, 16 and 32 bar (see Appendix A).

The values of the Mach number at the nozzle exit, M_e, were compared with the theoretical Mach number in the isentropic flow table of perfect gases at approximately the same pressure ratios. Table 6 shows a comparison between the Mach number at the nozzle exit and the theoretical value of the Mach number [106].

Table 6: Comparison between Mach number at the nozzle exit and theoretical value of Mach number for the same pressure ratio

Pressure ratio $(\frac{P}{P_o})$	Mach number at the nozzle exit (M_e) [106]	Theoretical Mach number (M)
0.5	1	1.04
0.25	1.51	1.56
0.125	2.05	2.01
0.0625	2.43	2.46
0.03125	2.9	2.91

Here, M_e is nearly identical to the values of M calculated from the table of isentropic flows at all pressure ratios [106]. Therefore, the simulated air expansion model is validated by the table of isentropic flow at all inlet pressure conditions. The simulated gas jet expansion model in air is more suitable for studies in conventional laser cutting. This study concerns underwater laser cutting; therefore, a multiphase underwater gas jet expansion model was simulated.

2.6.6 Underwater multiphase flow modelling

Underwater gas jet expansion is encountered in a variety of engineering applications such as underwater propulsion [119], metallurgical processes [120, 121], aeration treatment of wastewater [122], underwater cutting [123], and so on [124]. In underwater laser cutting, the study of the gas jet expansion underwater is important because of the following:

- The gas jet creates a dry cavity which protects the optical lenses from spatter and removes molten material from the kerf [1];
- The dry cavitation protects the optical path of a high-power laser beam from losing energy because of absorption underwater [125].

The ability to deliver a dry cavity is sometimes proved in underwater laser cutting experiments by preliminary gas jet tests, whereby the gas jet impinges against a transparent surface from the inside of a water filled tank so that the resulting dry cavity can be observed from the outside. Such underwater gas jet expansion experiments were conducted by Meinecke [1], Matsumoto et al. [123] and Zhang et al. [126].

The multiphase flow characteristics of a gas jet expanding underwater are turbulent and unsteady; the high-density ratio between water and gas can induce many complicated phenomena [23]. Figure 16 shows a sonic or supersonic gas jet expanding in a water environment [119]:
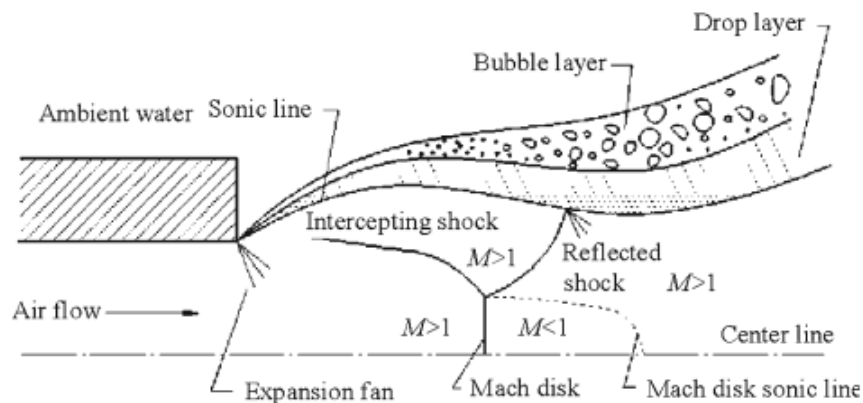
Figure 16: Under expanded gas jet injected underwater [119]

The dry cavity created by an underwater gas jet is surrounded by a gas–water mixing layer which consists of a drop layer and a bubble layer [119]. The shape of the nozzle is key to the underwater expansion process. The behaviour of the expansion process is largely dictated by pressure, both at the nozzle exit as well as at the external environment. If the external pressure is higher than the nozzle exit pressure, the expansion is referred to as over-expanded. If the external pressure is lower than the nozzle exit pressure, the expansion is referred to as under-expanded. The flow can also be fully expanded if the external pressure is equal to the nozzle exit pressure as in underwater laser cutting experiments by Seong et al. [127].

Seong et al. [127] performed underwater laser cutting experiments using a 6-kW fibre laser with two different nozzle configurations to extend the permissible cutting thickness of stainless steel workpieces underwater. The first nozzle configuration consisted of a single minimum length nozzle (MLN) operating at an upstream gas gauge pressure of 15 bar and the second dual configuration involved a truncated aerospike nozzle coupled with an MLN (see Figure 17). These configurations were designed to form an air cavity with denser and more lengthened characteristics for extending the possible transmission distance of the laser beam, which is vulnerable to water absorption [127].
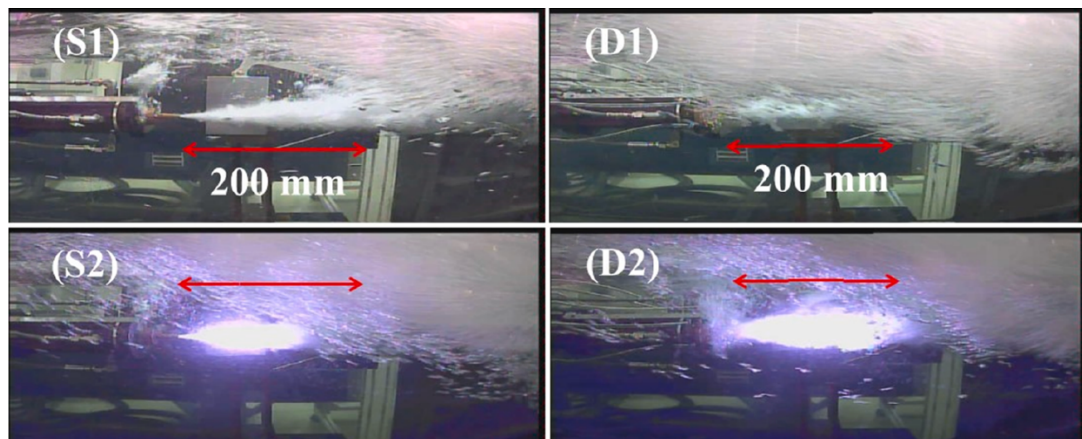
Figure 17: (S1) and (S2) are images of the submerged jet from the single nozzle at 15 Bar before and after 1 kW laser beam radiation. (D1) and (D2) are images of the submerged jet from the dual nozzle (inner MLN: 15 Bar, outer aerospike nozzle: ~10 Bar before and after 1-kW laser beam radiation [127].

Figure 17 (S1 and D1) clearly shows that the flow for both air jets is nonlinear and unsteady as buoyancy continuously expands the width of the submerged jet column that penetrates the water and simultaneously drives the jet toward the water surface [22]. This is because, inherently, there is a density difference between the surrounding water and the air-jet discharging from the nozzle exit [127]. As shown in Figure 17 (S2 and D2), the scattered linear length of the laser beam with the dual nozzle was longer than that of the single nozzle indicating that the laser beam from the dual nozzle extends further. Therefore, it was possible to cut an 80 mm thick stainless steel plate underwater at a low cutting speed of 5 mm/min with a laser power of 6 kW with only the dual nozzle configuration [127].

The development of a high-pressure gas jet flow underwater can be characterised by four processes. These processes are expansion, bulging, necking/breaking and back attack respectively [23, 128]. These flow structures were observed in both past numerical and experimental results by many authors including Miaosheng et al. [129], Shi et al. [130] and Tang et al. [23, 128]. Figure 18 shows the development of a gaseous jet injected underwater, where the results in column 1 are observed by Shi et al. [130] via experimental methods, and the results in column 2-4 are obtained via Navier-Stokes flow computation by Tang et al. [23]. Although the experimental and numerical cases are based on different conditions, qualitatively similar flow structures are observed. The phenomena of expansion, necking/breaking, and back-attack [131] have been highlighted, indicating that the flow development of and underwater gas jet is an unsteady process.
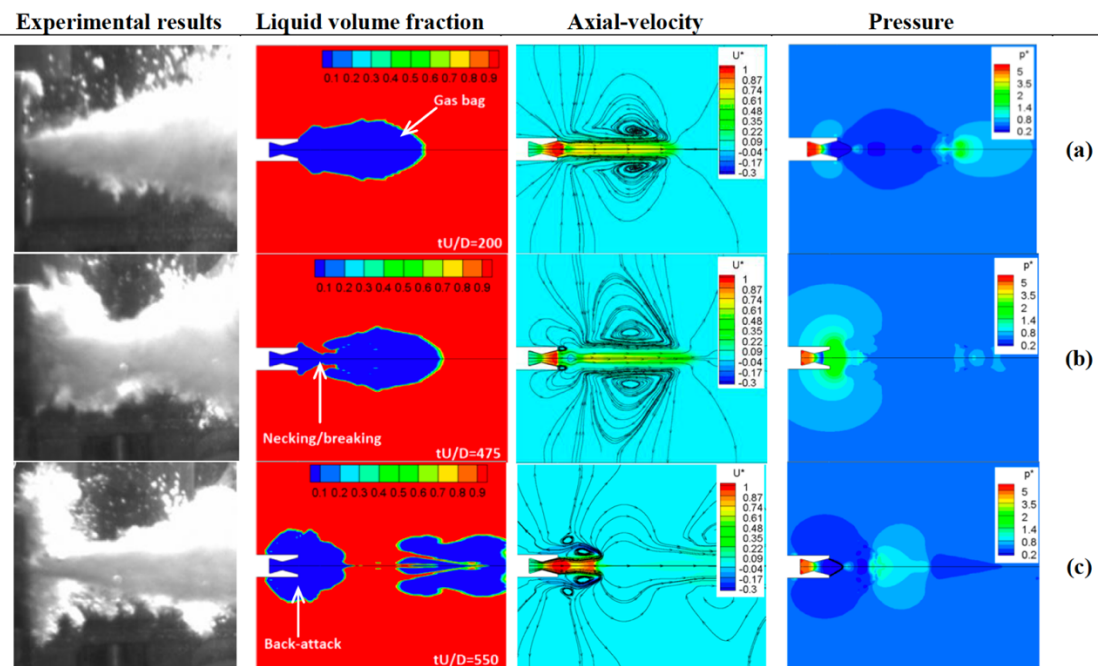
Figure 18: Flow structures of (a) expansion, (b) necking/breaking, and (c) back-attack process [23]

2.6.6.1 Expansion

Initially, when the gas is injected into the water, the gas pressure is not high enough to overcome the inertia effect of the water due to the large density ratio between the two fluids. Therefore, a 'gas bag' is formed behind the nozzle exit [130]. The pressure inside the 'gas bag' continues to increase and accumulate until it is high enough to overcome the suppression of the water. The gas then expands freely to complete the expansion process [23]. After the expansion process is complete, the bulging flow structure occurs.

2.6.6.2 Bulging

During bulging, a small bulged bubble appears near the nozzle exit. This occurs due to the shock wave movement in the gas region. The bulged bubble does not collapse and

is usually swept downstream. The bulged bubble appears several times before the necking/breaking flow structure [130, 132].

2.6.6.3 Necking

During necking, the air bag collapses and separates the gaseous jet into two parts. This occurs due to the air bag which becomes unstable as a result of the abrupt change in the pressure difference between the surrounding water and the bulged bubble [23]. After necking/breaking, the back-attack phenomenon occurs.

2.6.6.4 Back attack

Back-attack is characterised by the presence of a negative axial-velocity at the rear part of the nozzle [131, 133]. Shi et al. [130] proposed that back attack is caused by shock wave feedback but Tang et al. [23] explained that the gas jet propagating in a water environment has difficulties moving downstream after necking, this creates the backflow which impacts the nozzle surface.

An underwater gas jet expansion model based on a study by Tang et al. [119] was simulated and compared to the volume fraction of water and velocity contours observed during the development of the gas jet. This model was simulated as it is nearly similar to the subject of this study. As a benchmark for all underwater gas jet expansion models that were simulated in this research, an underwater gas jet expansion model based on a study by Tang et al. [134] was simulated using ANSYS Fluent 18.2 [21].

Tang et al. [134] investigated the flow characteristics that occur during the development of a gas jet underwater from a horizontal nozzle, where a converging-diverging Laval nozzle is used. A multiphase transient axisymmetric flow was simulated using the volume of fluid model, k-ε two-equation turbulence model and energy transfer were considered. The numerical model by Tang et al. [134] was simulated as it is more similar to the subject of this study. The geometry, boundary conditions, setup and solution procedure of this model were adapted.

The set of governing equations adapted consists of the conservative form of the Navier-Stokes equations, the original k-ε two-equation turbulence closure, and a transport equation for the gas volume fraction. The continuity, momentum, energy and VOF model equations for underwater gas jets are listed as follows [23, 134-136]:

Continuity conservation equation:

$$\frac{\partial \rho_m}{\partial t} + \frac{\partial (\rho_m u_i)}{\partial x_i} = 0 \tag{26}$$

Momentum conservation equation:

$$\frac{\partial(\rho_m u_i)}{\partial t} + \frac{\partial(\rho_m u_i u_j)}{\partial x_j} = -\frac{\partial p}{\partial x_i} + \frac{\partial y}{\partial x_j}[\mu_m(\frac{\partial u_i}{\partial x_j} + \frac{\partial u_j}{\partial x_i})] \tag{27}$$

Energy conservation equation:

$$\frac{\partial}{\partial t}\sum_{k=w,g}(a_k \rho_k E_k) + \frac{\partial}{\partial x_j}u_j\sum_{k=w,g}[a_k(\rho_k E_k + p)] = \frac{\partial}{\partial x_j}\left(k_{eff}\frac{\partial T}{\partial x_j}\right) \tag{28}$$

Volume transfer equation:

$$\frac{\partial}{\partial t}\left(a_g \rho_g\right) + \frac{\partial}{\partial x_i}\left(\rho_g u_g u_i\right) = 0 \tag{29}$$

Where ρ_m is the density of the mixture, u_i and u_j are velocity components, t is the time, x_i and x_j are distance components, p is the pressure, a_k is the volume fraction of the fluid (subscript k denotes gas or water), ρ_k is the density, E_k is the energy, k_{eff} is the effective thermal conductivity, T is the temperature, a_g is the volume fraction of gas, ρ_g is the density of gas and u_g is the velocity of the gas. The effective thermal conductivity k_{eff}, can be expressed as [23, 134-136]:

$$k_{eff} = k_t + k, \tag{30}$$

Here k_t is the turbulent thermal conductivity and k is the thermal conductivity. Since the Froude number (a dimensionless number representing the ratio of inertial and gravitational forces) in the gaseous jets is $O(10^3)$, the energy, E_k in equation (28) is as follows [23, 134-136]:

$$E_k = \begin{cases} h_k - \frac{p}{\rho} + \frac{v_k^2}{2}, & k = g, \\ h_k, & k = w. \end{cases} \tag{31}$$

Where h_k is the enthalpy based on the specific heat capacity at constant pressure and the temperature (subscript k denotes gas or water - see equation (31)), ρ is the density and v_k is the normal velocity.

The physical property of the mixture, ϕ_m can be specified as density, coefficient of viscosity and so on. This term can be expressed as [23, 134-136]:

$$\phi_m = \phi_g a_g + \phi_{gw}(1 - a_g) \tag{32}$$

Where subscript w denotes water and g represent gas. The volumes of the water and gas phases satisfy [23, 134-136]:

$$a_w + a_g = 1 \tag{33}$$

Where a_w is the volume fraction of water. The density of two phases is as follows [137]:

$$\rho_k = \begin{cases} p/RT, & k = g, \\ const, & k = w. \end{cases} \tag{34}$$

Where R is the ideal gas constant.

2.6.7   Turbulence model

The original k-ε turbulent model has been used in this study. The turbulence kinetic energy, k, and its rate of dissipation, ε, are obtained from the following equations [134]:

$$\frac{\partial}{\partial t}(\rho_m k) + \frac{\partial}{\partial x_j}(\rho_m k u_j) = \frac{\partial}{\partial x_j}\left[\left(\mu_m + \frac{\mu_t}{\sigma_k}\right)\frac{\partial k}{\partial x_j}\right] + G_k \tag{35}$$
$$+G_b - \rho\varepsilon - Y_m$$

$$\frac{\partial}{\partial t}(\rho_m \varepsilon) + \frac{\partial}{\partial x_j}(\rho_m \varepsilon u_j) = \frac{\partial}{\partial x_j}\left[\left(\mu_m + \frac{\mu_t}{\sigma_\varepsilon}\right)\frac{\partial \varepsilon}{\partial x_j}\right]$$
$$+C_{1\varepsilon}\frac{\varepsilon}{k}(G_k + C_{3\varepsilon}G_b) - C_{2\varepsilon}\rho\frac{\varepsilon^2}{k} \tag{36}$$

Here μ_m is the dynamic viscosity of mixture, μ_t is the turbulent viscosity, G_k represents the generation of turbulence kinetic energy due to the mean velocity gradients, G_b is the generation of turbulence kinetic energy due to buoyancy, and Y_m represents the contribution of the fluctuating dilatation in compressible turbulence to the overall dissipation rate; it is defined as $Y_m = 2\rho\varepsilon M^t$ and $M^t = \sqrt{k/\gamma RT}$ is the turbulent Mach number (γ is the ratio of specific heats of gas). The constants $C_{1\varepsilon} = 1.44$ and $C_{2\varepsilon} = 1.92$. The values for the turbulent Prandtl numbers for k and ε, are $\sigma_k = 1.0$, and $\sigma_\varepsilon = 1.3$, respectively. The turbulent viscosity of the model is defined as [134]:

$$\mu_t = \frac{C_\mu \rho_m k^2}{\varepsilon}, \qquad C_\mu = 0.09 \tag{37}$$

The main flow characteristics that occur during the development of a gas jet underwater were simulated and compared to the findings from the study.

2.6.8 Flow characteristics of an underwater supersonic gas jet

The main flow characteristics that occur during the development of a gas jet underwater, such as (a) expansion, (b) necking/breaking, and (c) back-attack, are highlighted in Figure 19. The results in the first column were observed via experimental methods by Shi et al. [130], the results in the second column were obtained via Navier-Stokes flow computation by Tang et al. [134] and the results from the third column were simulated in this study based on the literature study by Tang et al. [134]. The solution time, tU/D, indicated in the results of the second column is a dimensionless parameter. The simulated liquid volume fraction contours are placed side-by-side with the results from previous studies for comparison.
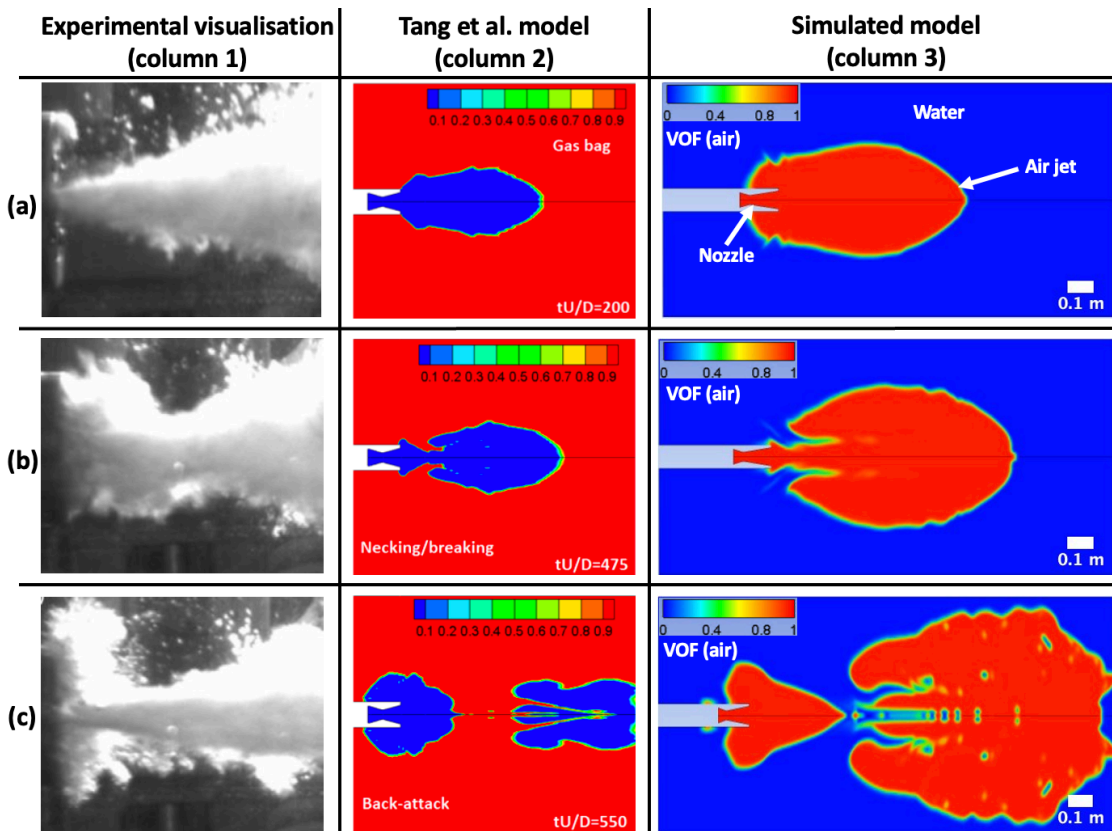
Figure 19: Comparison of the air volume fraction contour for an underwater gas jet expansion during (a) expansion, (b) necking/breaking, and (c) back-attack process from Shi et al. [130] (column 1), Tang et al. [134] (column 2) and simulated model from this study (column 3)

Although the experimental and numerical cases are based on different conditions, qualitatively, similar flow structures are observed. The phenomena of expansion, necking/breaking, and back-attack have been highlighted, indicating that the flow development of an underwater gas jet is an unsteady process. Overall, Figure 19 shows that the water volume fraction contour plotted by the developed model is substantially the same as the findings from previous structures.

Figure 20 shows a comparison of the axial velocity flow field for the main flow structures in the development of an underwater gas jet. The findings in the first

44

column were reported by Tang et al. [134] and the results in the second column were generated from the simulated model. The normalised axial-velocity, U^*, indicated in the legend of the first column can be expressed as:

$$U^* = {u}/{U} \tag{38}$$

Where u is the axial velocity and the nozzle exit velocity, U, is 1957 m/s [134]. When $U^* = 1$, the axial velocity, $u = 1987 \; m/s$. Therefore, the range of the simulated axial velocity is relatively similar to that reported in [134].
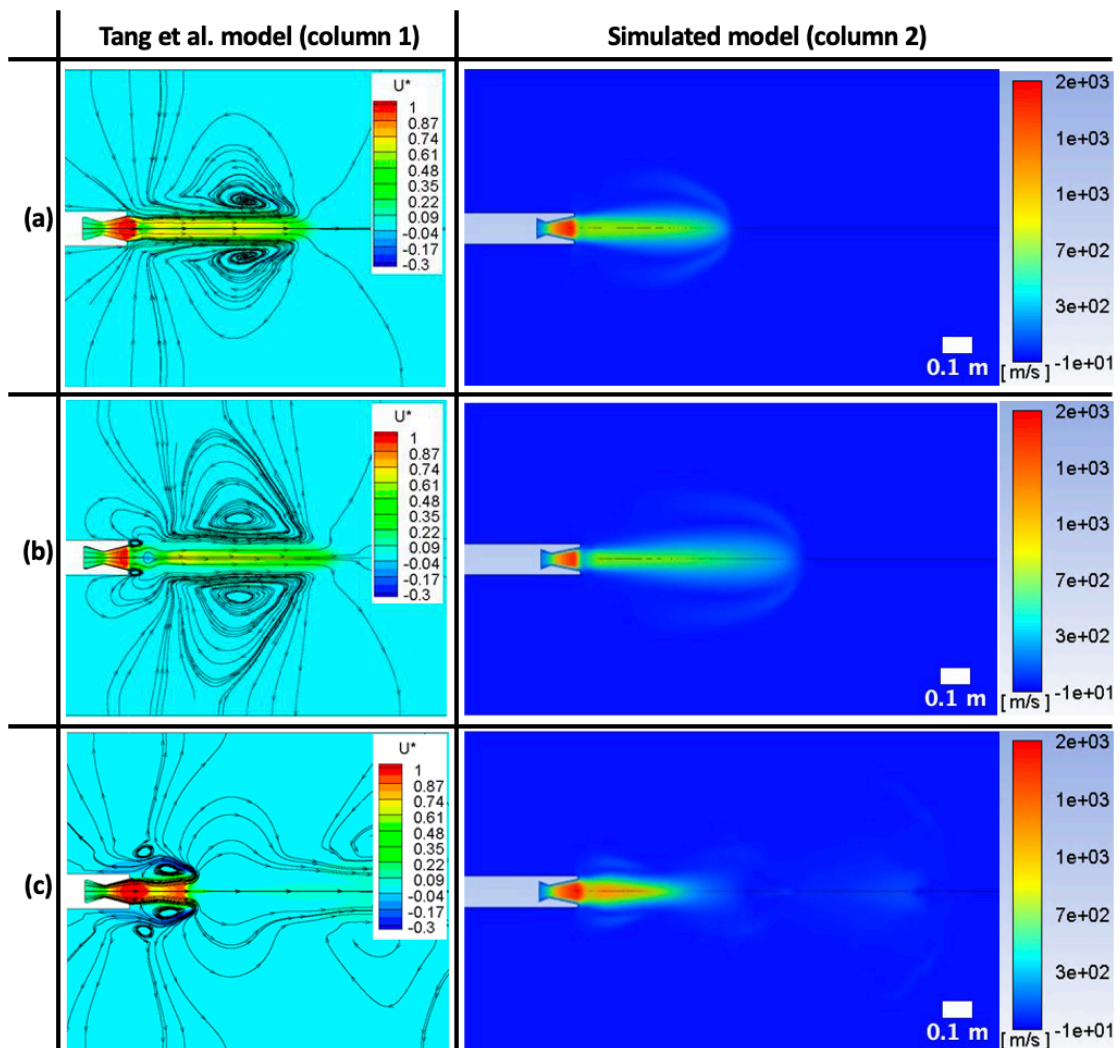
Figure 20: Comparison of the axial velocity contour for an underwater gas jet expansion during (a) expansion, (b) necking/breaking, and (c) back-attack process from Tang et al. [134] (column 1) and simulated model from this study (column 2).

Figure 20 indicates that the axial velocity field structure is nearly identical to that of the previous study. The presence of a negative value in the axial-velocity range is a typical characteristic of the back-attack process. However, as seen from the axial-velocity contour shown in Figure 20 (c), it is clear that the negative velocity only appears near and along the edges of the main flow passage, so that back-attack is not the whole gas jet blowing backward [23, 134].

45

It is vital to note that two forces act on a submerged jet when it is injected underwater: a downward force called gravity and an upward force called buoyancy. Both gravity and buoyancy have a significant effect on the flow field structure [128]. These forces were not considered in the underwater gas jet expansion model by Tang et al. [134] as it is axisymmetric.

2.7 Underwater laser cutting parameters and process performance

2.7.1 Maximum cut thickness

The maximum cutting speed at which a through cut is possible decreases as the thickness of the material being cut increases [20, 91, 92, 138]. The best cutting performance in terms of speed and thickness for the same laser power among the reported results of thick steel underwater laser cutting using air as an assist gas were achieved by Shin et al. [91, 92]. At a power of 6 kW, stainless steel with thicknesses of 50 and 60 mm were cut at a cutting speed of 80 and 40 mm/min, respectively [92]. At a laser power of 9 kW, the maximum cutting speeds at thicknesses of 50, 60 and 70 mm were 180, 110, 80 mm/min, respectively [91]. This high process performance was attributed to the step-like increase of the cutting speed which is implemented in the initial stage of cutting. Figure 21 shows a detailed description of the initial cutting of 60 mm thickness for the cutting speed of 40 mm/min at a low water depth [92]:
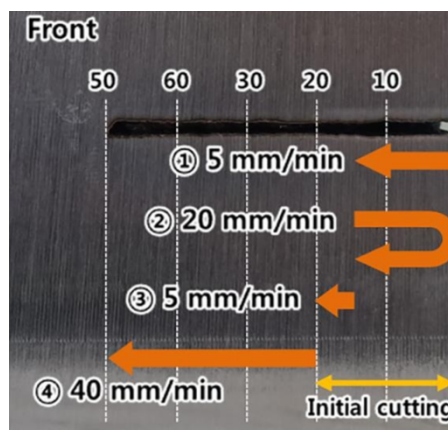
Figure 21: The step-like increase of the cutting speed to cut a 60 mm thick stainless steel using 9 bar assist air pressure at 6 kW [92]

The highest metal thickness cut underwater was also achieved by Shin et al. [91]. At a laser power of 9 kW, an initially pierced specimen or a double nozzle was required to successfully cut 80 to 100 mm thick stainless steel workpieces at very low cutting speeds of 5 - 10 mm/min [91].

2.7.2 Power

In underwater laser cutting, the maximum cutting speed normally increases with increasing laser power provided the power intensity on the workpiece surface increases. The effect of laser power on the cutting speed was investigated by Hilton & Khan [20] when cutting 6 mm and 12 mm thick C-Mn steel and stainless steel at 2-5 kW using 8 bar air pressure. The cutting speed increased linearly with laser power and the increase in cutting speed was more significant in 6 mm than 12 mm for both materials. This is because increasing the cutting speed decreases the conductive loses from the cut zone thereby the cutting efficiency is increased. As a result, cutting a thinner workpiece is more efficient than cutting a thicker workpiece and increases in the laser power lead to greater cutting speeds for thinner materials [20].

2.7.3 Gas pressure

The gas pressure is one of the most important parameters in underwater laser cutting because it creates a dry cavity which shields the beam from the hydrostatic pressure conditions underwater and removes molten material from the kerf. As the gas pressure increases, the cutting performance generally increases slightly. Figure 22 shows the maximum underwater cut thicknesses in C-Mn steel as a function of set cutting speed for two stand-off distances at assist air pressures of 2, 4, and 8 Bar [20]:
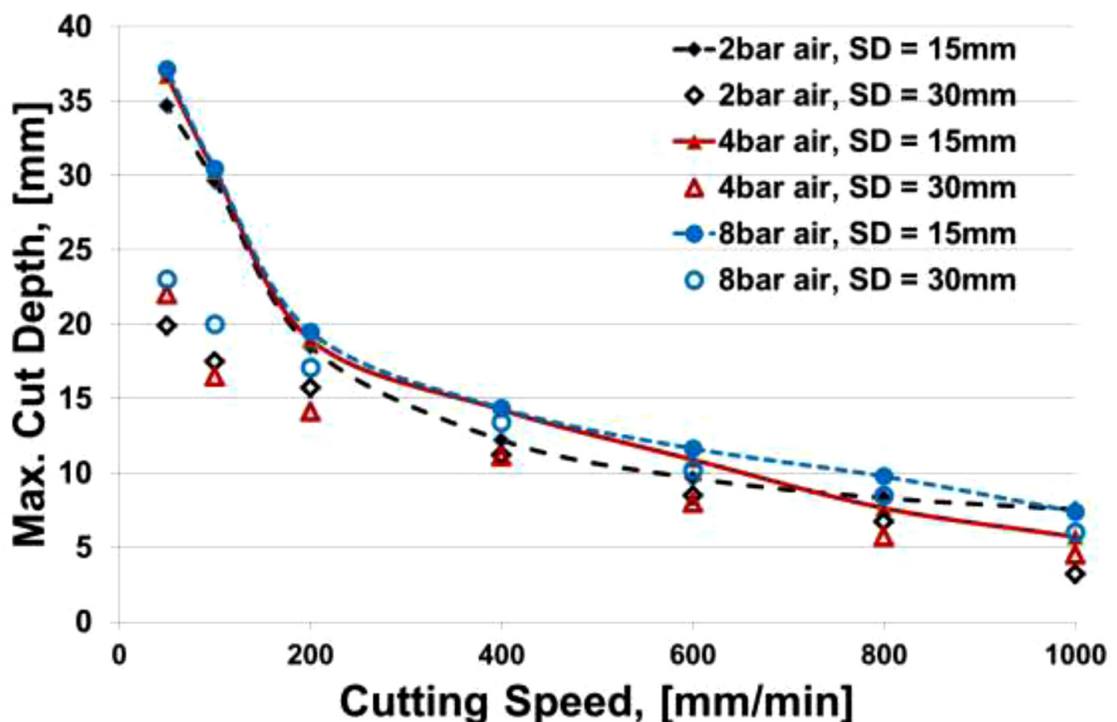
Figure 22: Maximum underwater cut depths in C-Mn steel as a function of set cutting speed for two stand-off distances at assist air pressures of 2, 4, and 8 Bars [20]

Figure 22 also indicates that increasing the stand-off distance decreases the maximum cut depth particularly for lower cutting speeds below 200 mm/min.

2.7.4 Stand-off distance

The effect of stand-off distance on the process performance was also investigated in underwater laser cutting trials on a 14 mm thick stainless-steel plate at 4 kW using air as an assist gas by Chida et al. [138]. Figure 23 shows the effect of stand-off distance on cutting speed.
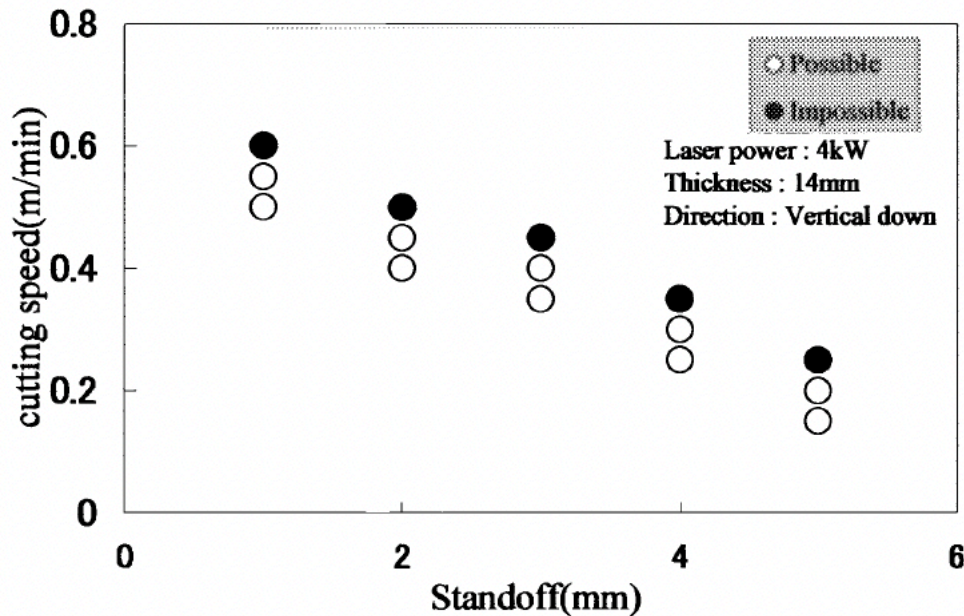
Figure 23: Effect of stand-off distance on cutting speed [138]

Figure 23 indicates that at a low water depth of 500 mm, the cutting speed decreased with increasing stand-off distance. The low cutting performance was attributed to the decrease of the gas jet momentum which occurs as the stand-off distance increases. Moreover, a wider spot size on the surface of the test-piece causes a lower power density, which leads to poor cutting performance underwater [138].

2.7.5 Water depth

As a general rule, as the water depth increase by 10 m, the hydrostatic pressure increases by 1 bar [139]. Hydrostatic pressure is exerted by a fluid (water) at equilibrium at a given point within the fluid, due to the force of gravity. The hydrostatic pressure, P_{hydro} acting on a submerged body underwater is expressed as [139]:

$$P_{hydro} = \rho g h \qquad (39)$$

Here, ρ is the density of the fluid, g is the gravitational constant and h is the height of the fluid column (water depth). Therefore, water depth controls the hydrostatic pressure acting on a body since all the other variables on the right-hand side of the

48

equation are generally constant. The hydrostatic pressure increases with water depth due to the increasing force being exerted downwards by the weight of the fluid.

In the researched literature, the greatest water depth found for underwater fibre delivered laser cutting using air or an inert gas is less than 1 m. The greatest water depth in which underwater laser cutting was carried out using oxygen assist gas is 50 m [88]. Laser cutting of 30 mm thick steel plates was carried out by simulating the circumstance of underwater conditions at 50 m by Wang et al. [88]. The influence of oxygen pressure, stand-off distance, cutting speed on the kerf width and surface roughness were investigated. The kerf width decreased with increasing cutting speed. Furthermore, difficulties in cutting the lower part of the workpiece were observed at low assist gas pressures but these were resolved by increasing the oxygen pressure [88].

Also using oxygen, Alfille et al. [140] investigated and compared the cutting capabilities of a YAG laser with an average power of 1.2 kW and a 5 kW CO_2 laser. Underwater cutting trials were performed on stainless steel (304L) plates with a thickness of 10 to 40 mm at a water depth of 0.5, 4 and 7 m. The maximum cut thickness decreased rapidly with increasing cutting speed. A 31 mm thick stainless-steel plate was cut using an oxygen pressure of 4-bar, a water depth of 7 m and low cutting speeds under 30 mm/min. A detailed description of the experiment setup and the advantages of a pulsed YAG laser over CO_2 lasers in operation (beam transport by fibre optics), cut quality and maximum cut thicknesses are described by Alfille et al. [140].

2.8   Cut quality underwater

2.8.1   Dross height

The effect of various process parameters on dross height in underwater laser cutting using a 5kW Yb fibre laser was investigated by Hilton & Khan [77]. In this study, 304 stainless and C-Mn (S275JR) steel, at thicknesses of up to 32 mm were cut using air as a cutting gas at a water depth of 600 mm. Dross height at the base of the underwater laser cut S275JR C-Mn steel workpiece was significantly larger than that produced when cutting 304 stainless steel. This was attributed to the decrease of oxide formation in C-Mn steel, a significant volume of the dross produced is metal which tends to attach at the base of the cut in long filaments. These filaments re-solidify at a faster rate, when compared to filaments in stainless steel. For both materials, the attached dross height increased with decreasing cutting speed and increased with increasing power (under specific conditions), thickness, stand-off distance and an increase in the focus position above the material surface [18, 77].

2.8.2 Kerf width

The effect of stand-off distance and thickness on kerf width in underwater laser cutting was also investigated by Chida et al. [138]. Chida et al. [138] cut a 14 mm thick stainless-steel plate at 4 kW using air as an assist gas and observed that the kerf width on the surface was very narrow but the kerf width on the back tended to be getting wider when the stand-off distance or thickness was increased. This widening effect of kerf width was also observed in underwater laser cutting experiments by Matsumoto et al. [123] and Singh [141]. No reason was given as to why the kerf width was widening. This limited information might be because the major focus in most of the early published literature in underwater laser cutting was to see if cutting was feasible [1].

In recent published studies, underwater cutting of 50 and 60 mm thick stainless steel plates with a 6-kW fibre laser were performed by Shin et al. [92]. The kerf width of the rear surface was smaller than that of the front surface when the stand-off distance or thickness were kept constant. The reason for the narrowing effect of the kerf width was that the amount of heat conduction throughout the kerf was small because the workpiece was rapidly cooled by water [92].

2.9 Comparison between conventional laser cutting and underwater laser cutting

Compared with in-air cutting, the performance in underwater cutting is greatly reduced. This was found by Meinecke [1], Shin et al. [92] and Hilton & Khan [20]. Shin et al. [92] conducted conventional and underwater laser cutting experiments of 50 and 60 mm thick stainless-steel plates using a 6-kW fibre laser and air as an assist gas. The reasons the underwater cutting performance was worse than in-air cutting when using the same process parameters can be assumed as follows [92]:

- The specimen is quickly cooled by the surrounding water;
- The dry cavity is not well formed, and the laser is absorbed into the water before it reaches the front surface of the specimen;
- The assist gas jet cannot blow the melt well due to the resistance of the water.

Among them, it was concluded that the cooling effect is the dominant reason which reduces the cutting speed in underwater laser cutting. This is because the process performance was not significantly influenced by changing the stand-off distance from 1 to 10 mm or cutting with a shroud. Therefore, the local dry zone is well formed and assist air pressure of 10 Bar was sufficient to blow the melt at the low water depth used in their study [92].

Meinecke [1] also performed experiments which compared laser cutting in air and underwater using the same process parameters. Underwater laser cutting experiments were conducted on 10 mm C-Mn steel workpieces at 4 kW using 9 bar

assist nitrogen pressure at a water depth of 50 mm. It was concluded that the limiting effect of underwater laser cutting is the melt removal behind the laser beam. This is because the kerf width which is related to the beam's spot diameter was almost the same in air and underwater. This indicates that the interaction of the beam from the nozzle to the workpiece was not significantly affected by the water environment due to the dry cavity [1].

However, bridges (connections from the left and right side of the cut kerf – see Figure 24) mostly occurred in underwater laser cutting than in air, indicating that the water environment interacts with the melt. These bridges occurred in the lower part of the cut kerf [1].
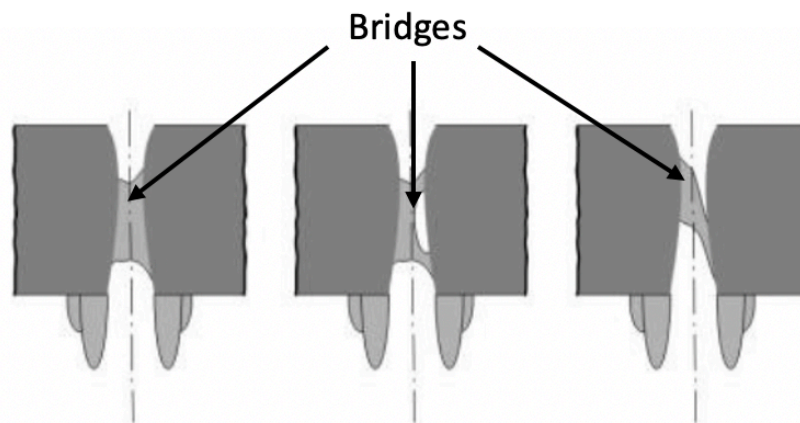
Figure 24: Bridges occurring in underwater laser cutting workpieces [1]

Two explanations were proposed as to how the water may interact with the melt. These explanations are [1]:

1. The melt is completely solidified before reaching the bottom of the kerf due to the interaction of water with the rear of the gas jet in the kerf;
2. Water is transported into the kerf by the vortex created at the bottom of the kerf caused by the exiting gas jet. The water then cools and solidifies the melt before it reaches the bottom of the kerf [1].

Therefore, bridges occur because of poor melt removal and the rapid solidification of molten material to be removed. Conclusively, the occurrence of bridges in the turbulent region of the kerf is due to the excessive amount of melt per unit kerf length produced inside the kerf at low cutting speeds [1]. Therefore, provided the laser power intensity is high enough to melt the material, choosing process parameters that optimise the melt removal process and cutting at a high speed is important in underwater laser cutting.

Overall, this study seeks to develop a fundamental understanding of underwater laser cutting and, subsequently, apply the technology to develop industrially acceptable solution for offshore decommissioning applications. This research aims to develop an underwater laser-based technology for working in deep and hazardous environments which is cheaper, safer and relatively faster. The current state-of-the-art of underwater laser cutting consist of performing cutting trials using air as an assist gas

at a water depth of less than 1 m. Therefore, this study is necessary to develop an underwater laser cutting system capable of cutting thick steel structures at a water depth of up to 200 m. Additionally, this study aims to develop an analytical model for underwater laser cutting as research in this field is mainly experimental.

3   Equipment and experimental procedures

This chapter presents the equipment and experimental procedures used for the investigation of underwater laser cutting. The experimental work in this project was organised into two sets of cutting trials, both conducted at TWI. The first set of underwater laser cutting trials were carried out in a 1 m^3 tank. These trials address the influence of laser power, cutting speed, assist gas pressure and power intensity on the corresponding maximum cut thickness, dross height and kerf width. The second set of underwater laser cutting experiments were conducted inside a high pressure vessel, designed and manufactured by TWI.

This section also describes the equipment and experimental procedures for the first and second set of cutting trials. This concerns the materials, laser cutting system, cutting head, cutting parameters and experimental procedures used for the cutting trials inside a 1m^3 tank and high-pressure vessel. Underwater laser cutting was performed in horizontal as well as vertical up and down directions, thus demonstrating the practical applicability of underwater fibre laser cutting in offshore decommissioning applications when cutting complex structural geometries. Figure 25 shows the cutting orientation and process variables that were examined for the two sets of underwater laser cutting trials.
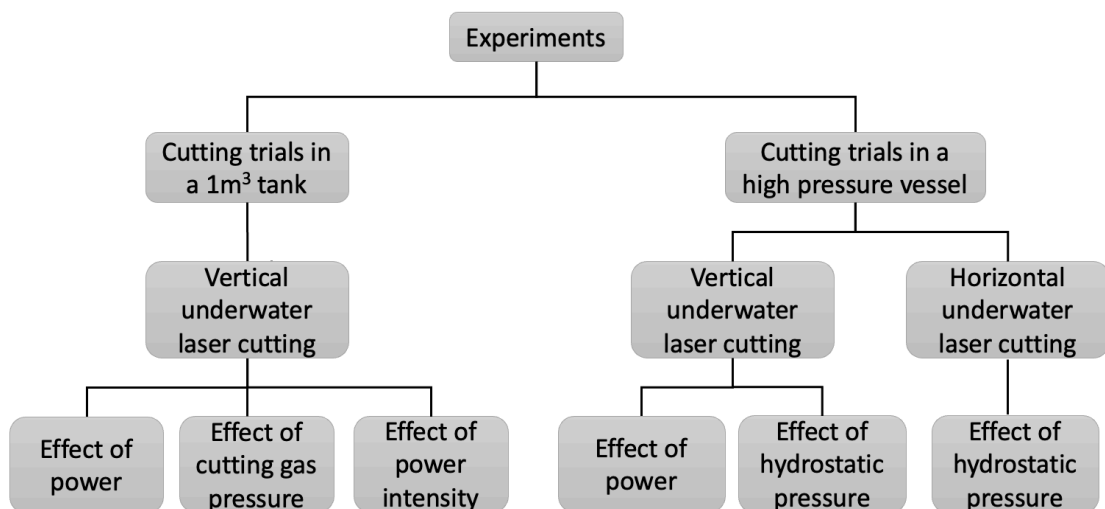
Figure 25: Process variables that were examined during the cutting trials

3.1   Cutting trials in a 1m^3 tank

3.1.1   Material

The material used in this study is S355 C-Mn steel, widely used in the nuclear sector and in the most demanding environments such as the offshore industry. The typical chemical compositions and mechanical properties of the test materials are given in Table 7 and Table 8, respectively [35].

Table 7: S355 C-Mn steel chemical composition [35]

Element (Percentage by weight - wt%) S355 C-Mn steel					
S355	C max	Mn max	P max	S max	Si max
	0.20	1.60	0.025	0.025	0.55

Table 8: S355 C-Mn steel mechanical properties [35]

S355	**Tensile Strength (MPa)**	**Yield Strength min (MPa)**
	470-630	355

The specimen design consisted of a C-Mn steel plate, with part of its edge machined away at 30° to offer a range of thickness to the laser beam. Therefore, the maximum cut thickness achieved for a set of cutting parameters could be determined. Figure 26 shows the dimensions of the workpiece used for this study (in millimetres).
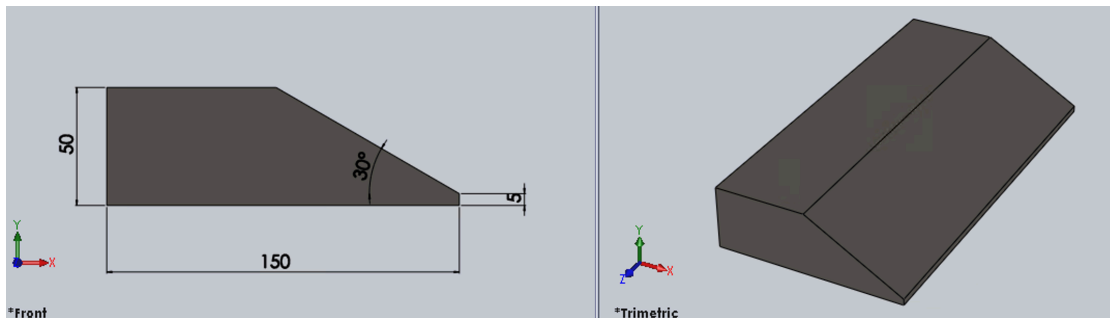
Figure 26: Workpiece specification - front (left) and trimetric view (right)

A specimen of 300 mm x 150 mm x 50 mm was used which allowed the execution of several laser cuts without changing the specimen. Different process settings could be applied when cutting the workpiece underwater and this includes variation of the cutting speed, cutting gas pressure, power intensity and laser power.

3.1.2 Specifications of the laser system used

The main laser equipment used in this study was a solid-state ytterbium fibre laser (model YLS – 10000) manufactured by IPG Photonics (see Figure 27). This laser system delivers a maximum output power of 10 000 W at continuous wave (CW) mode with emission wavelength of 1060 – 1080 nm. The fibre laser is compact having dimensions (W x D x H) of $856 * 806 * 1517$ and a net weight of 380 kg [96].

Figure 27: IPG fibre laser system

The laser beam generated by the ytterbium fibre laser was transferred to the cutting head via a 150 µm diameter optical fibre giving a nominal beam parameter product (BPP) of 6 mm.mrad.

3.1.3 Cutting head

An underwater laser cutting head designed and manufactured by TWI was used in this study (see Figure 28). A BIMO laser processing optical system from HIGHYAG Lasertechnologie GmbH was mounted inside the cutting head. The cutting head used high power laser optics in the form of coated fused silica collimating and focusing lenses, of lengths 120 and 300 mm, respectively. A coated fused silica cover slide was positioned in front of the focusing optic to prevent spatter from the cutting process reaching the focusing lens. In front of the fused silica cover slide, the arrangement was such that cutting gas could be introduced at various pressures through a conventional laser cutting nozzle tip, coaxial with the focusing beam.
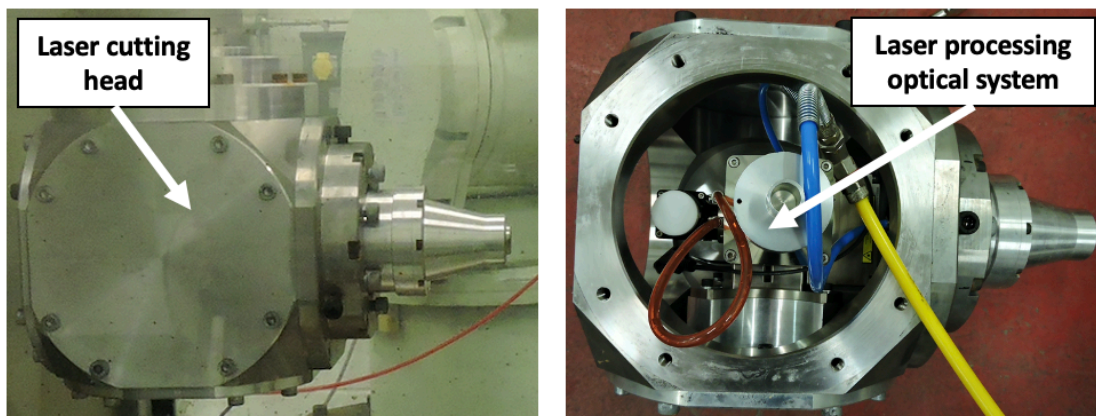
Figure 28: Cutting head - side (left) and top view (right)

The cutting head used a coaxial air jet to maintain an effective dry area (dry cavity) on the laser-material interaction zone and remove molten material from the cut kerf. A copper converging nozzle with a diameter of 3.5 mm was used to create a dry cavity and deliver the assist gas jet to the cutting zone.

3.1.4 Experiment setup

A view of the underwater laser cutting setup and geometry is shown in Figure 29. The workpiece was mounted to a 6-axis Kawasaki robot, via a solid metal arm, so that it could be inserted and removed from the water tank. The same robot was used to manipulate the specimen and support arm, across the cutting head. Therefore, during the cutting procedure, the cutting head was stationery, and the robot moved the workpiece at various cutting speeds. The robot moved the workpiece instead of the cutting head because it was impractical to mount the cutting head to the robot's end effector. The water tank had a volume of approximately 1 m^3 and the cutting head was mounted vertically from the top of the tank. A graphite plate was also mounted inside the water tank as a safety measure (beam stop).
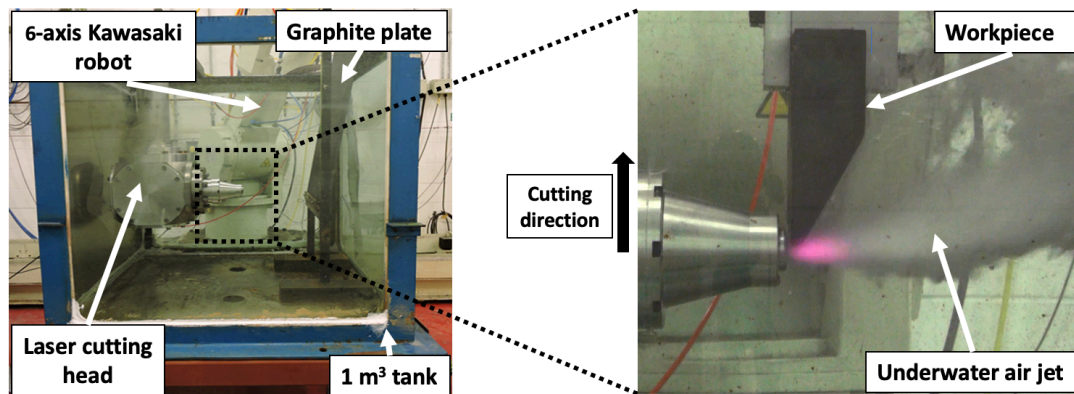
Figure 29: Experiment setup

The cutting procedure was as follows. First, a small amount of assist gas was supplied to prevent water from entering the nozzle assembly before filling up the tank with water to the required level. At this time, a C-Mn steel workpiece was lowered underwater to a shallow water depth of approximately 600 mm using the robot. At the start of the cutting process, the desired laser power and assist air pressure were supplied. The workpiece was moved with incremental increases in cutting speed, in the range of 50 – 1000 mm/min. Straight line cut slots were made at approximately 10 mm from each other. Overall, 65 cuts were made on nine C–Mn steel workpieces. The cut length was determined by the presence of a cutting flame at the back of the workpiece (kerf exit). If the flame was absent, laser emission was stopped.

The cutting parameters used in the underwater laser cutting trials in a 1m^3 tank are shown in Table 9.

Table 9: Cutting parameters

Parameters	Values
Laser power (kW)	2–10
Cutting speed (mm/min)	50–1000
Focus position from the workpiece surface (mm)	4
Standoff distance (mm)	4
Nozzle diameter (mm)	3.5
Gas type	Air
Gas pressure (bar)	2–8
Thickness (mm)	5–50
Beam waist diameter (mm)	0.4

The magnitude of the cutting parameters (gas pressure, stand-off distance, focus position and focus position) were selected based on previous studies of underwater laser cutting trials by Hilton and Khan [18, 20, 77, 78]. The beam waist diameter, d_{waist}, can be calculated as [24]:

$$d_{waist} = \left(\frac{d_{focus}}{d_{collimator}}\right) d_{fibre} \tag{40}$$

Were d_{focus} is the focusing lens focal length, $d_{collimator}$ is the collimator lens focal length and d_{fibre} is the delivery optical fibre diameter. When a laser beam propagates along its optical path, its diameter is continually changing. If we consider the ideal case of a Gaussian beam, the beam diameter, $d(z)$ along the propagation axis, z, is expressed as [24]:

$$d(z) = d_{waist} \sqrt{1 + \left(\frac{z}{z_r}\right)^2} \tag{41}$$

Here, z_r denotes the Rayleigh length which is the distance along the propagation direction of the laser beam from the waist to a location where the area of the cross section is doubled. The Rayleigh length can be expressed as [24]:

$$z_r = \frac{\pi (d_{waist})^2}{4\lambda} \tag{42}$$

The power intensity along the path of the laser beam, $P(z)$, can be calculated as [24]:

$$P(z) = \frac{4P}{\pi (d(z))^2} \tag{43}$$

As a result, equation (41) and equation (43) can be used to calculate the beam diameter and power intensity along the beam path at a laser power of 10 kW, as illustrated in Figure 30 and Figure 31.
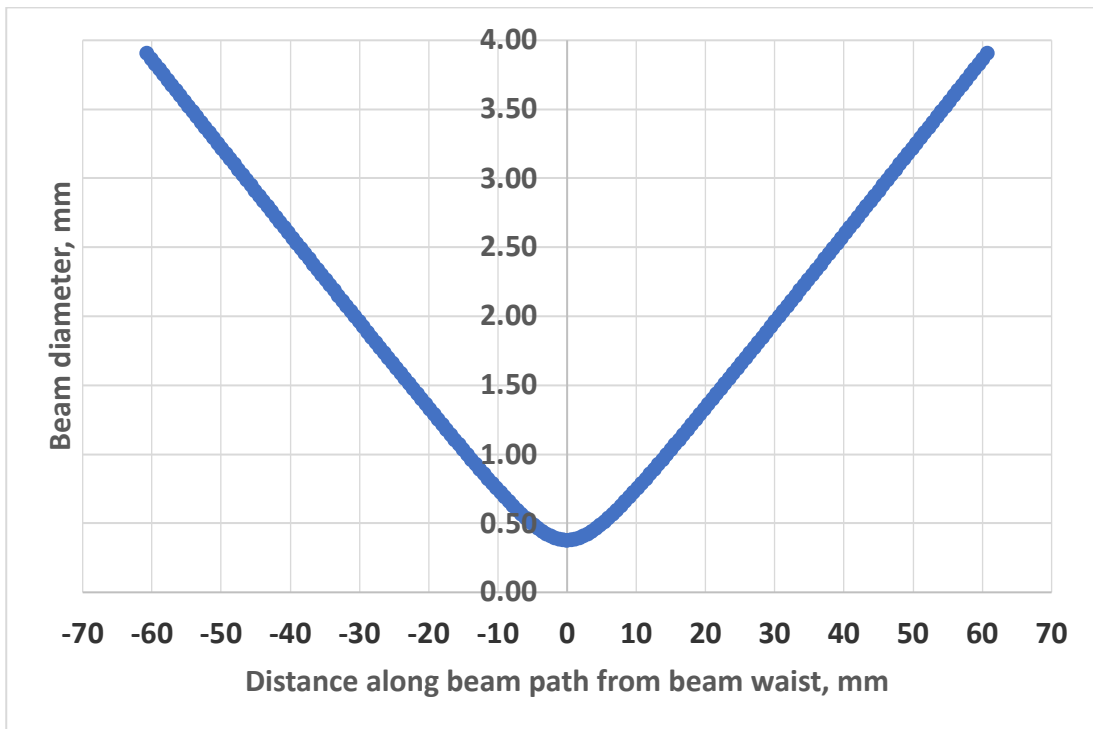
Figure 30: Beam diameter along the beam path
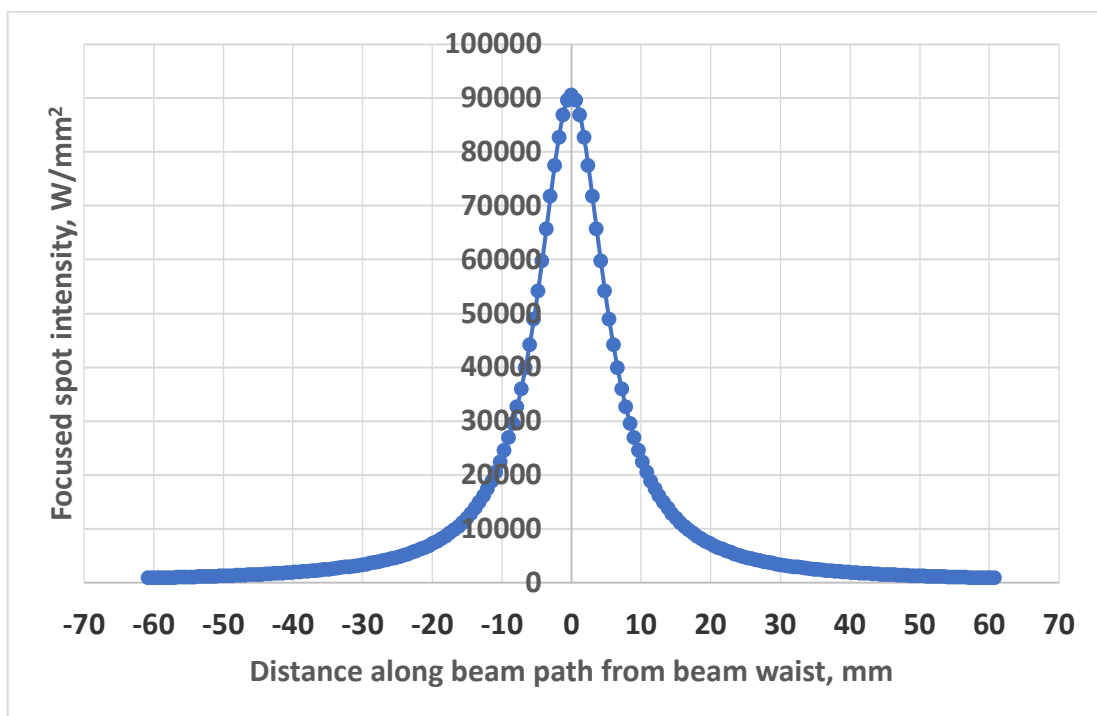
Figure 31: Power intensity along the beam path at a laser power of 10 kW

For a point on the centreline of a circular cross section beam with a spot diameter $d(z)$ moving at a speed V the interaction time T_i is given by [70]:

$$T_i = \frac{d(z)}{V} \tag{44}$$

Therefore, for a point on the centreline of the beam at the workpiece surface, the interaction time is in the range of 0.028 to 0.55 s for a cutting speed of 50-1000 mm/min.

All underwater laser beam cutting experiments were recorded using a Panasonic camera which was positioned outside the water tank. A vernier calliper was used to measure the kerf width, dross height and maximum cut thickness on all cuts. This device was used due to its availability and capability to measure the kerf width, dross height and maximum cut thickness. For all workpieces, the attached dross was removed by a Bosch grinder prior to measuring the kerf width.

3.2 Cutting trials in a high pressure vessel

The cutting trials carried out inside the high-pressure vessel used the same workpiece specification, fibre laser cutting system, cutting head, and type of assist gas as the preliminary experiment.

3.2.1 High pressure vessel

In order to simulate offshore conditions, a first-of-its-kind pressure vessel was designed and manufactured by TWI (see Figure 32). The design and manufacturing process of the high pressure vessel was not part of this research. The vessel was integrated with capability to move the workpiece with 3-degrees of freedom and dynamically balance the hydrostatic pressure up to 35 bar, representing a water depth of ~350 m. Moreover, the high pressure vessel provided process visual monitoring and recording capability. The underwater laser cutting system can be pressured to a desired level within minutes.
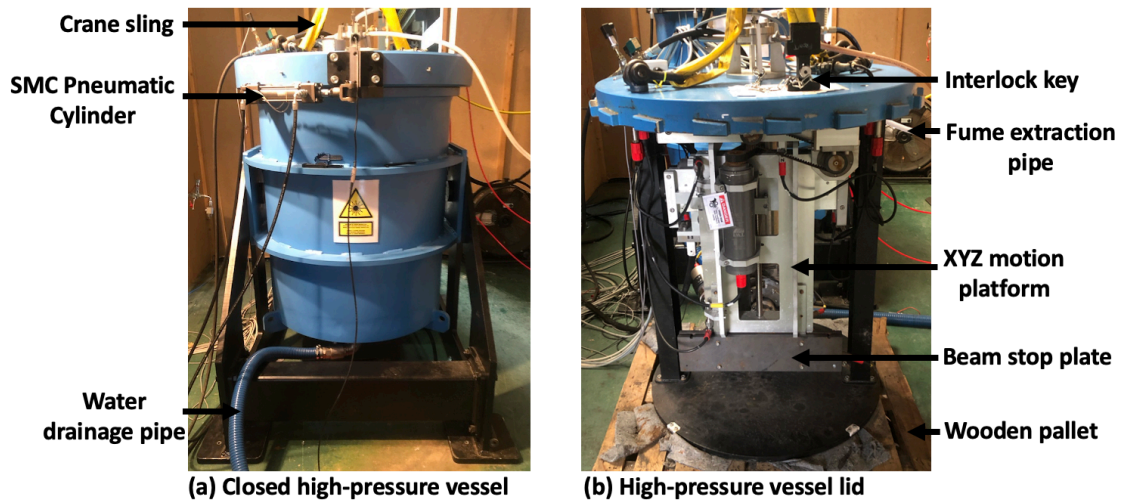
Figure 32: High pressure vessel

The vessel was equipped with a fume extraction pipe, water drainage pipe, XYZ motion platform, two pneumatic cylinders, two LUXUS industrial cameras and all necessary electrical components to perform the underwater cutting process. The fume extraction pipe was used to exhaust the fumes produced by the underwater laser cutting process to the atmosphere. The pneumatic cylinders were used to interlock the vessel. As a safety measure, the laser beam could not be emitted unless the key was inserted when the vessel was closed. The laser beam generated by the Ytterbium fibre laser was transferred to the cutting head via a 200 μm diameter optical fibre. A 200 μm diameter optical fibre was used due its availability at the time of the cutting trials. The cutting trials in the high pressure vessel were limited to a hydrostatic pressure condition of 20 bar as a safety precaution and for a cost-effective usage of the cutting gas jet.

3.2.2   Cutting head

The cutting head used high power laser optics in the form of coated fused silica collimating and focusing lenses, of lengths 120 and 250 mm, respectively. The cutting head was mounted on the lid of the vessel with a beam emerging horizontally and impinging on a sample to be cut (see Figure 33). Multiple cuts could be made on the same sample by varying the horizontal position between each cut without opening the vessel. The cutting head was stationary, and the workpiece was mounted onto the XYZ motion platform which moved the workpiece at various cutting speeds to cut the material. The XYZ motion platform's hardware was developed by Hohner Automation Ltd and the computer numerical control (CNC) control software was developed by Amtech.

As a safety measure, a graphite plate was mounted on the XYZ motion platform to act as a beam stop (prevent laser scattering). A light-emitting diode (LED) light source was mounted onto the side of the cutting head and emitted light at the laser-workpiece interaction region. Two cameras, one at each side of the cutting head, recorded the underwater laser cutting process for all the cuts made on the workpieces.
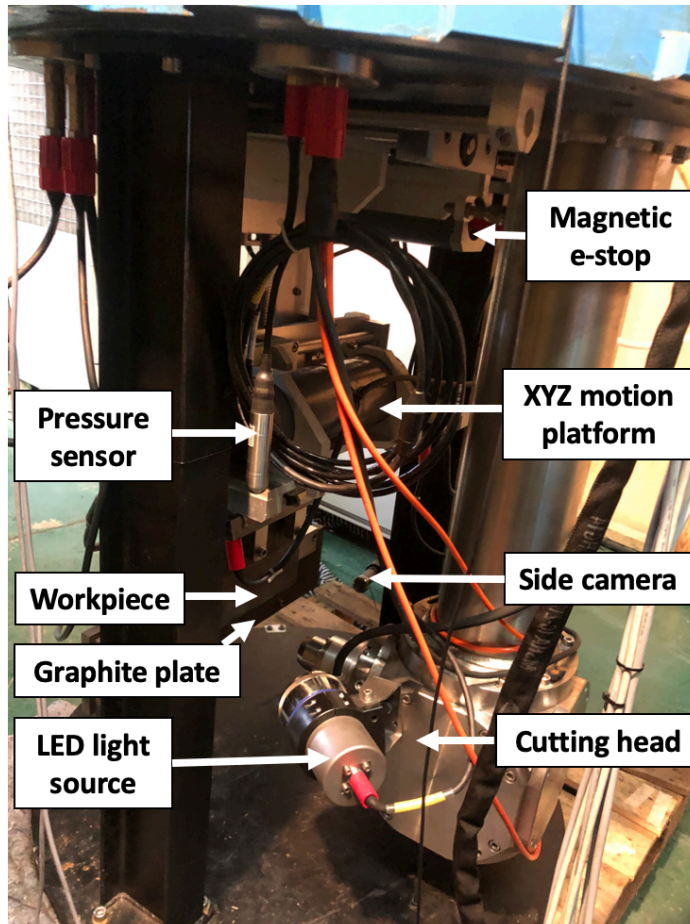
Figure 33: Cutting head assembly

An overhead crane was used to lift and move the lid of the vessel in a precise manner to insert and remove the cutting head from the pressure vessel.

3.2.3 Crane components

The lid of the vessel was lifted by the hook of the crane using a 3-tonne sling (see Figure 34). A basket hitch which equally distributes the load between the two legs of a sling was used. Two bow shackles with a screw collar pin provided an easy way of fastening the sling securely. The crane was also used to move and replace the air bottle bank supply for the cutting head once it was depleted.
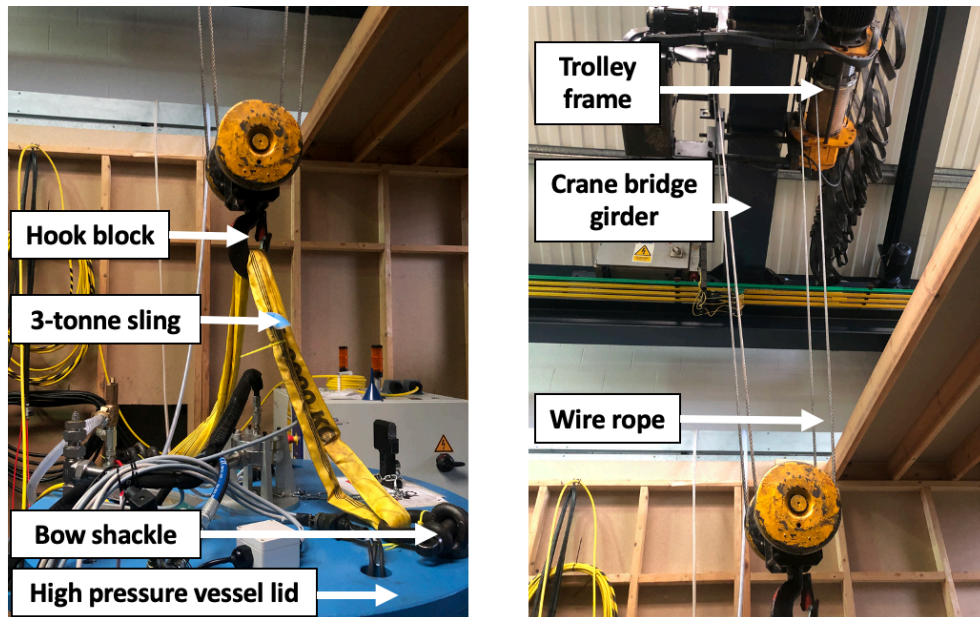
Figure 34: Crane components – bottom (left) and top view (right)

3.2.4 Underwater laser cutting control and monitoring station

The underwater laser cutting system's control and monitoring station is comprised of a CNC control interface developed by Amtech, two LUXUS camera monitors, a Panasonic DMR-EX77 DVD recorder, a laser control unit (LCU) and an IPG laser software interface. The CNC software interface was used to programme the sequencing and speed of all cutting operations. All cutting experiments were recorded using an underwater LUXUS compact camera and stored on a DVD recorder's hard drive. The LCU was used to monitor the pressure inside the vessel as well as the assist gas pressure supplied to the cutting head. Figure 35 is a photograph of the underwater laser cutting workstation showing the laser and camera monitoring units.
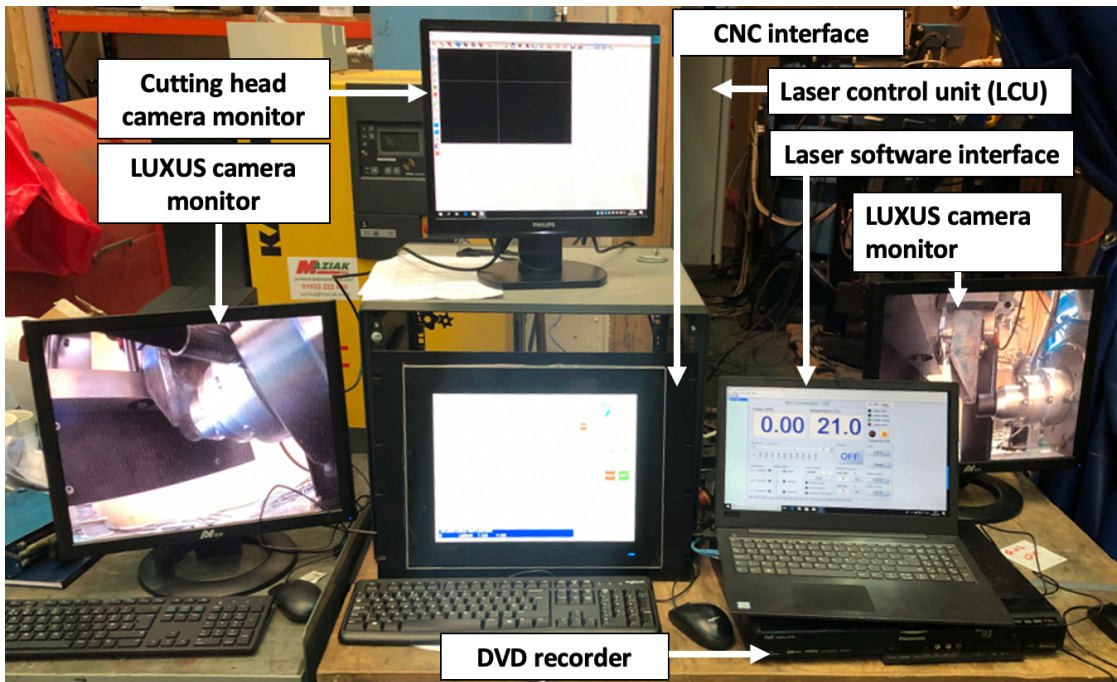
Figure 35: Underwater laser cutting control and monitoring system

3.2.5 Experiment procedures

The experimental procedures comprised, in addition to the actual cutting experiments, supplementary tests and adjustments to ensure the correct setup of the underwater laser cutting system, which are briefly stated to allow the evaluation of the integrity of the work. These supplementary tests included aligning the laser beam to the process gas nozzle and confirming the focal spot position.

3.2.5.1 Alignment of the laser beam to the process gas nozzle

The alignment of the laser beam to the process gas nozzle was performed in two stages. First, the cone nozzle of the cutting head was removed, and the tip of the cutting head was covered with a piece of adhesive tape (see Figure 36 a). The power of the laser beam was set to a level that causes the tape to melt, leaving a hole at the point where the laser pierced the tape. This permitted an estimation of the alignment of laser beam relative to the cutting head. Once the laser beam was centralised with the cutting head, the conical nozzle was reinstalled, and the mouth of the process gas nozzle was covered with a piece of adhesive tape (see Figure 36 b – bottom view). Another hole was created when the laser pierced the tape, (see Figure 36 c). This allowed an estimation of the alignment of laser beam relative to the cutting gas nozzle.
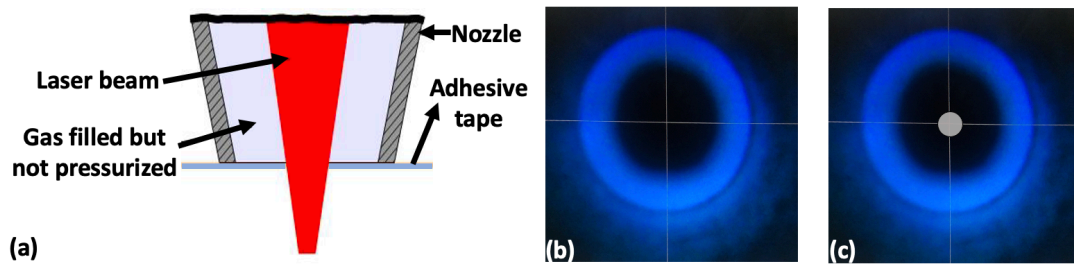
Figure 36: Alignment of the laser beam to the process gas nozzle

3.2.5.2   Confirming the focal spot position

This test served as confirmation of the focal spot position from the tip of the nozzle. For this experiment, the laser cutting head was positioned normal to a flat aluminium plate (see Figure 37). The distance between the tip of the nozzle and the specimen, l, was altered in defined steps of 1 mm, a. For each of these steps the laser beam was switched on with high enough power to produce a round mark with a diameter, d, on the flat aluminium plate. The distance, l, where the laser burn mark (spot size) was the smallest, d_3, was noted as the focus position from the tip of the nozzle.
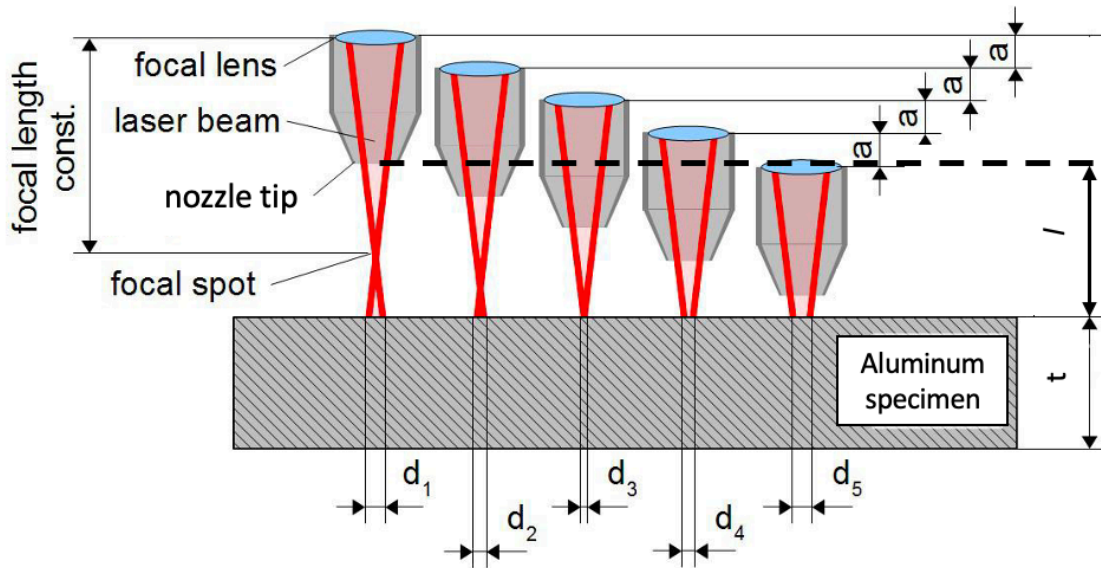
Figure 37: Finding the focal spot position relative to the tip of the gas nozzle

3.2.6   Experiment procedure for underwater laser cutting trials in a high pressure vessel

An IPG fibre laser with a maximum power of 10 kW, 1.06 μm wavelength was used in the CW mode. Powers in the range of 4 kW to 10 kW were used. The laser beam was delivered to the cutting head by a 200 µm diameter optical fibre, a collimator lens focal length of 120 mm and focussed by a 250 mm focal length lens into a spot with a diameter of 400 µm. The optical fibre and all associated services were delivered through a prototype laser cutting head capable of withstanding the hydrostatic

conditions underwater. Figure 38 shows an illustration of the experimental setup using a high-pressure vessel.
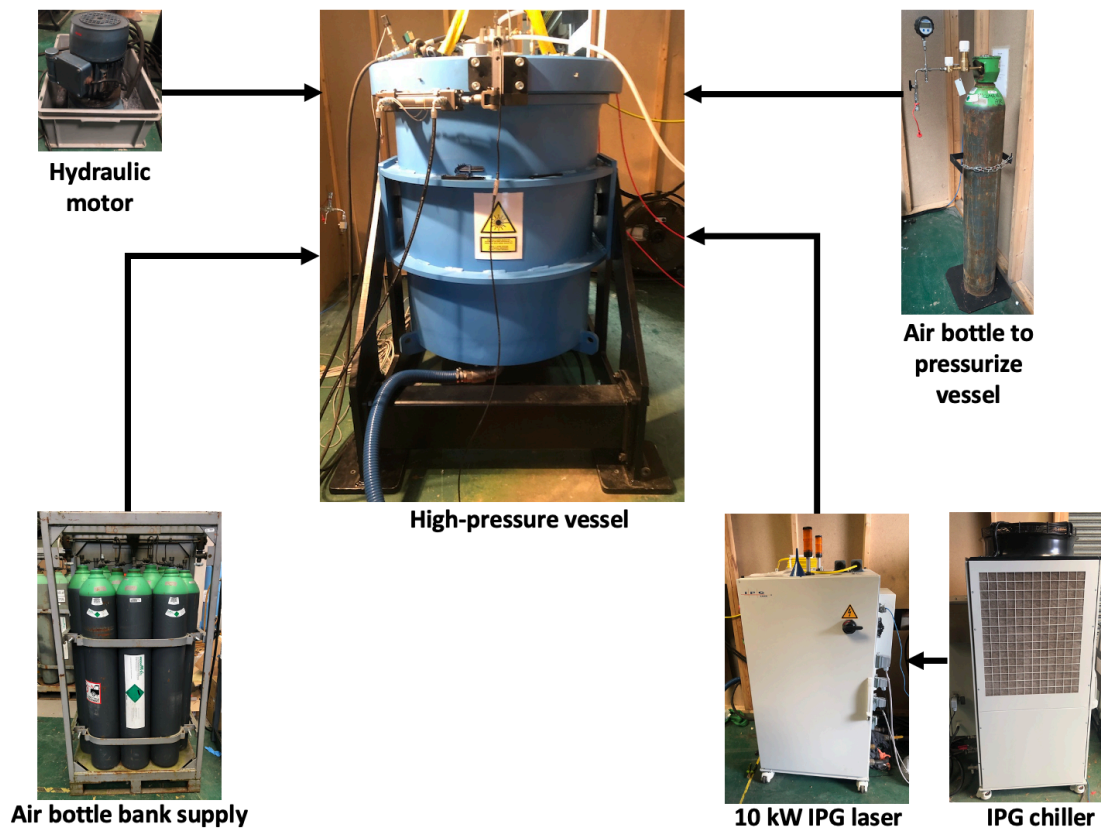
Figure 38: Experimental setup

The cutting procedure was as follows. First, the workpiece was mounted onto the XYZ motion platform before filling up the high-pressure vessel with water to the required level. Afterwards, a 3-tonne crane was used to lift the lid to the top of the vessel before supplying a small amount of assist gas to prevent water from entering the nozzle assembly. At this time, the workpiece was lowered inside the vessel and the lid was interlocked to the vessel using two hydraulic cylinders powered by a hydraulic motor. Thereafter, the required cutting gas pressure was supplied to the cutting head and an air bottle was used to pressurise the vessel to the desired hydrostatic pressure condition, respectively. To start the cutting process, the desired laser power was set and a CNC program was run to move the workpiece at the programmed cutting speed in order to make the cut. The cut length was determined by the presence of a flame at the back of the workpiece (kerf exit). If a flame was absent, laser emission was stopped.

Throughout the experimental procedure, the pressure inside the vessel was measured by a pressure sensor and dynamically balanced at the desired hydrostatic pressure condition set using the air bottle. Also, the cutting gas pressure was always set to be higher than the hydrostatic pressure conditions inside the vessel to prevent the backflow of water into the cutting head. Table 10 shows the cutting parameters used in the cutting trials.

Table 10: Cutting parameters

Parameters	Values
Laser power (kW)	4–10
Cutting speed (mm/min)	50–300
Focus position from the workpiece surface (mm)	5, 10 and -18
Standoff distance (mm)	5 and 10
Nozzle diameter (mm)	3.5
Gas type	Air
Gas pressure (bar)	8, 9, 13, 18, 23 and 28
Thickness (mm)	5–50
Beam waist diameter (mm)	0.4
Hydrostatic pressure (Bar)	0, 1, 5, 10, 15 and 20

The magnitude of the cutting parameters (gas pressure, stand-off distance, focus position and focus position) were selected based on previous studies of underwater laser cutting trials by Hilton and Khan [18, 20, 77, 78]. Equation (41) and equation (43) can be used to calculate the Gaussian beam diameter and power intensity along the beam path at a laser power of 10 kW, as illustrated in Figure 39 and Figure 40
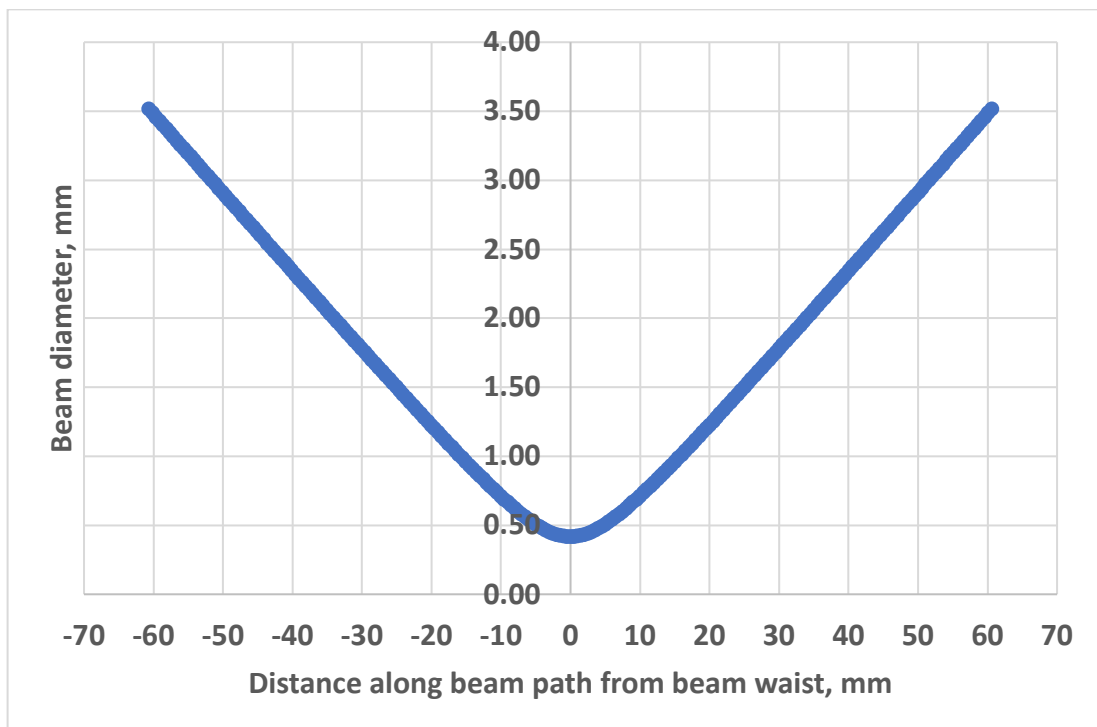
Figure 39: Beam diameter along the beam path
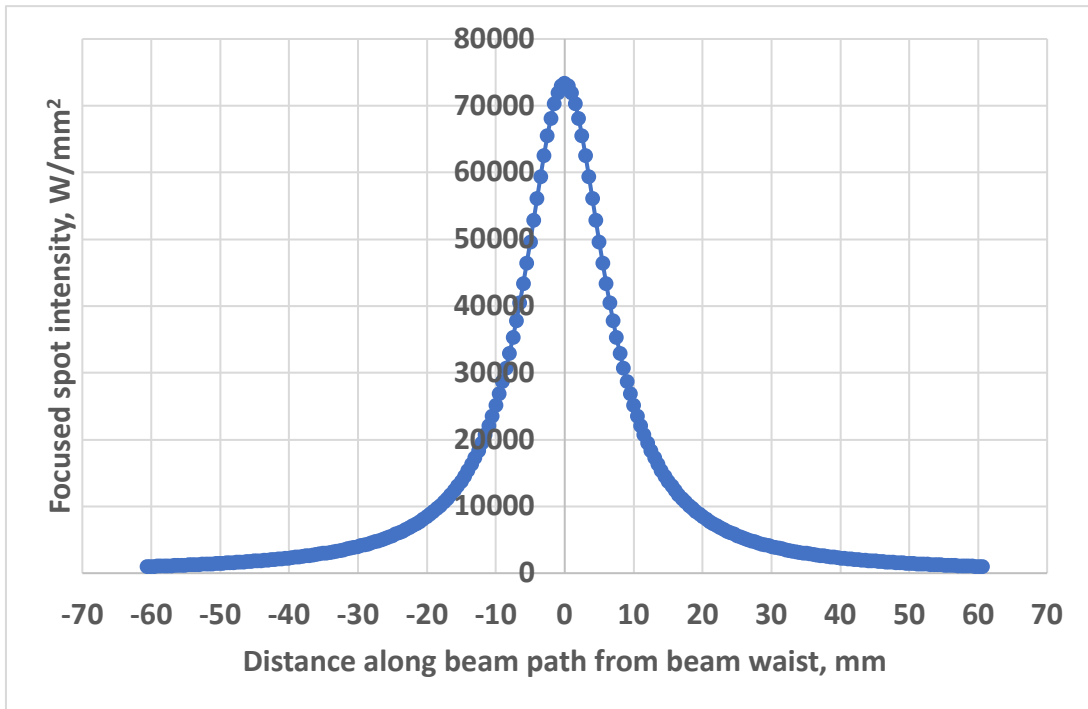
Figure 40: Power intensity along the beam path at a laser power of 10 kW

Underwater laser beam cutting was performed in horizontal as well as vertical up and down directions, thus demonstrating the practical applicability of underwater fibre laser cutting in offshore decommissioning applications. The practical applicability of underwater laser cutting has been proven by Matsumoto [123] when cutting a stainless steel plate up to a thickness of 65 mm using a 5 kW CO laser, with the laser beam advanced in horizontal as well as vertical up and down directions. For offshore decommissioning applications, the ability to cut complex geometries in various orientations is essential.

3.2.6.1 Vertical cutting

Vertical underwater laser cutting trials were only performed at 1 atmosphere (unpressurised vessel) and 1 bar hydrostatic pressure with a dynamic nozzle. Figure 41 shows a view of the vertical underwater laser cutting trials, before and during the cutting process with cutting direction going vertically up along the y-axis.

Figure 41: Views of the vertical underwater laser cutting process with cutting direction going vertically up: (a) before the cutting process began (b) during cutting

Before vertical cutting, the shroud (black cap covering the nozzle – see Figure 41) of the dynamic nozzle is pushed against the workpiece to reduce its length until the stand-off distance was 10 mm. The nozzle is dynamic because it has a shroud which can retract so that it can reduce its length during the cutting process. Vertical cutting trials were carried out with the focus position located at the tip of the dynamic nozzle, thus giving a focus position of 10 mm from the surface of the material.

3.2.6.2   Horizontal cutting

Horizontal underwater laser cutting trials were performed by a static nozzle with the focus position located at the tip of the nozzle (5 mm outside the surface of the material) and 18 mm inside the material. The nozzle is static because it has a shroud

which is stationery throughout the cutting process. Figure 42 shows a view of the horizontal underwater laser cutting trials, before and during the cutting process with cutting direction going along the x-axis.
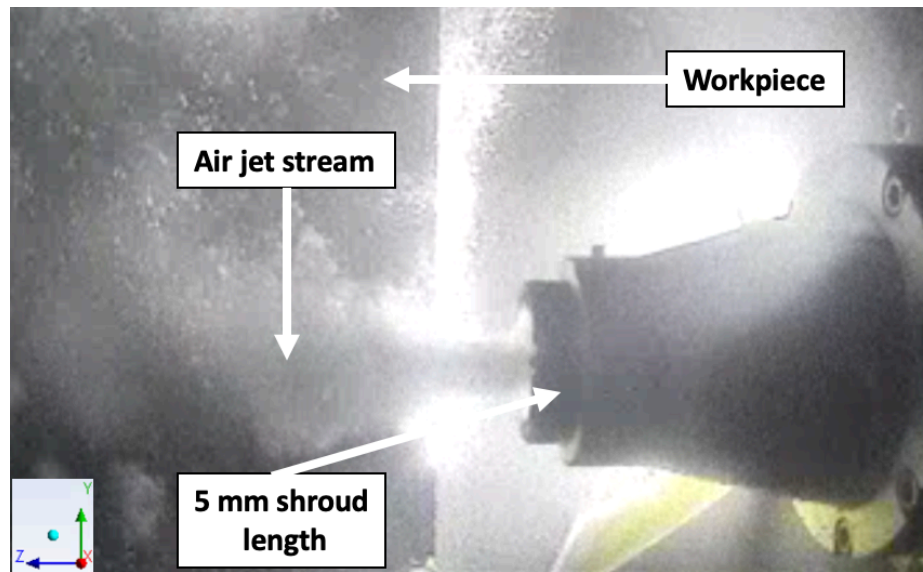
(a) Before cutting
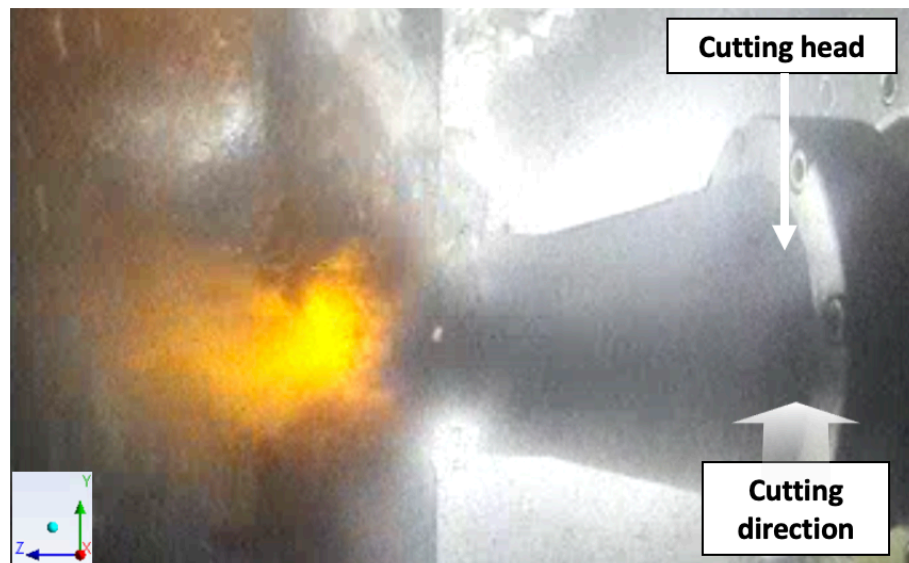
(b) During cutting

Figure 42: Views of the horizontal underwater laser cutting process with cutting direction going along the x-axis: (a) before the cutting process began (b) during cutting

Horizontal cutting trials were carried out in increasing hydrostatic pressure conditions of 0, 5, 10, 15 and 20 bar inside the vessel. The goal was to cut at 8 bar relative compressed air pressure to that of the vessel, so the cutting gas pressure varied from 8, 13, 18, 23 and 28 bar depending on the hydrostatic pressure condition of the vessel. Overall, ninety-seven cuts were performed inside the vessel on fifteen C–Mn steel workpieces and a Vernier calliper was used to measure the kerf width, dross height and maximum cut thickness.

4 Presentation of experimental results

4.1 Overview

This chapter presents experimental results of underwater fibre laser cutting of C-Mn steel in a 1m^3 tank and high-pressure vessel. The first section of this chapter describes the preliminary underwater laser cutting results from the cutting trials conducted in a 1m^3 tank, while the second section characterises the findings from the cutting trials performed in a high-pressure vessel. Both sets of results were gathered and analysed at TWI.

The aim of the cutting trials in a 1m^3 tank is to understand the general characteristics of underwater laser cutting in terms of process performance, capability, kerf width and dross height at atmospheric pressure conditions. All the attempted laser cuts on 50 mm thick C-Mn steel workpieces fully penetrated the specimens up to a specific thickness, although some of the kerfs contained bridges. A complete separation of a 50 mm thickness C-Mn steel workpiece was achieved using a 10-kW laser power, 8 bar compressed air at a stand-off distance of 4 mm and a cutting speed of 125 mm/min.

The objective of the cutting trials in a high-pressure vessel is to investigate the effect of power, cutting speed, and hydrostatic pressure on the maximum cut thickness, kerf width and dross height. This study is necessary to prove the applicability of underwater laser cutting in hyperbaric conditions and to investigate the optimum process performance for cutting a 50 mm C-Mn steel workpiece at a hydrostatic pressure of 20 bar, corresponding to a water depth of 200 m. The results in this section are divided into three subsections based on the location of the focus position and cutting orientation used in the cutting trials. The focus position could be varied by moving the laser operating system inside the cutting head. An important finding for these series of tests is that a 50 mm thick C-Mn steel workpiece can be adequately cut at a laser power of 10 kW (a power intensity of 10174 W/mm^2 on the material surface), a maximum cutting speed of 200 mm/min, a stand-off distance of 5 mm and a hydrostatic pressure condition of up to 20 bar, corresponding to a water depth of 200 m.

4.2 Underwater laser cutting trials in a 1 m^3 tank

This section concerns the effect of power, gas pressure and power intensity on the corresponding maximum cut thickness, dross height and kerf width. The experimental results will now be discussed starting with the effect of laser power on the maximum cut thickness.

4.2.1 Effect of power

In this set of experiments, a 50 mm thick C-Mn steel workpiece was used with part of its edge machined away at 30° to offer a range of thickness to the laser beam. The influence of laser power on underwater cutting of the machined workpiece was investigated. Laser powers between 4 and 10 kW were used to cut the workpiece. For all the trials, an assist gas jet pressure of 8 bars was chosen, the beam focus was positioned at the tip of the nozzle, and the stand-off distance was maintained at 4 mm. The workpiece was traversed across the laser beam focused by the cutting head, with incremental increases in cutting speed, until the material could not be cut. The maximum cut thickness achieved was measured afterwards using a Vernier calliper. Figure 43 shows the maximum cutting thickness achieved with the corresponding cutting speed at different laser power magnitudes.
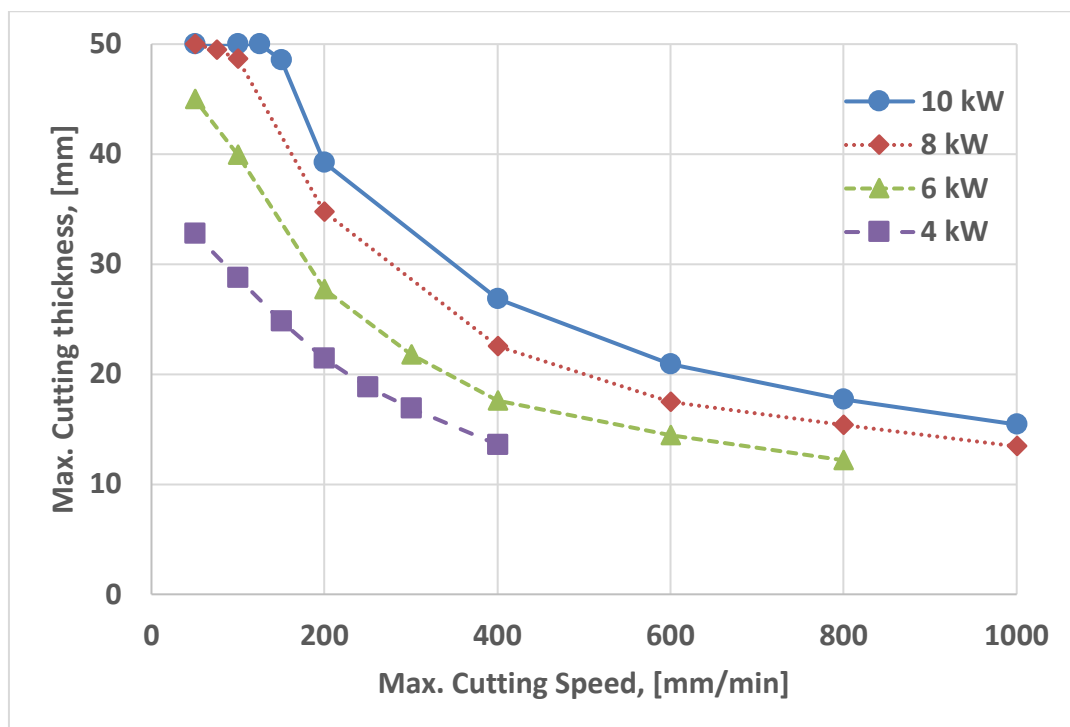
Figure 43: Maximum underwater cut thicknesses as a function of set cutting speed for different laser power magnitudes, an assist gas jet pressure of 8 bar, a focus position of 4 mm and a stand-off distance of 4 mm

Figure 43 indicates that the maximum cut thickness is directly proportional to the laser power and inversely proportional to the cutting speed. The influence of power on the maximum cut thickness is more significant at lower cutting speeds below 400 mm/min. Thereafter, the effect of power slightly decreases. A similar trend in the influence of maximum cutting speed and power on the maximum cut thickness was also found in previous underwater laser cutting studies by Chida et al. [138], Shin et al. [91] and Hilton & Khan [18, 20]. For this study, a complete separation of a 50 mm thick C-Mn steel workpiece was achieved using a laser power of 10 kW (a power intensity of 59775

W/mm^2 on the surface of the workpiece), 8 bar compressed air at 4 mm standoff distance and a maximum cutting speed of 125 mm/min.

The results from this study show a relatively high cutting performance in terms of speed and thickness for the same laser power among the reported results of underwater laser cutting of steels using air as an assist gas (see Table 11).

The process performance achieved is higher than previous studies by Chida et al. [138], Hilton & Khan [20] and Matsumoto et al. [123] but lower than studies by Shin et al. [91, 92]. The high process performance achieved by Shin et al. [91, 92] was attributed to the step-like increase of the cutting speed which is implemented in the initial stage of cutting. Moreover, the high process performance achieved could be attributed to the lower thermal conductivity (21.4 W/mK) and melting temperature (1673-1723 K) of 304 stainless steel, compared to C-Mn steel with a thermal conductivity of 42.7 W/mK and melting temperature in the range of 1698 – 1813 K [77, 81]. Therefore, carbon steel requires more energy to melt and conducts more heat energy into the material than 304 stainless steel during the cutting process [93].

Table 11: Process performance achieved in past studies of underwater fibre laser cutting of stainless-steel

Past literature	Maximum cut thickness (mm)	Power (kW)	Cutting speed (mm/min)
Shin et al. [92]	50	6	80
Shin et al. [91]	50	9	180
Chida et al. [138]	25	4	~100
Matsumoto et al. [123]	50	5	~60
Hilton & Khan [20]	32	5	100

4.2.2 Effect of cutting gas pressure

In this series of tests, the influence of assist gas pressure on the maximum cut thickness was examined at 6 and 10 kW. For each laser power magnitude, assist gas pressures of 2, 4, and 8 bar were used. The workpiece was cut from 5 mm at various cutting speeds until it was clear that cutting had stopped. The focus position of the beam was at the level of the exit of the cutting nozzle tip and the stand-off distance was 4 mm. All cutting trials were carried out with the laser beam emerging horizontally and impinging on a sample to be cut. Afterwards, the maximum cut thickness achieved was measured and the results are shown in Figure 44 for assist gas pressures of 2, 4, and 8 bar.
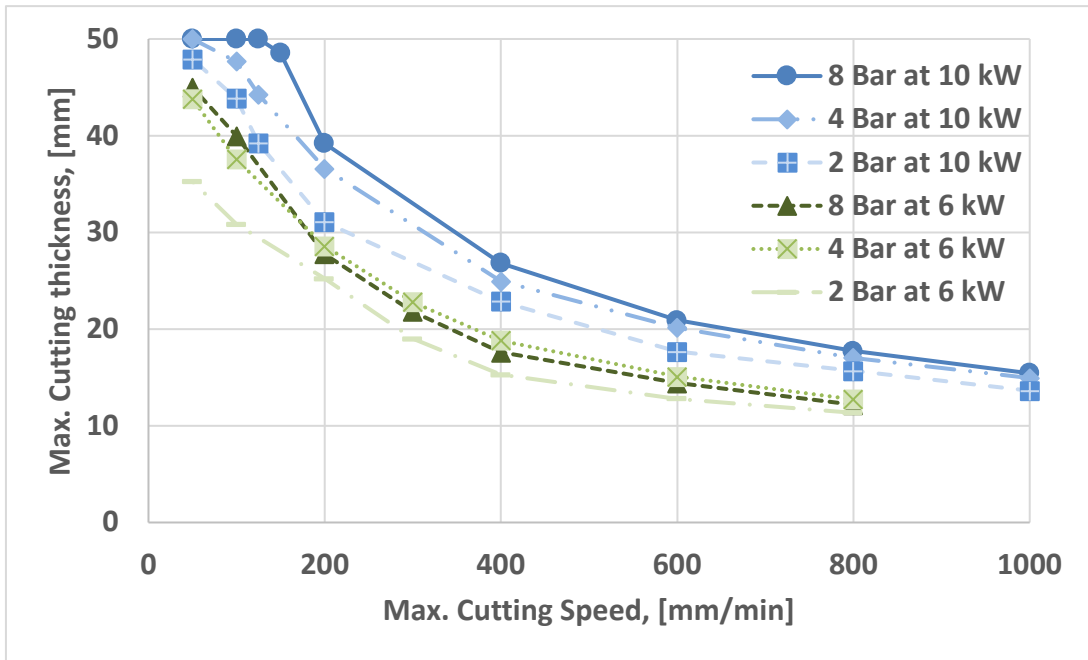
Figure 44: Maximum underwater cut thicknesses as a function of set cutting speed for various assist gas pressures, different laser power magnitudes, a focus position of 4 mm and a stand-off distance of 4 mm

Figure 44 indicates that in terms of maximum cut thickness obtained, the process perfomance increases slightly with increasing assist gas pressure especially at a laser power of 10 kW. The major differences in performance occur at cutting speeds less than 200 mm/min, corresponding to cutting depths of approximately 28 mm for 6 kW and nearly 37 mm for 10 kW. Below this speed, the performance is a little better for an assist gas pressure of 8 bar for both laser power magnitudes. Above this speed, the exact influence of cutting gas pressure is unclear, but relatively constant with changes in cutting speed. In this region, cutting C-Mn steel with 4 bar assist gas pressure gave a slightly better cutting performance than 8 bar for 6 kW and cutting with 8 bar assist air pressure produced a slightly better cutting performance than 4 bar for 10 kW.

A comparison between Figure 43 and Figure 44 clearly shows that laser power has a greater influence on the maximum cut thickness than assist gas pressure. This is because when the assist gas pressure is constant in Figure 43, increasing the power results in a greater increase in the magnitude of the maximum cut thickness achieved than when the assist gas pressure is varied at a constant laser power in Figure 44.

4.2.3 Effect of power intensity

In this set of experiments, the influence of the power intensity on the process performance in terms of the maximum cut thickness was investigated. The cutting gas pressure, laser power and cutting speed were kept constant at 8 bar, 10 kW and 100 mm/min, respectively. The stand-off distance was increased from 5 to 30 mm to vary the power intensity on the surface of the material. Six cuts were performed on a C-Mn

steel workpiece. Figure 45 shows the power intensity on the surface of the material at various stand-off distances for a laser power of 10 kW.
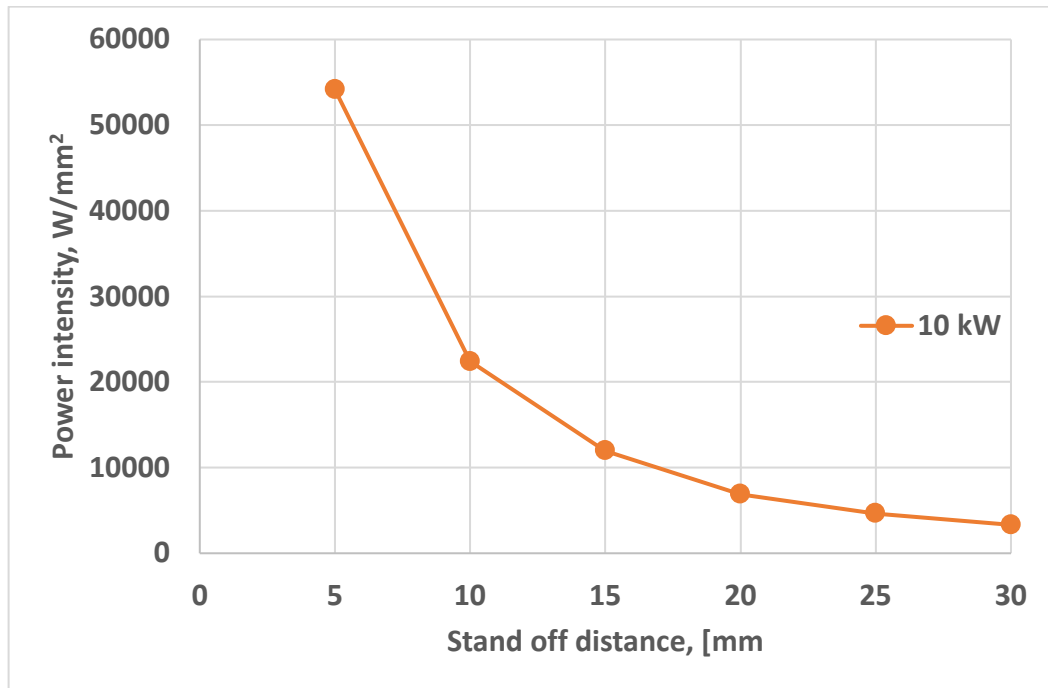
Figure 45: Power intensity on the surface of the material as a function of set stand–off distances at a laser power of 10 kW

Figure 45 indicates that the power intensity on the surface of the material is inversely proportional to the stand-off distance. This can be attributed to the increase of the beam spot diameter on the surface of the material which occurs as the stand-off distance increases. The beam diameter on the surface of the material increases from 0.49 to 1.96 mm when the stand-off distance increases from 5 to 30 mm. The decrease of the power intensity with increasing stand-off distance is more significant at stand-off distances below 15 mm.

Figure 46 shows the maximum underwater cut thicknesses of C-Mn steel as a function of the power intensity on the surface of the material at a laser power of 10 kW, a constant cutting speed of 100 mm/min and an assist gas jet pressure of 8 bar.
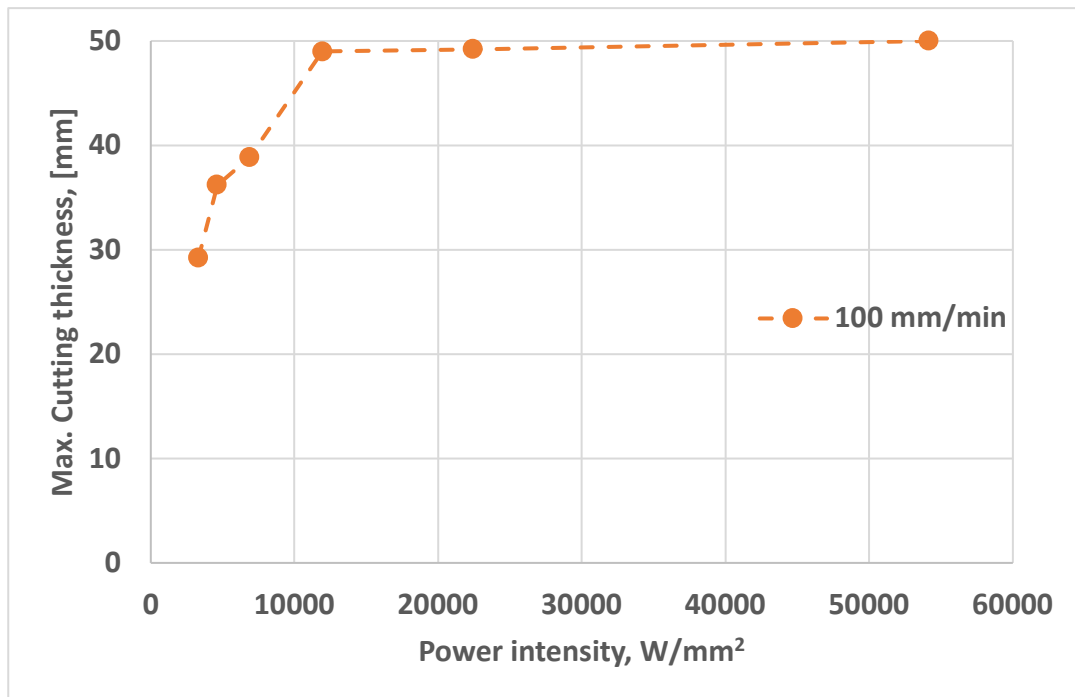
Figure 46: Maximum underwater cut thicknesses as a function of power intensity at a constant cutting speed of 100 mm/min, an assist gas jet pressure of 8 bar and a laser power of 10 kW

As expected, the maximum cut thickness is directly proportional to the power intensity on the surface of the material. The increase of the maximum cut thickness with increasing power intensity is more significant at power intensities below 12 000 W/mm^2, corresponding to stand off distances above 15 mm. The decrease in the process performance with decreasing power intensity can also be attributed to the following:

- When the power intensity on the surface of the material was decreased by increasing the stand-off distance, air pressure at the surface of test-piece got weaker and molten metal couldn't be removed toward the back of the test-piece [138];
- Decreasing the power intensity on the material's surface by increasing the stand-off distance to up to 30 mm could increase the power losses that could occur due to scattering between the nozzle and the workpiece. These power losses may also continue to occur inside the cut kerf if water vapour is present [1].

4.2.4 Dross height analysis

As mentioned in Chapter 2.5, the laser cut edge quality is insignificant, but minimum production and release of secondary waste is. Other cutting techniques such as diamond wire sawing, plasma arc cutting and abrasive water jet produce significantly higher secondary waste compared with laser cutting technology [138]. Management of secondary waste emission is critical in both nuclear and offshore decommissioning applications for reducing the size of irradiated material and achieving low waste production, respectively [18, 92]. If, during laser cutting, as much of the molten material removed from the kerf can be induced to remain attached to the lower sides of the cut, the less material that will end up as sedimentary dross [18].

The main features on the 50 mm C-Mn steel laser cut edge that signify the efficiency of melt removal from the cut kerf include the dross attachment on the lower cut edge and the boundary layer separation point [66]. The dross composition of a C-Mn steel workpiece cut underwater using air comprise of a mixture of metal dross and metal oxide. The elemental composition of metal dross is similar to that of the parent material. For C-Mn steel, the dross composition is mostly iron oxide and manganese [77]. Figure 47 shows the cut cross section of a C-Mn steel workpiece and the workpiece's shape is indicated by the white lines provided.
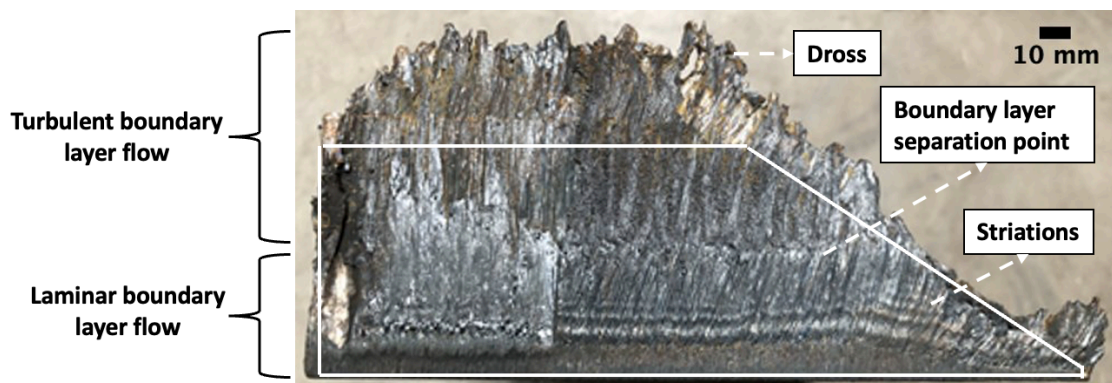
Figure 47: C-Mn steel cut cross section

The profile of the cut edges show that the melt flow starts out from the bottom of the cut kerf as a laminar boundary layer flow in which the melt streamlines follow straight paths. As the melt flow progresses up the cut kerf, the boundary layer thickness increases, and a point is reached where the flow regime transitions into a turbulent boundary layer flow in which the melt particles move in haphazard paths as shown by the nature of the streamlines in Figure 47. The striation pattern below the separation line is uniform following straight contours along the cut thickness and the striation pattern above the boundary layer separation point is irregular with slanting contours [66]. Figure 47 also shows that the attachment dross height in the turbulent boundary layer region increases with increasing C-Mn steel thickness.

The assessment of the dross height comprises of the measurement of the dross which remained adhered to the base of the material after cutting and its dependence, primarily on laser power, cutting gas pressure and stand-off distance. The influence of

laser power on the average dross height was investigated at 4, 6, 8 and 10 kW. The stand-off distance and cutting gas pressure were kept constant at 4 mm and 8 bar, respectively. The laser beam focus position was positioned at the tip of the nozzle. The dross height at each millimetre of the cut length was measured using a Vernier calliper. Afterwards, the average dross height of each cut length was calculated using Microsoft Excel [142]. Figure 48 shows the average dross height with the corresponding maximum cutting speed at different laser power magnitudes.
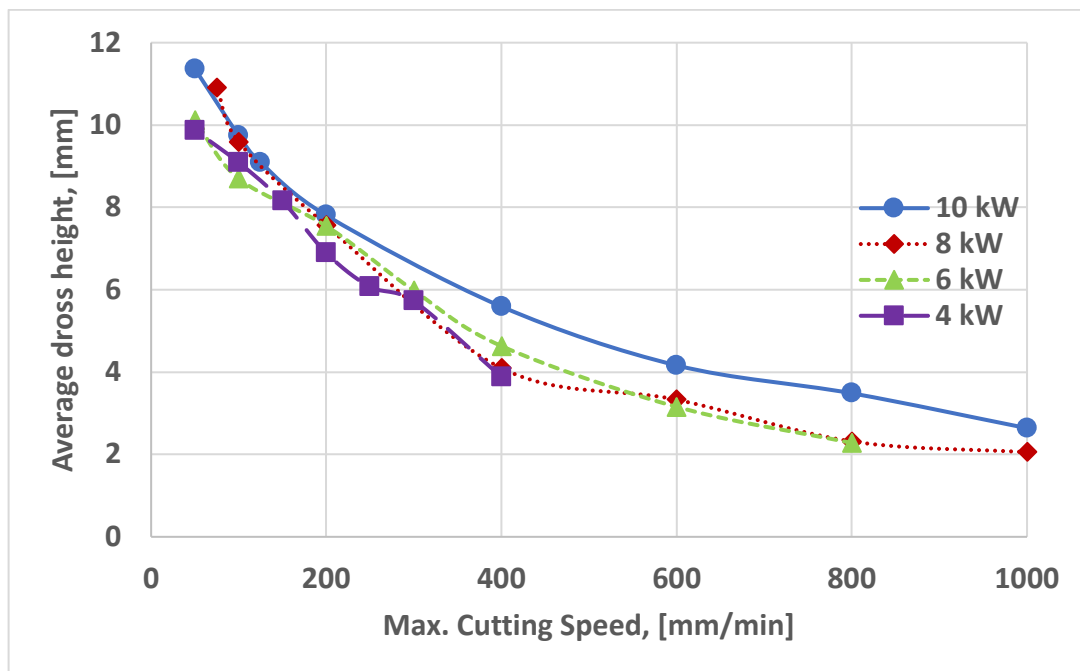
Figure 48: Average dross height as a function of set cutting speed for different laser power magnitudes, an assist gas jet pressure of 8 bar, a focus position of 4 mm and a stand-off distance of 4 mm

Here, it is shown that the level of adhering dross produced is inversely proportional to the cutting speed, and directly proportional to the laser power. Therefore, in offshore decommissioning applications, using a higher laser power provides a larger operating window: higher laser power will be especially useful to minimise secondary emissions as structures have variable thicknesses. It is advantageous to the oil and gas industry to use a laser-based decommissioning technology that retains as much dross attached to the offshore structures as possible. This would imply a low level of secondary waste production and a minimal post clean-up operation. These factors normally lead to reduction in the decommissioning cost and a safer water environment. The same logic can be applied when decommissioning irradiated structures in the nuclear industry [18].

Figure 48 also indicates that a cutting speed of 400 mm/min or below is beneficial if high dross adhesion to the material being cut is required. The cutting speed was the most influencing factor in dross adhesion for the process parameters used.

The influence of assist gas pressure on the average dross height was also investigated for different laser power magnitudes of 6 and 10 kW. The average dross height was calculated for cutting gas pressures of 2, 4 and 8 bar for both laser powers magnitudes. Figure 49 and Figure 50 show the average dross height variation on the kerf exits of the C-Mn steel plates, with respect to cutting speed. Figure 49 and Figure 50 show the dross height variation at a laser power of 6 kW and 10 kW, respectively.
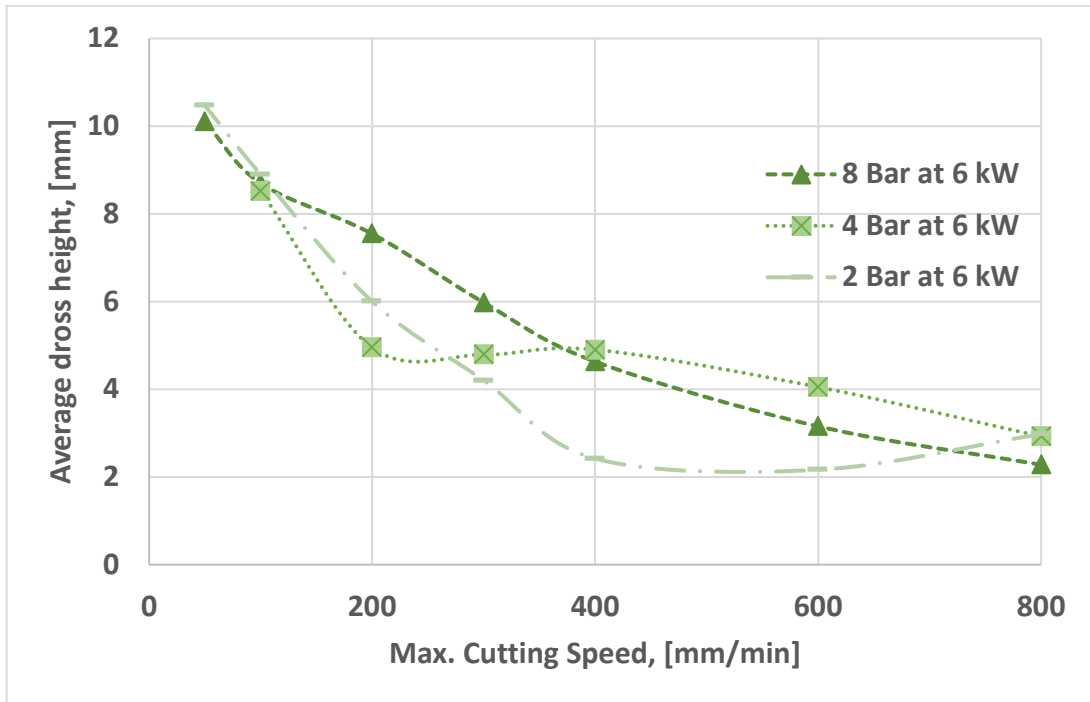
Figure 49: Average dross height as a function of set cutting speed for different assist gas pressures, a laser power of 6 kW, a focus position of 4 mm and a stand-off distance of 4 mm
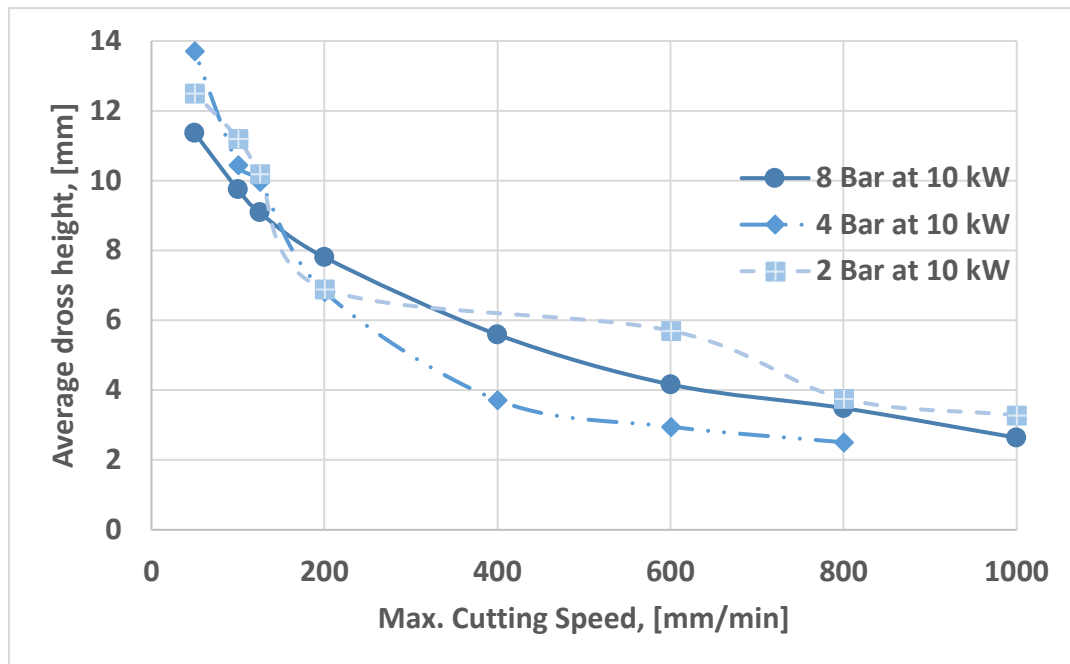
Figure 50: Average dross height as a function of set cutting speed for different assist gas pressures, a laser power of 10 kW, a focus position of 4 mm and a stand-off distance of 4 mm

Variations in the cutting gas pressure did not show any significant influence on dross adhesion for both laser power magnitudes. However, at a laser power of 10 kW, an increase in dross adhesion was noticed at the lowest cutting gas pressure of 2 bar. At a laser power of 6 kW, cutting with a low assist gas pressure of 4 bar gave the highest average dross height for cutting speeds above 400 mm/min.

The influence of power intensity at the material's surface on cut quality in terms of average dross height was also investigated. The cutting gas pressure, laser power and cutting speed were kept constant at 8 bar, 10 kW and 100 mm/min, respectively. The focus position was positioned 4 mm above the surface of the material and the power intensity was varied by increasing the stand-off distance from 5 to 30 mm. Figure 51 shows the average dross height in C-Mn steel as a function of power intensity.
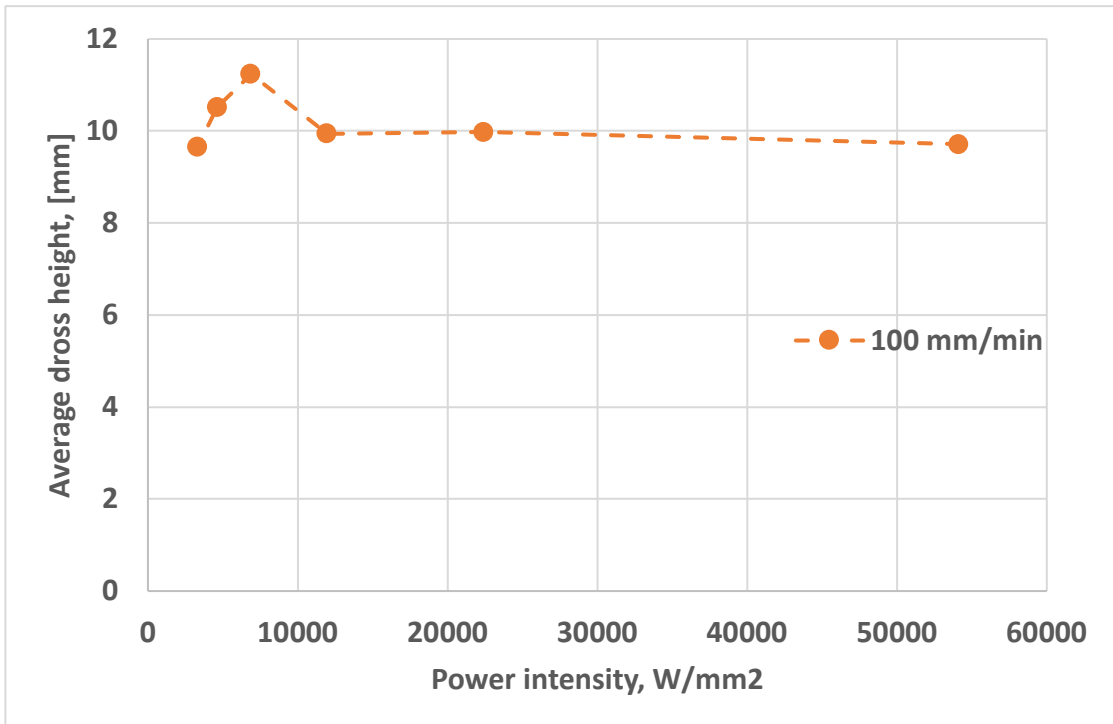
Figure 51: Average dross height as a function of power intensity at a cutting speed of 100 mm/min, an assist gas jet pressure of 8 bar and a laser power of 10 kW

Overall, the relationship of the average dross height with power intensity is unclear. Figure 51 indicates that when the power intensity increases, the variation of the average dross height appears to be random. Generally, the average dross height increases with power intensity from 3318 to 6883 W/mm^2. Above a power intensity of 6883 W/mm^2, the average dross height decreases with increasing power intensity. Figure 51 shows that the optimum cutting conditions for dross adhesion on the side of the cut kerf is using a power intensity of 6883 W/mm^2, corresponding to a stand-off distance of 20 mm.

4.2.5 Kerf width analysis

The influence of laser power on the kerf width was investigated for all the cut workpieces at different laser power magnitudes. The kerf width was measured for laser powers of 4, 6, 8 and 10 kW using a vernier calliper. The width was measured 2 mm from the start and end of each cut. All kerf width measurements were taken from the kerf exit (inclined surface of the workpiece). Afterwards, the average kerf width for each cut length was calculated. For these cutting trials, the stand-off distance was maintained at 4 mm, an assist gas jet pressure of 8 bar was chosen and the beam focus was positioned at the tip of the nozzle. Figure 52 shows the average kerf width with the corresponding maximum cutting speed at different laser power magnitudes.
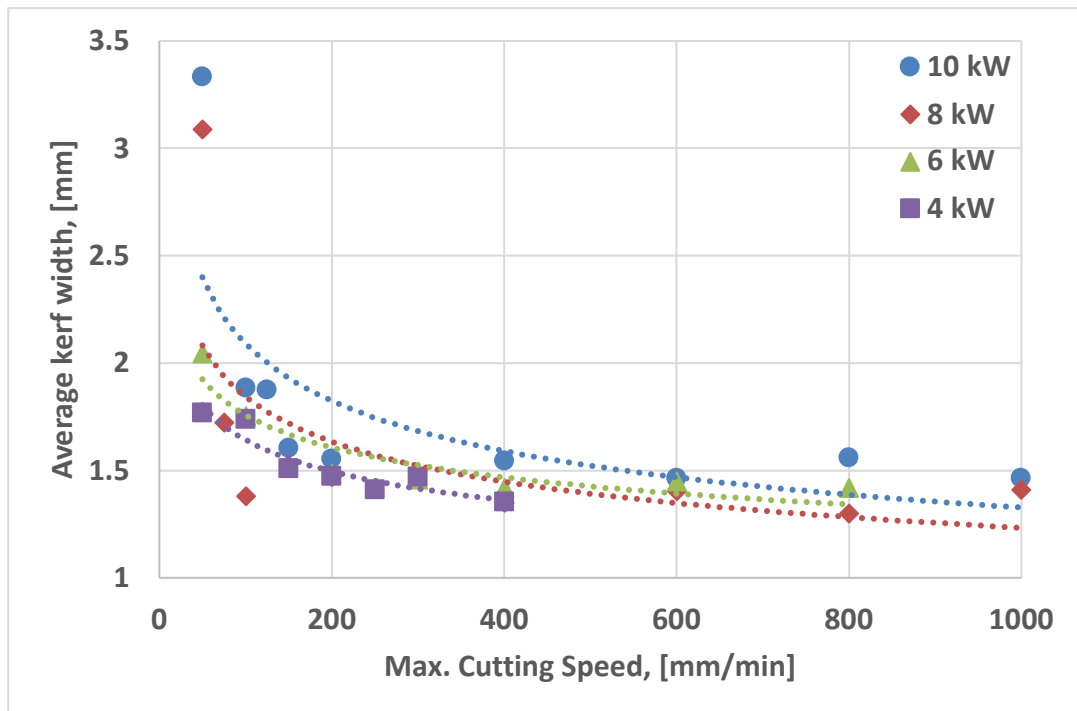
Figure 52: Average cut kerf width as a function of set cutting speed for different laser power magnitudes, an assist gas jet pressure of 8 bar, a focus position of 4 mm and a stand-off distance of 4 mm

The trendlines plotted in Figure 52 show that the average kerf width decreases slightly with increasing cutting speed for at all laser power magnitudes. The average kerf width is also directly proportional to the laser power. For the process parameters used, laser power had a greater impact on the average kerf width than cutting speed. The kerf width of all the cuts was very narrow, ranging from 1.4 to 3.3 mm. In decommissioning applications, a narrow kerf width is necessary to minimise secondary waste and reduce the cost of waste disposal [143].

The influence of assist gas pressure on the average kerf width was studied for different laser power magnitudes of 6 and 10 kW. The average kerf width was calculated for cutting gas pressures of 2, 4 and 8 bar for both laser powers magnitudes. Figure 53 and Figure 54 shows the average kerf width with the corresponding cutting speed at 6 and 10 kW, respectively.
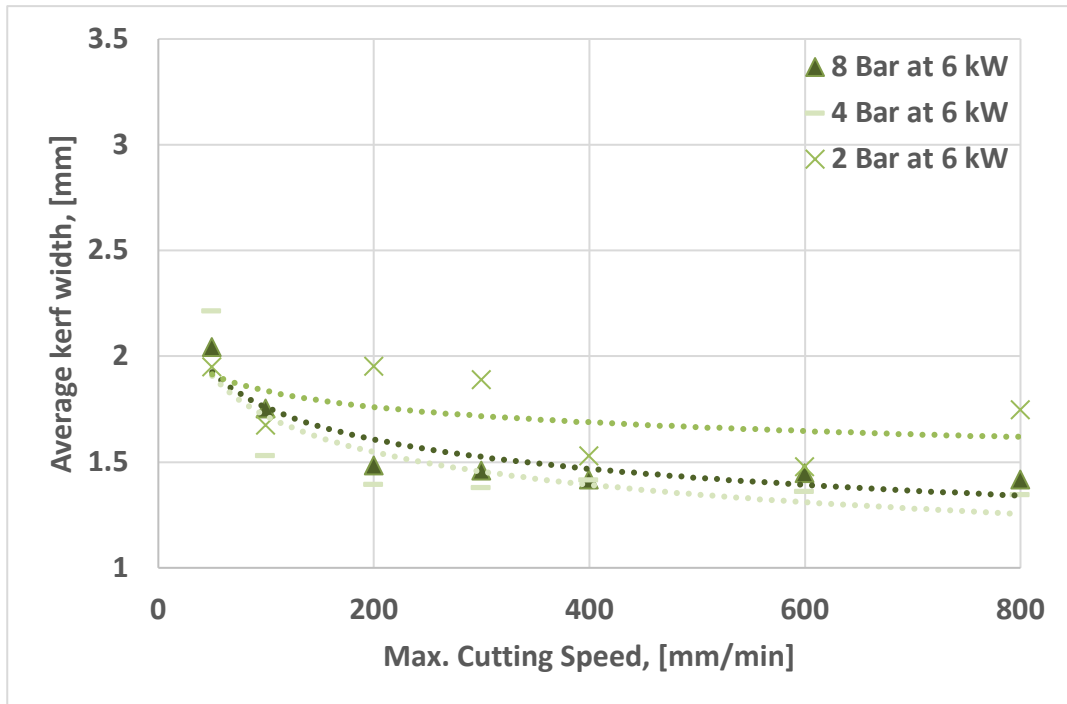
Figure 53: Average cut kerf width as a function of set cutting speed for different assist gas pressures, a laser power of 6 kW, a focus position of 4 mm and a stand-off distance of 4 mm
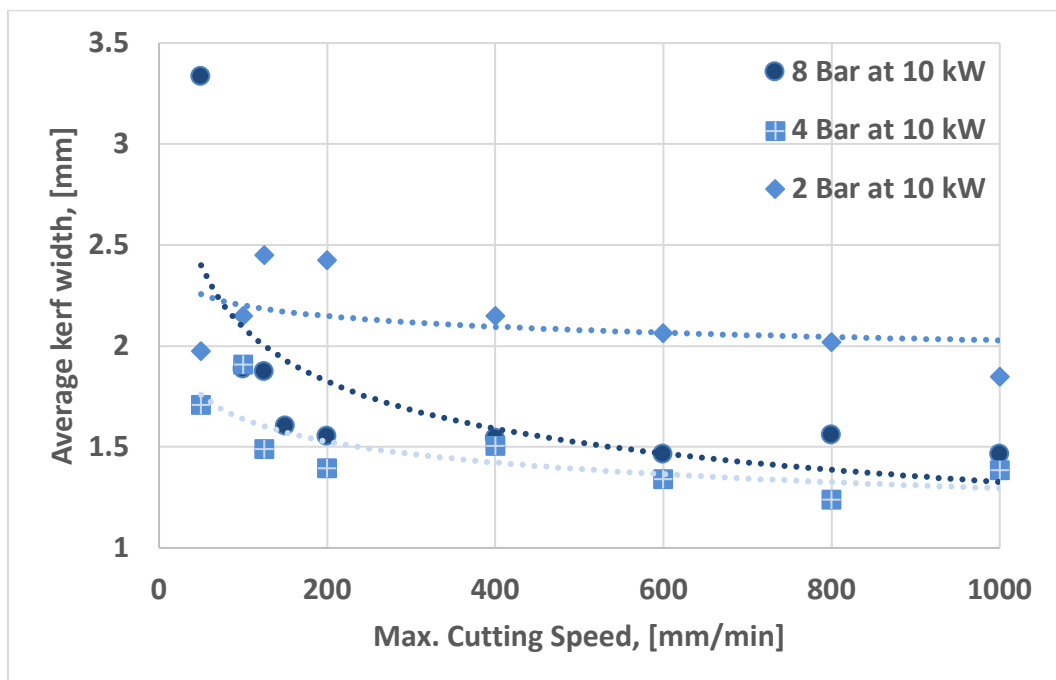
Figure 54: Average cut kerf width as a function of set cutting speed for different assist gas pressures, a laser power of 10 kW, a focus position of 4 mm and a stand-off distance of 4 mm

The effect of cutting gas pressure on the average kerf width is unclear but show the same characteristics for both laser power magnitudes. The changes of the average kerf width at different assist gas pressures could be attributed to changes in the shock structure of the gas jet and the associated mass flow rate having a direct impact on

the underwater laser cutting process. Underwater laser cutting of C-Mn steel with the lowest assist gas pressure of 2 bar gave the widest kerf width at most cutting speeds for both 6 and 10 kW. Cutting at a 4 bar assist gas pressure provided the narrowest kerf width for most cutting speeds at 6 kW and 10 kW.

The influence of the power intensity on the cut quality in terms of the average cut kerf width was also examined. The cutting gas pressure, laser power and cutting speed were kept constant at 8 bar, 10 kW and 100 mm/min, respectively. The stand-off distance was increased from 5 to 30 mm to change the power intensity on the surface of the material. Figure 55 shows the average cut kerf width as a function of power intensity at the constant assist gas pressure, laser power and cutting speed parameters stated.
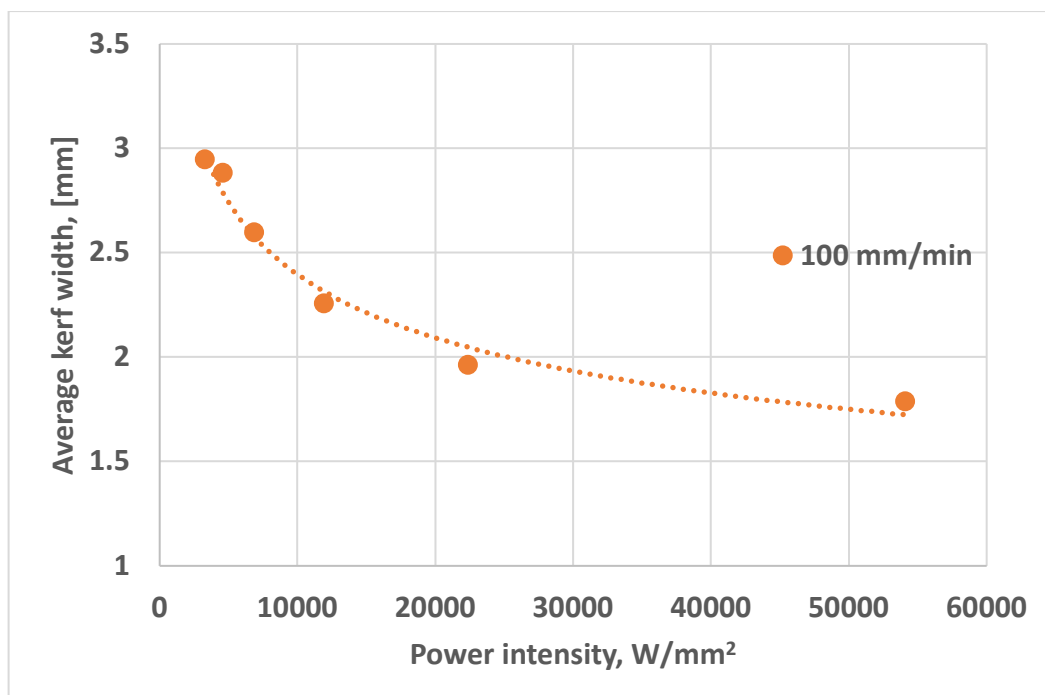
Figure 55: Average cut kerf width as a function of power intensity at a cutting speed of 100 mm/min, a cutting speed of 100 mm/min, an assist gas jet pressure of 8 bar and a laser power of 10 kW

Overall, the average kerf width decreased with increasing power intensity. As the kerf width is strongly dependant on the beam diameter [70, 72], the increase in the kerf width can be attributed to the increasing beam spot diameter on the surface of the workpiece which occurs as the power intensity decreases. The kerf width on the surface of the workpiece was narrow for most of the cuts formed but the width at the back tended to get wider as the thickness or power intensity decreased (increasing the stand-off distance). This widening effect of the kerf width was also observed by Chida et al. [138] who performed underwater laser cutting trials on stainless steel workpieces.

4.2.6 Summary of experimental results in a 1 m³ tank

Underwater cutting of eight C-Mn steel workpieces with a 10-kW fibre laser were performed as a fundamental study for nuclear and offshore decommissioning applications. The presented results of the cutting trials in a 1m³ tank can be summarised as follows:

- A complete separation of a 50 mm thickness C-Mn steel was achieved using a laser power of 10 kW (a power intensity of 59775 W/mm² on the surface of the workpiece), 8 bar compressed air at 4 mm standoff distance and a maximum cutting speed of 125 mm/min;
- The process performance, in terms of the maximum cut thickness, was directly proportional to the laser power and inversely proportional to the cutting speed;
- Power had a greater influence on the maximum cut thickness than assist gas pressure;
- The power intensity on the surface of the material is inversely proportional to the stand-off distance;
- The maximum cut thickness is directly proportional to the power intensity on the surface of the material;
- The average kerf width decreased with increasing power intensity. This can be attributed to the increasing beam spot diameter on the surface of the workpiece which occurs as the power intensity decreases;
- The average kerf width decreases slightly with increasing cutting speed for at all laser power magnitudes;
- Laser power had a greater impact on the average kerf width than cutting speed;
- The effect of cutting gas pressure on the average kerf width is unclear but show the same characteristics at different laser powers of 6 and 10 kW. The changes of the average kerf width at different assist gas pressures could be attributed to changes in the shock structure of the gas jet and the associated mass flow rate having a direct impact on the underwater laser cutting process;
- The level of adhering dross produced is inversely proportional to the cutting speed, and directly proportional to the laser power;
- The attached dross height is directly proportional to the material thickness;
- The optimum cutting conditions for dross adhesion were evident at a power intensity of 6883 W/mm², corresponding to a stand-off distance of 20 mm.

4.3 Underwater laser cutting trials in a high-pressure vessel

The experimental results in this section are divided into three subsections based on the location of the focal position and cutting orientation used in the cutting trials. The first section presents vertical underwater laser cutting trials with a focal position

located at the tip of the dynamic nozzle. The next sections present horizontal underwater laser cutting trials with a focal position located at the tip of a static nozzle and 18 mm inside the material, respectively.

4.3.1 Vertical underwater laser cutting trials with the focal position located at the tip of a dynamic nozzle

Vertical underwater laser cutting trials were conducted using a dynamic nozzle. The influence of power on the corresponding maximum cut thickness, kerf width and dross height was investigated at a hydrostatic pressure of 1 bar, corresponding to a water depth of 10 m. To demonstrate the practical application of underwater laser cutting at a relatively low hydrostatic pressure, the initial cutting trials in a high pressure vessel were carried out at 1 bar hydrostatic pressure. The goal was to cut at 8 bar relative compressed air pressure to that of the vessel, therefore, an assist gas pressure of 9 bar was used. Laser powers of 4, 8 and 10 kW were used to cut the workpiece. For these cutting trials, the stand-off distance was maintained at 10 mm and the laser beam focus was positioned at the tip of the nozzle. The workpiece was moved across the laser beam with incremental increases in cutting speed, until the material could not be cut. The maximum cut thickness, dross height and kerf width created were measured afterward using a Vernier calliper.

Figure 56 shows the maximum underwater cut thicknesses in C-Mn steel as a function of set cutting speed for different laser power magnitudes at a hydrostatic pressure of 1 bar.
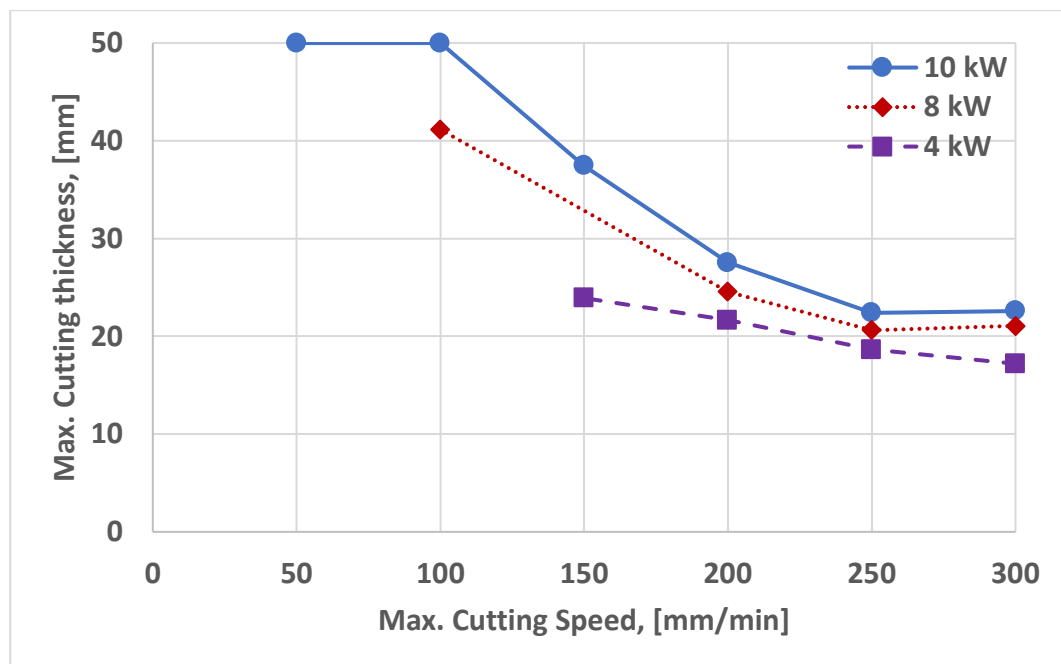
Figure 56: Maximum underwater cut thicknesses as a function of set cutting speed for different laser power magnitudes at a hydrostatic pressure of 1 bar, a cutting gas pressure of 9 bar, stand-off distance of 10 mm and a focal position of 10 mm

As expected, the maximum cut thickness achieved is directly proportional to the laser power and inversely proportional to the cutting speed for the process parameters used. The influence of cutting speed on the maximum cut thickness is more significant at higher laser power magnitudes. As a result, the gradient of the line for 10 kW is greater than that at 4 kW.

Figure 56 also indicate that for high cutting speeds above 200 mm/min, the maximum cut thickness achieved at 4 kW is slightly different than that achieved at 10 kW. Therefore, it is beneficial to use a lower laser power of 4 kW than 10 kW to cut structures with a low thickness to lower energy costs. Overall, a 50 mm thick C-Mn steel workpiece was cut using a laser power of 10 kW, compressed air pressure of 8 bar, a stand-off distance of 10 mm, and a maximum cutting speed of 100 mm/min.

The effect of laser power on the kerf width was also investigated for the cuts formed by the vertical underwater laser cutting process. The kerf width was measured 2 mm from the start and end of each cut. All kerf width measurements were taken from the kerf exit (inclined surface of the workpiece). The average kerf width for each cut length was recorded. Figure 57 shows the average cut kerf width in C-Mn steel as a function of set cutting speed for different laser power magnitudes.
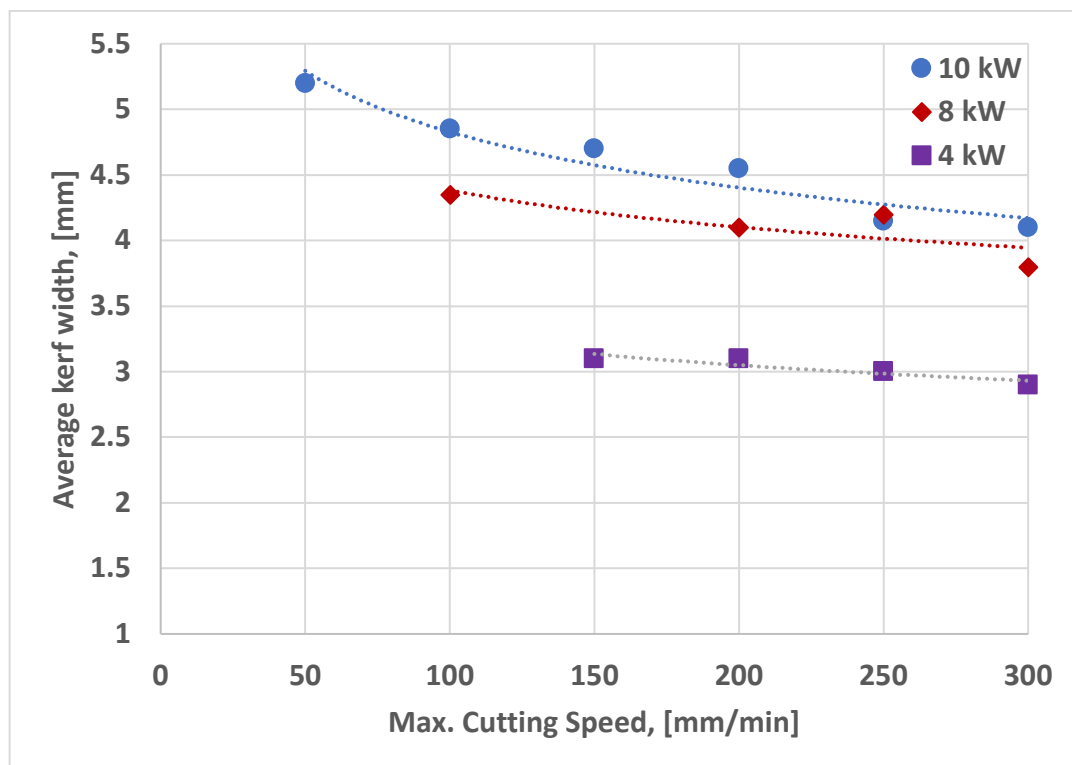
Figure 57: Average cut kerf width as a function of set cutting speed for different laser power magnitudes, a cutting gas pressure of 9 bar, stand-off distance of 10 mm and a focal position of 10 mm

The average cut kerf width decreases slightly with increasing cutting speed and increases with laser power. The laser power had a more significant influence on the average kerf width than cutting speed. The kerf width of all the cuts was relatively wide, ranging from 2.9 to 5.2 mm. The wide kerf width formed can be attributed to

focusing the laser beam at the tip of the nozzle while using a relatively long stand-off distance of 10 mm. As a result, a relatively large spot size of 0.75 was formed on the surface of the workpiece which produced a wide cut kerf width at the kerf exit.

The influence of laser power on the dross height attached on the side of the cut kerf was investigated at 4, 8 and 10 kW. The dross height at each millimetre of the cut length was measured using a Vernier calliper and an average dross height was calculated. To acquire the dross height profile on the cut length, measuring the dross height with a Vernier calliper is fairly precise. Figure 58 shows the average dross height as a function of set cutting speed for different laser power magnitudes.
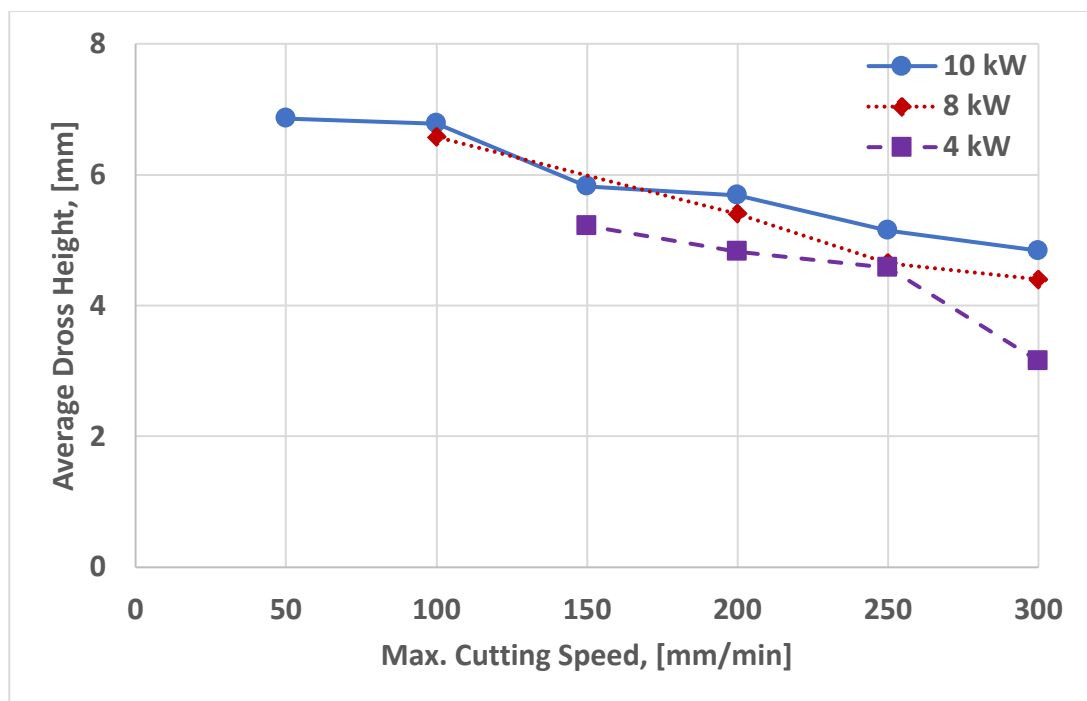
Figure 58: Average dross height as a function of set cutting speed for different laser power magnitudes, cutting gas pressure of 9 bar, stand-off distance of 10 mm and a focal position of 10 mm

According to the results shown in Figure 58, the average dross height is directly proportional to the laser power and inversely proportional to the cutting speed. The most significant parameter affecting the average dross height at 1 bar hydrostatic pressure is the cutting speed. The best cutting conditions for dross adhesion are at high laser powers and low cutting speeds.

Another result worth mentioning for the assessment of adhering dross is related to the creation of bridges within the cut kerf and volume of material removed. Figure 59 (a), Figure 59 (b) and Figure 59 (c) shows the dross attachment on a C-Mn steel workpiece at a laser power of 10, 8 and 4 kW, respectively.
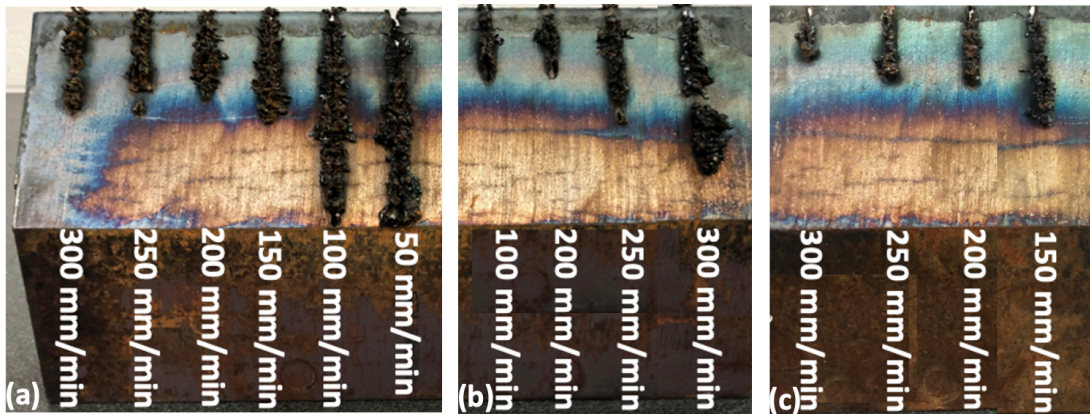
Figure 59: Dross attachment on the C-Mn steel workpiece at a laser power of (a) 10, (b) 8 and (c) 4 kW

For all cut cross sections, a large volume of molten material was not removed during the cutting process and bridges were formed within the cut kerf. It has been found that bridges are made of debris that has not been removed from the kerf and have a greater likelihood to appear when cutting underwater than in air [1]. The creation of bridges could indicate an interaction of the beam or molten material with the water environment. Therefore, the limiting effect of underwater laser cutting is the melt removal process [1]. Accordingly, provided the laser power intensity is high enough to melt the material, choosing process parameters that optimise the melt removal process is vital.

4.3.2 Summary of vertical underwater laser cutting results

Vertical underwater laser cutting trials were carried out with a 10-kW fibre laser at atmospheric pressure conditions and 1 bar hydrostatic pressure. The presented results of vertical underwater laser cutting trials at a hydrostatic pressure of 1 bar can be summarised as follows:

- A 50 mm thick C-Mn steel workpiece was cut with a laser power of 10 kW, a cutting gas pressure of 9 bar, a 10 mm standoff distance, and a maximum cutting speed of 100 mm/min;
- The maximum cut thickness achieved is directly proportional to the laser power and inversely proportional to the cutting speed. The influence of cutting speed on the maximum cut thickness was more significant at higher laser power magnitudes;
- In general, the average cut kerf width decreases slightly with increasing cutting speed and increases with laser power. The laser power had a more significant influence on the average kerf width than cutting speed;
- The average adhering dross height is directly proportional to the laser power and inversely proportional to the cutting speed. The most significant parameter affecting the average dross height at 1 bar hydrostatic pressure is the cutting speed.

4.3.3 Horizontal underwater laser cutting trials with the focal position located at the tip of a static nozzle

Horizontal underwater laser cutting trials were performed using a static nozzle. For these series of tests, the influence of hydrostatic pressure on the corresponding maximum cut thickness, kerf width and dross height was examined at a constant cutting speed of 100 mm/min. Four cuts were made on a C-Mn steel specimen at increasing hydrostatic pressure conditions of 1, 5, 10 and 15 bar, corresponding to a water depth of 10, 50, 100 and 150 m, respectively. The goal was to cut at 8 bar relative compressed air pressure to that of the vessel, therefore, a cutting gas pressure of 9, 13, 18 and 23 bar was used, respectively. All experiments were carried out at a laser power of 10 kW and the stand-off distance was maintained at 5 mm. The maximum cut thickness, dross height and kerf width achieved was measured afterwards using a Vernier calliper.

Table 12 shows the maximum underwater cut thicknesses achieved at different assist gas pressures and hydrostatic pressure conditions inside the vessel.

Table 12: Results and parameters at increasing hydrostatic pressure conditions using a laser power of 10 kW and the stand-off distance of 5 mm

Cutting speed (mm/min)	Cutting pressure (Bar)	Chamber hydrostatic pressure (Bar)	Maximum cut thickness (mm)
100	9	1	50
100	13	5	50
100	18	10	50
100	23	15	50

Table 12 indicates that a maximum cutting speed of 100 mm/min was able to cut a 50 mm thick C-Mn steel workpiece at a hydrostatic pressure of 1, 5 10 and 15 bar. A higher cutting speed would likely be able to cut a 50 mm thick C-Mn workpiece for the process parameters used.

The kerf width formed on the C-Mn steel workpiece was investigated for the process parameters used. The width was measured 2 mm from the start and end of each cut. All kerf width measurements were taken from the kerf exit (inclined surface of the workpiece). Afterwards, the average kerf width of each cut length was recorded. Figure 60 shows the average cut kerf width as a function of set hydrostatic pressure at a constant cutting speed of 100 mm/min.
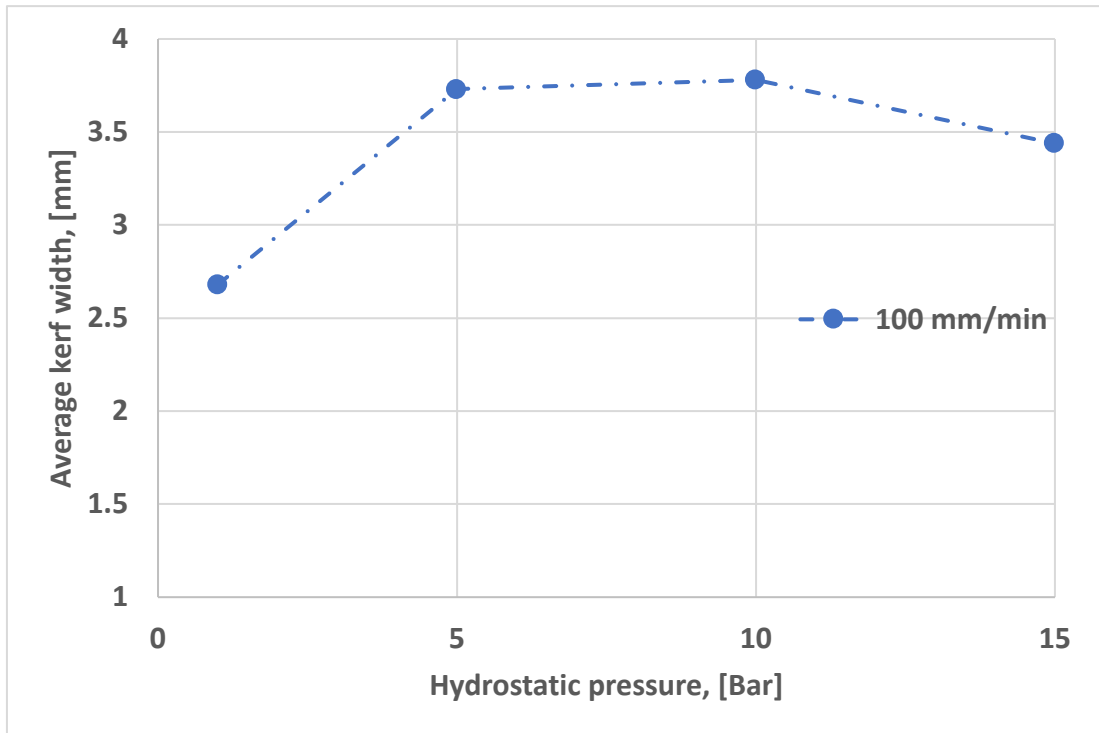
Figure 60: Average cut kerf width as a function of set hydrostatic pressure at a constant cutting speed of 100 mm/min, a laser power of 10 kW and the stand-off distance of 5 mm

The variations of the average kerf width with increasing hydrostatic pressure appear to be random. The lowest average kerf width was achieved when cutting at a hydrostatic pressure of 1 bar and the highest average cut width was achieved at 10 bar hydrostatic pressure. The kerf widths for all the cuts are narrow, ranging from 2.5 – 4 mm.

The influence of hydrostatic pressure on the average dross height was also investigated. The dross height at each millimetre of the cut length was measured using a Vernier calliper and the average dross height was calculated. Figure 61 graphically shows the average dross as a function of set hydrostatic pressure at a constant cutting speed of 100 mm/min.
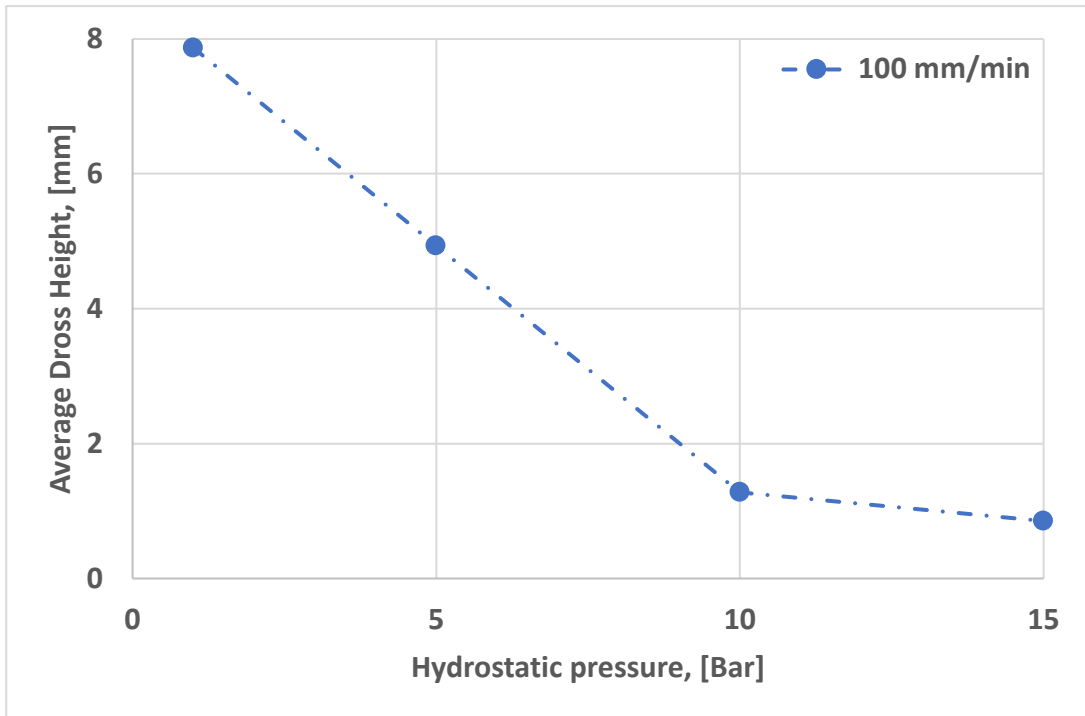
Figure 61: Average dross height as a function of set hydrostatic pressure at a constant cutting speed of 100 mm/min, a laser power of 10 kW and the stand-off distance of 5 mm

Here the average dross height decreases with increasing hydrostatic pressure. The decrease of the average dross height was more significant at lower hydrostatic pressure conditions between 1 and 10 bar. The best cutting conditions for dross adhesion are at the lowest hydrostatic pressure of 1 bar, as shown in Figure 62.
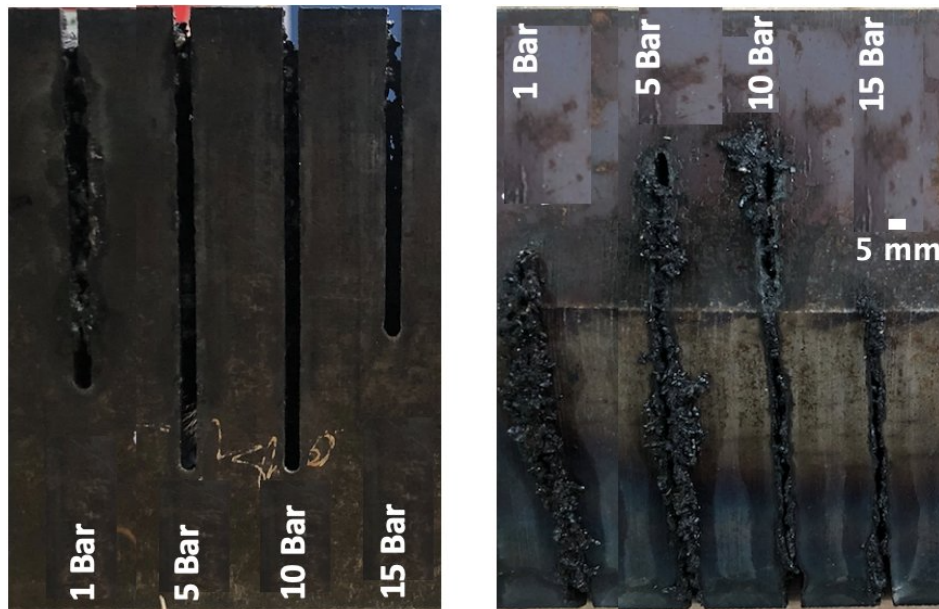
Figure 62: Cut entrance (left) and exit (right) at 1, 5, 10 and 15 bar hydrostatic pressure

4.3.4 Horizontal underwater laser cutting trials at a focal position 18 mm inside the material in increasing hydrostatic pressure conditions

Horizontal cutting trials were carried out in increasing hydrostatic pressure conditions of 0, 5, 10, 15 and 20 bar inside the vessel using a static nozzle. Overall, 34 cuts were carried out on 5 C-Mn steel workpieces. The focal position used in these cutting trials was influenced by the design of the cutting head (ability to move the laser processing optical system inside the cutting head). The focal position was determined experimentally by blip tests on a thin sheet of aluminium. The smallest spot size on the aluminium surface was taken to be the focal position from the tip of the nozzle. The focal position for these cutting trials was located 23 mm from the tip of the nozzle (18 mm inside the material when a stand-off distance of 5 mm is used).

At 1 atmosphere pressure conditions inside the vessel, the influence of laser power on the corresponding maximum cut thickness was investigated. Laser powers of 6, 8 and 10 kW were used to cut the workpiece. For the specified laser power, an assist gas jet pressure of 8 bar was chosen, and the stand-off distance was maintained at 5 mm. The workpiece was moved across the laser beam focused by the cutting head, with incremental increases in cutting speed, until the material could not be cut. Afterwards, the maximum cut thickness achieved was measured using a Vernier calliper.

At 5 to 20 bar hydrostatic pressure conditions inside the vessel, corresponding to a water depth of 50 to 200 m, the influence of hydrostatic pressure on the maximum cut thickness, kerf width and dross height was investigated for a set of cutting speeds. The goal was to cut at 8 bar relative compressed air pressure to that of the vessel, so the cutting gas pressure varied from 8, 13, 18, 23 and 28 bar depending on the hydrostatic pressure condition of the vessel. All experiments were carried out at a laser power of 10 kW and the stand-off distance was maintained at 5 mm. The workpiece was moved across the laser beam by an XYZ motion platform, at a constant cutting speed, until the material could not be cut. The maximum cut thickness, dross height and kerf width achieved was measured afterwards using a Vernier calliper.

The results of the horizontal cutting trials will now be addressed, beginning with the effect of power on maximum cut thickness at 1 atmospheric pressure conditions. Figure 63 shows the maximum underwater cut thicknesses in C-Mn steel as a function of set cutting speed for different laser power magnitudes at 1 atmospheric pressure conditions.
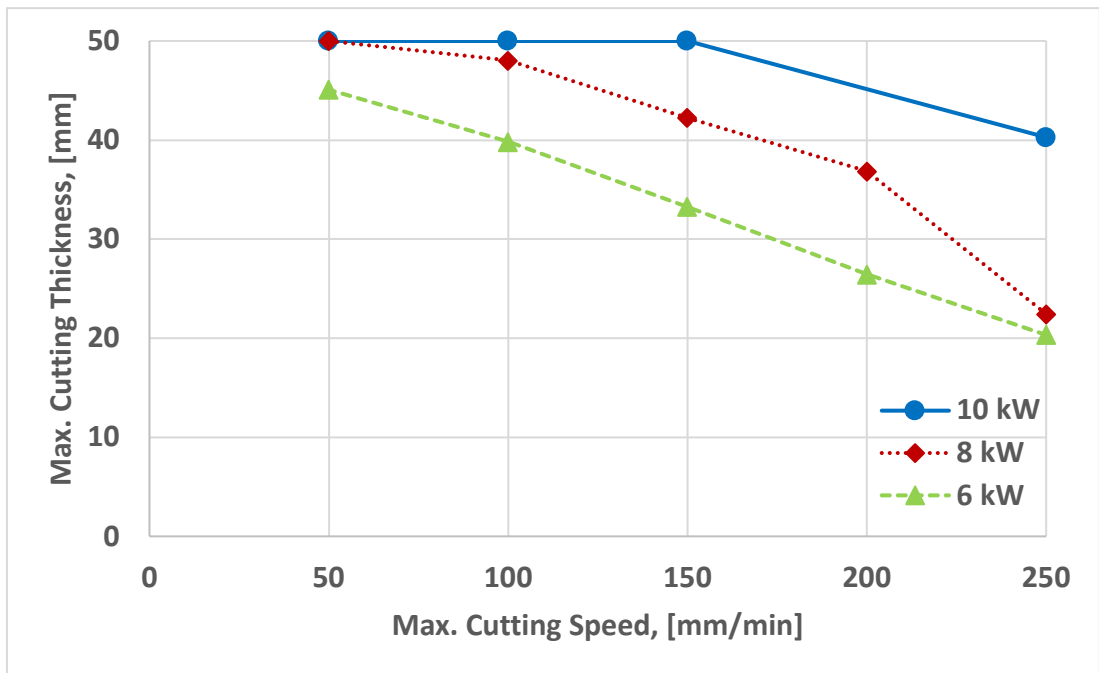
Figure 63: Maximum underwater cut thicknesses as a function of set cutting speed for different laser power magnitudes at 1 atmospheric pressure conditions, a relative cutting gas pressure of 8 bar, a laser power of 10 kW, a focal position located 18 mm inside the material and a stand off distance of 5 mm

As expected, the maximum cut thickness increased with increasing laser power and decreased with increasing cutting speed. A 50 mm thick C-Mn steel workpiece was cut using a laser power of 10 kW, a cutting gas pressure of 8 bar, a stand-off distance of 5 mm and a maximum cutting speed of 150 mm/min. This gives a process capability of cutting 5 mm per kW for the process parameters used. The process capability would likely increase by using a lower cutting speed to cut a higher thickness of C-Mn steel.

The process performance, in terms of the maximum cut thickness, was also investigated at increasing hydrostatic pressure conditions. Figure 64 shows the maximum cut thickness with the corresponding cutting speed at different hydrostatic pressure conditions.
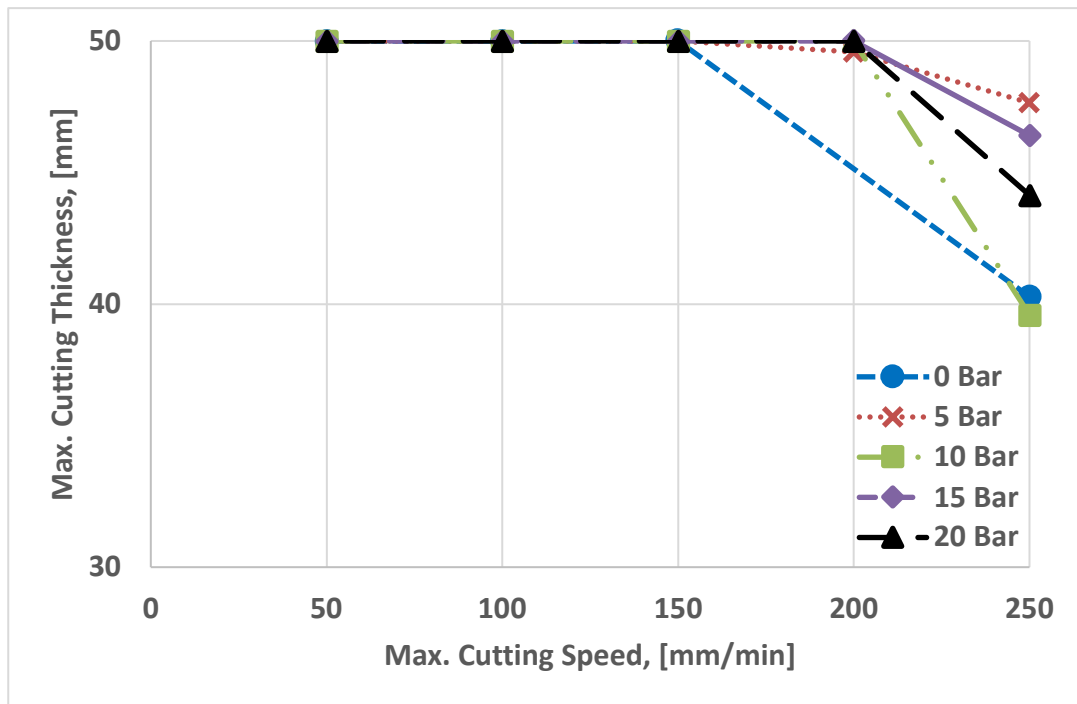
Figure 64: Maximum underwater cut thicknesses as a function of set cutting speed for various hydrostatic pressure conditions, a relative cutting gas pressure of 8 bar, a laser power of 10 kW, a focal position located 18 mm inside the material and a stand off distance of 5 mm

Here, a 50 mm thick C-Mn steel workpiece can be adequately cut with a maximum cutting speed of 200 mm/min at almost all hydrostatic pressures. At 5 bar hydrostatic pressure, the maximum cut thickness is 49.58 mm at 200 mm/min due to an experimental error of stopping laser emission early during the cutting process. At atmospheric pressure conditions, a cut was not made at 200 mm/min due to the depletion of the air bottle bank during the cutting trials.

The maximum cut thickness is inversely proportional to the cutting speed for all hydrostatic pressure conditions after a specific cutting speed (150 mm/min for 0 and 5 bar hydrostatic pressure, and 200 mm/min for 10, 15 and 20 bar hydrostatic pressure). When using an 8 bar relative compressed air pressure to that of the vessel, the effect of the hydrostatic pressure condition of vessel on the maximum cut thickness achieved is minimal. Overall, Figure 64 shows that underwater laser cutting is achievable with excellent performance at a hydrostatic pressure of up to 20 bar, representing an extreme water depth of up to 200 m.

Figure 65 shows the cut workpieces at (a) 0, (b) 5, (c) 10, (d) 15 and (e) 20 bar hydrostatic pressure.
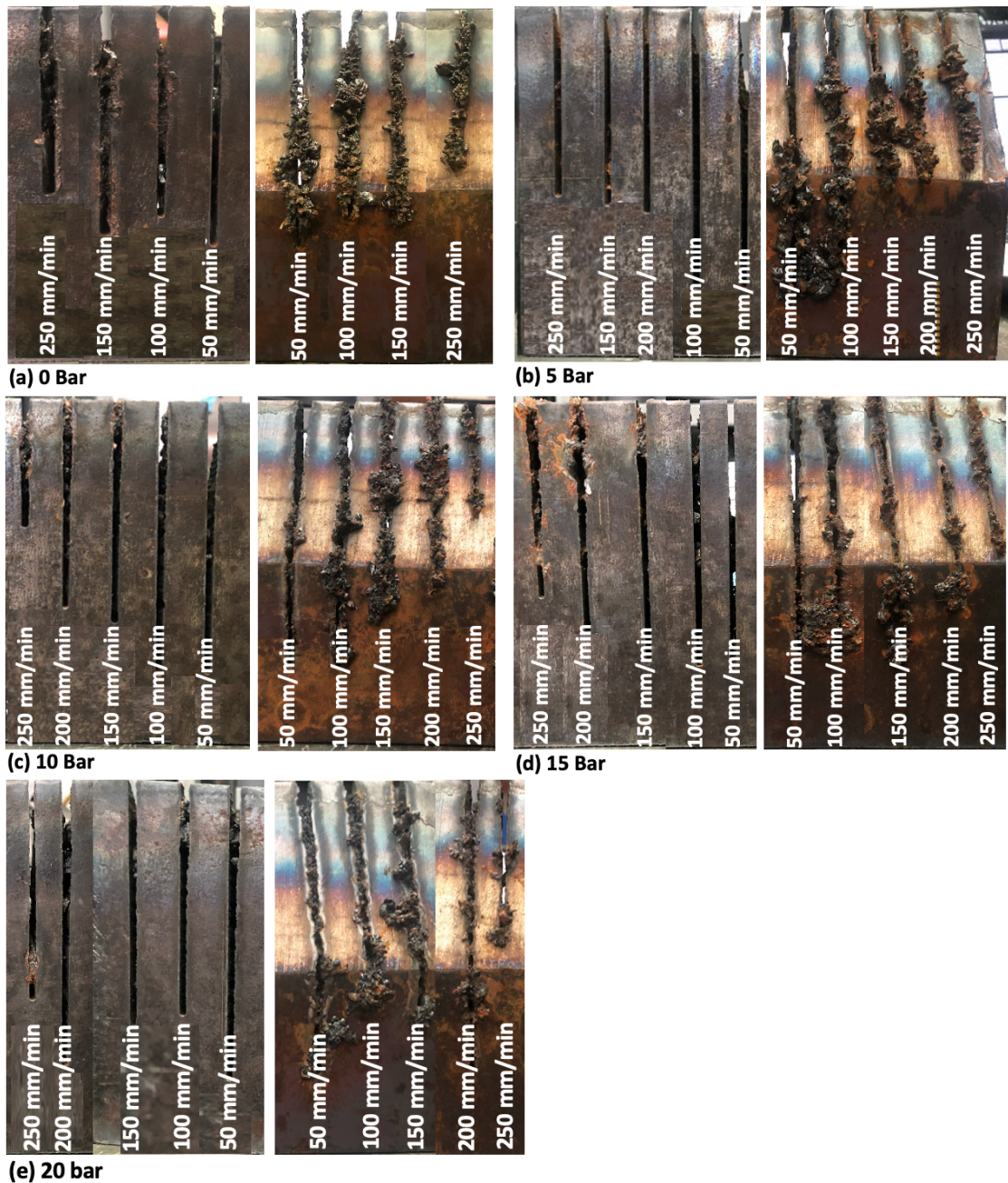
Figure 65: Cut workpiece at a hydrostatic pressure of (a) 0 bar front (left) and back (right), (b) 5 bar front (left) and back (right), (c) 10 bar front (left) and back (right), (d) 15 bar front (left) and back (right) and (e) 20 bar front (left) and back (right) with set cutting speed

Compared to the vertical cutting trials (see Figure 59), Figure 65 shows that a significant volume of the melt is removed from the cut kerf at all hydrostatic pressure conditions particularly for cutting speeds lower than 200 mm/min. The significant volume of molten material ejected from the cut kerf can be attributed to locating the focal point inside the material. A focal position located 18 mm inside the workpiece creates a wider kerf width. Consequently, the melt removal process is optimised as the area in which the gas jet interacts with the melt increases.

Figure 65 also indicate that the back of the cut workpiece shows that the attached dross height decreased with increasing hydrostatic pressure from 0 to 20 bar. As a result, the weight of sedimented dross increases with increasing hydrostatic pressure of up to 20 bar, representing a water depth of 200 m. The effects of sedimented dross in subsea decommissioning applications can cause marine pollution. Therefore, sedimented dross threatens the health of marine species, food safety and quality, ocean health and human health [144].

The dross height at each millimetre of each cut length was measured using a Vernier calliper and the average dross was calculated. Figure 66 shows the average dross height as a function of set cutting speed at different hydrostatic pressure conditions of the vessel.
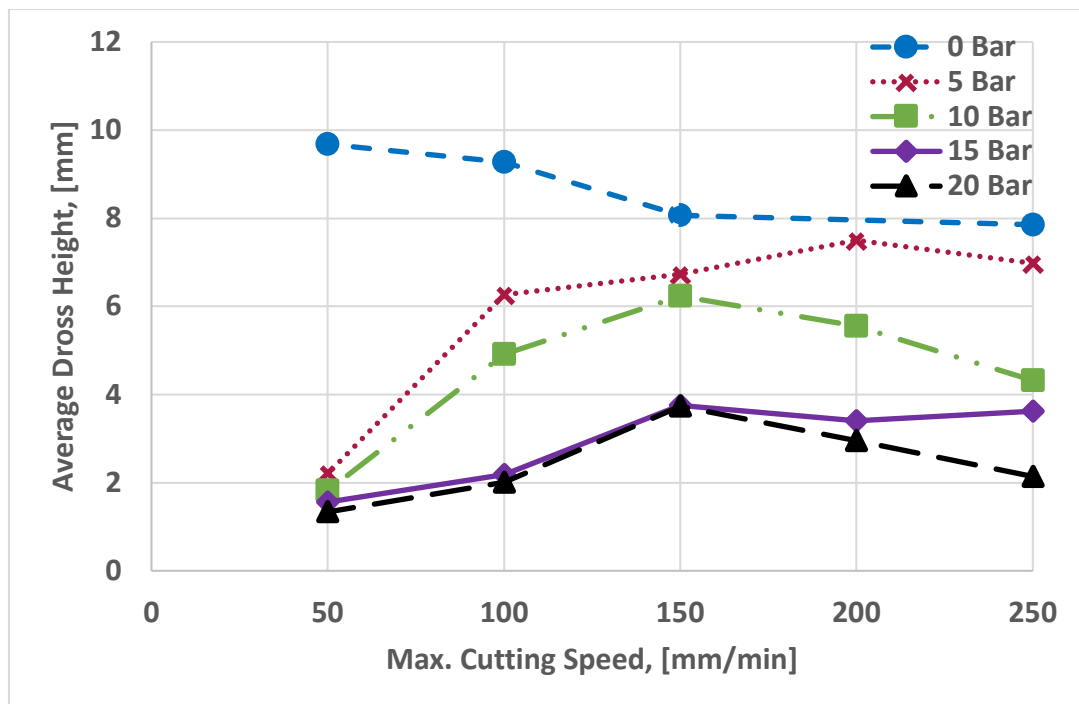
Figure 66: Average dross height with the corresponding cutting speed for various hydrostatic pressure conditions, a relative cutting gas pressure of 8 bar, a laser power of 10 kW, a focal position located 18 mm inside the material and a stand off distance of 5 mm

As expected, the average dross height decreased with increasing cutting speed for 1 atmosphere hydrostatic pressure condition. However, the relationship between the average dross height and cutting speed at higher hydrostatic pressure conditions is unclear. At 5 and 15 bar hydrostatic pressure, the average dross height increased with increasing cutting speed. At 10 and 20 bar, the average dross height increases with increasing cutting speed up to 150 mm/min then decreased. Therefore, the variation of the average dross height with increasing cutting speed is random above atmospheric pressure conditions. Figure 66 also shows that the average dross height decreases with increasing hydrostatic pressure at all cutting speeds.

The measurements for the attached dross height produced at a hydrostatic pressure of 20 bar were repeated to check for a measurement error. Figure 67 shows a

comparison of the average dross height calculated from the first and second set of measurements.
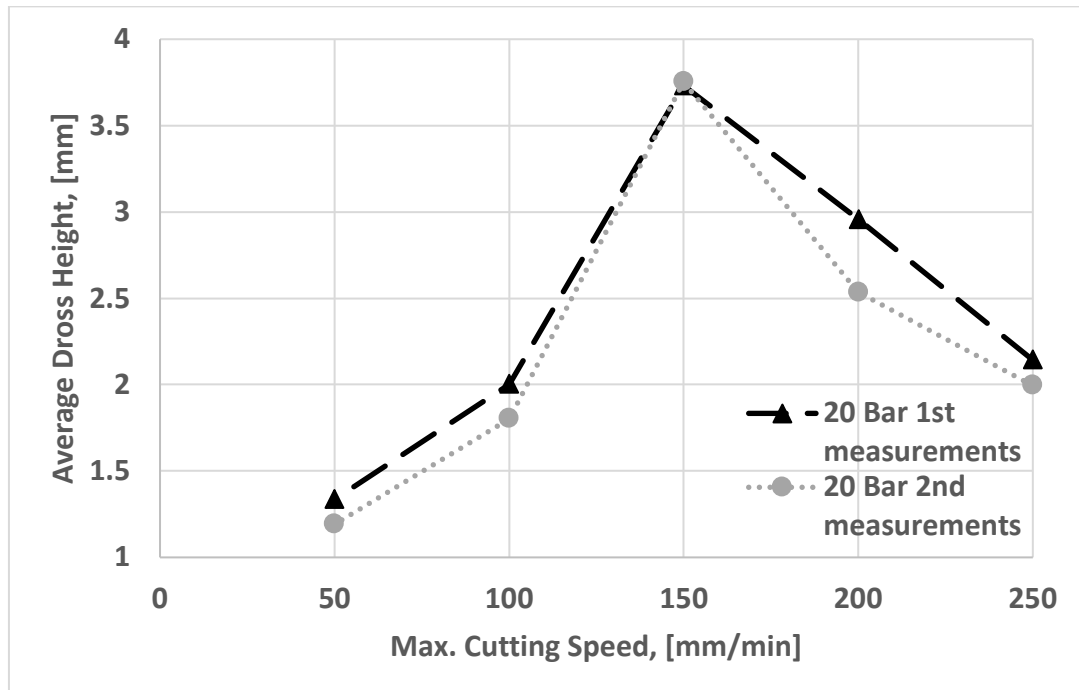
Figure 67: Average dross height with the corresponding cutting speed at a hydrostatic pressure of 20 Bar, a relative cutting gas pressure of 8 bar, a laser power of 10 kW, a focal position located 18 mm inside the material and a stand off distance of 5 mm

The average dross height calculated from the first set of measurements is nearly identical to that calculated from the second set of measurements. The small difference in the average dross height values can be attributed to an observation error. Additionally, the error could be due to dross filaments breaking before or during the measurements. The dross filaments of certain cuts was brittle, particularly at the top of the filament. The second set of dross height measurements may be lower than the first due to the Vernier calliper hitting the top of some dross filaments during the first set of measurements.

At all hydrostatic pressure conditions, the kerf width was measured using a Vernier calliper at 2 mm from the start and end of each cut length. All kerf width measurements were taken from the kerf exit (inclined surface of the workpiece). Figure 68 shows the average kerf width with the corresponding cutting speed.
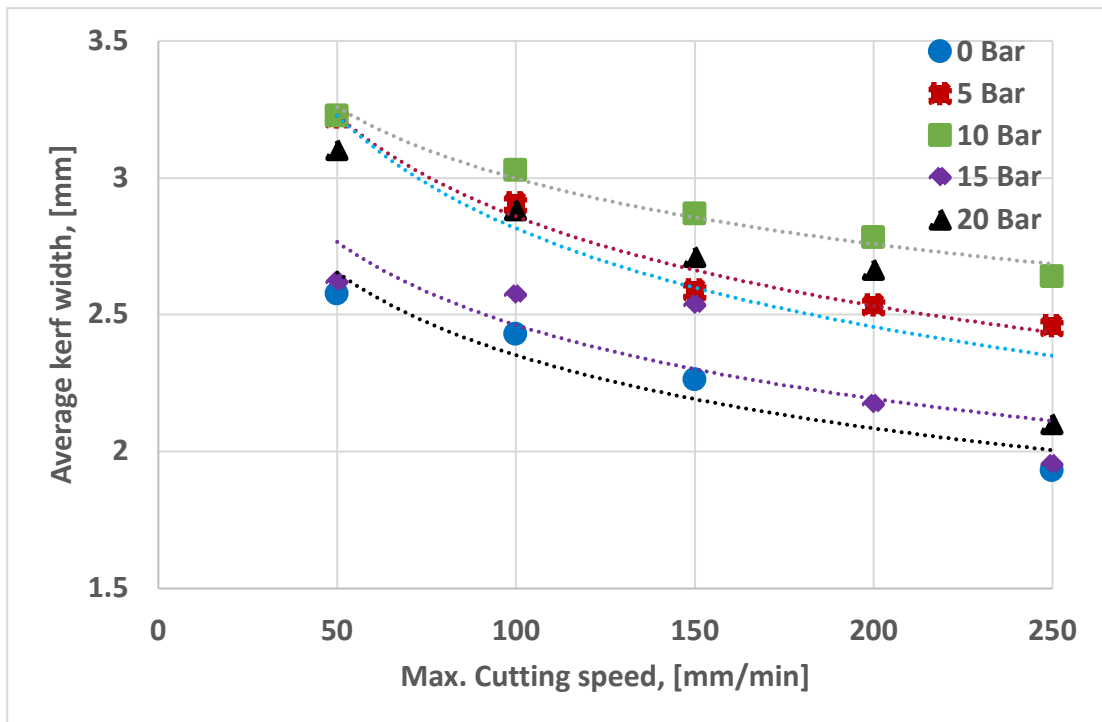
Figure 68: Average kerf width with the corresponding cutting speed, a relative cutting gas pressure of 8 bar, a laser power of 10 kW, a focal position located 18 mm inside the material and a stand off distance of 5 mm

The average kerf width decreased slightly with increasing cutting speed at all hydrostatic pressure conditions. The variations of the average kerf width with increasing hydrostatic pressure appear to be random. The lowest average kerf width was achieved when cutting at 1 atmosphere hydrostatic pressure and the highest average kerf width was achieved at 10 bar hydrostatic pressure. The kerf widths for all the cuts are narrow, ranging from 2 – 3.3 mm.

4.3.5   Summary of horizontal underwater laser cutting results

A 10-kW fibre laser was used to conduct horizontal underwater laser cutting trials of a 50 mm C-Mn steel workpiece in increasing hydrostatic pressure conditions inside the vessel, with the focal point positioned at the tip of a static nozzle. The influence of hydrostatic pressure on the maximum cut thickness, kerf width and dross height was examined at a constant cutting speed of 100 mm/min. The presented underwater laser cutting results can be summarised as follows:

- A 50 mm thick C-Mn steel workpiece was cut at all hydrostatic pressure conditions inside the vessel;
- The variations of the average kerf width with increasing hydrostatic pressure appear to be random;
- The average dross height decreased with increasing hydrostatic pressure. The decrease of the average dross height was more significant at lower hydrostatic pressure conditions between 1 and 10 bar.

An underwater cutting study was also conducted with the focal position located 18 mm inside the workpiece. With a laser power of 10 kW, cutting trials were performed on C-Mn steel at increasing hydrostatic pressure conditions of 0, 5, 10, 15 and 20 bar inside the vessel using a static nozzle. In an unpressurised vessel (1 atmospheric pressure conditions), the influence of laser power on the maximum cut thickness was investigated. At 5 to 20 bar hydrostatic pressure conditions inside the vessel, corresponding to a water depth of 50 to 200 m, the influence of hydrostatic pressure on the maximum cut thickness, kerf width and dross height was investigated for a set of cutting speeds. The results presented can be summarised as follows:

- At 1 atmospheric pressure conditions, the maximum cut thickness is directly proportional to the laser power and inversely proportional to the cutting speed;
- A maximum cutting speed of 200 mm/min was used to cut a 50 mm thick C-Mn steel workpiece at almost all hydrostatic pressure conditions;
- A high volume of molten material was removed during the cutting process at all hydrostatic pressure conditions;
- The average kerf width decreased slightly with increasing cutting speed at all hydrostatic pressure conditions;
- The average dross height decreased with increasing hydrostatic pressure at all cutting speeds;
- The average kerf width decreased slightly with increasing cutting speed at all hydrostatic pressure conditions.

5 Development of an energy balance theoretical model for underwater laser cutting

The development of a power balance theoretical model for underwater laser cutting was accomplished in two phases. The first phase comprises of modelling an energy balance theoretical model for conventional laser cutting and validating the results using experimental data. The second phase concerns modifying the power balance equation for conventional laser cutting with conduction and convection heat losses that occur underwater. The theoretical results are then validated by experimental results of underwater laser cutting trials in a 1 m³ tank. Figure 69 shows the stages of the development of an energy balance theoretical model for underwater laser cutting.
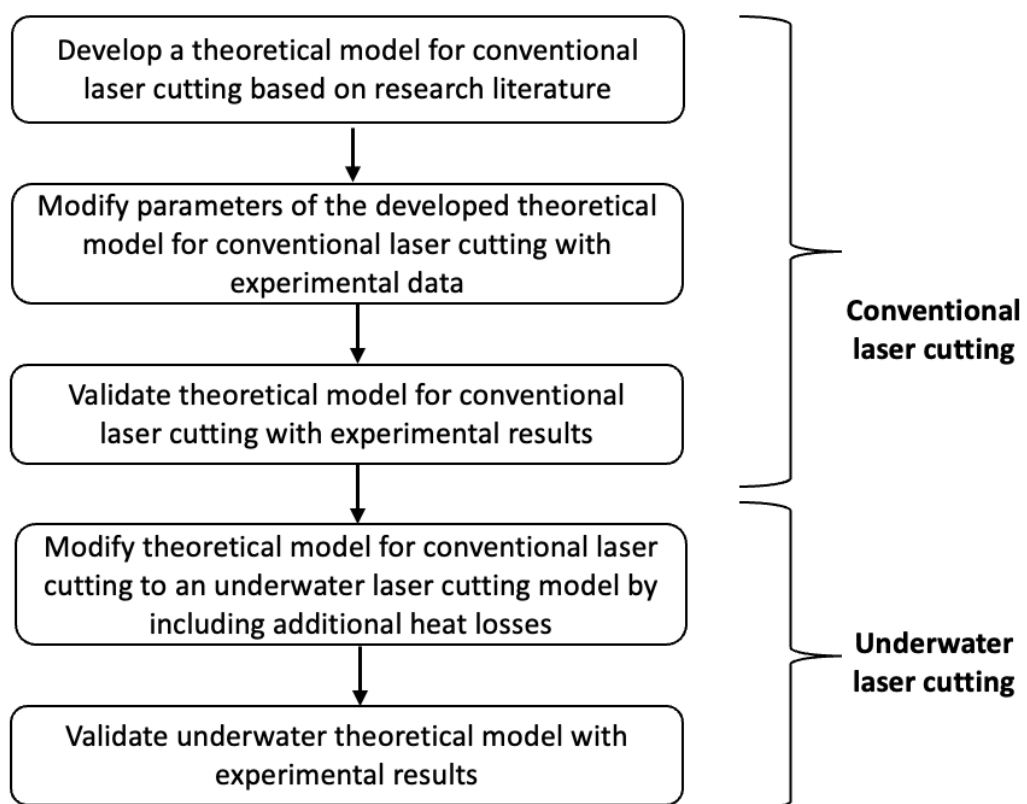
Figure 69: Development of an energy balance analytical model for underwater laser cutting

The stages employed to develop an energy balance model for underwater laser cutting will now be discussed in their chronological order, starting with the theoretical modelling for conventional laser cutting from literature using MATLAB R2017a [145].

5.1 Energy balance theoretical model for conventional laser cutting

An energy balance which describes the equilibrium setup in the cutting zone during laser oxygen cutting was developed based on a study by Seme & Schneider [146]. The governing principle for the energy balance can be expressed as [147]:

$$\textit{Energy supplied to the cut zone} = \textit{Energy used in generating a cut} + \textit{Energy losses} \qquad (45)$$

Equation (45) refers to a cut front with the geometry shown in Figure 70. It is assumed that energy is absorbed by this cut front and then redistributed as useful energy (which generates the cut) and losses (which do not) [33]. This is, of course, a great simplification but it does help to clarify the situation for a largely qualitative analysis such as this one.
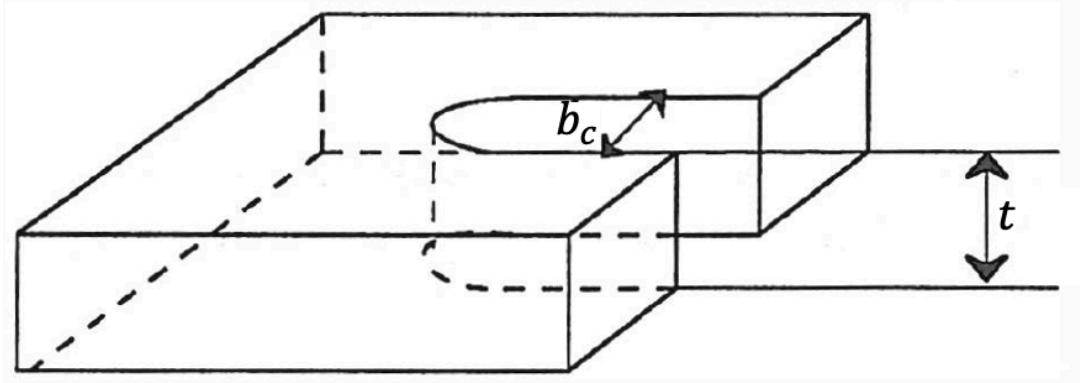
Figure 70: A schematic of the cut front geometry

The interactions in the cut zone can be described by an energy balance. The power balance for a steady-state laser oxygen cutting of a steel substrate can be expressed using a lumped parameter formulation as [146]:

$$P_{abs} + P_r = P_{hl} + P_m + P_w \qquad (46)$$

This energy balance contains P_{abs} the power absorbed, P_r the diffusion limited reactive power gain due to oxidation, P_{hl} the thermal leakage power (conduction losses) in the solid material, P_m the heat for melting the material and P_w denotes the power for heating of the molten material [146]. This equation has heat sources on the left and heat sinks on the right. Heat sinks on the right can be calculated as [146]:

$$P_m + P_w = v_c b_c t \rho (c_p (T_p - T_\infty) + H_m) \qquad (47)$$

$$P_{hl} = 4Kt(T_m - T_\infty)\left(\frac{P_e}{2}\right)^{0.36} \qquad (48)$$

Where v_c is the cutting speed, b_c is the cut kerf width, t is the material thickness, ρ is the density of the material, c_p is the specific heat capacity, T_p is the process temperature, T_∞ is the ambient temperature, H_m is the specific enthalpy of fusion of the material, K is the thermal conductivity, T_m is the melting temperature and P_e is the Peclet number. The Peclet number and thermal conductivity are dimensionless constants which can be stated as follows [146]:

$$P_e = v_c b_c / 2\kappa \qquad (49)$$

$$K = c_p \kappa \rho \qquad (50)$$

Here, κ is the thermal diffusivity. The Peclet number and thermal conductivity can be used to simplify and express the total power of heat sinks on the right. The total power of heat sinks on the right, P_c, can be expressed as [146]:

$$P_c = 4Kt \left[\left(T_p - T_\infty + (\frac{H_m}{c_p})\frac{P_e}{2} + (T_m - T_\infty)\left(\frac{P_e}{2}\right)^{0.36} \right) \right] \qquad (51)$$

Heat sources on the left-hand side of the energy balance equation are given by the diffusion limited reactive power gain due to oxidation, P_r and the absorbed laser power, P_{abs}. These heat sources can be established as [146]:

$$P_{abs} = P_L A \qquad (52)$$

$$P_r = v_c b_c t \rho H_{FeO} X_{abbr} = 2P_e \frac{K}{c_p} t H_{FeO} X_{abbr} \qquad (53)$$

Where P_L is the laser power at the workpiece, A is the absorption coefficient, H_{FeO} is the reaction enthalpy for the formation of FeO from air and X_{abbr} is the burn-off.

There is no chemical formula for air as it is a mixture of many different compounds with varying percentages. The major components in air are nitrogen (78.1%), oxygen (20.9%), carbon dioxide (0.03%) and many others in minute amounts [148]. The reaction enthalpy for the formation of iron oxide (FeO) from iron (Fe) and oxygen (0_2) is approximately 4 800 kJ per 1 kg iron [146]. Therefore, for the reactive power gain due to oxidation P_r, the reaction enthalpy in the theoretical model was decreased by 79.1% according to the oxygen content in air.

The assumptions for a power balance theoretical model for conventional laser cutting can be stated as follows [36, 146, 147, 149]:

- The theoretical model is based on the power balance equation, so the mass and momentum balance equations are neglected;
- Heat losses by convection and radiation are negligible compared to the power of the laser beam;
- Multiple reflections of laser radiation within the cutting kerf are neglected;
- At the melting point, the effects of melt evaporation and the recoil pressure are quite negligible, so the corresponding terms are omitted;
- All the melted material is removed to form the cut kerf and the kerf sides are heated but not melted so that the width of the melting front is equivalent to the kerf width;

- The surface temperature is kept constant at the melting temperature by using a high pressure assist gas flow;
- The width b_c of the cutting front is constant for the entire cutting depth. This corresponds to the creation of perpendicular cutting edges;
- An absorption degree, A, of 80% was assumed since the oxide layer on the cut front caused by the combustion leads to an increase of absorption.

5.1.1 Validation of theoretical model of conventional laser cutting using experimental data

The material properties and cutting parameters in the theoretical model were altered to validate the model using experimental data of conventional fibre laser cutting experiments. The experimental data concerns laser cutting trials performed in air using a 10-kW fibre laser system as the cutting light source. The laser beam generated by the Ytterbium fibre laser was delivered to the cutting head via a 200 µm diameter optical fibre. The cutting head used high power laser optics in the form of coated fused silica collimating and focusing lenses, of lengths 120 and 250 mm, respectively. A cutting gas pressure of 8 bar was used to cut S355J2+N, a high tensile strength and low carbon steel workpiece with thickness of up to 70 mm. Table 13, Table 14 and Table 15 shows the thermophysical properties of S355J2+N mild steel, chemical composition S355J2+N mild steel, and cutting parameters used in the cutting trials, respectively.

Table 13: Thermophysical and mechanical properties of S355J2+N mild steel [1, 150]

Material properties	Values
Specific heat capacity (J/kgK)	460 - 480
Melting temperature (K)	1780
Thermal conductivity (W/mK)	36 - 54
Thermal diffusivity (m^2/s)	8 e-6
Reaction enthalpy (J/kg)	1392000
Density (kg/m^3)	7850
Yield strength (N/mm^2)	355 - 550
Tensile strength (N/mm^2)	490 - 630

Table 14: Chemical composition S355J2+N mild steel [151]

Element (Percentage by weight - wt%) S355J2+N mild steel						
S355J2+N	C max	Si max	Mn max	P max	S max	Ce max
	0.22	0.55	1.60	0.035	0.035	0.047

Table 15: Cutting parameters

Parameters	Values
Laser power (kW)	5 and 10
Cutting speed (mm/min)	50–1000
Focal position from the workpiece surface (into the material) (mm)	15
Standoff distance (mm)	10
Nozzle diameter (mm)	3.5
Gas pressure (bar)	8
Beam waist diameter (mm)	0.36
Cutting gas type	Air
Maximum thickness (mm)	70

The effect of laser power on cutting S355J2+N mild steel was examined. The maximum cut thickness with the corresponding cutting speed for both the theoretical and experimental work was plotted at 5 and 10 kW. The MATLAB code for the theoretical and practical maximum cut thickness achieved with the corresponding cutting speed is presented in Appendix B. Figure 71 shows a comparison of the theoretical and practical maximum cut thickness achieved with the corresponding cutting speed at different laser power magnitudes.
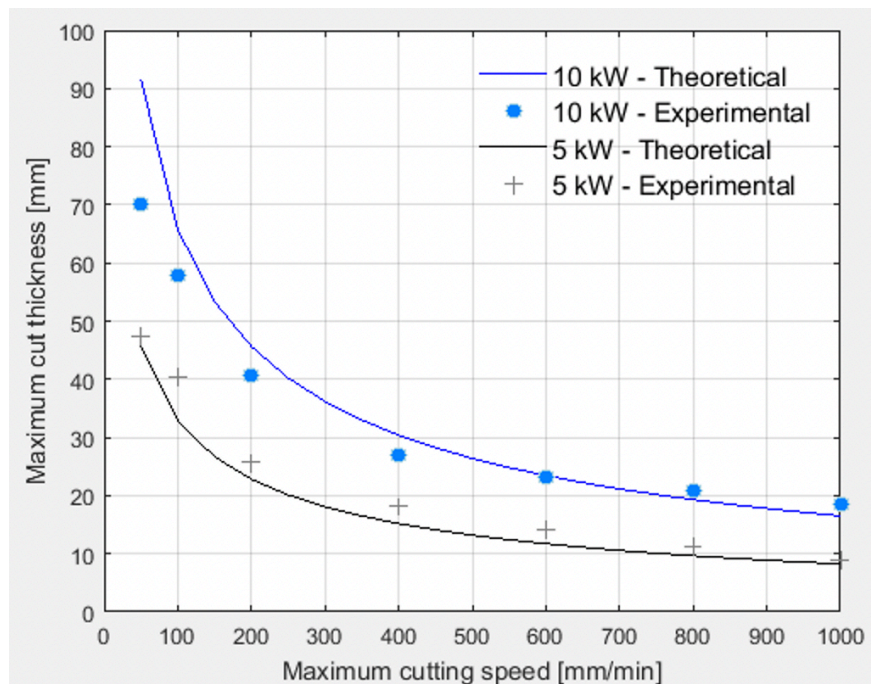
Figure 71: Comparison of the theoretical and experimental maximum cutting thickness achieved with the corresponding cutting speed at 5 and 10 kW

As expected, the maximum cut thickness increases with increasing laser power and decreases with increasing cutting speed at 5 and 10 kW. A S355J2+N steel workpiece with a thickness of 70 mm was cut using a laser power of 10 kW, an assist gas pressure of 8 bar, a 10 mm standoff distance and a maximum cutting speed of 50 mm/min. Figure 71 shows that the predicted theoretical process performance is nearly identical

to the experimental laser cutting performance at 5 and 10 kW. However, they is a better correlation between the theoretical and practical process performance at 10 kW than 5 kW. The slight variation between the theoretical and practical process performance at 5 kW could be attributed to a measurement error of the maximum cut thickness from the experimental data.

5.2 Energy balance for a theoretical model for underwater laser cutting

The energy balance equation was modified by two key heat losses that occur in underwater laser cutting. The energy losses considered in this model are the conduction of heat to the base material and power losses from solid or molten material to water. Conduction losses were investigated because they are the dominant reason which reduces the cutting performance in underwater laser cutting than in air [92]. Convection losses are studied because buoyancy makes it difficult to produce a steady dry cavity where the laser can travel for long distances without being absorbed by water [91].

5.2.1 Conduction of heat to the base material

A high temperature gradient between the solid base material and the solid-melt interface causes heat transfer by conduction. The temperature gradient is higher underwater than in air because the solid base material is continuously cooled by the surrounding water [92]. The solid-melt interface is assumed to be at the melting temperature of the workpiece. The rate of conduction loss to the base material, q_s, can be expressed as [152]:

$$q_s = \frac{K(T_m - T_\infty)}{n\delta_{df}}$$
(54)

Here, n is a constant term which depends on the temperature distribution in the radial direction and δ_{df} is the thermal diffusion length. The product $n\delta_{df}$ denotes the depth from melt front where the workpiece is at ambient temperature [152]. The thermal diffusion length, δ_{df}, which is a function of laser interaction time, $\frac{d}{v_c}$, can be expressed as [152]:

$$\delta_{df} = 2\sqrt{\frac{Kd}{c_p v_c \rho}}$$
(55)

5.2.2 Heat losses from solid or molten material to water

During underwater laser cutting, if water/water vapour is present at the laser–workpiece interface or inside the cut kerf, heat is lost to the surrounding water environment. In a situation when the water at the laser–workpiece interface is vaporised by the laser beam, the high pressure assist gas jet does not allow formation of a stable vapour film at the interaction zone. The heat transfer at the laser–workpiece interface can be assumed to be forced convection and the convective heat transfer coefficient (H_c) can be estimated using [152]:

$$H_c = 0.797 \frac{K_w}{b_c} Re_w^{0.5} Pr_w^{0.33} \qquad Pr > 3 \tag{56}$$

Here, K_w is the thermal conductivity of water, Re_w is the Reynolds number and Pr_w is the Prandtl number of water. The equation of the convective heat transfer coefficient in this model is assumed because it is an experimentally determined parameter whose value depends on all the variables influencing convection such as surface geometry, nature of fluid motion, properties of the fluid, and bulk fluid velocity. The Reynolds number was also assumed to be constant. The rate of convective heat loss, q_w, from the surface of molten layer to water/water vapour can be estimated using [152, 153]:

$$q_w = h_c(T_l - T_\infty) \tag{57}$$

Where T_l is the melt front temperature. The energy balance in equation (46) can be modified for underwater laser cutting as follows:

$$P_{abs} + P_r = P_{hl} + P_m + P_w + q_s + q_w \tag{58}$$

Further assumptions were applied to the energy balance analytical model for underwater laser cutting. The following are the theoretical model's assumptions [101, 152, 154]:

- The values of different thermo-physical properties of water (ρ_w, C_{pw}, K_w) are taken as the average of temperature dependent properties in the range from room temperature to boiling temperature;
- The melting temperature of the specimen is assumed to be the temperature at the solid-melt interface;
- The laser power absorbed at the surface is partly lost by convection to water and the rest is conducted into the material;
- The Reynolds number is calculated with a constant velocity of an underwater gas jet expanding at an inlet pressure of 8 bar.

The theoretical model for underwater laser cutting was validated by the process performance and kerf width analysis results for underwater laser cutting trials in a 1m^3 tank.

5.2.3   Validation of theoretical model for underwater laser cutting

The maximum underwater cut thickness and kerf width for both the theoretical and experimental work was examined. The MATLAB code for the theoretical and practical maximum cut thickness achieved with the corresponding cutting speed is presented in Appendix C. Figure 72 shows a comparison of the theoretical and practical maximum cut thickness with the corresponding cutting speed for underwater laser cutting at different laser power magnitudes.
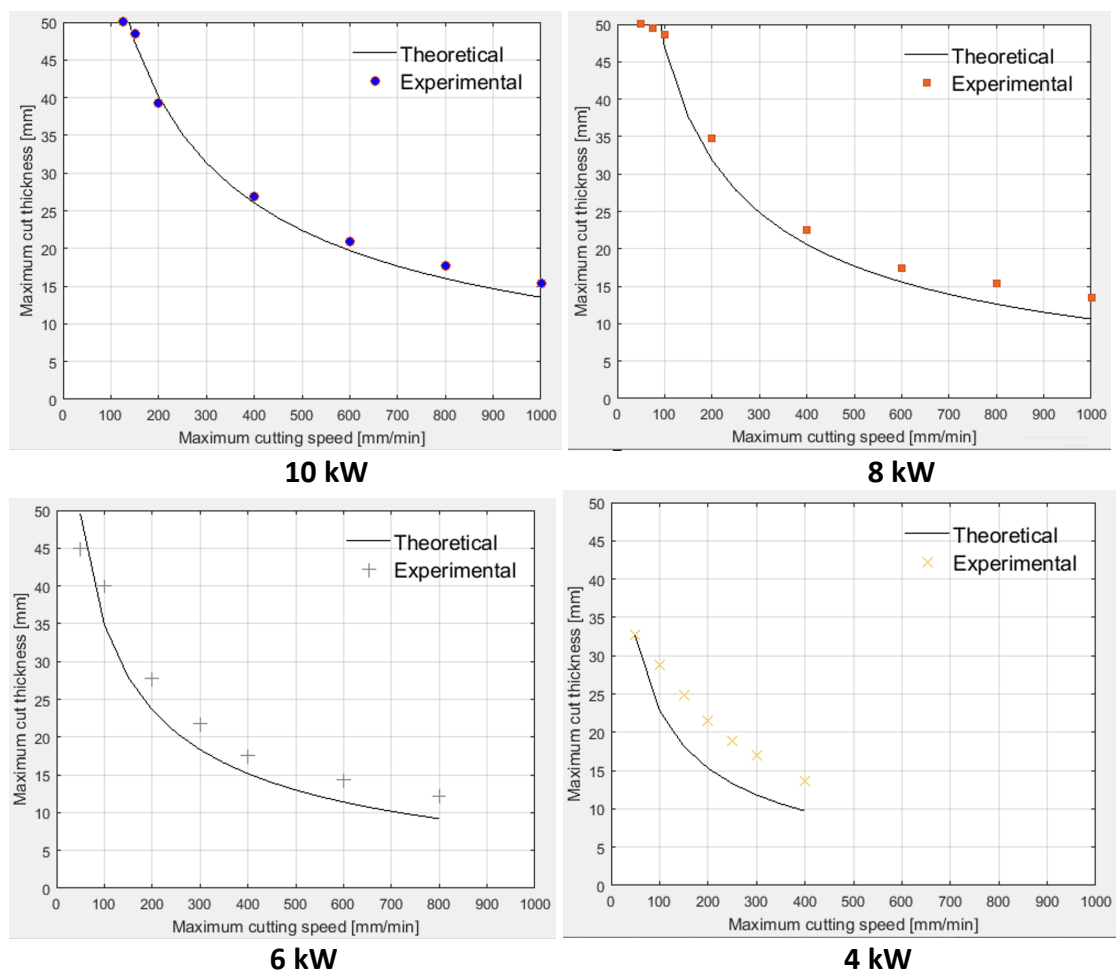
Figure 72: Comparison between the maximum cut thickness with the corresponding maximum cutting speed at a laser power of 10, 8, 6 and 4 kW

As expected, the maximum cut thickness increases with increasing laser power and decreases with increasing cutting speed. A complete separation of a 50 mm thickness C-Mn steel was achieved using a laser power of 10 kW, 8 bar compressed air and a maximum cutting speed of 125 mm/min. Here, the maximum cutting speed for cutting 50 mm C-Mn steel at 10 kW is 125 mm/min for both the theoretical and experimental results.

Overall, the predicted theoretical process performance is substantially the same as the experimental laser cutting results particularly for higher laser power magnitudes of 6, 8 and 10 kW. At 4 kW, the predicted maximum cut thickness is lower than that of the experimental values, especially for higher cutting speeds. The differences in the process performance at 4 kW could be attributed to the fact that the theoretical model only considers the energy balance in underwater laser cutting. Therefore, the theoretical model is limited as the mass and momentum balance equations for underwater laser cutting are neglected.

The influence of laser power on the kerf width was also investigated at different laser power magnitudes of 4, 6, 8 and 10 kW. For the experimental work, the kerf width was measured at a constant thickness of 6 mm (2 mm from the start of the cut) for different cutting speeds. For the theoretical model of underwater laser cutting, the kerf width, b_c, was calculated from the power balance equation as:

$$b_c = \frac{P_L A + 2P_e \frac{K}{c_p} t H_{FeO} X_{abbr} - \left(\frac{K(T_m - T_\infty)}{n\delta_{df}}\right) - (h_c(T_l - T_\infty)) - \left(4Kt(T_m - T_\infty)\left(\frac{P_e}{2}\right)^{0.36}\right)}{v_c t \rho(c_p(T_p - T_\infty) + H_m)} \tag{59}$$

The kerf width is limited by the beam diameter at the location where the kerf width was measured. This condition indicates that the kerf width is larger than the beam diameter where the kerf width was measured, $d(z)$, and can be expressed as [24]:

$$b_c \geq d(z) \tag{60}$$

The MATLAB code for the theoretical and practical kerf width achieved with the corresponding cutting speed is presented in Appendix D. Figure 73 shows a comparison of the theoretical and practical kerf width values for underwater laser cutting at different laser power magnitudes.
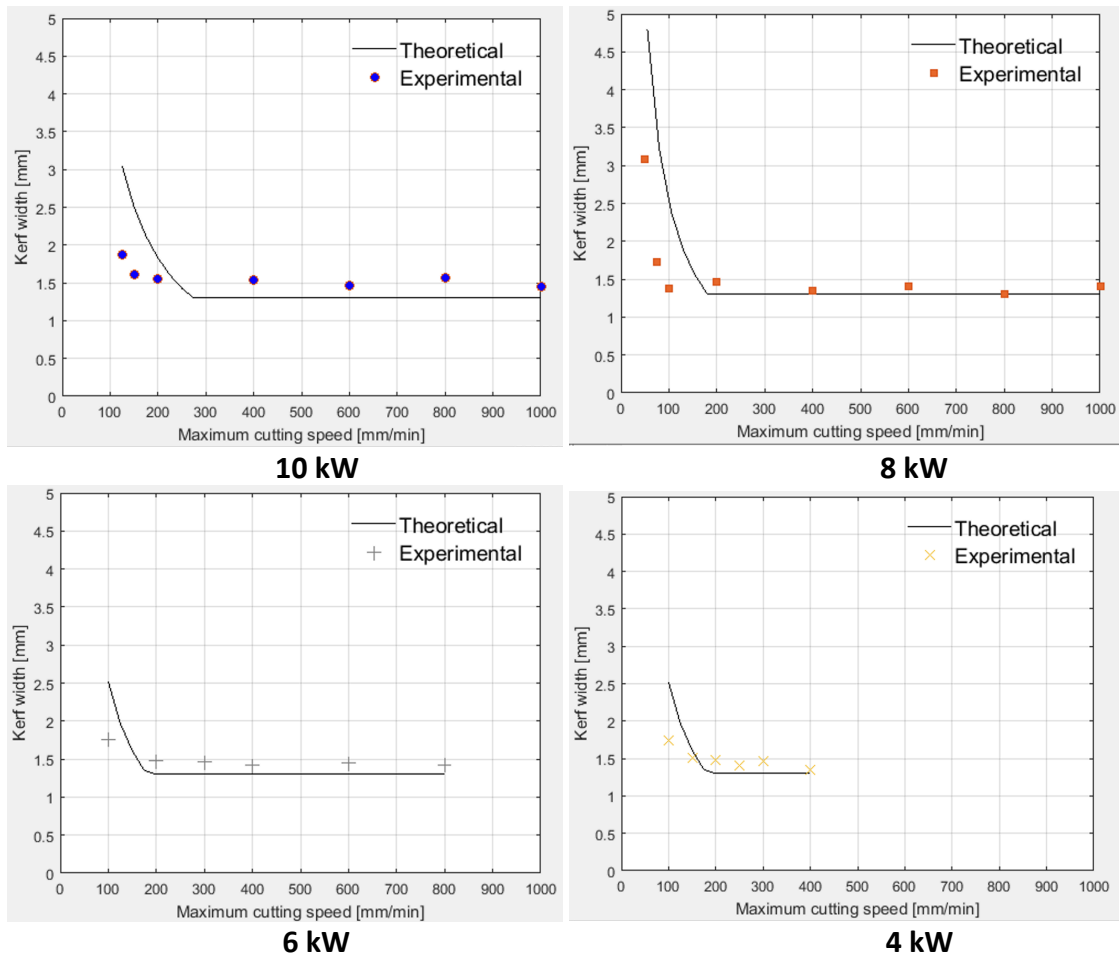
Figure 73: Comparison between the kerf width with the corresponding maximum cutting speed at different laser power magnitudes

The kerf width decreases with increasing cutting speed for low cutting speeds below 200 mm/min at all laser power magnitudes. This could be attributed to a higher thermal energy being transferred to the cut zone at lower cutting speeds. Afterwards, the kerf width remains constant with increasing cutting speed. The predicted kerf width is substantially the same as the measured cut width. In decommissioning applications, a narrow kerf width is necessary to minimise secondary waste and reduce the cost of waste disposal [92].

5.3   Summary of theoretical model for underwater laser cutting

A theoretical model which describes the power balance of underwater laser cutting was developed. A clear comparison of the theoretical and experimental results was presented. The results can be summarised as follows:

- The maximum cut thickness is directly proportional to laser power and inversely proportional to cutting speed;
- The maximum cutting speed for cutting 50 mm C-Mn steel at 10 kW is 125 mm/min from both the analytical model and experimental results;

- The predicted process performance is substantially the same as the experimental laser cutting results, particularly for higher laser power magnitudes and lower cutting speeds;
- The predicted kerf width is nearly identical to the measured width of the cut;

6 Development and application of a gas jet expansion numerical model for underwater laser cutting

The main objective of this chapter is to investigate the effect of fluid flow on the underwater laser cutting process to identify a mixed phase (water, water vapour (steam) and air) medium along the path of the laser beam. A mixed phase region along the path of the laser beam can cause optical effects such as reflection, refraction, scattering, and absorption of the laser beam to occur [100, 101]. A mixed phase medium within the kerf can also affect the melt removal process underwater [1]. As a result, a mixed phase region at the laser-material processing zone can affect both the cutting performance and quality in underwater laser cutting. Therefore, the variation of the volume fraction of air along the path of the laser beam was investigated. The velocity contours were generated at different inlet pressure conditions to investigate the velocity flow field properties under the effect of gravity and buoyancy. This study is necessary as it is difficult to quantify the volume fraction of air and velocity in the path of the laser beam using experimental visualisation as an underwater gas jet expansion flow is unsteady and turbulent [22, 23].

The development of an underwater gas jet expansion model for underwater laser cutting was accomplished in two key stages. These stages can be summarised as follows:

I.   A 2-dimensional (2D) underwater buoyant gas jet expansion model was simulated and compared to an image of a submerged air jet expanding underwater during the cutting trials in a 1m³ tank. Two models were created with the same dimensions as the cutting geometry of the underwater laser cutting trials in a 1m³ tank. The first model (Chapter 6.1) presents the characteristics of a gas jet expanding underwater. This model is necessary to understand the characteristics and expansion of an underwater gas jet with convergent nozzles. The second model (Chapter 6.2) examines the characteristics of a gas jet expanding underwater through an opening/virtual kerf of an obstacle. The obstacle represents the workpiece and the opening/virtual kerf represents the kerf created during underwater laser cutting;

II. 3-dimensional (3D) underwater gas jet expansion models based on the 2D models were simulated for a more realistic simulation and to accurately represent the real fluid flow problem. The 3D models were compared to an image of a submerged air jet expanding underwater during the cutting trials in a 1m³ tank to validate the model. This model examines the variation of the volume fraction of air along the path of the laser beam in underwater laser cutting. Chapters 6.3 and Chapters 6.4 include descriptions of the models.

The stages of the development of a gas jet expansion model for underwater laser cutting will now be discussed, starting with a 2-dimensional (2D) underwater buoyant gas jet expansion model.

6.1 2D underwater gas jet expansion model

A numerical model of a gas jet expanding underwater was simulated using ANSYS Fluent 18.2 [21]. This model was simulated using the same nozzle geometry specification and inlet pressure conditions used in the underwater laser cutting trials in a 1 m³ tank to investigate the characteristics of a gas jet expanding underwater without an obstacle (workpiece) with an opening (virtual kerf). The simulated volume fraction of air under the influence of gravity and buoyancy was compared with an experimental image of a submerged gas jet at the same inlet pressure condition to validate the model.

In this model, a pressure based transient model was adapted. A transient model is considered because the flow velocity and pressure change with time. The set of governing equations consists of the following:

- Conservative form of the Navier-Stokes equations - set of partial differential equations which mathematically express conservation of momentum and conservation of mass for Newtonian fluids (see Chapter 2.6.6) [155];
- The energy equation - the first law of thermodynamics or the law of conservation of energy (see Chapter 2.6.6) [156];
- A transport equation for the gas volume fraction which represents a robust method for tracking the air-water interface, and offers several alternatives for reconstructing the interface with accuracy while conserving the fractional volume of fluid (see Chapter 2.6.6) [157];
- A Large Eddy Simulation (LES) turbulence model. This turbulence model was selected as it reduces the computational cost by ignoring the smallest length scales, which are the most computationally expensive to resolve, via low-pass filtering of Navier–Stokes equations [158].

6.1.1 LES turbulence model

The LES method resolves large scale structures with the spatially filtered Navier-Stokes equations, whereas the effect of small scales is modelled. Fluid components are assumed to share the same velocity field in the simulation. The spatially filtered governing equations of continuity, momentum and energy can be listed as follows [159]:

Filtered continuity equation:

$$\frac{\partial p_m}{\partial t} + \frac{\partial (p_m \bar{u}_j)}{\partial x_j} = 0 \tag{61}$$

Filtered momentum equation:

$$\frac{\partial(\rho_m \bar{u}_i)}{\partial t} + \frac{\partial(\rho_m \bar{u}_i \bar{u}_j)}{\partial x_j} = -\frac{\partial \bar{p}}{\partial x_i} + \frac{\partial}{\partial x_j}(\mu_m \frac{\partial \bar{u}_i}{\partial x_j}) - \frac{\partial \tau_{ij}}{\partial x_j} \tag{62}$$

Filtered energy equation:

$$\frac{\partial E_k}{\partial t} + \frac{\partial E_k}{\partial x_j} + \frac{1}{\rho}\frac{\partial \bar{u}_i \bar{p}}{\partial x_i} + \frac{\partial \bar{u}_i \tau_{ij}}{\partial x_j} - 2v\frac{\partial \bar{u}_i \bar{S}_{ij}}{\partial x_j} = -\mathcal{E}_f - \prod \tag{63}$$

Where, ρ_m is the density of the mixture, $\bar{u}_i$ and $\bar{u}_j$ are filtered velocity components, t is the time, x_i and x_j are distance components, $\bar{p}$ is the filtered pressure, τ_{ij} is the subgrid-scale (SGS) stress, E_k is the kinetic energy, $\bar{S}_{ij}$ is the rate-of-strain tensor, $\mathcal{E}_f$ is the dissipation of kinetic energy of the filtered velocity field by viscous stress and $\prod$ is the sub-filter scale (SFS) dissipation of kinetic energy. The subgrid-scale (SGS) stress, τ_{ij}, sub-filter scale (SFS) dissipation of kinetic energy, $\prod$ and dissipation of kinetic energy of the filtered velocity field by viscous stress, $\mathcal{E}_f$, can be expressed as [159]:

$$\tau_{ij} = \rho_m(\overline{u_i u_j} - \overline{u_i}\overline{u_j}) \tag{64}$$

$$\prod = \tau_{ij}\bar{S}_{ij} \tag{65}$$

$$\mathcal{E}_f = 2v\bar{S}_{ij}\bar{S}_{ij} \tag{66}$$

The terms on the left-hand side of the filtered energy equation represent transport, and the terms on the right-hand side are sink terms that dissipate kinetic energy.

6.1.2   VOF multiphase model

The VOF multiphase model was used to trace the interfaces between different phases: the model tracks two or more immiscible fluid interfaces by solving momentum equations and phase volume fraction equations. It is widely used in the prediction of jet break-up, the motion of large bubbles in liquid, and dam-break problems in engineering [136]. For numerical study of underwater gas jets, the VOF model has been validated by Tang et. al [23]. The phase volume fraction conservation equation is [136]:

$$\frac{\partial}{\partial t}(\alpha_q \rho_q) + \nabla \cdot (\alpha_q \rho_q \vec{V_q}) = S_{\alpha_q} + \sum_{p=1}^{n}(\dot{m}_{pq} - \dot{m}_{qp}) \tag{67}$$

where, α_q is volume fraction of phase q, ρ_q is the density of phase q, $\vec{V}_q$ is velocity of phase q, S_{α_q} is the source item of phase q, $\dot{m}_{pq}$ is the mass flow rate from phase q to phase p, and $\dot{m}_{qp}$ is the converse transfer rate. The phase volume fraction is constrained by the following requirement:

$$\sum_{q=1}^{n} \alpha_q = 1 \qquad (68)$$

Here, two phases are considered. Phase q is defined as water and phase p is air. A 2D VOF (Volume of Fluid) multi-phase flow model was adopted to simulate the interface between air and water. This method was selected over other approaches such as the Mixture and Eulerian model because it is designed for two or more immiscible fluids where the position of the interface between the fluids is of interest [160]. The advantages of the VOF model include [161]:

- The VOF's use, reliability and effectiveness are widespread: the method has been known for several decades, has gone through a continuous process of improvement and is used by many commercially available software programs such as ANSYS Fluent 18.2 [21];
- The VOF method is easy to extend to 3D and simple to implement;
- Applications of the VOF model include stratified flows or the steady or transient tracking of any liquid-gas interface, which correspond to our case.

The limitations of the VOF method include [161]:

- The VOF method involves massive calculations and data burden, which leads to a high computational cost;
- The accuracy of VOF decreases with interface length scale getting closer to the computational grid scale;
- Typical problems include the air jet breakup and motion of large bubbles in a liquid (water).

The density of air conforms to the ideal gas law and the density of water is assumed to be constant [23, 134]. Air is assumed to be an ideal compressible gas, and water an incompressible fluid. A model which considers the influence of gravity and buoyancy was developed based on the 2-D axisymmetric model by Tang et al. [134]. The geometry and boundary conditions were the main changes applied to the model.

6.1.3 Geometry and boundary conditions

This geometry consists of a convergent nozzle (air domain) and a water domain (see Figure 74). The inlet, wall, outlet, and interior boundary conditions are indicated by A, B, C and D, respectively. This model's boundary settings have the same pressure, type, and temperature conditions as that of the model in air, together with an air volume fraction of 1 at the inlet.
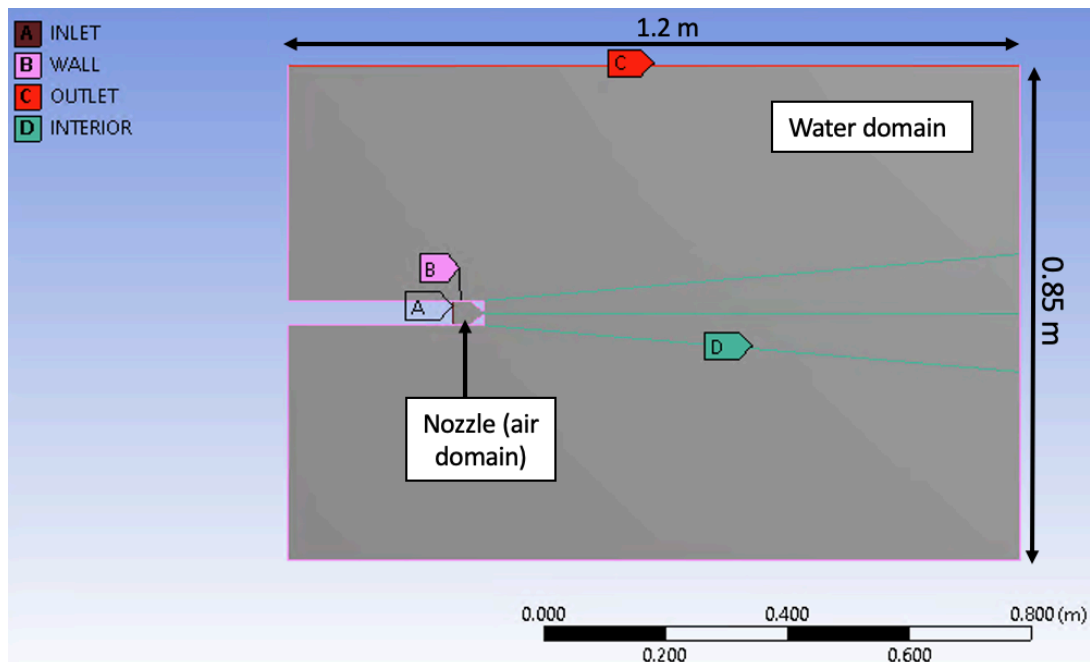
Figure 74: Geometry and boundary conditions

The design parameters of the nozzle geometry are as follows: length of nozzle throat is 2 mm; width of the nozzle throat is 2 mm; vertical height of the nozzle inlet is 20 mm; total length of the nozzle is 52 mm; length of the converging part of the nozzle is 20 mm; depth of nozzle from the outlet is 400 mm. The throat size is chosen to choke the flow and set the mass flow rate through the nozzle. The flow in the throat is sonic which means the Mach number is equal to one in the throat [107]. The concerned flow field of the geometry is the external region along the centreline of the nozzle as this is the expansion region of the gas jet. Therefore, split lines surrounding the flow field were chosen to establish a finer mesh in this area and all the split lines of the geometry were defined as interior boundary conditions.

Initially, a face sizing with an element size of 10 mm was adapted to set a fine quadrilateral mesh on all faces. Afterwards, a finer mesh with a maximum face size of 5 mm was set for the faces inside the interior boundary condition and the nozzle (see Figure 75). Finally, edge sizing with 120 divisions was specified at the interior boundary condition to set the finest mesh of the geometry with a face size of 0.1 mm at the flow field region (see Figure 75 for the finest mesh around the nozzle region). The generated mesh for the whole geometry comprises of 16 474 nodes and 16 164 elements.
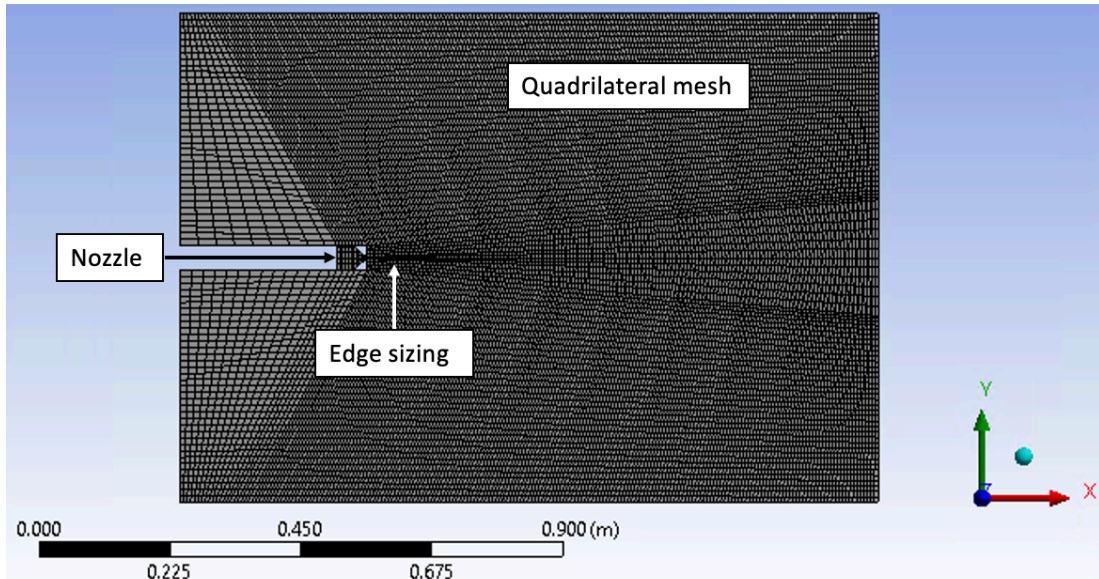
Figure 75: Mesh configuration

The quality of the mesh which plays a significant role in the accuracy and stability of the numerical computation was checked for errors [162]. The mesh quality measures used to generate a suitable mesh for the model are smoothness (change in size from one face or cell to the next) and skewness (a primary quality measure for a mesh which determines how close to ideal a face or cell is) [112]. The skewness was set such that it does not exceed 0.9. A medium smoothing was specified as large differences in size between adjacent faces or cells will result in a poor computational grid because the differential equations being solved assume that the cells shrink or grow smoothly. After setting up the geometry, mesh and boundary conditions of the model, the setup of the underwater gas expansion model was configured.

6.1.4 Setup

A double-precision parallel solver was adapted at the beginning of the setup to compute a more definite solution. A 2D analysis type and pressure based unsteady transient model was specified. An explicit scheme was fixed for this model as it has better numerical accuracy than implicit formulation. Moreover, this formulation is mostly used in multiphase simulations of compressible flow were surface tension is vital [161]. The operating density was set to zero as it is the required condition for simulating compressible flows with buoyancy [161]. The flow field is influenced by gravity, inertial forces, surface tension, and buoyancy. The direction of action of gravity is in the negative y-direction, at 9.81 m/s^2 and the whole air jet flow field is asymmetric.

A multiphase simulation with two phases of water and air was set. The primary and secondary phase were adapted as water and air, respectively. The phase interactions between water and air had a surface tension of 0.072 N/m [163]. The interface modelling type was specified as sharp because it is the recommended option to use when a distinct interface is present between different phases [161]. The default

116

properties defined for the gas jet expansion model in air, together with water properties shown in Table 16, were specified for this model.

Table 16: Water properties [21]

Properties	Value
Reference temperature (K)	298
Thermal conductivity (W/m·K)	0.6
Specific heat capacity (kJ/kg·K)	4.182
Molecular weight (kg/kmol)	18.0152
Viscosity (kg/m-s)	0.001003
Standard state enthalpy (J/kgmol)	2858.4 e+05 (Exothermic)
Density (kg/m^3)	998.2

6.1.5 Solution procedure

The coupling of the velocity and pressure terms in the momentum equation were solved by the well-known Pressure-Implicit with Splitting of Operators (PISO) algorithm. The PISO scheme is part of the SIMPLE (Semi-Implicit Method for Pressure Linked Equations) family of algorithms. It is based on the higher degree of the approximate relation between the corrections for pressure and velocity. This scheme was used because it is more efficient and precise than SIMPLE per iteration cycle [164, 165].

In relation to the spatial discretisation (the processes and protocols that were used to convert the equations of the momentum, energy and density into a form that can be used to calculate numerical solutions), the first order upwind scheme was adapted. This scheme was selected because the second order formulation is computationally expensive. The compressive scheme was set to discretise the volume fraction and PRESTO! (PREssure STaggering Option) scheme was used to compute the cell face pressure [166].

The Least Squares Cell-Based method was also selected to compute the gradients needed not only for constructing values of a scalar at the cell faces, but also for computing secondary diffusion terms and velocity derivatives. This method was adapted as it has less computational cost than other node-based gradient methods [116]. The implicit transient formulation of the first order was selected to compute the solution because the second order, though offering improved precision, could be computationally costly [167]. The solution controls set for this model are shown in Table 17.

The model was initialised with values for pressure, velocity, temperature and air volume fraction specified for the boundary conditions. After initialisation, the mesh was adapted such that the initial phase of the nozzle is gaseous (air), while the outer field is water. These two parts are relatively static. An initial time step of 10^{-6} s was set to calculate the solution for 50 000-time steps. Afterwards, the time step was reduced

to 10^{-5} s to speed up the calculation process. The maximum number of iterations per time step were set as 10 and a fixed time step approach was implemented [167]. The volume fraction of air and velocity contours of an underwater gas jet expansion model were generated at an inlet pressure of 8 bar up to a flow time of 2.2 s. The simulation was stopped at this time because the flow had fully developed from the nozzle inlet to the outlet.

Table 17: Solution controls

Control factor	Value
Energy (J)	1
Turbulent kinetic energy (J/kg)	0.8
Turbulent dissipation rate (J/kg.s)	0.8
Turbulent viscosity (kg/m.s)	1
Density (kg/m^3)	1
Momentum (kg.m/s)	0.03
Pressure (bar)	0.3

6.1.6   Gas jet development

The physical problem investigated in this model is a supersonic gaseous jet injected underwater by a converging nozzle. The nozzle is operated in the under-expansion condition - the pressure at the nozzle exit is larger than the back pressure so the flow of a buoyant gas jet must continue to expand upon leaving the nozzle [1].

A buoyant jet can be defined as the fluid motion caused by the sustained injection of a low-density fluid (air) with large momentum through an orifice into a fluid ambient of higher density (water). Due to Rayleigh–Taylor instability (instability of an interface between two fluids of different densities which occurs when a lighter fluid is pushing a heavier fluid), the jet breaks up into a train of bubbles. Depending on its initial momentum and the density difference between the two fluids, the gas jet breaks up either immediately at the nozzle exit or at some distance downstream. As the jet expands underwater, it gradually evolves along a trajectory within it [22].

The volume fraction of air at the external region of the nozzle exit is 1 for the flow time simulated (see Figure 76). The horizontal distance from the nozzle exit's centreline to the point when the flow becomes a mixed phase was measured using ImageJ, a Java-based image processing program [168]. The volume fraction of air is 1 at the nozzle exit's centreline for a horizontal distance of 0.12 to 0.15 m. This shows that a dry cavity is well formed in this area of the flow field.
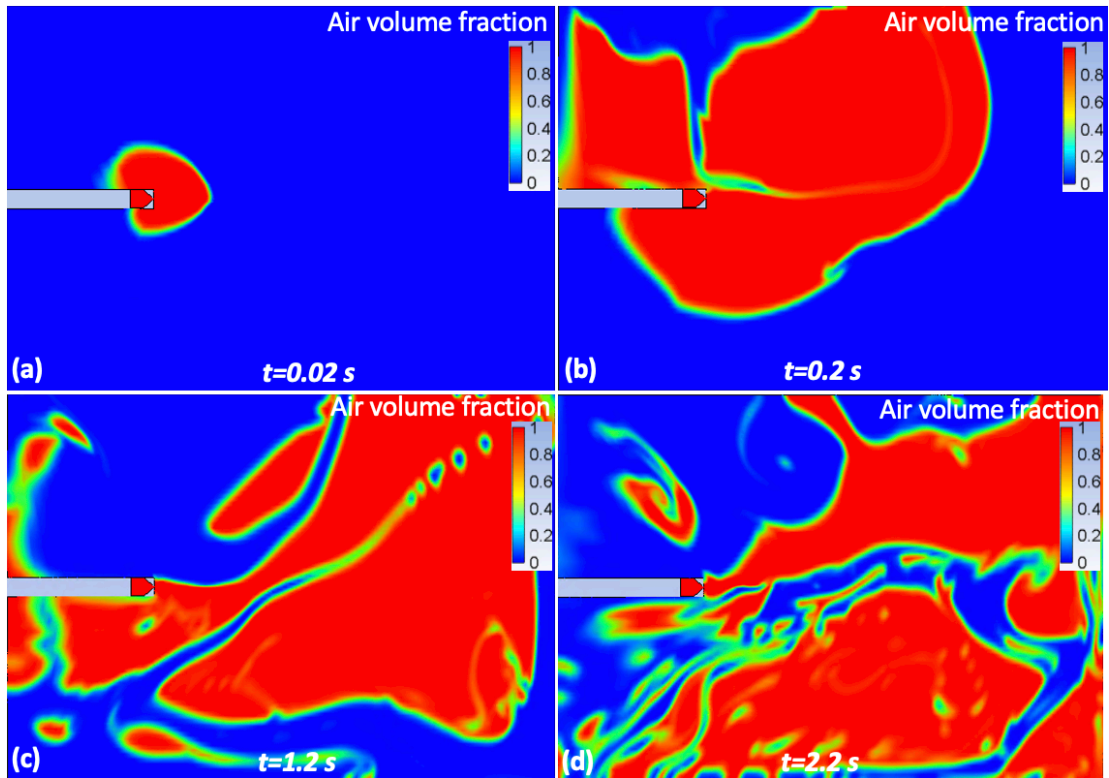
Figure 76: Air volume fraction contour at an inlet pressure of 8 bar for a flow time of (a) 0.02 s, (b) 0.2 s, (c) 1.2 s and (d) 2.2 s

It was also observed clearly that the submerged jet expanded continuously and rose toward the water surface because of the large density difference between water and air. The flow structure and processes are essentially unsteady and turbulent. The unsteady and turbulent characteristics together with the large density ratio across the interfaces lead to difficulties in modelling underwater gas jet expansion with numerical approaches [22].

The gas jet air volume fraction at an inlet pressure of 8 bar was compared to an image of a submerged air jet expanding underwater during the cutting trials in a 1m^3 tank. Figure 77 (a) depicts the gas jet air volume fraction at a flow time of 2 s, whereas Figure 77 (b) shows an image of a submerged air jet captured 2 seconds after the gas jet pressure was increased to 8 bar.
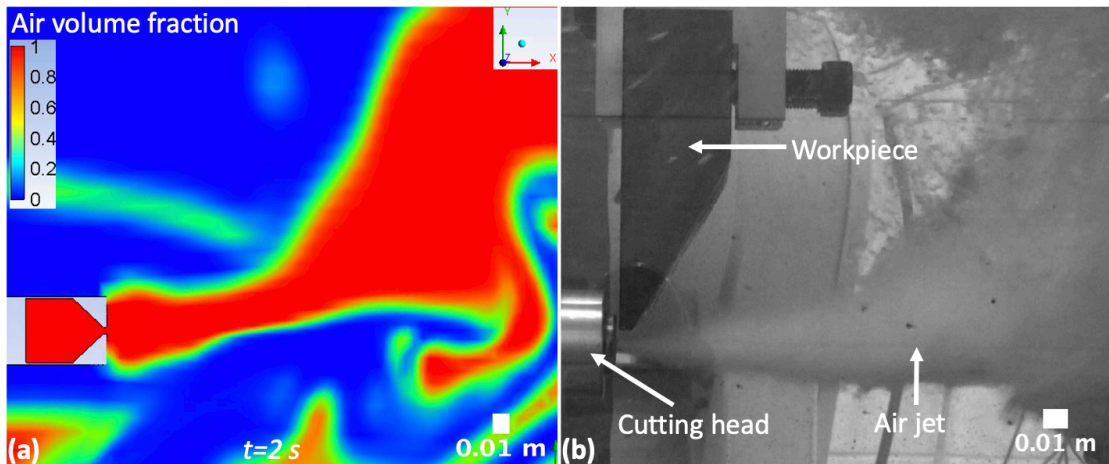
Figure 77: Air volume fraction of (a) numerical model and (b) submerged air jet expanding underwater during the cutting trials in a 1m^3 tank

Figure 77 (a) shows that the simulated gas jet trajectory is comparable to that of the submerged air jet in Figure 77 (b). In the initial section of the submerged air jet, the jet shape remains straight or is slightly diverging due to the high momentum of the jet. As the jet continues to expand underwater, buoyancy makes the jet bend towards the free surface [22]. The momentum of the gas decreases as the gas jet develops such that the influence of gravity and buoyancy dominate. As a result, buoyancy and density effects cause bubbles to move upwards [119, 169].

6.1.7 Velocity distribution

An assessment of the velocity distribution was also investigated. Figure 78 shows the velocity contour at an inlet pressure of 8 bar for a flow time, t, of (a) 0.02 s, (b) 0.2 s, (c) 1.2 s and (d) 2.2 s.
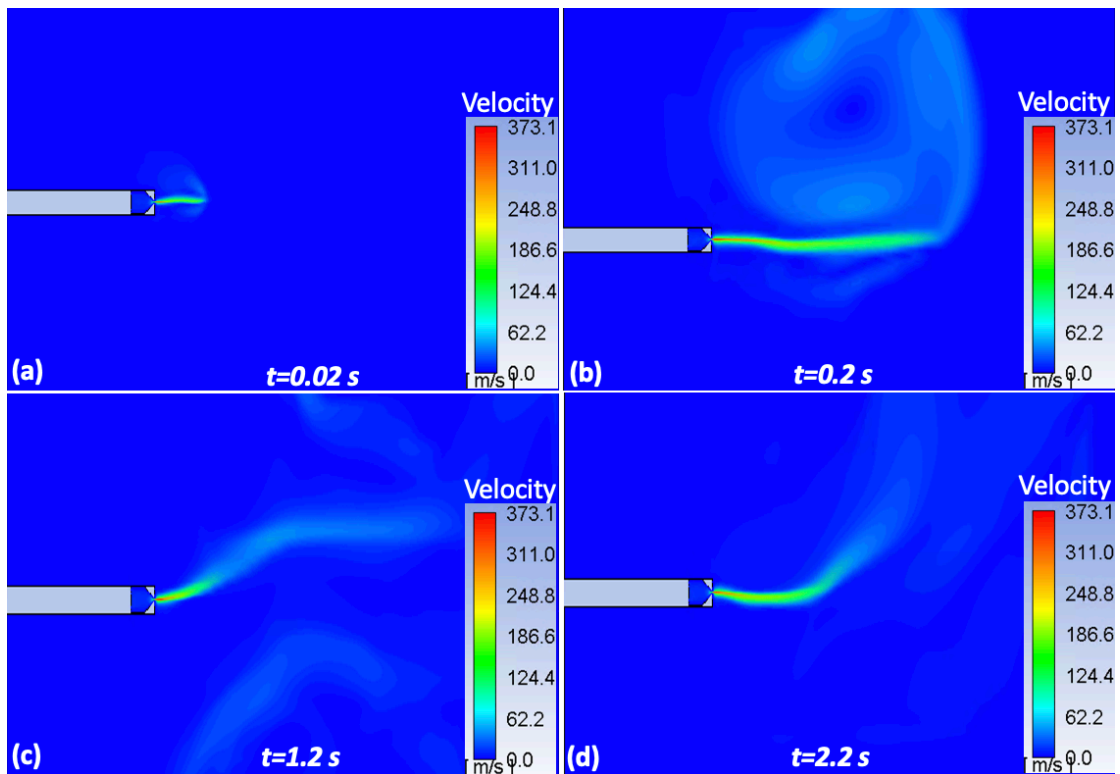
Figure 78: Velocity contour at an inlet pressure of 8 bar for a flow time of (a) 0.02 s, (b) 0.2 s, (c) 1.2 s and (d) 2.2 s

The velocity distribution during the development of the gas jet is nonlinear but bends towards the outlet because of buoyancy. The velocity magnitude in the flow field decreases with increasing horizontal or vertical distance from the nozzle exit due to the inertia forces of the water [130]. As a result, the velocity magnitude is greatest at the nozzle exit. The velocity at the throat of the nozzle is nearly 320 m/s, indicating that the condition of choked flow is achieved.

Figure 79 depicts a velocity contour comparison for a flow time of approximately 0.5 s at different inlet pressure conditions of (a) 2, (b) 4, (c) 8, (d) 16 and (e) 32 bar.
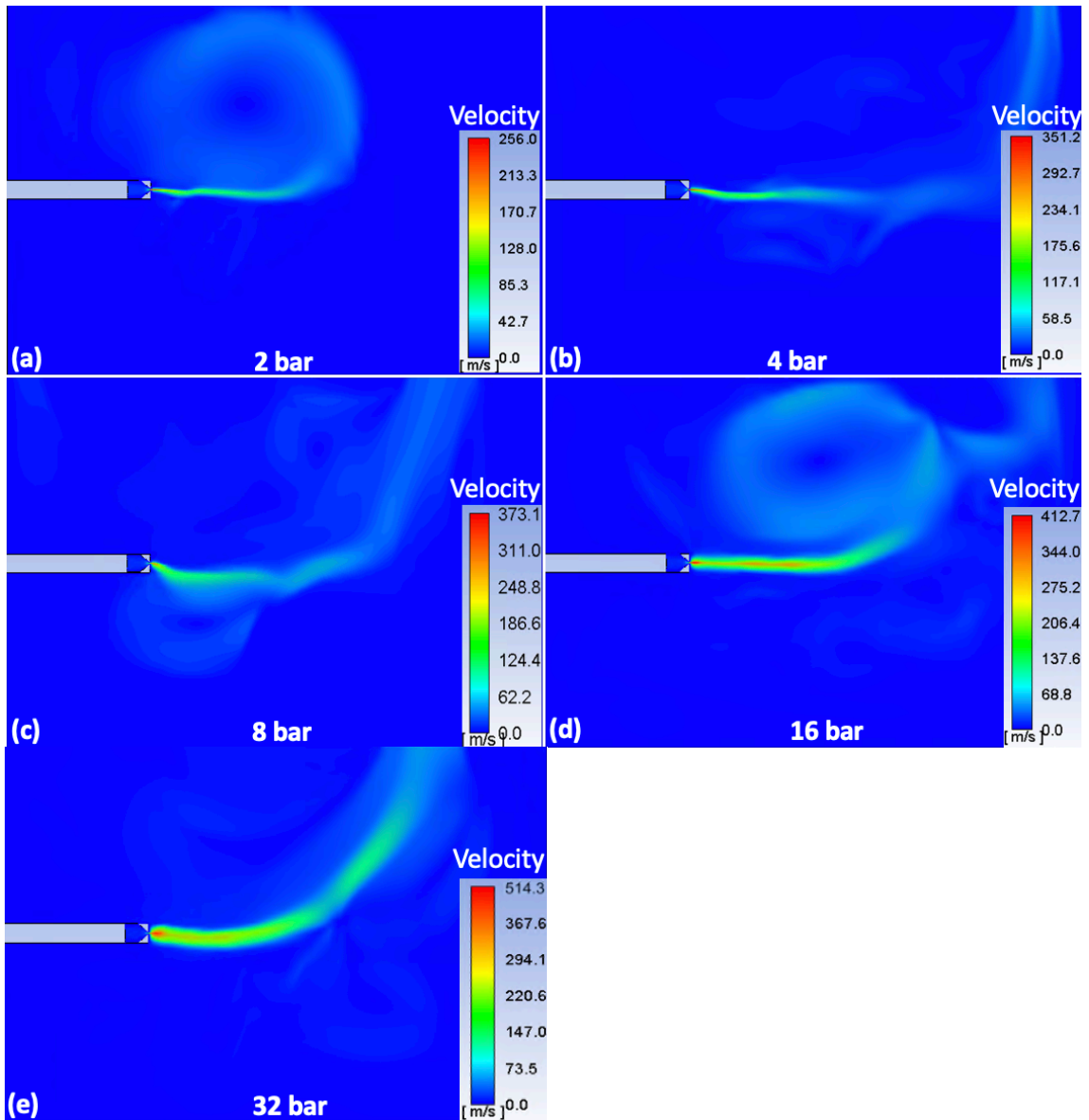
Figure 79: Velocity contour comparison for a flow time of approximately 0.5 s at an inlet pressure of (a) 2, (b) 4, (c) 8, (d) 16 and (e) 32 bar.

At all inlet pressure conditions, when an air jet is injected underwater, an under-expanded supersonic air jet is formed which expands along the centreline of the nozzle. The expansion process is turbulent and unsteady. As a result, the velocity fluctuates during the flow, increasing and decreasing in different regions along the flow field. The velocity magnitude in the flow field is proportional to the inlet pressure condition of the nozzle. Accordingly, the velocity flow field area distribution increases with inlet pressure. At all inlet pressure conditions, the velocity flow field trajectory is nonlinear and bends towards the outlet due to buoyancy.

It is crucial to form an air cavity with denser and more linear characteristics to extend the permissible thickness of steel workpieces for underwater laser cutting [170]. The nozzle exit velocity and mass flow rate are important variables that have a significant effect on the underwater cavity formation. The two variables are correlated to the nozzle thrust, and their values are determined by the nozzle throat diameter,

upstream stagnation pressure, and internal geometry of the underwater cutting nozzle [170].

6.2   2D underwater gas jet expansion model of an obstacle with a virtual kerf/opening

A 2D underwater gas jet expansion model of an obstacle with a virtual kerf was simulated to study the characteristics of a gas jet expanding through an opening/virtual kerf of an obstacle. The obstacle represents the workpiece, and the opening represents the kerf created during the underwater cutting process. This model was simulated using the same nozzle geometry specification and inlet pressure conditions used in the underwater laser cutting trials in a 1 m³ tank. The volume fraction of air was generated to identify a mixed phase (water, water vapour (steam) and air) region along the path of the laser beam. The velocity contours were generated at different inlet pressure conditions to investigate the velocity flow field under the effect of gravity and buoyancy.

A 2D underwater gas jet expansion model with an obstacle and an opening was simulated based on the previous 2D gas jet expansion model influenced by gravity and buoyancy. Therefore, the governing equations specified in the previous model were adapted. The geometry and boundary conditions were the main modifications applied to the model.

6.2.1   Geometry and boundary conditions

The geometry consists of the nozzle, an obstacle with a virtual kerf/opening and a water domain. The geometry is based on the dimensions of the cutting geometry of the underwater laser cutting trials in a 1m³ tank. Figure 80 shows the 2D geometry and boundary conditions.
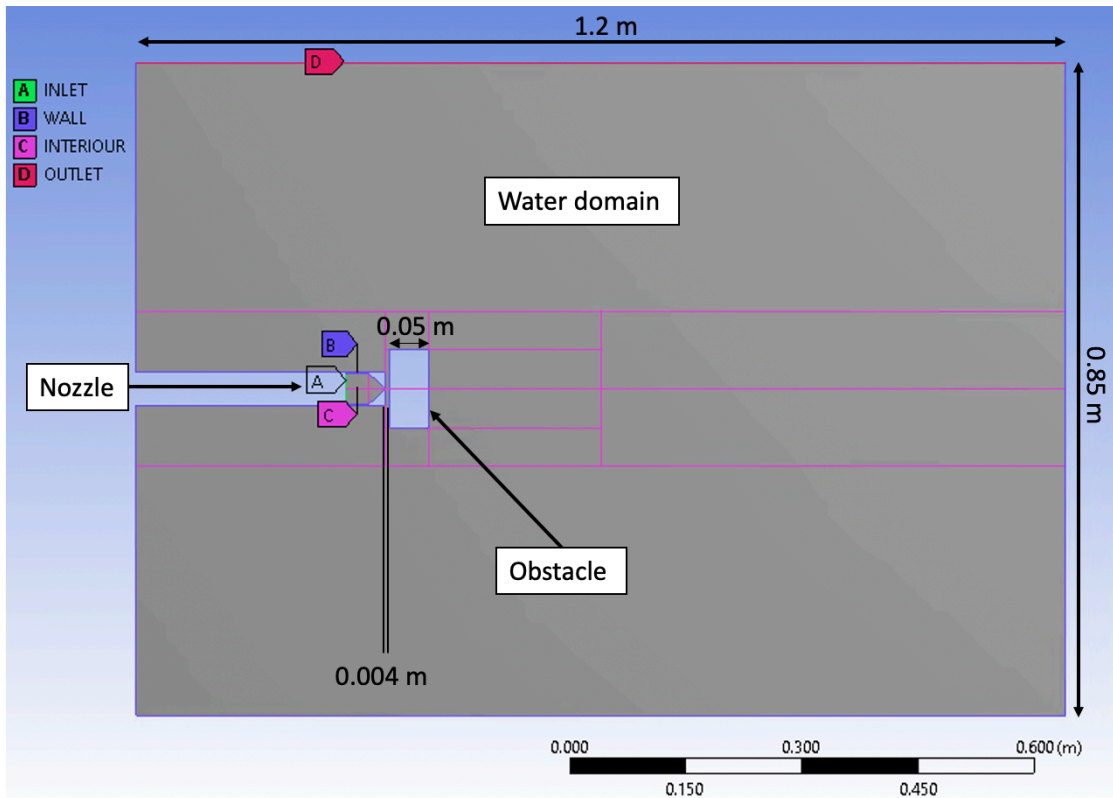
Figure 80: 2D geometry and boundary conditions

The inlet, wall, interior and outlet boundary conditions are indicated by A, B C and D, respectively. The concerned flow field of the geometry is the external region of the nozzle through the opening as this is the path of the laser beam. Therefore, split lines were set to establish a finer mesh in this region to allow an efficient definition of mesh densities to ensure sufficient resolution of interfaces. All the split lines of the geometry were defined as interior boundary conditions.

The length of the obstacle is set as 0.05 m, which corresponds to the maximum cut thickness achieved in the underwater laser cutting trials. The horizontal distance between the nozzle and obstacle is 0.004 m, which corresponds to the stand-off distance adapted in the cutting experiments. The vertical distance of the opening in the geometry is defined as 0.0015 m, which corresponds to an estimate of the average kerf width produced on the workpiece during the underwater cutting process.

Initially, face meshing and sizing were adapted to set a fine quadrilateral mesh with a maximum element size of 15 mm on all faces of the geometry. Afterwards, face sizing with an element size of 5 mm was set to generate a finer mesh on the faces around the nozzle exit and obstacle (see Figure 81). Edge sizing was then specified at the interior boundary conditions within this region to set a face size of 0.15 mm. The generated mesh for the whole geometry consists of 8 823 nodes and 8 469 elements.
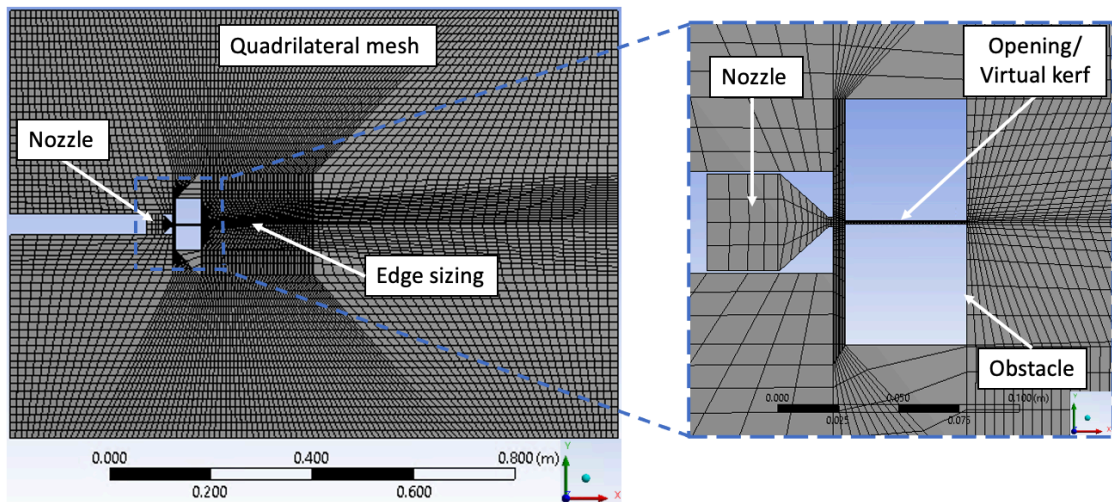
Figure 81: Mesh configuration

The quality of the mesh was assessed by checking for errors, together with adapting medium smoothing and setting a target skewness of 0.9 [112, 162]. After setting up the mesh conditions, all the previous model's setup and solution settings were adapted. The solution of an underwater gas jet was simulated up to a flow time, t, of 1.1 s.

6.2.2 Gas jet development

The flow structures of a 2D gas jet expanding though an opening of a 50 mm obstacle were generated. Figure 82 shows the air volume fraction contours at an inlet pressure of 8 bar for a flow time of (a) 0.01 s, (b) 0.35 s, (c) 0.75 s and (d) 1.1 s.
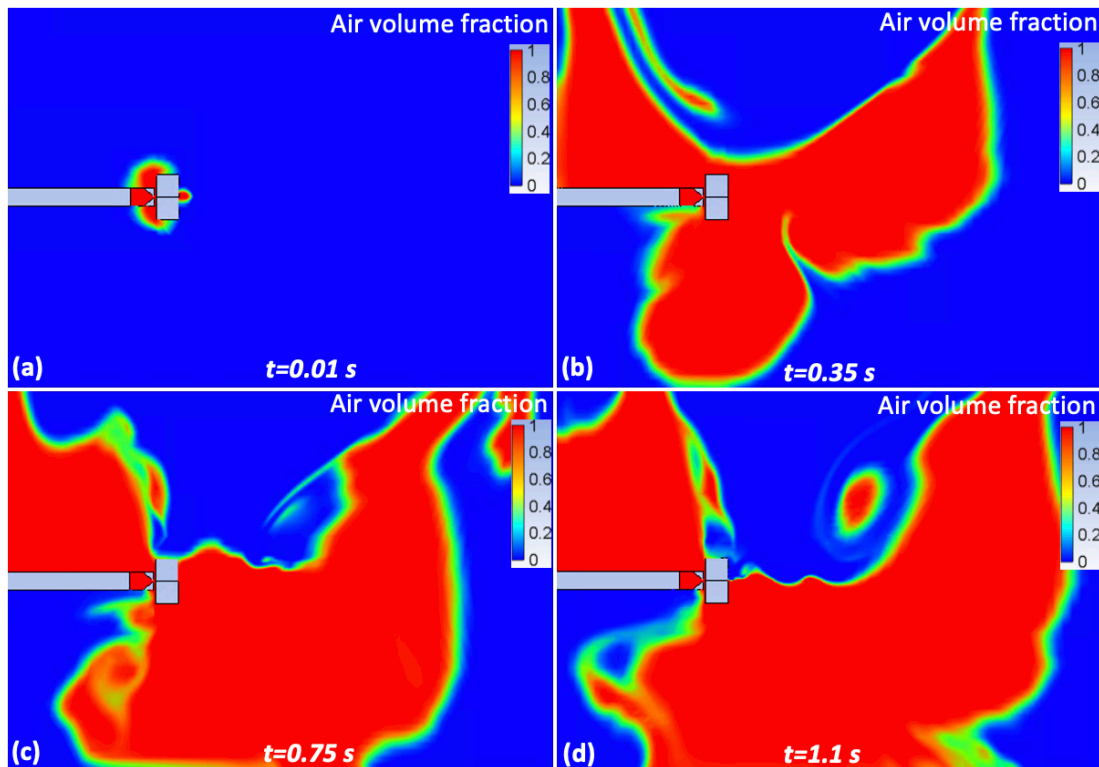
Figure 82: Air volume fraction contour at an inlet pressure of 8 bar for a flow time of (a) 0.01 s, (b) 0.35 s, (c) 0.75 s and (d) 1.1 s

Initially in Figure 82 (a), when air is injected into the water, the jet expands until it impinges onto the obstacle. Only a portion of the gas jet that impinges on the obstacle enters the opening. This fraction of the gas jet continues to expand throughout the opening until it exits as an unsteady and turbulent flow (see Figure 82 (b) and Figure 82 (c)). When the gas jet exits the opening, it flows upwards due to buoyancy (see Figure 82 (d)). The part of the air jet that does not enter the opening expands downwards and upwards along the obstacle.

Figure 83 provides a closer look of the air volume fraction of air through the virtual kerf/opening at an inlet pressure of 8 bar for a flow time of (a) 0.01 s, (b) 0.35 s, (c) 0.75 s and (d) 1.1 s.
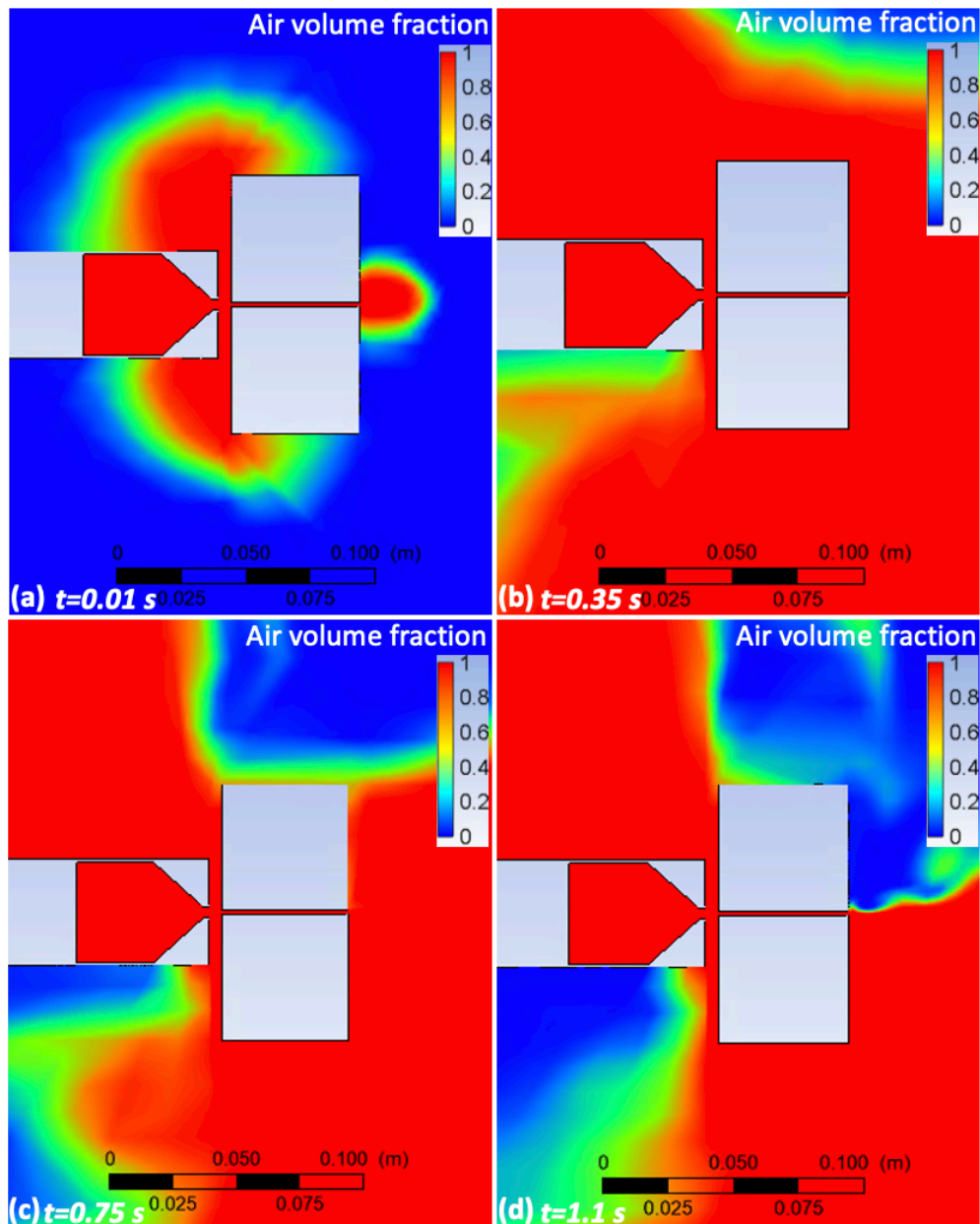
Figure 83: Air volume fraction contour through the opening/virtual kerf at an inlet pressure of 8 bar for a flow time of (a) 0.01 s, (b) 0.35 s, (c) 0.75 s and (d) 1.1 s

An air volume fraction of 1 was observed within the virtual kerf/opening for the flow time simulated. A mixed volume fraction is present near the kerf exit when the gas jet exits the opening (see Figure 83(d)). As a result, the opening exit is the location where water will most likely interact with the beam or molten material during underwater laser cutting.

The air volume fraction contour was compared to an image of a submerged air jet expanding underwater during the cutting trials in a 1m^3 tank. Figure 84 (a) indicates the gas jet flow structure at a flow time of 1 s. Figure 84 (b) depicts an image of a submerged air jet captured during the underwater laser cutting process when a thickness of 50 mm was being cut. Figure 84 (a) corresponds to the x-plane of Figure 84 (b) at the centreline of the nozzle.
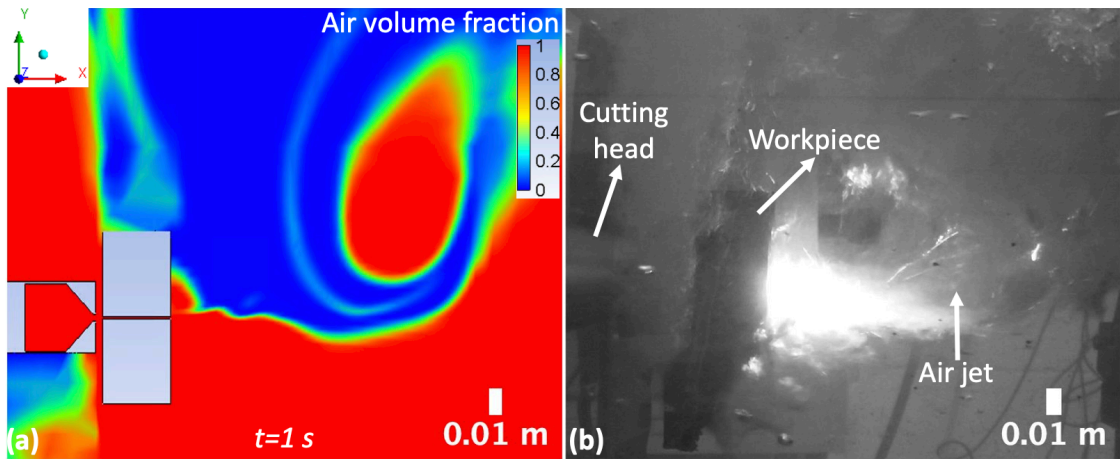
Figure 84: Air volume fraction at an inlet pressure of 8 bar for (a) numerical model and (b) submerged air jet expanding underwater during the cutting trials in a 1m^3 tank

Figure 84 (a) shows that the simulated gas jet has similar characteristics to that of the submerged air jet in Figure 84 (b). The part of the gas jet that impinges on the workpiece surface flows sideways along the workpiece in both air jet flow structures. The influence of buoyancy can be seen in both gas jets, as a part of the gas jet that enters the opening expands and rises toward the water surface. Figure 84 (a) shows that at a flow time of 1 s, the opening/kerf is enclosed with air. This would likely change as bridges normally occur in underwater laser cutting (poor melt removal) than in conventional laser cutting.

6.2.3 Velocity distribution

The velocity distribution of the flow field through the opening was simulated. Figure 85 shows the velocity contour at an inlet pressure of 8 bar for a flow time, t, of (a) 0.01 s, (b) 0.35 s, (c) 0.75 s and (d) 1.1 s.
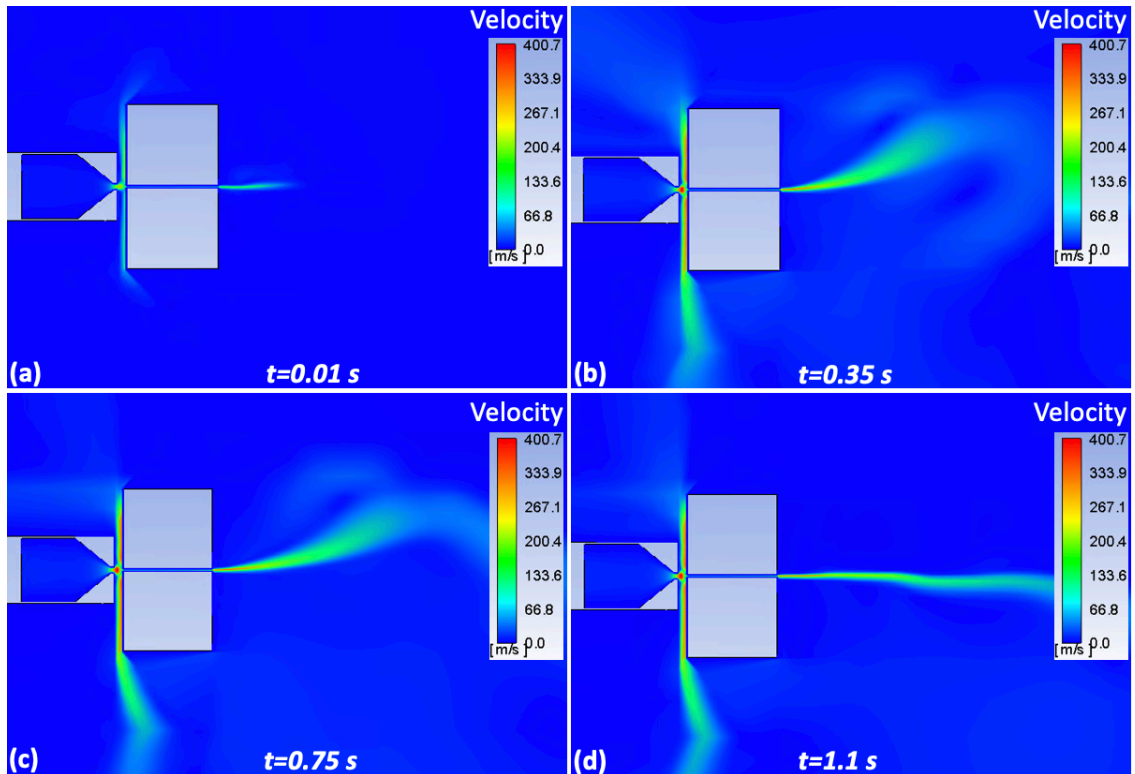
Figure 85: Velocity contour at an inlet pressure of 8 bar for a flow time of (a) 0.01 s, (b) 0.35 s, (c) 0.75 s and (d) 1.1 s

Initially, when the gas jet is injected underwater, an under-expanded supersonic air jet is created that expands along the obstacle and through the opening. The under-expansion condition occurs because the external pressure of the environment is lower than the exit pressure of the nozzle [1]. The velocity magnitude in the flow field decreases with increasing horizontal or vertical distance from the nozzle exit due to the inertia forces of the water [130]. The velocity flow field that exits the opening is nonlinear and fluctuates with time.

Figure 86 shows a velocity contour comparison for a flow time of approximately 0.5 s at various inlet pressure conditions of (a) 2, (b) 4, (c) 8 and (d) 16 bar.
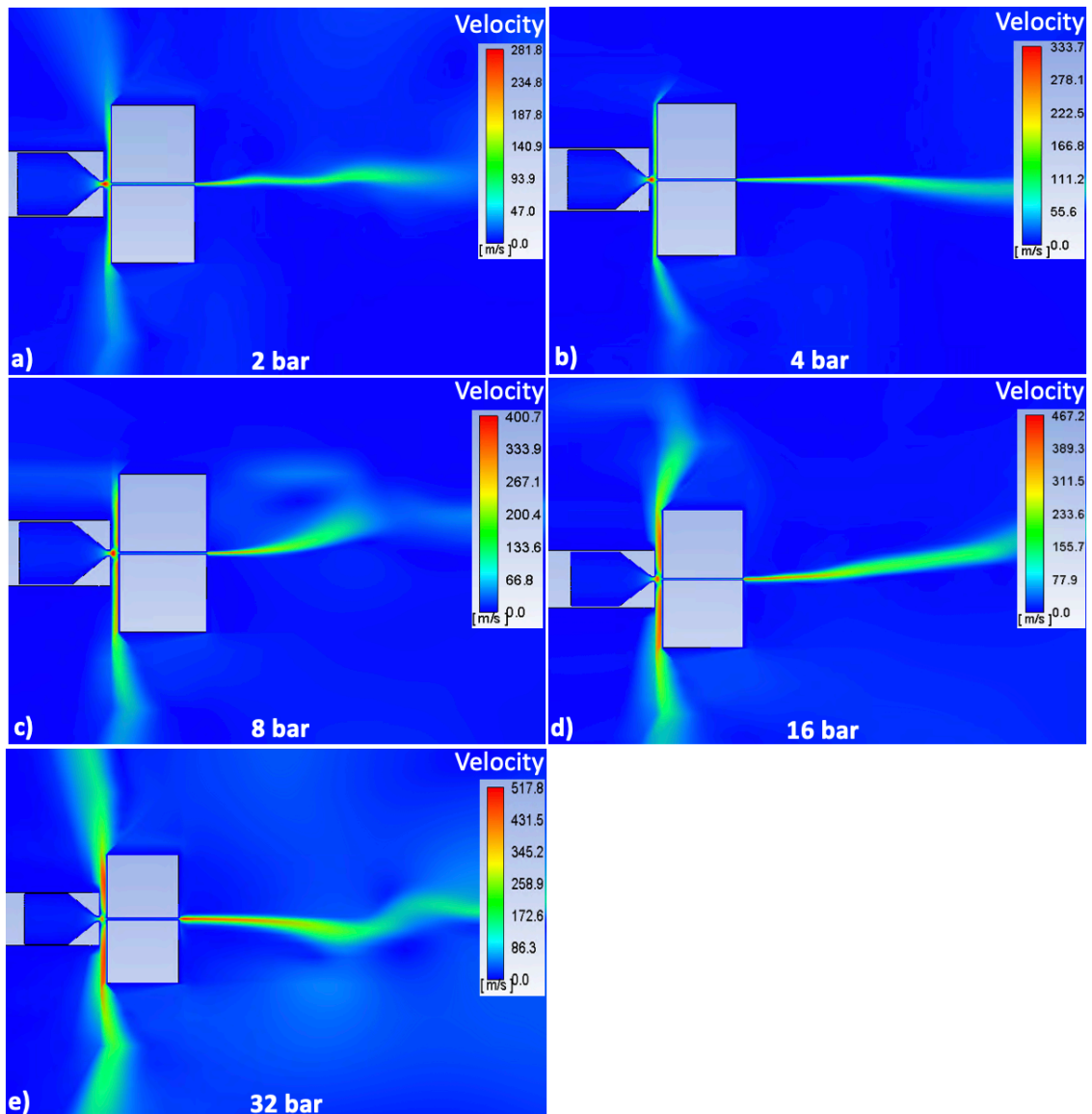
Figure 86: Velocity contour comparison for a flow time of approximately 0.5 s at an inlet pressure of (a) 2, (b) 4, (c) 8, (d) 16 and (e) 32 bar

The velocity magnitude in the flow field increases with the inlet pressure condition of the nozzle. As a result, the inlet pressure increases with the velocity flow field area distribution. At all inlet pressure conditions, the velocity flow field is nonlinear and bends towards the outlet due to buoyancy.

To plot the velocity of the gas jet within the kerf, a line was specified at the centreline of the nozzle, from the inlet to a point 5 mm from the kerf exit. Figure 87 shows the definition of the line at the centreline of the nozzle.
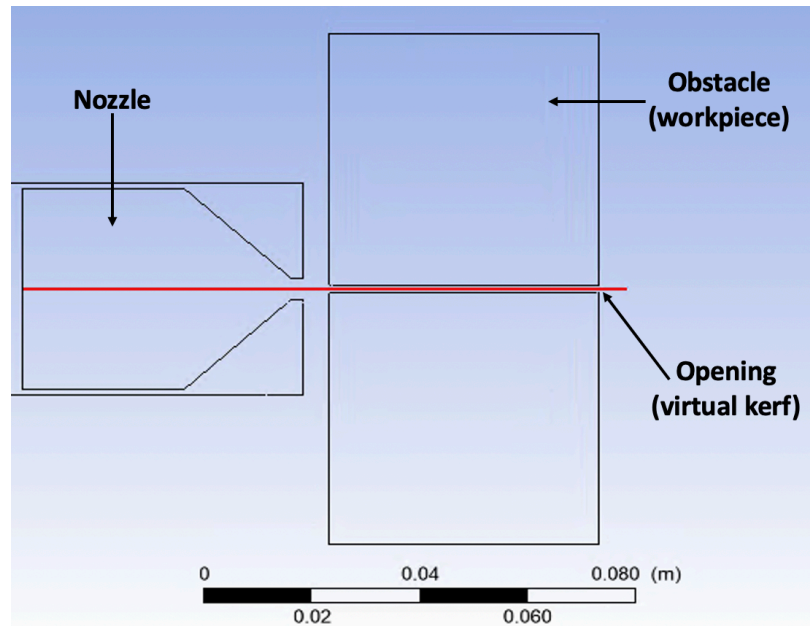
Figure 87: Definition of line at the centreline of the nozzle

The velocity along the along the centreline of the nozzle was plotted at different inlet pressure conditions. Figure 87 shows the velocity plot comparison for a flow time of approximately 0.5 s at various inlet pressure conditions of (a) 2, (b) 4, (c) 8, (d) 16 and (e) 32 bar.
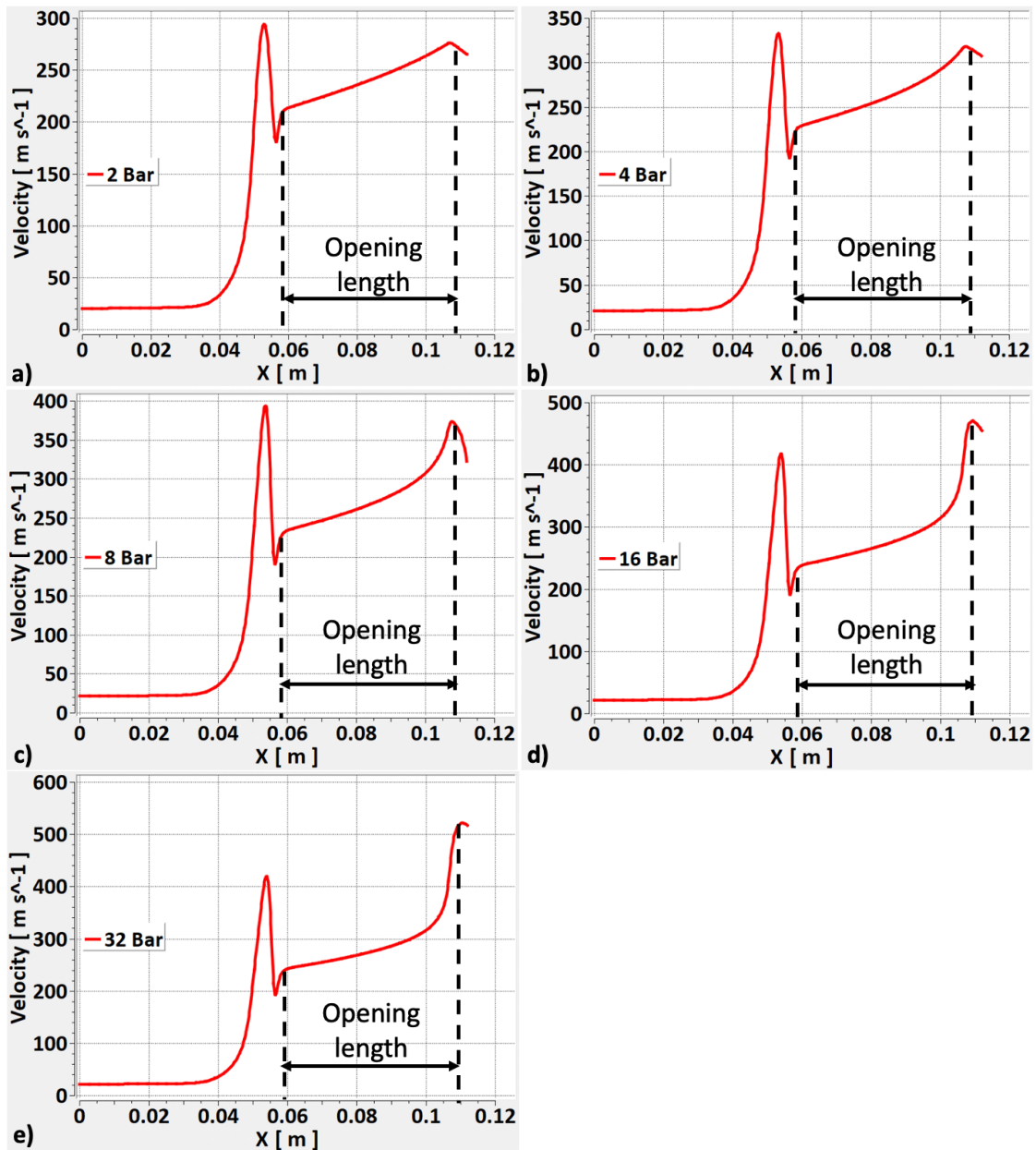
Figure 88: Velocity plot comparison for a flow time of approximately 0.5 s at an inlet pressure of (a) 2, (b) 4, (c) 8, (d) 16 and (e) 32 bar

Figure 88 indicates that immediately after leaving the nozzle, a supersonic jet is created at almost all inlet pressure conditions. In the case of a 4 mm stand-off, as used in this project, the air jet continues to expand until it impinges on the workpiece surface whereby a shockwave between the nozzle and the workpiece is created, below which the flow is subsonic [1]. Therefore, the lowest velocity in the concerned flow field for this study is before the opening entrance. In general, the velocity of the gas jet that enters the opening increases along the length of the opening at all inlet pressure conditions. After the gas jet exits the opening, the velocity starts to decrease.

For underwater laser cutting, the locations where the velocity decreases can cause a mixed phase (water, water vapour (steam) and air) medium to interfere with the laser beam and affect the melt removal process. The occurrence of bridges in some of the

cuts for underwater laser cutting could be due to a mixed phase medium being transported into the kerf.

6.3 3D underwater gas jet expansion

A 2D underwater gas jet expansion model for underwater laser cutting is enough to capture essential flow features but creating a 3D model is necessary for a more realistic simulation. A 3D model is more realistic than 2D because it can capture gradients along the 3D direction, which are indefinitely extended in a 2D model. Therefore, 3D computations accurately represent the real fluid flow problem, whereas 2D computations are normally made by assuming that the net mass flow in one of the spatial dimensions is zero and the surface and body forces acting in that direction are neglected [171]. As a result, a more realistic simulation of a gas jet expanding underwater was created to investigate the flow field characteristics under the action of gravity and buoyancy.

A 3D underwater gas jet expansion model was simulated using the same nozzle geometry specification and inlet pressure condition used in the underwater laser cutting trials in a 1 m^3 tank to investigate the characteristics of a gas jet expansion underwater. The simulated volume fraction of air was compared to an experimental image of the gas jet expansion underwater to validate the model. The velocity contour was generated to examine the velocity flow field characteristics underwater.

The set of governing equations adapted for the 3D model consists of the conservative form of the Navier-Stokes equations, the original k-ε two-equation turbulence closure, and a transport equation for the gas volume fraction. The continuity, momentum, energy, VOF model equations and turbulence model are specified in Chapter 2.6.6.

All the previous model's setup and solution settings were adapted except for the turbulence model and pressure-velocity coupling method. The original k-ε two-equation turbulence model used in previous studies of modelling horizontal underwater gaseous jets by Tang et al. [23, 128, 134] and a SIMPLE pressure-velocity coupling method were specified. These changes were made to reduce computational cost. The most significant adjustments to the model for 3D analysis were alterations to the geometry and boundary conditions.

6.3.1 Geometry and boundary conditions

The geometry of the 3D model was designed using SOLIDWORKS 2017 [108] and imported into ANSYS Fluent 18.2 [21]. Figure 89 shows a 3D geometry of a horizontal convergent nozzle submerged underwater.
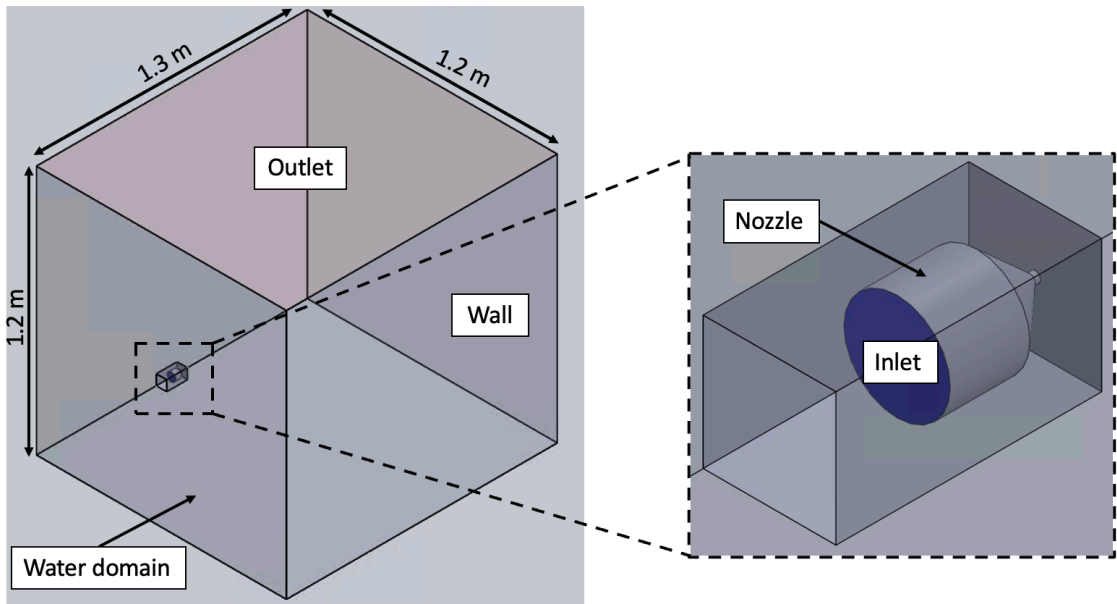
Figure 89: 3D geometry and boundary conditions

The outlet (red), wall (grey) and inlet (blue) boundary conditions of the geometry are indicated. The nozzle design parameters of the geometry are as follows: length of nozzle throat is 2 mm; diameter of the nozzle exit is 4 mm; diameter of the nozzle inlet is 40 mm; total length of the nozzle is 52 mm; length of the converging part of the nozzle is 20 mm; depth of nozzle exit from the outlet is 600 mm.

Initially, a fine mesh with a maximum face size of 100 mm is adapted on all faces of the geometry. Afterwards, edge sizing was specified at the nozzle region (concerned flow field) to give a finer mesh of 0.6 mm. Figure 90 shows the 3D mesh configuration
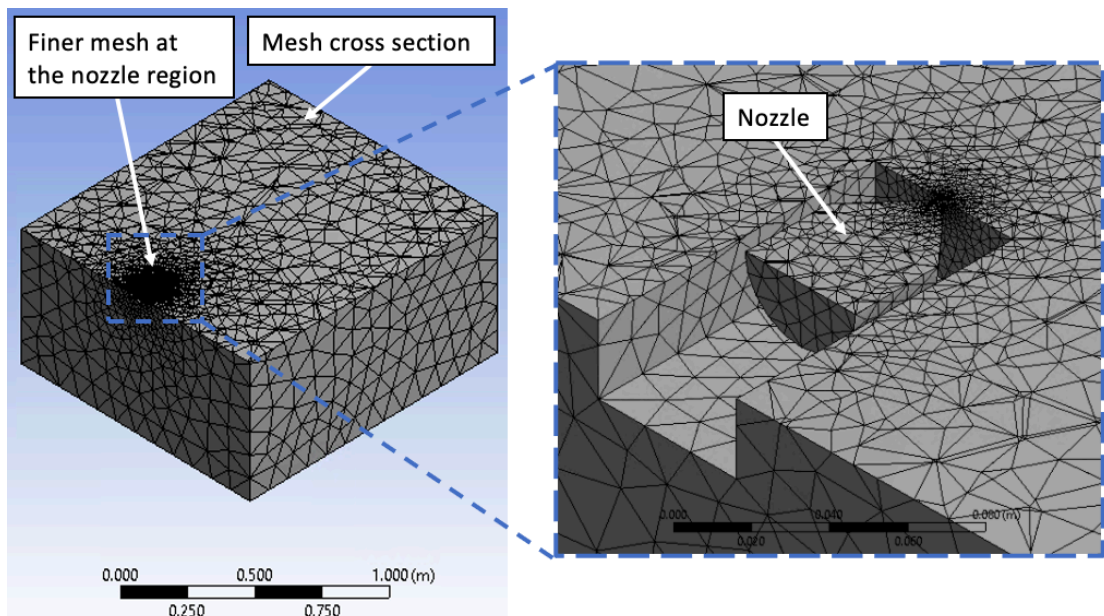
Figure 90: 3D mesh configuration

The generated mesh for the whole geometry consists of 9 116 nodes and 47 795 elements. The quality of the mesh was assessed by checking for errors, smoothness

and skewness. After setting up the mesh conditions, the setup and solution procedure of the 3D model was configured.

6.3.2 Setup and solution procedure

All the previous model's setup and solution settings were adapted except for the turbulence model and pressure-velocity coupling method as specified in Chapter 6.3.

6.3.3 Gas jet development

Figure 91 shows the air volume fraction contour at an inlet pressure of 8 bar for a flow time, t, of (a) 0.05 s, (b) 0.5 s, (c) 0.9 s and (d) 1.45 s
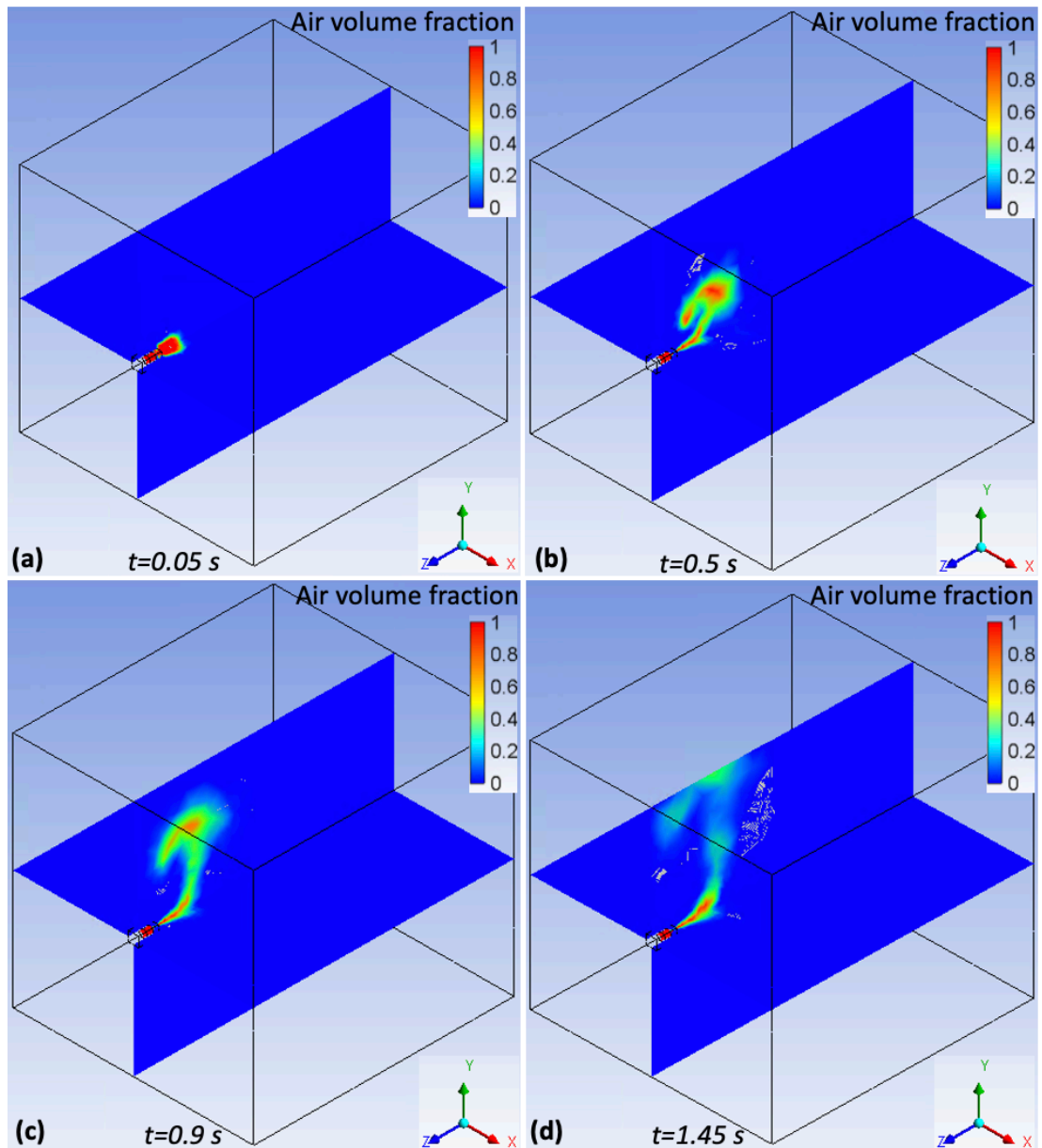
Figure 91: Air volume fraction contour at an inlet pressure of 8 bar for a flow time of (a) 0.05 s, (b) 0.5 s, (c) 0.9 s and (d) 1.45 s

Initially when the air is injected into water, a 'gas bag' is formed behind the nozzle exit in Figure 91 (a). Here the jet is mainly controlled by its initial momentum and an expansion flow structure is observed. The pressure inside the 'gas bag' continue to increase and accumulate until it is high enough to overcome the suppression of the water in Figure 91 (b). In Figure 91 (c) the effect of buoyancy causes the gas jet trajectory to bend upwards towards the outlet [23, 134]. The gas jet continues to follow this flow trajectory in Figure 91 (d).

Past underwater gas jet expansion studies (e.g. [172, 173]) suggested that a buoyant jet flow can be divided into three main flow regions, which characterise the development of the gas flow after leaving the nozzle. These flow regions are: (i) the jet regime region, (ii) the transition region, and (iii) the plume region (see Figure 92).
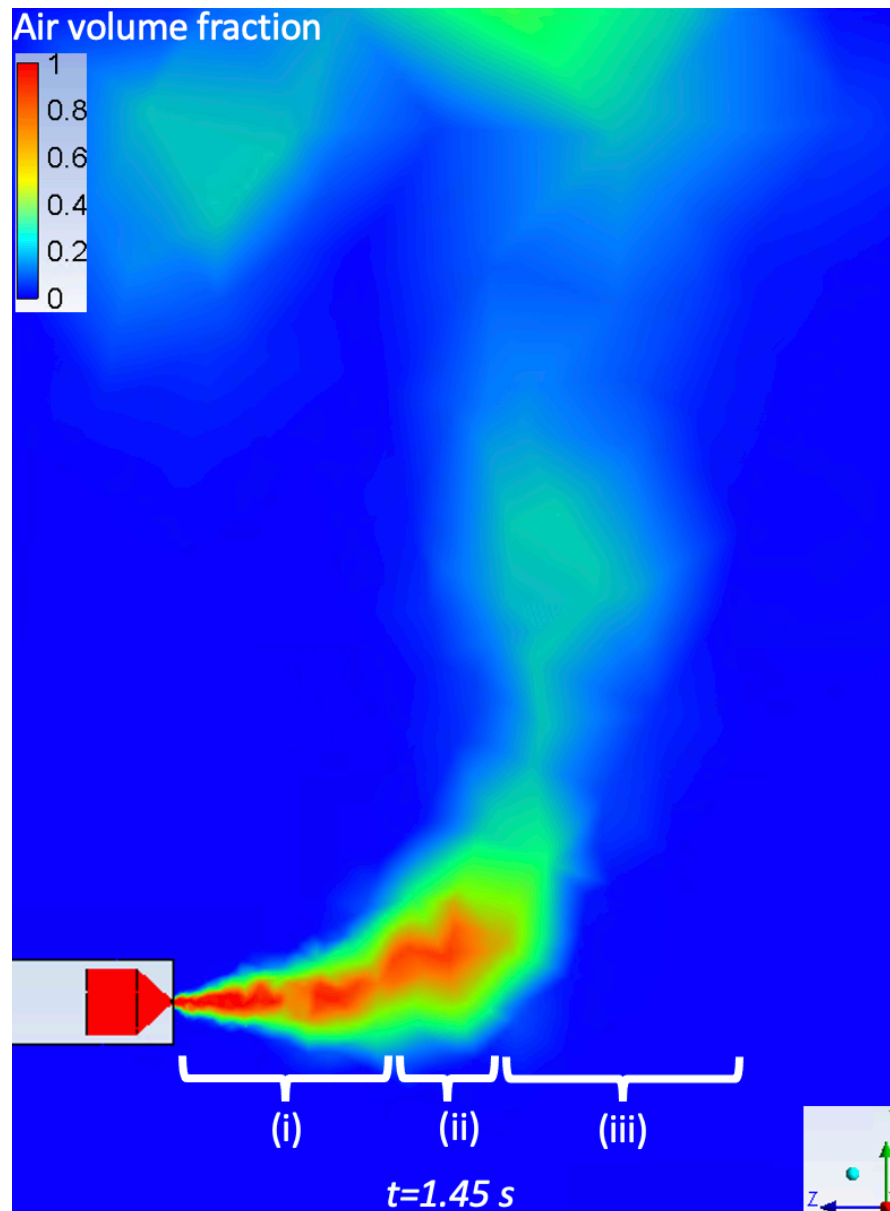
Figure 92: Air volume fraction contour at an inlet pressure of 8 bar for a flow time of 1.45 s. The flow regions are indicated as: (i) jet regime region, (ii) transition region, and (iii) plume region.

In each of these regions, the flow is dominated by a group of independent flow parameters, and the overall flow behaviour can therefore be described by a sequence of these distinct flow regimes. In the jet regime region, the discharged flow is mainly governed by the jet momentum force and the self-generated turbulence plays a dominated role in the path of the jet; the gas jet does not disintegrate until it reaches some distance from the nozzle, where the jet breaks up into a column of rising bubbles. In the plume regime region, the flow is chiefly controlled by the buoyancy force and characterised by the production of bubbles that break and rise independently in the direction dictated by gravitational or buoyancy effects. Between the jet and plume regimes, there exists an intermediate regime called transition stage [174]. In the transition stage, the effluent flow is governed by both momentum and buoyancy force and will cause the jet to curve from horizontal to upward direction [22].

137

The gas jet air volume fraction at an inlet pressure of 8 bar was compared to an image of a submerged air jet expanding underwater during the cutting trials in a 1m³ tank. Figure 93 (a) indicates the gas jet air volume fraction at a flow time of 1 s, whereas Figure 93 (b) shows an image of a submerged air jet captured a second after the gas jet pressure was increased to 8 bar.
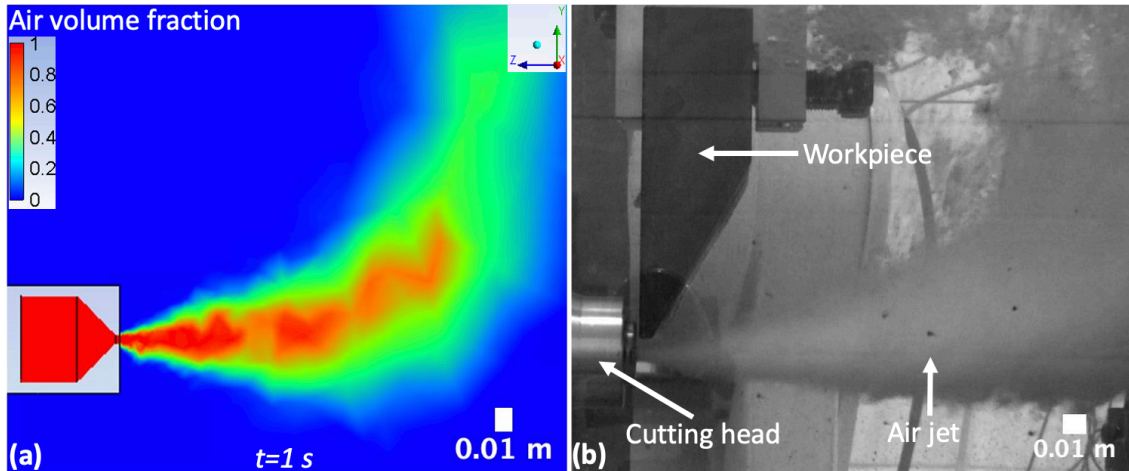
Figure 93: Air volume fraction of (a) 3D numerical model and (b) submerged air jet expanding underwater during the cutting trials in a 1m³ tank

Here it can be seen that the flow behaviour of the gas jet simulated in the 3D model is almost similar to that of the image captured during the cutting trials in a 1m³ tank. Both the simulated and submerged air jet expanded continuously and rose toward the water surface due to buoyancy [22]. The expansion of the gas jet upwards under the action of gravity and buoyancy is more defined for the 3D model than the previous 2D model. The disparities between the 2D and 3D model can be related to the limitations of using a 2D numerical technique to represent a 3D situation.

The jet penetration distance is defined as the maximum length along the jet centreline, and it is governed by several parameters, such as the diameter of the nozzle, the water depth, and the jet mass flow rate. The jet penetration length in the ambient water is pulsated and the penetration distance varies in time along the jet axis [22]. The jet penetration distance was measured using ImageJ, a Java-based image processing program [168]. The simulated gas jet penetration length is approximately 0.21 m. The submerged air jet penetration length could not be estimated due to the angle of the camera, but it is slightly greater than 0.19 m.

6.3.4   Velocity distribution

An evaluation of the velocity distribution throughout the flow field was also examined at an inlet pressure of 8 bar. Figure 94 shows the velocity contour at a flow time, t, of (a) 0.05 s, (b) 0.5 s, (c) 0.9 s and (d) 1.45 s.

138
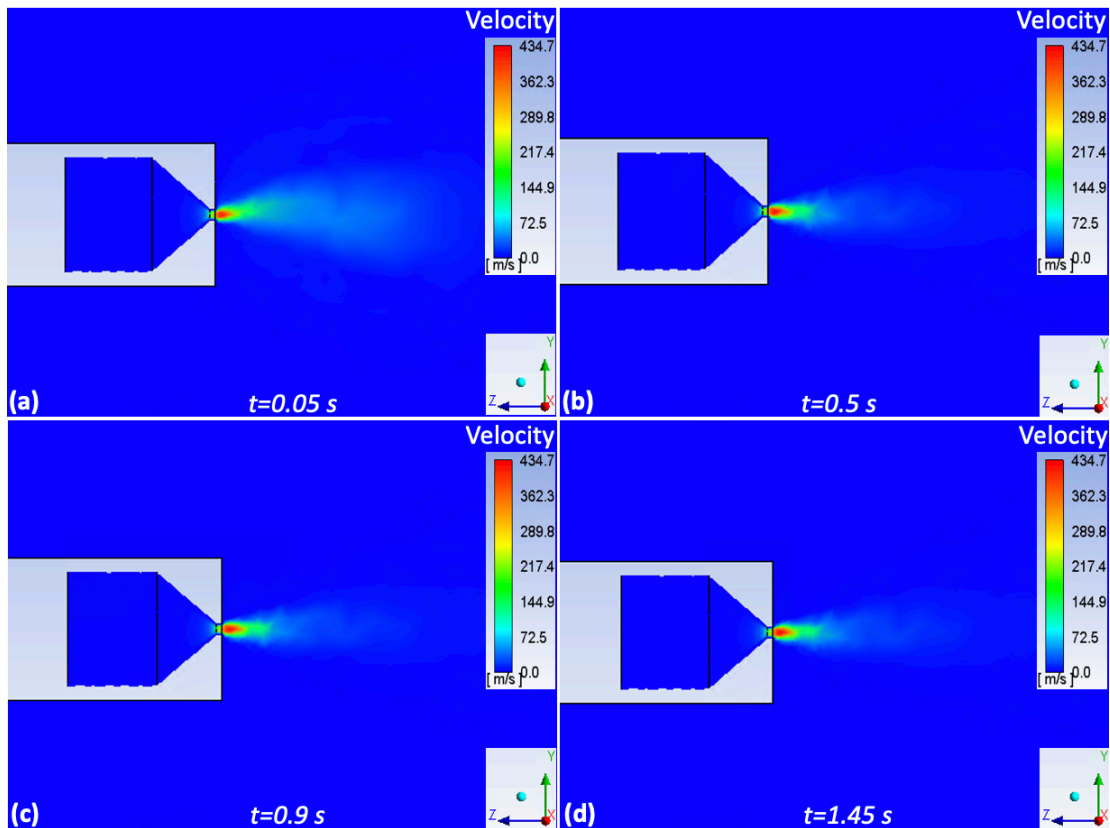
Figure 94: Velocity contour at an inlet pressure of 8 bar for a flow time of (a) 0.05 s, (b) 0.5 s, (c) 0.9 s and (d) 1.45 s

Figure 94 shows that the velocity distribution characteristics described for the 2D model are also presented in the 3D model. Moreover, the range of the velocity magnitude of the 3D model is comparable to that of the 2D model. A velocity plot along the centreline of the nozzle is presented in Appendix E.

6.4 3D underwater gas jet expansion of an obstacle with an opening/virtual kerf

A 3D underwater gas jet expansion model of an obstacle with an opening/virtual kerf was simulated to identify a mixed phase (water, water vapour (steam) and air) region along the path of the laser beam during underwater laser cutting. This model was simulated using the same nozzle geometry specification, cutting geometry and inlet pressure condition used in the underwater laser cutting trials in a 1 m^3 tank. The 3D model is a more realistic simulation of the 2D model of an obstacle with a virtual kerf/opening. Modifications to the geometry and boundary conditions are the most significant changes made to the model.

6.4.1 Geometry and boundary conditions

The geometry consists of the nozzle and an opening located inside the water domain. The outlet (red), wall (grey) and inlet (blue) boundary conditions of the geometry are indicated (see Figure 95).
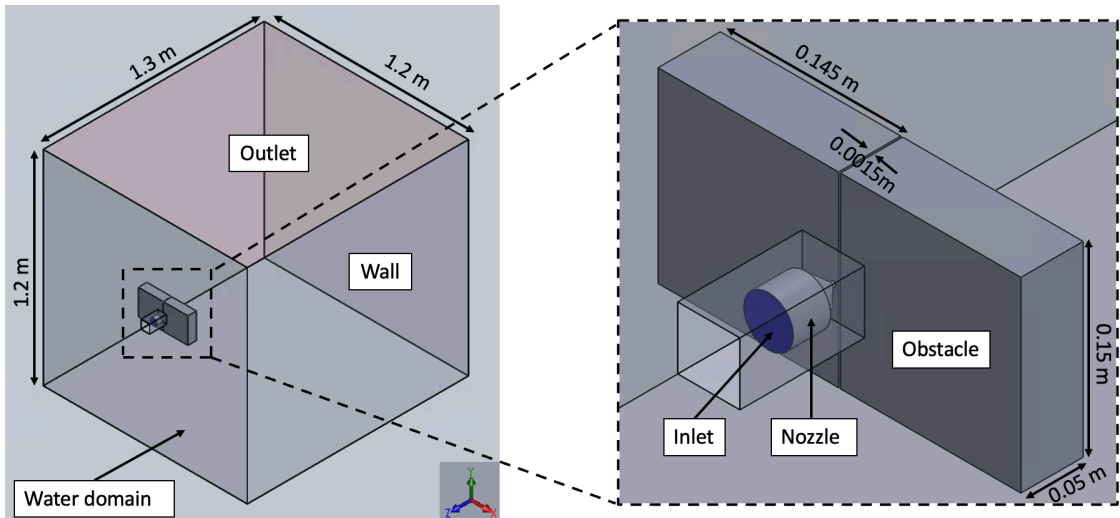
Figure 95: 3D geometry and boundary conditions

All the nozzle and obstacle design specification of the 2D geometry of an obstacle with an opening were implemented in this model.

Initially, face meshing was adapted to set a fine quadrilateral mesh with a maximum face size of 500 mm on the geometry. Afterwards, face sizing with an element size of 5 mm was set to generate a finer mesh on the faces around the nozzle exit and obstacle Finally, edge sizing was specified at the interior boundary conditions within the nozzle and opening region to set a size of 0.5 mm (see Figure 96). The generated mesh for the whole geometry consists of 6 369 nodes and 31 732 elements.
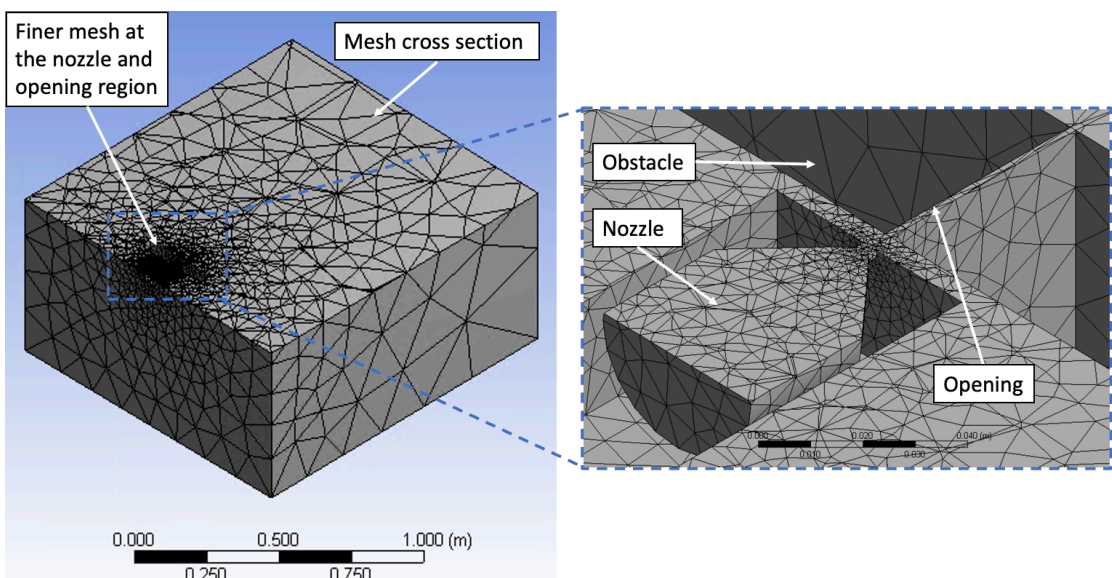
Figure 96: 3D mesh configuration (left) and cross section (right)

The solution was computed up to a flow time of approximately 1.25 s using all the preceding model's setup and solution settings.

6.4.2 Gas jet development

Figure 97 shows an air volume fraction contour at an inlet pressure of 8 bar for a flow time, t, of (a) 0.04 s, (b) 0.4 s, (c) 0.8 s and (d) 1.2 s.
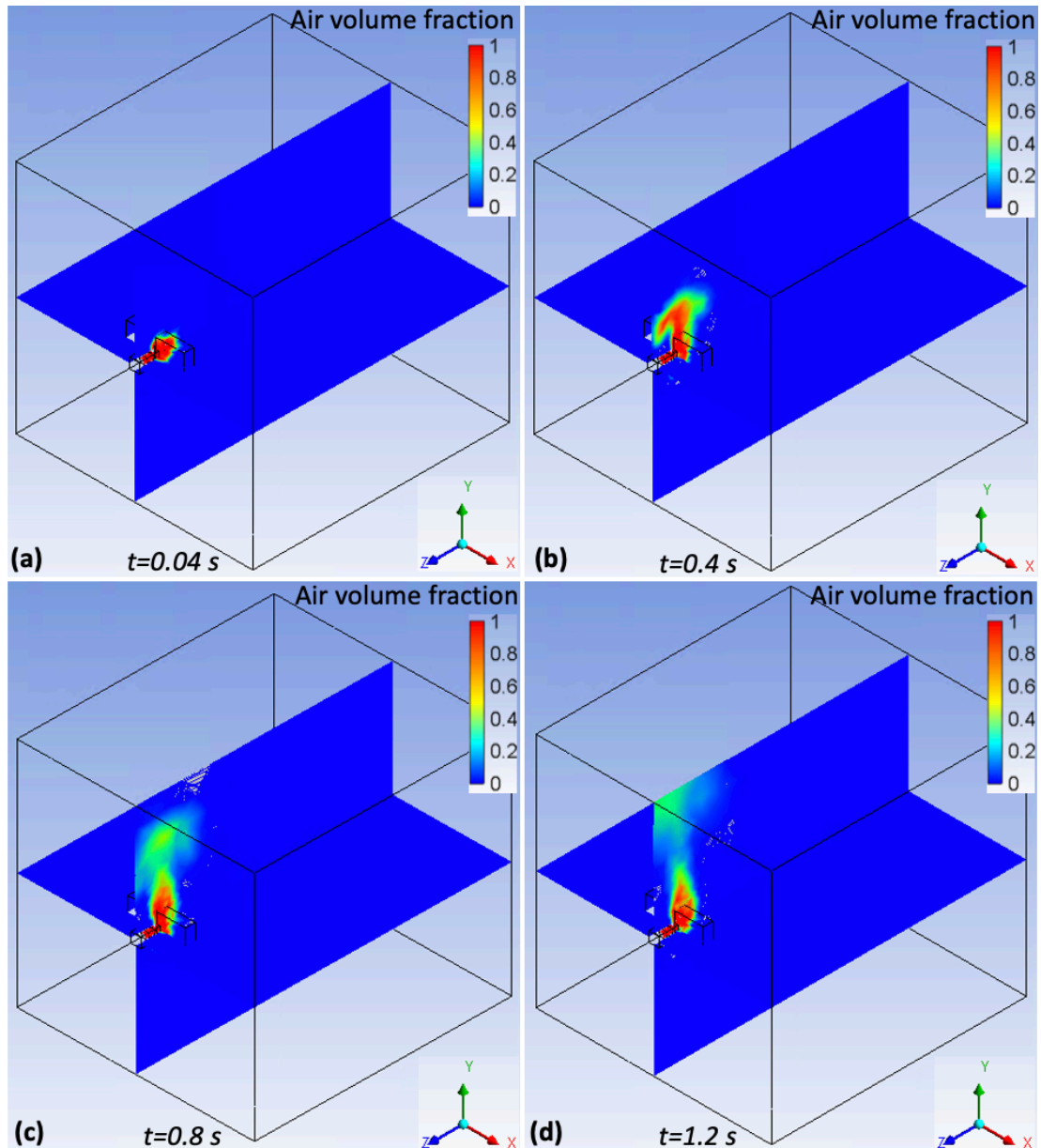
Figure 97: Air volume fraction contour at an inlet pressure of 8 bar for a flow time of (a) 0.04 s, (b) 0.4 s, (c) 0.9 s and (d) 1.2 s

The flow characteristics of the gas jet in the 3D model is almost similar to that of the 2D model of an obstacle with a virtual kerf. The gas jet expands through the virtual kerf/opening and rises towards the water surface due to buoyancy [22]. The expansion of the gas jet upwards under the action of gravity and buoyancy is more defined in the

3D model than the 2D model of an opening with an obstacle. Figure 98 provides a closer look at the air volume fraction contour at an inlet pressure of 8 bar for a flow time of 1 s.
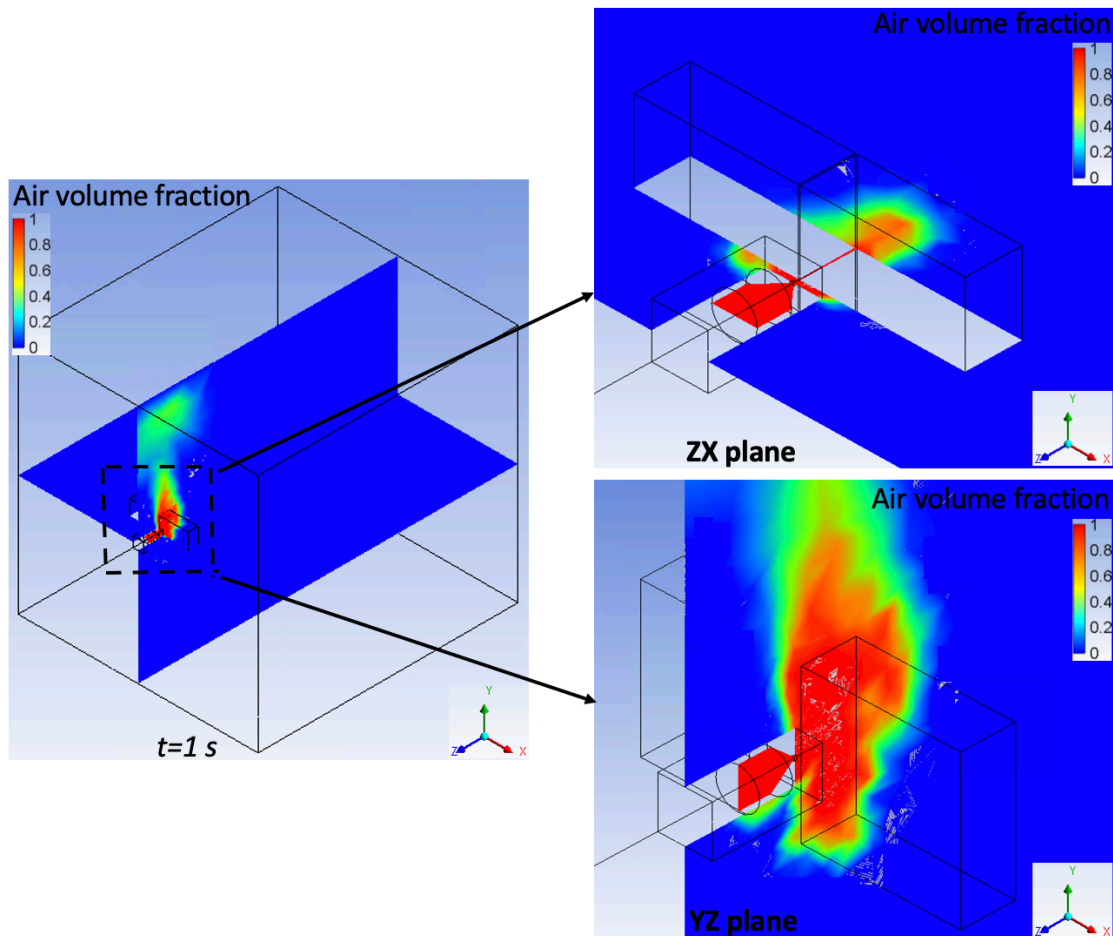
Figure 98: Air volume fraction contour at an inlet pressure of 8 bar for a flow time of 1 s

The air volume fraction from the nozzle to the entrance of the opening is 1 (see ZX plane). This shows that the local-dry-zone is well formed within this region. Therefore, it can be concluded that the transmission of the laser beam between the cutting head nozzle and the workpiece as well as the interaction zone of the laser beam with the workpiece material are not affected by the underwater environment due to sufficient shielding by the cutting gas jet. This can be attributed to the high gas jet momentum within this region. This agrees with experimental studies of underwater laser cutting, by Meinecke [1] and Shin et al. [92], which assume that the laser beam is not disturbed by water from the tip of the nozzle to the workpiece surface at atmospheric pressure conditions (see Chapter 2.8).

Figure 99 (a) indicates the gas jet air volume fraction at a flow time of 1 s, whereas Figure 99 (b) shows an image of a submerged air jet captured during the underwater laser cutting process when a thickness of 50 mm was being cut.
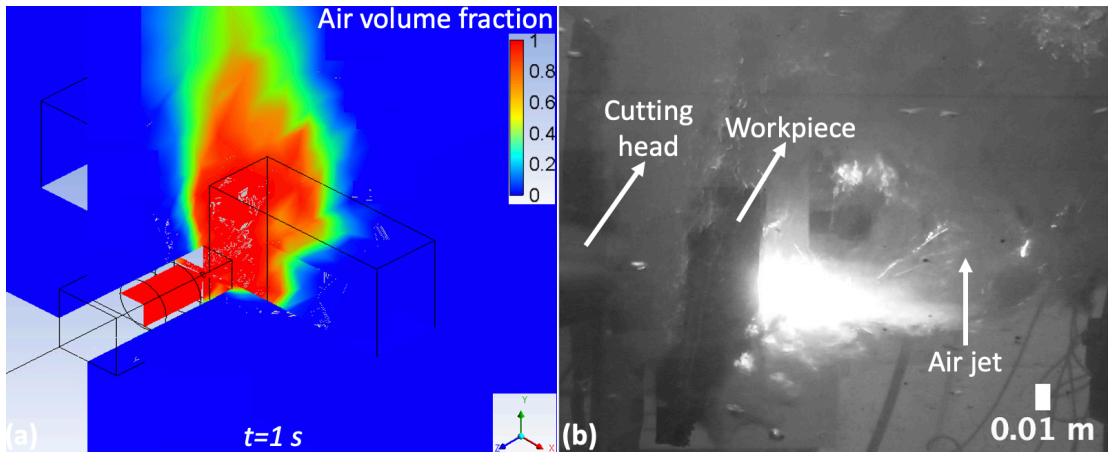
Figure 99: Air volume fraction of (a) numerical model and (b) submerged air jet expanding underwater during the cutting trials in a 1m^3 tank

The simulated gas jet in Figure 99 (a) exhibits comparable characteristics to the submerged air jet in Figure 99 (b). Both gas jets show the effect of buoyancy, as a portion of the gas jet that enters the virtual kerf/opening width expands and rises toward the water surface. Furthermore, in both air jet flow structures, the part of the gas jet that impinges on the specimen or obstacle travels sideways along the workpiece before rising to the water surface.

To investigate the variation in volume fraction of air with flow time, locations were defined along the path of the laser beam. These locations were defined at the nozzle exit, opening/virtual kerf entrance, middle of the opening/virtual kerf, opening/virtual kerf exit and 5 mm from the opening/virtual kerf exit. Figure 100 depicts the location of the defined interfaces in the model and Figure 101 indicates the variation in volume fraction of air with flow time.
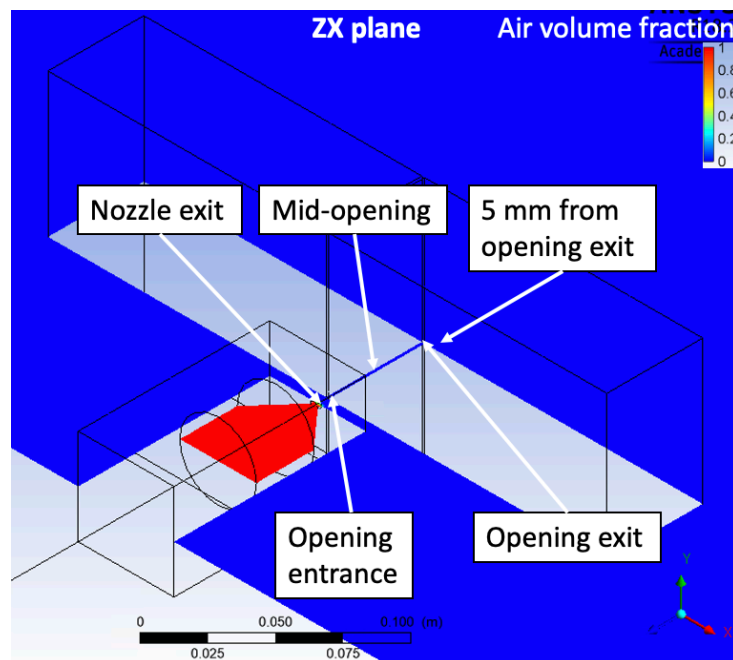
Figure 100: Definition of various locations along the path of the laser beam in the ZX plane
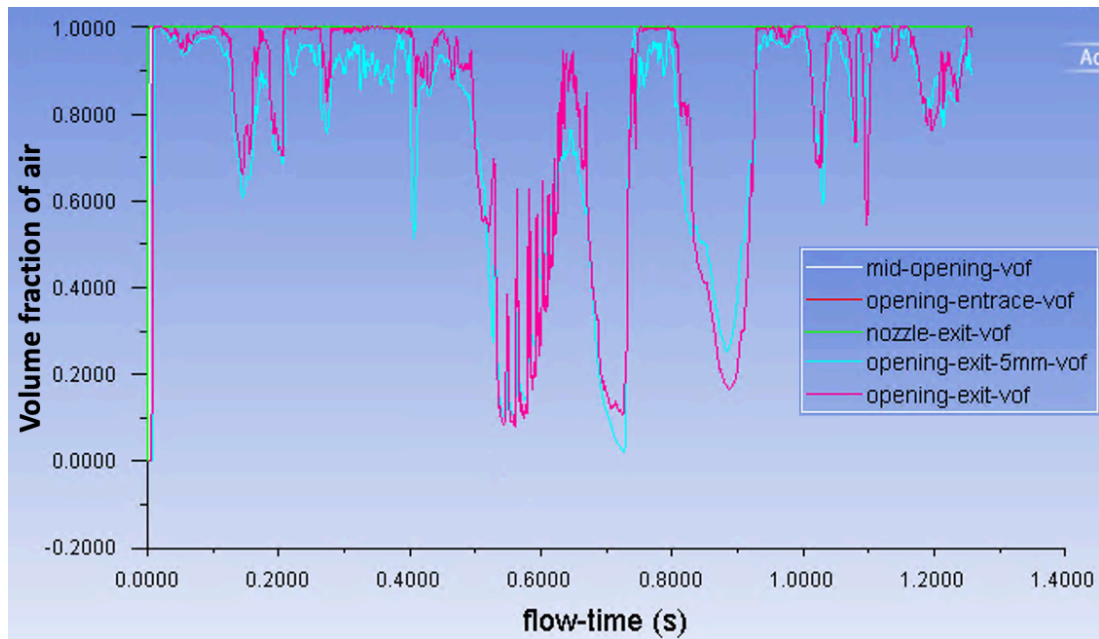
Figure 101: Volume fraction of air with corresponding flow time at various locations along the path of the laser beam

Initially, as the flow time increases, the phase changes from water to air at all points along the path of the laser beam. As the gas jet continues to expand, a mixed phase flow only occurs at the nozzle exit and at a location 5 mm from the nozzle exit. Except for the nozzle exit and a location 5 mm from the nozzle exit, the volume fraction of air is one for all the defined locations. This shows that the transmission of the laser beam between the cutting head nozzle and the workpiece as well as location at the middle of the opening/virtual kerf are not affected by the underwater environment due to sufficient shielding by the cutting gas jet.

The exit of the opening/virtual kerf is the location where water will most likely interact with the beam or molten material during underwater laser cutting. An interaction of water with molten material might be able to cool the melt to the point where its viscosity is too high for a complete removal from the kerf by the gas jet. The creation of bridges inside the kerf might be explained by increased viscosity of melt due to cooling effects and consequently poor melt removal by the gas jet [1].

If a mixed phase (water, water vapour (steam) and air) medium interacts with the laser beam at the exit of the opening/virtual kerf, optical effects such as reflection, refraction, scattering, and absorption of the laser beam can occur [100, 101]. These effects can change the beam diameter at the exit of the virtual kerf due to possible variations in the refractive index of a mixed phase. As a result, the energy supplied to the cut zone at the opening exit decreases, resulting in a low cutting performance in underwater laser cutting. Mixed phase locations at the exit of the opening/virtual kerf might explain why underwater laser cutting is less efficient than traditional laser cutting.

6.4.3 Mach number distribution

The Mach number distribution of the flow field through the virtual kerf was also generated. Figure 102 shows the velocity contour at an inlet pressure of 8 bar for a flow time, t, of (a) 0.4 s, (b) 0.7 s, (c) 1 s and (d) 1.2 s.
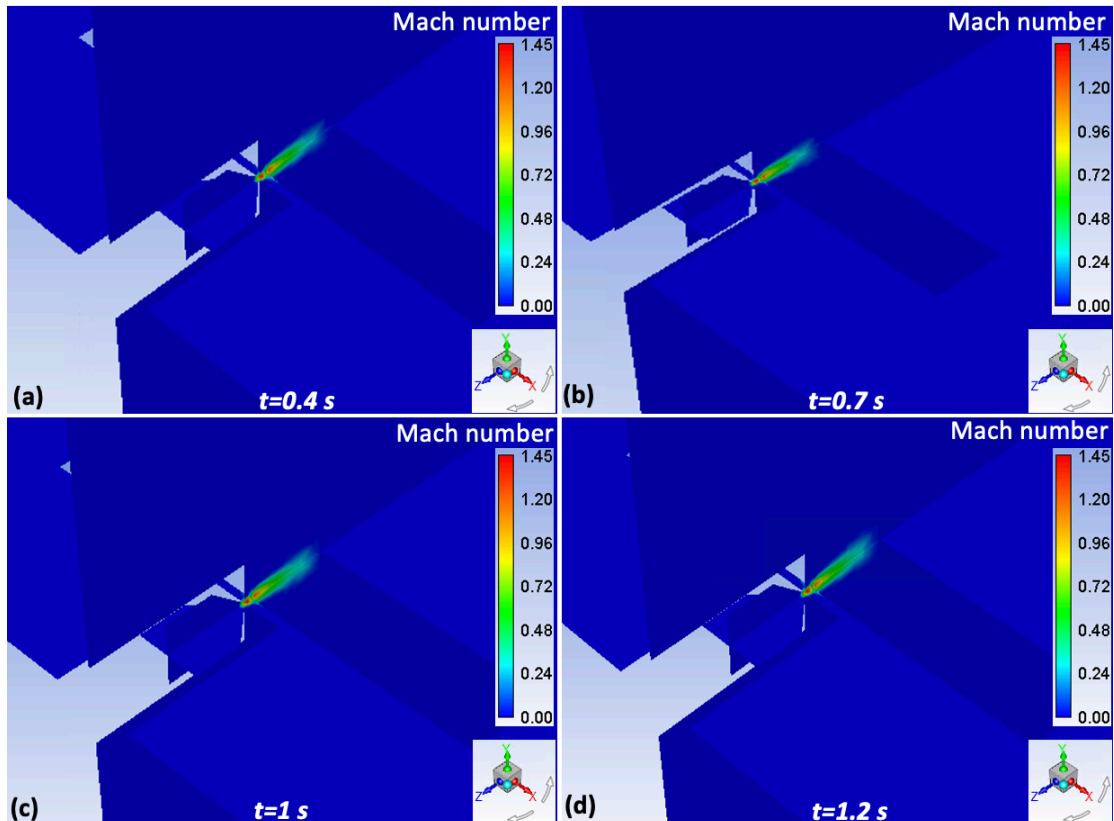
Figure 102: Mach number contour at an inlet pressure of 8 bar for a flow time of (a) 0.4 s, (b) 0.7 s, (c) 1 s and (d) 1.2 s

When the gas jet is injected underwater, it creates a supersonic under-expanded air jet that expands along the obstacle and through the opening. Under-expansion occurs as the external pressure of the environment is lower than the exit pressure of the nozzle. The nozzle exit and the opening entry have the highest Mach numbers, as seen in Figure 102. The lowest Mach number can be found in the region close to the opening exit. The range of the Mach number in the 3D model is comparable to velocity range of the 2D model.

Figure 103 shows the variation of the Mach number at different locations along the path of the laser beam.
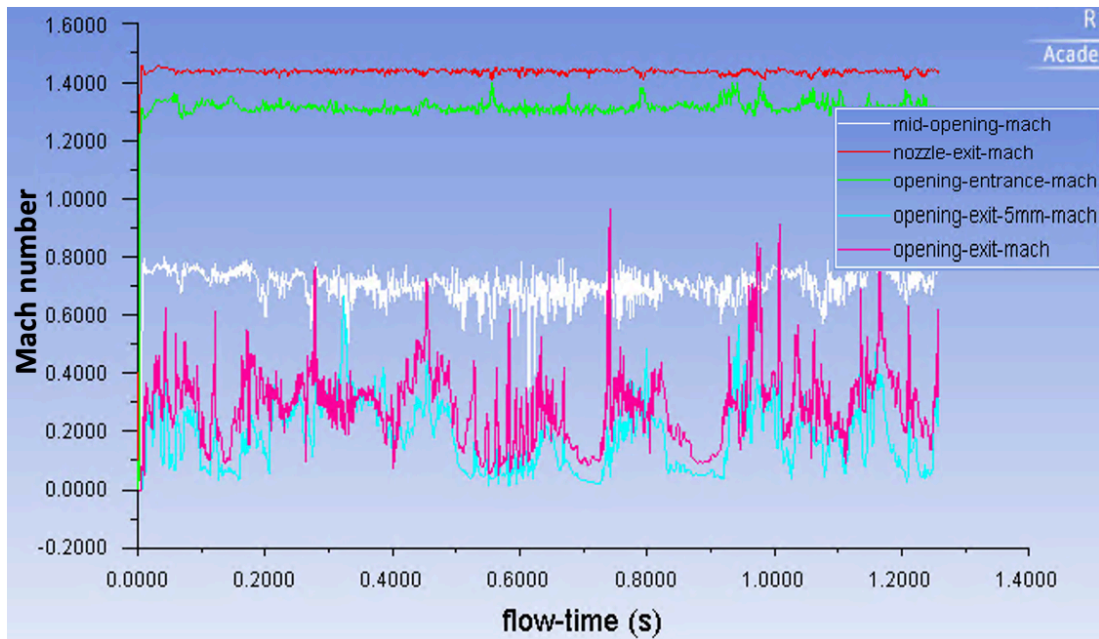
Figure 103: Mach number with corresponding flow time at various locations along the path of the laser beam

The Mach number fluctuates with time at all positions along the path of the laser beam. This can be attributed to the flow's turbulent and unsteady nature. The Mach number also decreases with increasing horizontal distance from the nozzle exit. At all locations, the amplitude of the Mach number appears to be random and occurs at indiscriminate frequencies. As the distance from the nozzle exit increases, the variations of the Mach number increase as the flow becomes more turbulent and unsteady.

The limitation of simulating a 3D gas jet expansion multiphase flow for underwater laser cutting is modelling the heat transfer process. The 3D model only considers the multiphase interaction between air and water; the influence of the laser beam on these fluids and obstacle is ignored. The influence of the beam on the flow field is not considered as modelling heat transfer in multiphase flows is complex and computationally expensive.

6.5 Conclusions of the development of a gas jet expansion model for underwater laser cutting

In this chapter, five models were simulated to develop a 3D model which examines the effect of fluid flow on the cutting performance and quality in underwater laser cutting. The most significant results are presented in the 3D underwater gas jet expansion model of an obstacle with an opening/virtual kerf. At an inlet pressure of 8 bar, a volume fraction of air and Mach number contour of an underwater gas jet expansion model were generated. The variation of the volume fraction of air along the path of the laser beam was examined. The following are conclusions of the most important findings:

- The volume fraction of air from the nozzle to the entrance of the opening is one for the flow time simulated. This shows that the local-dry-zone is well formed within this region. This finding is supported by experimental studies of underwater laser cutting in [1] and [92], which assume that the laser beam is not disturbed by water from the tip of the nozzle to the workpiece surface;

- The exit of the opening/virtual kerf is the location where a mixed phase (water, water vapour (steam) and air) will most likely interact with the beam or molten material during underwater laser cutting;

- An interaction of a mixed phase (water, water vapour (steam) and air) medium with molten material might be able to cool the melt to the point where its viscosity is too high for a complete removal from the kerf by the gas jet, resulting in a poor cut quality in underwater laser cutting;

- An interaction of the beam with a mixed phase (water vapour (steam) and air) region at the opening/virtual kerf exit can decrease the energy supplied to the cut zone, resulting in a low cutting performance in underwater laser cutting;

- The flow behaviour of the gas jet simulated in the 3D model of an obstacle with a virtual kerf is comparable to that of an image of a submerged air jet captured during the underwater laser cutting process when a thickness of 50 mm was being cut;

- As the distance from the nozzle exit increases, the amplitude and fluctuations of the Mach number increase as the flow becomes more turbulent and unsteady.

7 Conclusions

7.1 Summary

The goal of this work has been set to develop a scientific understanding of the underwater laser cutting process and influencing parameters up to a hydrostatic pressure of 20 bar on steel structures up to 50 mm in thickness. Three approaches were taken to investigate underwater laser cutting of C-Mn steel using a 10 kW IPG Ytterbium fibre laser system with a wavelength of 1.06 μm. These approaches comprise of an experimental study of underwater laser cutting, the development of a power balance theoretical model for underwater laser cutting, and the development and application of a gas jet expansion numerical model for underwater laser cutting.

Underwater laser reactive cutting of a 50 mm thick C-Mn steel workpiece using a solid-state Ytterbium fibre laser system with a wavelength of 1.06 μm has been conducted. Air, released from a coaxial nozzle, was used as a cutting gas and to provide a local dry volume between the laser cutting head and the cutting location. Air was adopted as an assist gas because of safety concerns regarding the use of oxygen underwater in both nuclear and offshore decommissioning applications [1, 20].

Underwater laser cutting trials were carried out at atmospheric pressure conditions and increasing hydrostatic pressure conditions of up to 20 bar. The experimental results at atmospheric pressure conditions were analysed for the effect of power, cutting gas pressure and stand-off distance on the corresponding maximum cut thickness, kerf width and dross height. The experimental results at increasing hydrostatic pressure conditions were analysed for the effect of hydrostatic pressure on the corresponding maximum cut thickness, kerf width and dross height. Chapter 4 presents the underwater laser cutting results at atmospheric pressure conditions and increasing hyperbaric conditions.

A complete separation of a 50 mm thickness C-Mn steel workpiece was achieved at a cutting speed of 125 mm/min in the experimental study of underwater laser cutting in a 1m^3 tank. The highlight of the experimental study in increasing hyperbaric conditions is that a 50 mm thick C-Mn steel workpiece was adequately cut with a maximum cutting speed of 200 mm/min for hydrostatic pressure conditions of up to 20 bar, representing a water depth of ~200 m.

Also incorporated in this work was the development of a power balance theoretical model for underwater laser cutting. The energy balance for underwater laser cutting was developed by modifying the power balance equation in conventional laser cutting with conduction and convection heat losses that occur underwater. The predicted process performance is substantially the same as the experimental laser cutting results, particularly for higher laser power magnitudes and lower cutting speeds. The predicted kerf width is nearly identical to the measured width of the cut.

Additionally, in the course of this work, the development and application of a gas jet expansion numerical model for underwater laser cutting was investigated. The objective of this study was to investigate the effect of fluid flow on the underwater laser cutting process to identify a mixed phase (water, water vapour (steam) and air) medium along the path of the laser beam. As shown by the 3D underwater gas jet expansion model of an obstacle with an opening/virtual kerf, a mixed phase (water, water vapour (steam) and air) medium along the path of the laser beam was found at the exit of the opening/virtual kerf. A variation in volume fraction of air along the path of the laser beam is presented in Chapter 6. An image of a submerged air jet captured during the underwater laser cutting process when a thickness of 50 mm was being cut is also compared to the generated 3D model of an obstacle with an opening/virtual kerf.

7.2 Conclusions

The conclusions for this work are summarised according to the three technical chapters presented: Chapter 4, Chapter 5 and Chapter 6. Specific key observations and conclusions for the experimental investigation of underwater laser cutting are:

- The most significant parameters influencing process performance in underwater laser cutting were the laser power intensity on the surface of the material and cutting speed;
- The most important variable affecting the kerf width was the beam diameter on the surface of the material, which is determined by the focal position and stand-off distance;
- For cutting trials in a $1m^3$ tank, the most significant parameter affecting the dross height is cutting speed. The average dross height is inversely proportional to the cutting speed;
- For cutting trials in a high-pressure vessel, the relationship between the average dross height and corresponding cutting speed is unclear for 5, 10, 15 and 20 bar hydrostatic pressure. The average dross height is inversely proportional to the hydrostatic pressure at all cutting speeds.

This work on developing an energy balance model for underwater laser cutting has allowed the following principal conclusions to be made:

- The theoretical process performance is substantially the same as the experimental laser cutting results, particularly for higher laser power magnitudes and lower cutting speeds;
- The predicted kerf width is nearly identical to the measured width of the cut.

The development and application of a gas jet expansion numerical model for underwater laser cutting was also investigated. Crucial conclusions are summarised as follows:

- The transmission of the laser beam between the cutting head nozzle and the workpiece as well as location at the middle of the opening/virtual kerf are not affected by the underwater environment due to sufficient shielding by the cutting gas jet. This agrees with conclusions drawn in [1] and assumptions in [92];
- The exit of the opening/virtual kerf was found to be the location where water will most likely interact with the beam or molten material during underwater laser cutting. A mixed phase region at the exit of the opening can interact with the beam or molten material during underwater laser cutting, affecting both process performance and quality.

This work extends the knowledge currently published on underwater laser cutting of thick section C-Mn steel by high power Yb fibre laser operating in cw mode for decommissioning by:

- investigating the underwater laser cutting process on C-Mn steel in increasing hydrostatic pressure conditions of up to 20 bar, corresponding to increasing water depth of up to 200 m. The greatest water depth reported for underwater fibre laser cutting using air or an inert gas in literature is less than 1 m;
- showing that a 50 mm thick C-Mn steel workpiece can be adequately cut with a maximum cutting speed of 200 mm/min for hydrostatic pressure conditions of up to 20 bar, representing a water depth of ~200 m;
- investigating a theoretical model for underwater laser cutting as research in this field is mainly experimental;
- showing that the predicted maximum cut thickness and kerf width are substantially the same as the practical underwater laser cutting results;
- establishing a correlation between a 3D underwater gas expansion multiphase model and an experimental submerged gas jet flow behaviour;
- showing that the exit of the opening/virtual kerf is the location where water will most likely interact with the beam or molten material during underwater laser cutting.

7.3 Outlook and Recommendation for further work on underwater laser cutting

Further work on the technique of underwater laser cutting will need to spread in different directions based on the multidisciplinary character of the process. Specific areas of interest are:

- Thermal monitoring of the underwater laser cutting process;
- Using different underwater laser cutting techniques such as the step like increase of the cutting speed or oblique cutting in increasing hydrostatic pressure conditions to cut thicker materials. The general ability for cutting 100 mm stainless steel underwater has been confirmed at atmospheric pressure conditions by Shin et al. [91];

150

- Underwater gas jet visualisation experiments through an obstacle with a virtual kerf;
- Wider numerical investigation of a 3D underwater gas jet expansion model of an obstacle with an opening/virtual kerf at different inlet pressure conditions and obstacle thicknesses;
- A mathematical model for underwater laser cutting which extends the work done in this study by including a set of balance equations for mass and momentum.

8 References

1. Meinecke TV. Experimental Study of Underwater Laser Cutting of Steel with a View on Subsea Decommissioning. Aberdeen: University of Aberdeen; 2012.

2. Knudsen S. Decommissioning Concrete Structures - Environmental and Safety Challenges. SPE: Society of Petroleum Engineers; 2011.

3. Barale V. The European Marginal and Enclosed Seas: An Overview. In: Barale V, Gade M, editors. Remote Sensing of the European Seas. Dordrecht: Springer Netherlands; 2008. p. 3-22.

4. OSPAR. 2013 Update of the Inventory of Oil and Gas Offshore Installations in the OSPAR Maritime Area. OSPAR Commission London: OSPAR Commission; 2013 [Available from: https://www.ospar.org/documents?v=7329

5. Day MD. Decommissioning of Offshore Oil and Gas Installations. In: Orszulik ST, editor. Environmental Technology in the Oil Industry. Dordrecht: Springer Netherlands; 2008. p. 189-213.

6. EEEGR. Reuse & Decommissioning: EEEGR; 2022 [Available from: https://eeegr.com/sigs/late-life-decommissioning/#:~:text=Many%20of%20the%20structures%20producing,lengthy%20and%20high%20cost%20operation.

7. Palkar S, Markeset T. Extending the Service Life Span of Ageing Oil and Gas Offshore Production Facilities2012. 213-21 p.

8. Palkar S. Lifetime Extension of Ageing Oil and Gas Platforms Stavanger, Norway: University of Stavanger; 2010.

9. Bull AS, Love MS. Worldwide oil and gas platform decommissioning: A review of practices and reefing options. Ocean & Coastal Management. 2019;168:274-306.

10. Gledhill PL. Cutting and deployment system development for decommissioning of underwater steel structures. Aberdeen: University of Aberdeen; 2012.

11. UK Legislation. Energy Act 2008: Crown copyright; 2008 [cited 2008. Available from: https://www.legislation.gov.uk/ukpga/2008/32/pdfs/ukpga_20080032_en.pdf.

12. Decom North Sea. Decommissioning in the North Sea. SCOTTISH INTERPRISE; 2012.

13. OGUK. 2010 DECOMMISSIONING INSIGHT. OIL & GAS; 2010.

14. Decommissioning NNPfR-ua. DECCOMMISSIONING EXPLAINED: Nexstep – National Platform for Re-use and Decommissioning; 2017 [Available from:

https://www.nexstep.nl/decommissioning-landscape/decommissioning-explained/.

15.   OGUK. DECOMMISSIONING INSIGHT 2021. 2021.

16.   OGUK. DECOMMISSIONING INSIGHT 2020. OIL & GAS UK; 2020.

17.   OGUK. DECOMMISSIONING INSIGHT 2018. OGUK; 2018.

18.   Hilton P, Khan A. UNDERWATER LASER CUTTING: AN APPLICATION TECHNOLOGY FOR DISMANTLING AND SIZE REDUCTION OF IRRADIATED NUCLEAR STRUCTURES. 2014.

19.   Hilton P. Cutting Stainless Steel with Disc and CO2 Lasers. Proceedings of LAMP2009 - the 5th International Congress on Laser Advanced Materials Processing; Kobe, Japan: Japan Laser Processing Society; 2009.

20.   Hilton P, Khan A. Underwater cutting using a 1 µm laser source. Journal of Laser Applications. 2015;27(3).

21.   ANSYS. ANSYS FLUENT: Ansys, Inc; 2018 [Available from: https://www.ansys.com/en-gb/products/fluids/ansys-fluent.

22.   Harby K, Chiva S, Muñoz-Cobo JL. An experimental investigation on the characteristics of submerged horizontal gas jets in liquid ambient. Experimental Thermal and Fluid Science. 2014;53:26-39.

23.   Tang J, Li S, Wang N. Flow structures of gaseous jets injected into water for underwater propulsion. Acta Mechanica Sinica. 2011;27(4):461.

24.   Steen W, Watkins KG, Mazumder J. Laser Material Processing: Springer London; 2010.

25.   Gould RG. "The LASER, Light Amplification by Stimulated Emission of Radiation". The Ann Arbor Conference on Optical Pumping; 1959; University of Michigan.

26.   Hintze C. Gordon Gould: The Long Battle For The Laser Patent. ELECTRONIC DESIGN. 2006.

27.   Maiman TH. Stimulated optical radiation in ruby. . NATURE. 1960.

28.   Koester CJ, Snitzer E. Amplification in a Fiber Laser. Appl Opt. 1964;3(10):1182-6.

29.   Snitzer E. Proposed Fiber Cavities for Optical Masers. Journal of Applied Physics. 1961;32(1):36-9.

30.   Edelson AM. "In the beginning…,". The journal of ECT. 2009;25:23–4.

31. Sullivan ABJ, Houldcroft PT. Gas-jet laser cutting. British Welding Journal. 1967:443.

32. Groover MP. Fundamentals of Modern Manufacturing: materials, processes and systems. Fourth Edition ed. USA: John Wilsely & Sons inc; 2010 21/10/2017.

33. Powell J. The Basic Principles. In: Powell J, editor. CO2 Laser Cutting. London: Springer London; 1993. p. 1-22.

34. Grand View Research. Laser Processing Market Analysis By Product (Gas, Solid-state, Fiber), By Process (Material Processing, Marking, Micro-Processing), By Application (Automotive, Aerospace, Medical), And Segment Forecasts, 2014 - 2025: Grand View Research; 2017 [Available from: https://www.grandviewresearch.com/industry-analysis/laser-processing-market.

35. Lopez MBA. Laser cutting in decommissioning of Nuclear Power Stations. Lisborn: TECNICO LISBOA; 2015.

36. Wandera C. PERFORMANCE OF HIGH POWER FIBRE LASER CUTTING OF THICK-SECTION STEEL AND MEDIUM-SECTION ALUMINIUM. Lappeenranta, Finland: Lappeenranta University of Technology,; 2010.

37. Chagnot C, De Dinechin G, Canneau G. Cutting performances with new industrial continuous wave ND:YAG high power lasers: For dismantling of former nuclear workshops, the performances of recently introduced high power continuous wave ND:YAG lasers are assessed. Nuclear Engineering and Design. 2010;240(10):2604-13.

38. Hashemzadeh M. Investigations into fibre laser cutting. Nottingham: University of Nottingham; 2014.

39. Kaplan AFH. Theoretical Analysis of Laser Beam Cutting. Germany: Shaker Verlag GmbH 2002.

40. Mahrle A, Beyer E. Theoretical aspects of fibre laser cutting. Journal of Physics D: Applied Physics. 2009;42(17):175507.

41. Petring D, Schneider F, Wolf N, Nazery-Goneghany V. The influence of beam quality, power and wavelength on laser cutting and welding. The laser user. 2009(56):20-3.

42. TRUMPF. Sublimation cutting: TRUMPF; 2017 [Available from: https://www.trumpf.com/en_GB/applications/laser-cutting/sublimation-cutting/.

43. Ion JC. Laser Processing of Engineering Materials: Principles, Procedure and Industrial Application: Elsevier Science; 2005.

44. Radovanović M. Some Possibilities for Determining Cutting Data when Using Laser Cutting. Journal of Mechanical Engineering. 2006;52(10):645-52.

45. IPG. Laser Cutting Techniques: IPG Photonics Corporation; 2021 [Available from: https://www.ipgphotonics.com/en/applications/materials-processing/cutting.

46. TRUMPF. Fusion cutting: TRUMPF; 2017 [Available from: https://www.trumpf.com/en_GB/applications/laser-cutting/fusion-cutting/.

47. Hackett CM, Garg S. Visualization of thermal cutting fluid flows. The European Physical Journal Special Topics. 2010;182(1):145-59.

48. Wandera C, Kujanpää V, Salminen A. Laser power requirement for cutting thick-section steel and effects of processing parameters on mild steel cut quality. Proceedings of the Institution of Mechanical Engineers, Part B: Journal of Engineering Manufacture. 2011;225(5):651-61.

49. Chaki S, Ghosal S. LASOX cutting: Principles and evolution. 2019. p. 1-12.

50. O'Neill W, Gabzdyl JT. New developments in laser-assisted oxygen cutting. Optics and Lasers in Engineering. 2000;34(4):355-67.

51. Wandera C, Salminen A, Kujanpaa V. Inert gas cutting of thick-section stainless steel and medium-section aluminum using a high power fiber laser. Journal of Laser Applications. 2009;21(3):154-61.

52. Golnabi H, Bahar M. Investigation of optimum condition in oxygen gas-assisted laser cutting. Optics & Laser Technology. 2009;41(4):454-60.

53. Khan A, Hilton P. Yb-Fibre laser single sided tube cutting for nuclear decommissioning applications ICALEO Proceedings 2010; Anaheim, California, USA: Laser Institute of America; 2010.

54. Sparkes M, Gross M, Celotto S, Zhang T, O'Neill W. Practical and theoretical investigations into inert gas cutting of 304 stainless steel using a high brightness fiber laser. Journal of Laser Applications. 2008;20(1):59-67.

55. Ross IE. Thick section cutting with CO2 lasers. Industrial Laser Review. 1992.

56. Stelzer S, Mahrle A, Wetzig A, Beyer E. Experimental Investigations on Fusion Cutting Stainless Steel with Fiber and CO2 Laser Beams. Physics Procedia. 2013;41:399-404.

57. Himmer T, Pinder T, Morgenthal L, Beyer E. High brightness lasers in cutting applications. ICALEO 2007, 26th International Congress on Applications of Lasers & Electro-Optics; Orlando, FL, USA: Laser Institute of America; 2007.

58. Petring D, Schneider F, Wolf N, Nazery V. The relevance of brightness for high power laser cutting and welding. Temecula, CA: Laser Institute of America; 2008.

59. Wandera C, Salminen A, Olsen FO, Kujanpää V. Cutting of stainless steel with fiber and disc laser. In NOLAMP 11, Laser Materials Processing Proc of the 11th Nordic Conf; Lappeenranta, Finland: Lappeenranta University of Technology; 2007.

60. Seefeld T, O'Neill B. Cutting and welding with the new high brightness lasers. The Laser User. 2008;50:32-7.

61. Ion JC. Laser processing of engineering materials : principles, procedure and industrial application: Boston : Elsevier/Butterworth-Heinemann; 2005.

62. Fieret J, Terry M, Ward B. Invited Paper Overview Of Flow Dynamics In Gas-Assisted Laser Cutting: SPIE; 1987.

63. Zefferer H, Petring D, Beyer E. Investigation of the gas flow in laser beam cutting. Lectures and Posters of the 3rd International Beam Technology Conference; Karlsruhe: Fraunhofer-Publica - Publication Database of the Fraunhofer-Gesellschaft; 1991.

64. Man HC, Duan J, Yue TM. Behaviour of supersonic and subsonic gas jets inside laser cut kerfs. International Congress on Applications of Lasers & Electro-Optics. 1997;1997(1):27-36.

65. Shan J. 17 - Laser welding of magnesium alloys. In: Liu L, editor. Welding and Joining of Magnesium Alloys: Woodhead Publishing; 2010. p. 306-50.

66. Wandera C, Kujanpaa V. Characterization of the melt removal rate in laser cutting of thick-section stainless steel. Journal of Laser Applications. 2010;22(2):62-70.

67. Hügel H. New solid-state lasers and their application potentials. Optics and Lasers in Engineering. 2000;34(4):213-29.

68. Ulmanen P. THE EFFECT OF HIGH POWER ADJUSTABLE RING MODE FIBER LASER FOR MATERIAL CUTTING [Masters thesis]. Finland: Tampereen teknillinen yliopisto; 2017.

69. Wandera C, Kujanpää V. Optimization of parameters for fibre laser cutting of a 10 mm stainless steel plate. Proceedings of the Institution of Mechanical Engineers, Part B: Journal of Engineering Manufacture. 2011;225(5):641-9.

70. Hashemzadeh M, Suder W, Williams S, Powell J, Kaplan AFH, Voisey KT. The Application of Specific Point Energy Analysis to Laser Cutting with 1μm Laser Radiation. Physics Procedia. 2014;56(Supplement C):909-18.

71. Himmer T, Lütke M, Morgenthal L, Beyer E, Bratt C. CUTTING APPLICATIONS WITH HIGH BRIGHTNESS LASERS Journal for Technology of Plasticity. 2008;33(1-2).

72.	Lopez AB, Assunção E, Quintino L, Blackburn J, Khan A. High-power fiber laser cutting parameter optimization for nuclear Decommissioning. Nuclear Engineering and Technology. 2017;49(4):865-72.

73.	Schulz W, Kostrykin V, Nießen M, Michel J, Petring D, Kreutz EW, Poprawe R. Dynamics of ripple formation and melt flow in laser beam cutting. Journal of Physics D: Applied Physics. 1999;32(11):1219-28.

74.	European Committee for Standardization. Thermal cutting - Classification of thermal cuts, Geometrical product specification and quality tolerances. 2002.

75.	Goldstein JR. Fluid Mechanics Measurements. 2nd ed: CRC Press; 1996.

76.	Houghton EL, Carrithers NB. Aerodynamics for Engineering Students. 3rd ed. London: Edward Arnold Ltd; 1982.

77.	Hilton P, Khan A. Optimisation of underwater laser cutting for decommissioning purposes. ICALEO International Congress on Applications of Lasers and Electro-Optics; San Diego, CA, USA.: Laser Institute of America; 2014.

78.	Hilton P, Khan A. New developments in laser cutting for nuclear decommissioning. Proceedings of WM2014 Nuclear Waste Management Conference; 2014; Phoenix, Arizona: Waste Management Symposia, Inc.

79.	Donaghy J. Choose the gas that's right for the cutting operation. Welding Journal. 1995;74:55-61.

80.	Shin JS, Oh SY, Park H, Chung CM, Seon S, Kim TS, Lee L, Choi BS, Moon J. High-speed fiber laser cutting of thick stainless steel for dismantling tasks. Optics & Laser Technology. 2017;94:244-7.

81.	Shin JS, Oh SY, Park H, Chung CM, Seon S, Kim TS, Lee L, Lee J. Laser cutting of steel plates up to 100 mm in thickness with a 6-kW fiber laser for application to dismantling of nuclear facilities. Optics and Lasers in Engineering. 2018;100:98-104.

82.	Seon S, Shin JS, Oh SY, Park H, Chung C-M, Kim T-S, Lee L, Lee J. Improvement of cutting performance for thick stainless steel plates by step-like cutting speed increase in high-power fiber laser cutting. Optics & Laser Technology. 2018;103:311-7.

83.	Shin JS, Oh SY, Park H, Chung CM, Seon S, Kim TS, Lee L, Lee J. Cutting performance of thick steel plates up to 150 mm in thickness and large size pipes with a 10-kW fiber laser for dismantling of nuclear facilities. Annals of Nuclear Energy. 2018;122:62-8.

84.	Ohtani A, Matsushima N, Mori H, Kutsuna N, Higashiura H. Document collection of the 24th technical special committee on fugen decommissioning Fugen Decommisioning Engineering Center Tsuruga Head Office; 2012.

85. Leschke J, Barroi A, Emde B, Kaierle S, Hermsdorf J. Investigations on underwater laser cutting for decommissioning of marine constructions. Conference on Maritime Energy Hamburg, Germany: COME; 2017.

86. Leschke J, Barroi A, Kaierle S, Hermsdorf J, Overmeyer L. Studies on the Robustness of Underwater Laser Cutting of S355J2+N Using a Yb:YAG Disk Laser Source. Physics Procedia 2016;83:310-6.

87. Leschke J, Emde B, Hermsdorf J, Kaierle S, Overmeyer L. Controlling the kerf properties of underwater laser cutting of stainless steel with 3 mm thickness using an Yb:YAG laser source in nuclear decommissioning processes. Procedia CIRP. 2020;94:493-8.

88. Wang W, Tan C, Xu L, Wang X, Lin S. Laser cutting 30 mm steel plates under water of 50 m. Transactions of the China Welding Institution. 2015;36(1):35-8.

89. Roy N, Kuar AS, Mitra S. 7 - Underwater pulsed laser beam cutting with a case study A2 - Davim, J. Paulo. Microfabrication and Precision Engineering: Woodhead Publishing; 2017. p. 189-212.

90. Roy N, Kuar AS, Mitra S, Das A. Submerged pulsed Nd:YAG laser beam cutting of Inconel 625 superalloy: Experimental investigation. Lasers in Engineering. 2016;35(1-4):151-71.

91. Shin JS, Oh SY, Park S, Park H, Kim TS, Lee L, Kim Y, Lee J. Underwater laser cutting of stainless steel up to 100 mm thick for dismantling application in nuclear power plants. Annals of Nuclear Energy. 2020;147.

92. Shin JS, Oh SY, Park H, Kim TS, Lee L, Chung CM, Lee J. Underwater cutting of 50 and 60 mm thick stainless steel plates using a 6-kW fiber laser for dismantling nuclear facilities. Optics & Laser Technology. 2019;115:1-8.

93. Shin JS, Oh SY, Park SK, Park H, Lee J. Improved underwater laser cutting of thick steel plates through initial oblique cutting. Optics & Laser Technology. 2021;141.

94. Kruusing A. Underwater and water-assisted laser processing: Part 1—general features, steam cleaning and shock processing. Optics and Lasers in Engineering. 2004;41(2):307-27.

95. Fenneman DB, Geres RJ. Laser pile cutter. Google Patents; 1979.

96. IPG. High Power CW Fiber Lasers: IPG Photonics Corporation; 2021 [Available from: https://www.ipgphotonics.com/en/products/lasers/high-power-cw-fiber-lasers/1-micron/yls-sm-1-10-kw.

97. OFFSHORE ENERGY. TWI to Develop Underwater Laser Cutting for Decommissioning: Offshore Energy; 2017 [Available from: https://www.offshore-energy.biz/twi-to-develop-underwater-laser-cutting-for-decommissioning/.

98. Campanella B, Legnaioli S, Pagnotta S, Poggialini F, Palleschi V. Shock Waves in Laser-Induced Plasmas. Atoms. 2019;7(2):57.

99. Nejad S, Mirsaeidi M. Altitude measurement using laser beam reflected from water surface. Iranian Journal of Electrical and Electronic Engineering. 2005;1.

100. Mullick S, Madhukar YK, Roy S, Nath A. Development of a Water-Jet Assisted Underwater Laser Cutting Process. International Journal of Industrial and Manufacturing Engineering. 2013;7(4):365.

101. Mullick S, Madhukar YK, Roy S, Kumar S, Shukla DK, Nath AK. Development and parametric study of a water-jet assisted underwater laser cutting process. International Journal of Machine Tools and Manufacture. 2013;68:48-55.

102. Mullick S, Madhukar YK, Kumar S, Shukla DK, Nath AK. Temperature and intensity dependence of Yb-fiber laser light absorption in water. Journal of the Optical Society of America 2011;50(34):6319-26.

103. Glova AF, Lysikov AY. Drilling and cutting of thin metal plates in water with radiation of a repetitively pulsed Nd : YAG laser. Quantum Electronics. 2011;41(10):906.

104. Kundu PK, Cohen IM, Dowling DR. Chapter 15 - Compressible Flow. Fluid Mechanics (Sixth Edition). Boston: Academic Press; 2016. p. 819-79.

105. Anderson JD. Fundamentals of Aerodynamics: McGraw–Hill; 2007.

106. Kundu PK. Fluid mechanics. 4th ed. Cohen IM, editor: Academic Press; 2008.

107. Babu V. Fundamentals of gas dynamics. 2nd ed. Chichester, West Sussex, United Kingdom: John Wiley & Sons Ltd; 2015.

108. Dassault Systèmes. SOLIDWORKS Dassault Systèmes SolidWorks Corporation; 2019 [Available from: https://www.solidworks.com/.

109. Das P, Khan MMK, Saha SC, Rasul MG. Chapter 6 - Numerical Study of Flow Through a Reducer for Scale Growth Suppression. In: Khan MMK, Hassan NMS, editors. Thermofluid Modeling for Energy Efficiency Applications: Academic Press; 2016. p. 119-48.

110. Roache P. Perspective: A Method for Uniform Reporting of Grid Refinement Studies. Journal of Fluids Engineering. 1994;116:405-13.

111. Sakri F, Mat A, Mohamed S, Salim S. Computational investigations and grid refinement study of 3D transient flow in a cylindrical tank using OpenFOAM. AEROTECH VI - Innovation in Aerospace Engineering and Technology; 10/01; Kuala Lumpur, Malaysia: IOP Publishing; 2016.

112. ANSYS. Reporting Mesh Statistics: ANSYS, Inc; 2008 [Available from: https://romeo.univ-reims.fr/documents/fluent/tgrid/ug/chp15.pdf.

113. ANSYS. Convective Flux Types: ANSYS, Inc; 2009 [Available from: https://www.afs.enea.it/project/neptunius/docs/fluent/html/ug/node790.htm .

114. ANSYS. Overview of Using the Solver: ANSYS, Inc; 2009 [Available from: https://www.afs.enea.it/project/neptunius/docs/fluent/html/ug/node776.htm .

115. Eymard R, Gallouët T, Herbin R. Finite Volume Methods. In: Lions JL, Philippe C, editors. Solution of Equation in ℝn (Part 3), Techniques of Scientific Computing (Part 3). Handbook of Numerical Analysis. 7: Elsevier; 2000. p. 713-1020.

116. ANSYS. Evaluation of Gradients and Derivatives: ANSYS, Inc; 2009 [Available from: https://www.afs.enea.it/project/neptunius/docs/fluent/html/th/node368.htm.

117. ANSYS. 26.4.1 Changing the Courant Number: ANSYS, Inc; 2009 [Available from: https://www.afs.enea.it/project/neptunius/docs/fluent/html/ug/node789.htm .

118. ANSYS. 26.3.2 Setting Under-Relaxation Factors: ANSYS, Inc; 2009 [Available from: https://www.afs.enea.it/project/neptunius/docs/fluent/html/ug/node786.htm .

119. Dai Z, Wang B, Qi L, Shi H. Experimental study on hydrodynamic behaviors of high-speed gas jets in still water. Acta Mechanica Sinica. 2006;22(5):443.

120. Förster FJ, Baab S, Steinhausen C, Lamanna G, Ewart P, Weigand B. Mixing characterization of highly underexpanded fluid jets with real gas expansion. Experiments in Fluids. 2018;59(3):44.

121. Yang Q, Gustavsson H. Erosion of refractory during gas injection : a cavitation based model. Scandinavian journal of metallurgy. 1990;19(3):127-37.

122. Chang IJ, Judd S. Air sparging of a submerged MBR for municipal wastewater treatment. Process Biochemistry. 2002;37(8):915-20.

123. Matsumoto O, Sugihara M, Miya K. Underwater Cutting of Reactor Core Internals by CO Laser Using Local-Dry-Zone Creating Nozzle. Journal of Nuclear Science and Technology. 1992;29(11):1074 -9.

124. Rensen J, Roig V. Experimental study of the unsteady structure of a confined bubble plume. International Journal of Multiphase Flow. 2001;27(8):1431-49.

125. Curcio JA, Petty CC. The Near Infrared Absorption Spectrum of Liquid Water. Journal of the Optical Society of America 1951;41(5):302-4.

126. Zhang X, Ashida E, Shono S, Matsuda F. Effect of shielding conditions of local dry cavity on weld quality in underwater Nd:YAG laser welding. Journal of Materials Processing Technology. 2006;174(1):34-41.

127. Oh SY, Shin JS, Park S, Kim TS, Park H, Lee L, Lee J. Underwater laser cutting of thick stainless steel blocks using single and dual nozzles. Optics & Laser Technology. 2021;136.

128. Tang Y, Li S. Research into the characteristics of horizontal gaseous jets underwater. Journal of Vibroengineering. 2016;18:4678-91.

129. Miaosheng H, Lizi Q, Yu L. Oscillation Flow Induced by Underwater Supersonic Gas Jets from a Rectangular Laval Nozzle. Procedia Engineering. 2015;99:1531-42.

130. Shi H, Wang B, Dai Z. Research on the mechanics of underwater supersonic gas jets. Science China Physics, Mechanics and Astronomy. 2010;53(3):527-35.

131. Wei J, Ma J, Fan Y, Yu N, Yang S, Xiang S. Back-attack Phenomena of Gas Jets with Submerged Horizontally Blowing and Effects on Erosion and Wear of Refractory Lining. ISIJ International. 1999;39(8):779-86.

132. Shi HH, Wang BY, Qi L. A submerged supersonic gas jet (in Chinese). 7th Natl Congr on Hydrodynamics and 19th Natl Symp on Hydrodynamics; 2005; Beijing: Ocean Press.

133. Wang BY, Dai ZQ, Qi LX, Shi HH. Experimental study on back-attack phenomenon in underwater supersonic gas jets. Chinese Journal of Theoretical and Applied Mechanics 2007;39((2)):267–72 (in Chinese).

134. Tang J, Li S, Wang N, Wei Y, Shyy W. Flow Structures of Gaseous Jet Injected into Liquid for Underwater Propulsion. 46th AIAA/ASME/SAE/ASEE Joint Propulsion Conference & Exhibit2010.

135. Ferziger JH, Perić M. Introduction to Numerical Methods. Computational Methods for Fluid Dynamics. Berlin, Heidelberg: Springer Berlin Heidelberg; 2002. p. 21-37.

136. Zhang X, Li S, Yang B, Wang N. Flow structures of over-expanded supersonic gaseous jets for deep-water propulsion. Ocean Engineering. 2020;213:107611.

137. Tang Y, Li S. Numerical simulation of the relationship between underwater jets oscillation and shock wave. Journal of Vibroengineering. 2017;19.

138. Chida I, Okazaki K, Shima S, Kurihara K, Yuguchi Y, Sato I. Underwater cutting technology of thick stainless steel with YAG laser. 2003.

139. Sherwin KH, M. Thermofluids: Springer US; 2013.

140. Alfille JP, Pilot G, De Prunele D. New pulsed YAG laser performances in cutting thick metallic materials for nuclear applications. Lasers, Optics, and Vision for Productivity in Manufacturing I; Besancon, France: Society of Photo-Optical Instrumentation Engineers 1996.

141. Singh R, Choubey A, Jain RK, Agrawal DK, Vishwakarma SC, Ali S, Ganesh P, Kaul R, Upadhyaya BN, Oak SM. A comparative study of heat affected zone and cut quality in underwater laser cutting of mild steel and stainless steel. National Laser Symposium (NLS-22); Manipal, India: Indian Laser Association; 2014.

142. Microsoft Corporation. Microsoft Excel: Microsoft Corporation; 2018 [Available from: https://www.microsoft.com/en-gb/p/excel-mobile/9wzdncrfjbh3.

143. Shin JS, Oh, Seong Yong., Park, Hyunmin., Kim, Taek-Soo., Lee, Lim., Chung, Chin-Man & Lee, Jonghwan. Underwater cutting of 50 and 60 mm thick stainless steel plates using a 6-kW fiber laser for dismantling nuclear facilities. Optics & Laser Technology. 2019;115:1-8.

144. Sommer B, Fowler AM, Macreadie PI, Palandro DA, Aziz AC, Booth DJ. Decommissioning of offshore oil and gas structures – Environmental opportunities and challenges. Science of The Total Environment. 2019;658:973-81.

145. MathWorks. MATLAB: The MathWorks, Inc.; 2021 [Available from: https://uk.mathworks.com/products/new_products/release2017a.html.

146. Seme B, Schneider F. Cutting. In: Poprawe R, editor. Tailored Light 2: Laser Application Technology. Berlin, Heidelberg: Springer Berlin Heidelberg; 2011. p. 395-426.

147. Powell J, Ivarson A, Magnusson C. An energy balance for inert gas laser cutting. ICALEO® '93: Proceedings of the Laser Materials Processing Conference; Orlando, Florida, USA: Journal of Laser Applications; 1993.

148. Brimblecombe P, Campbell PGC, Harrison RM. Air Composition and Chemistry: Cambridge University Press; 1996.

149. Ahmadi B, Torkamany MJ, Jaleh B, Sabaghzadeh J. Theoretical Comparison of Oxygen Assisted Cutting by CO2 and Yb: YAG Fiber Lasers. Chinese Journal of Physics. 2009;47(4).

150. Milovanović V, Živković M, Jovičić G, Dišić A. Experimental determination of fatigue properties and fatigue life of S355J2+N steel grade. Materials Today: Proceedings. 2019;12:455-61.

151. Fittings RP. EN 10025 S355 J2+N Steel Grade Plate, S355J2 N Structural Steel Plates Suppliers, EN 10025 S355J2+N High Tensile Steel Plates Stockists, EN10025 S355J2 N Low Alloy Steel Plates in Vadodara, EN 10025 S355 J2+N Steel Grade Plate Supplier in Godavari, S355J2 N Carbon steel Plate in Gujarat, India 2018

[Available from: https://www.hicplates.com/en-10025-s355j2-n-plates-supplier-stockist.html#specification.

152. Mullick S, Madhukar YK, Subhransu R, Nath AK. An investigation of energy loss mechanisms in water-jet assisted underwater laser cutting process using an analytical model. International Journal of Machine Tools and Manufacture. 2015;91:62-75.

153. Li CF, Johnson DB, Kovacevic R. Modelling of heat transfer in waterjet guided laser drilling of silicon. Proceedings of the Institution of Mechanical Engineers, Part B: Journal of Engineering Manufacture. 2003;217(5):583-600.

154. Mullick S, Madhukar YK, Roy S, Nath AK. Performance optimization of water-jet assisted underwater laser cutting of AISI 304 stainless steel sheet. Optics and Lasers in Engineering. 2016;83:32-47.

155. McLean D. Understanding Aerodynamics: Arguing from the Real Physics. Chichester, West Sussex, United Kingdom: John Wiley & Sons; 2012.

156. McDavid RM. Macroscopic Modeling. In: Buschow KHJ, Cahn RW, Flemings MC, Ilschner B, Kramer EJ, Mahajan S, Veyssière P, editors. Encyclopedia of Materials: Science and Technology. Oxford: Elsevier; 2001. p. 4720-32.

157. Katopodes ND. Chapter 13 - Level Set Method. In: Katopodes ND, editor. Free-Surface Flow: Butterworth-Heinemann; 2019. p. 804-28.

158. ANSYS. 4.11 Large Eddy Simulation (LES) Model: ANSYS, Inc; 2009 [Available from: https://www.afs.enea.it/project/neptunius/docs/fluent/html/th/node93.htm.

159. Bai X, Cheng H, Ji B. LES Investigation of the noise characteristics of sheet and tip leakage vortex cavitating flow. International Journal of Multiphase Flow. 2022;146:103880.

160. ANSYS. 16.2.1 Approaches to Multiphase Modeling: ANSYS, Inc; 2009 [Available from: https://www.afs.enea.it/project/neptunius/docs/fluent/html/th/node293.htm.

161. ANSYS. Ansys Fluent Multiphase Flow Modeling: Ansys, Inc; 2020 [Available from: https://www.ansys.com/services/training-center/fluids/ansys-fluent-multiphase-flow-modeling.

162. ANSYS. 6.2.2 Mesh Quality Online: ANSYS, Inc; 2009 [Available from: https://www.afs.enea.it/project/neptunius/docs/fluent/html/ug/node167.htm .

163. Engineering ToolBox. Surface Tension of Water in contact with Air 2004 [Available from: https://www.engineeringtoolbox.com/water-surface-tension-d_597.html.

164. ANSYS. Pressure-Velocity Coupling: ANSYS, Inc; 2009 [Available from: https://www.afs.enea.it/project/neptunius/docs/fluent/html/th/node373.htm.

165. ANSYS. Choosing the Pressure-Velocity Coupling Method: ANSYS, Inc; 2009 [Available from: https://www.afs.enea.it/project/neptunius/docs/fluent/html/ug/node785.htm .

166. ANSYS. Discretization of the Momentum Equation: ANSYS, Inc; 2009 [Available from: https://www.afs.enea.it/project/neptunius/docs/fluent/html/th/node371.htm.

167. ANSYS. User Inputs for Time-Dependent Problems: ANSYS, Inc; 2009 [Available from: https://www.afs.enea.it/project/neptunius/docs/fluent/html/ug//node807.htm#:~:text=The%20First%20Order%20Implicit%20formulation,moving%20waves%2C%20such%20as%20shocks.

168. Abramoff MD, Magalhaes PJ, Ram SJ. Image Processing with ImageJ. Biophotonics International. 2004;11(7): 36-42.

169. Gong Z, Lu C, Li J, Cao J. The gas jet behavior in submerged Laval nozzle flow. Journal of Hydrodynamics. 2017;29(6):1035-43.

170. Oh SY, Shin JS, Park S, Kim TS, Park H, Lee L, Lee J. Underwater laser cutting of thick stainless steel blocks using single and dual nozzles. Optics & Laser Technology. 2020:106757.

171. Enterfea. 2D vs 3D Finite Element Analysis (with examples) 2021 [Available from: https://enterfea.com/2d-vs-3d-finite-element-analysis/.

172. Jirka GH. Integral Model for Turbulent Buoyant Jets in Unbounded Stratified Flows. Part I: Single Round Jet. Environmental Fluid Mechanics. 2004;4(1):1-56.

173. Davidson MJ, Pun KL. Hybrid model for prediction of initial dilutions from outfall discharges. Journal of Hydraulic Engineering. 1998;124(12):1188-97.

174. Miyahara T, Haga N, Takahashi T. BUBBLE FORMATION FROM AN ORIFICE AT HIGH GAS FLOW RATES. International chemical engineering. 1983;23(3):524-31.

Appendices

Appendix A

Figure 104 shows the Mach number distribution of a gas jet expansion model in air:
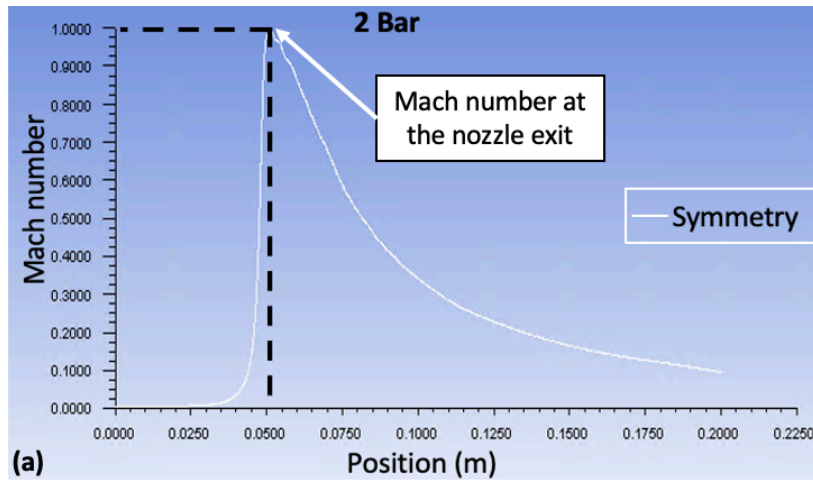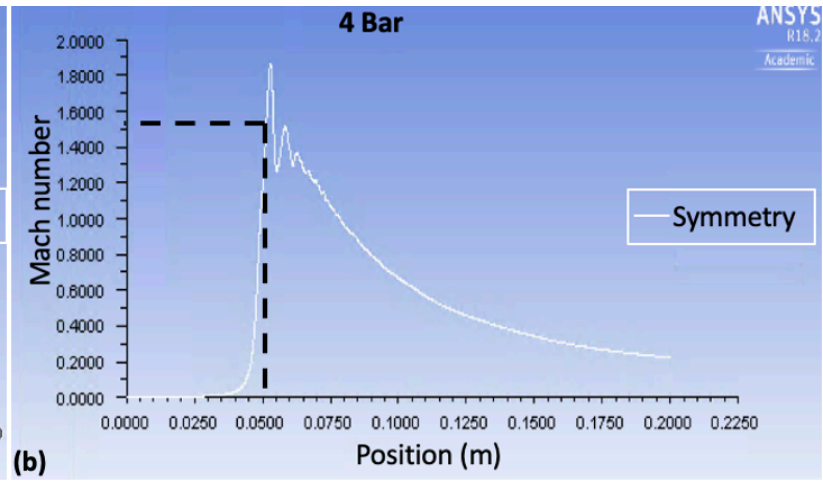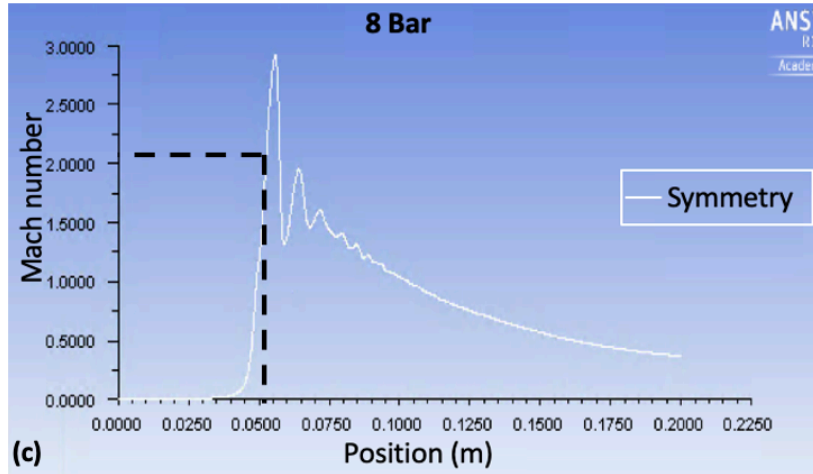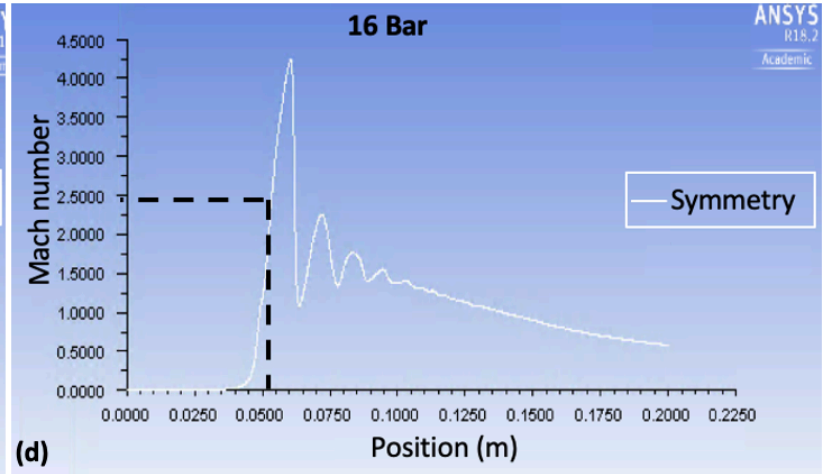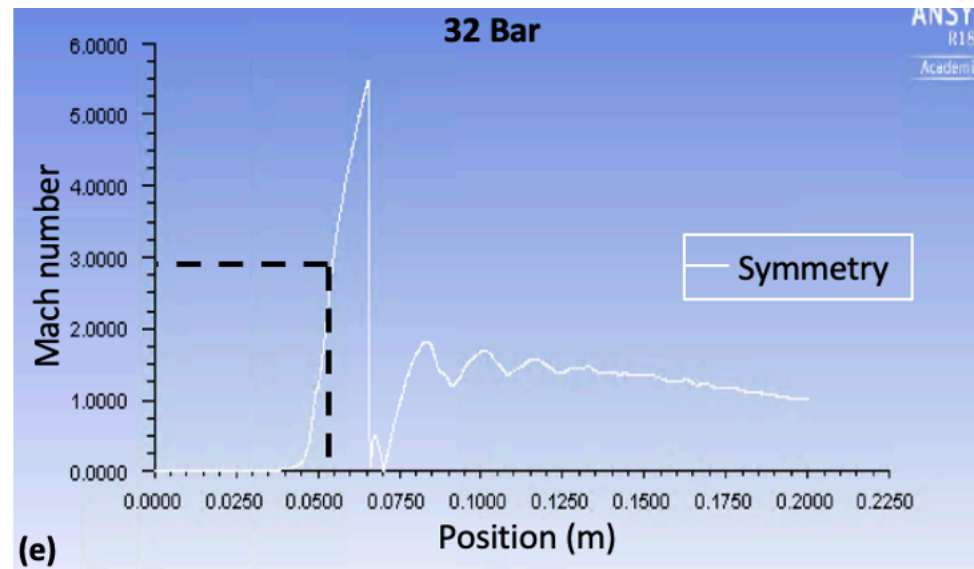
Figure 104: Mach number with the corresponding x-value position at an inlet pressure of (a) 2, (b) 4, (c) 8, (d) 16 and (e) 32 bar. The dotted line shows the Mach number at the nozzle exit.

Appendix B

MATLAB code for the process performance in conventional fibre laser cutting:

```matlab
%%% MODEL FOR LASER CUTTING IN AIR %%%
%%% Power must be balanced such that POWER ON THE LEFT=POWER ON THE
RIGHT %%%
%%% OBJECTIVE IS TO PLOT CUT THICKNESS AT DIFFERENT CUTTING SPEEDS %%%

%%----------------------------------CLEAR EVERYTHING--------------------------------------%%

close all
clear variables
clc

%%-----------------------------------------ALL VARIABLES------------------------------------------%%

syms d positive;                    %%Defining unknown variable of maximum cut
thickness d  (m)

b_c=0.0015;                    %%The average measured cut kerf width (m)
v_c=[50/60000:50/60000:1000/60000];    %%The cutting velocity (m/s)
ro_density=7850;          %%Density of S355J2+N mild steel (kg/m^3)
c_p=480;                %%Specific heat capacity of S355J2+N mild steel(460-480)(J/kgK)
T_p=2000;              %%The process temperature of mild steel(K)
T_infinity=293;         %%The ambient temperature (K)
H_m =205000;            %%The specific enthalpy of fusion of mild steel(205-281) (J/kg)
T_m=1780;               %%Melting temperature of mild steel(1537-1780) (K)
K=40;               %%Thermal conductivity of mild steel (36-54 depending on carbon
content)(W/mK)
k=8e-6;           %%Thermal diffusivity of mild steel (m^2/s)
[k=K/(c_p*ro_density)]
H_feo=4800000*0.209;      %%The reaction enthalpy of mild steel for oxygen (J/kg)
A=0.8;               %%Absorption (setting absorption to 80% of incident laser beam)
P_l_10=10000;          %%Laser Power at 10 KW (W)
P_l_5=5000;           %%Laser Power at 5 KW (W)

%%Velocities and Peclet numbers%%
v_diff=0.0078;                                  %%Diffusion velocity of mild steel
Pe_diff=v_diff/((2*k)/b_c);                     %%Peclet number at diffusion
velocity
Pe_min=2*(((H_feo-H_m)/((T_m-T_infinity)*c_p))-1)^(-1.5625);      %%Minimum
Peclet number
v_c_min=((2*k)/b_c)*Pe_min;                         %%Minimum autogen cutting
speed
```

```matlab
%%Burn off - the mass ratio of iron reacting in the kerf
X_abbr_diff=0.57;       %%Burn off of P_abs + diffusion-limited combustion capacity P_r
X_abbr_max=1;          %%%Maximum burn-off of 100%
% X_abbr=(c_p/H_feo)*((T_p-T_infinity)+(H_m/c_p)+((T_m-T_infinity).*(Pe(i)/2).^(-0.64)));     %%%Burn off

%%------------------------Calculate velocity in power balance equation----------------%%

for i = 1:length(v_c)

Pe(i)=(v_c(i)*b_c)/(2*k);       %%Peclet number

%%-----------------------------------RIGHT HAND SIDE------------------------------------%%
%%%POWER FOR HEATING THE LIQUID MATERIAL TO SURFACE TEMPERATURE, MELTING AND CONDUCTION
P_MW(i)=2*K*d*(T_p-T_infinity+(H_m/c_p)).*Pe(i);       %%%Melting and heating power WITH PECLET NUMBER (W)

P_hl(i)=4*K.*d*((T_m-T_infinity).*(Pe(i)/2).^0.36);     %%%Thermal leakage power/Conduction (W)

P_right(i)=4*K.*d*((T_p-T_infinity+(H_m/c_p)).*(Pe(i)/2)+ (T_m-T_infinity).*(Pe(i)/2).^0.36);    %%%Total power on the right hand side (W)

disp('TOTAL POWER ON THE RIGHT HAND SIDE')
disp(vpa(P_right(i)));                   %%% Display velocity expression of POWER ON THE RIGHT

%%----------------------------------------LEFT HAND SIDE------------------------------------%%
%%%POWER DUE TO ABSORPTION OF LASER BEAM AND REACTION ENERGY BY EXOTHEMAL OXIDATION

%P_r=ro_density*b_c*d*v_c_max*H_feo*X_abbr;  %%Power arising from the iron combustion
%P_r=2.*Pe*(K/c_p)*d*H_feo.*X_abbr;         %%Power arising from the iron combustion at diffusion-limited combustion capacity (W)
P_r = @(d) (2*Pe(i)*(K/c_p).*d*H_feo*X_abbr_max).*(d>0 & d<0.02)+(ro_density*b_c.*d*v_diff*H_feo*X_abbr_max).*(d>0.02 & d<0.05);   %%Power arising from the iron combustion at diffusion-limited combustion capacity (W)

P_abs=A*P_l_10;               %%Absorbed power for 10 kW (W)
P_abs_1=A*P_l_5;              %%Absorbed power for 5 kW(W)

P_left(i)=P_abs+P_r(i);        %%Velocity expression of power on the left (W)
P_left_1(i)=P_abs_1+P_r(i);      %%Velocity expression of power on the left (W)
```

```matlab
disp('TOTAL POWER ON THE LEFT HAND SIDE')
disp(vpa(P_left(i)));                    %% Display velocity expression of POWER ON THE
RIGHT

%%--------------------------------POWER BALANCE EQUATION----------------------------%%

POWER_BALANCE(i)=P_left(i)-P_right(i)==0;            %%% POWER BALANCE
EQUATION (W)
POWER_BALANCE_1(i)=P_left_1(i)-P_right(i)==0;        %%% POWER BALANCE
EQUATION (W)

disp('TOTAL POWER BALANCE EQUATION')
disp(vpa(POWER_BALANCE(i)));             %%% Display velocity expression of
POWER ON THE RIGHT

%%----------CALCULATE VELOCITY FROM POWER BALANCE EQUATION-----------%%

Thickness(i) = vpasolve(POWER_BALANCE(i), d);        %%% Calculate velocity from
power balance equation
Thickness_1(i) = vpasolve(POWER_BALANCE_1(i), d);    %%% Calculate velocity
from power balance equation


disp('Thickness in (m) is')
disp(vpa(Thickness(i)));                 %%% Display thickness VALUE in (m)

end

%%----------EXPERIMENT MAX CUT THICKNESS VS CUTTING SPEED AT 10 KW-------%%

v_exp_10=[50 100 200 400 600 800 1000];
d_exp_10=[70 58 40.81 27.01 23.1 20.83 18.5];     %%% focus position -15 stand-off
10 mm

d_exp_1=[70 60 42.03 30.03 22.25 19.01 15.1];  %%% focus position -15 stand-off 10
mm

%%-------EXPERIMENT MAX CUT THICKNESS VS CUTTING SPEED AT 5 KW-----------%%

v_exp_5=[50 100 200 400 600 800 1000];
d_exp_5=[47.5 40.4 25.9 18.3 14.1 11.3 8.8];

%%----------------PLOT MAX CUT THICKNESS VS CUTTING SPEED---------------%%

figure;
```

```matlab
p1=plot(v_c*60000,Thickness*1000,'b');
xlim([0 1000])
ylim([0 100])

hold on

p2=plot(v_exp_10,d_exp_10,'o','color',[0.67,0.84,0.9],'MarkerSize',7,
'Markerfacecolor',[0,0.5,1]);

p3=plot(v_c*60000,Thickness_1*1000,'k');

p4=plot(v_exp_5,d_exp_5,'+', 'Color',[0.5,0.5,0.5],'MarkerSize',7);

grid on
xlabel('Maximum cutting speed [mm/min]')
ylabel('Maximum cut thickness [mm]')

hold off

leg1=legend([p1 p2 p3 p4],{'10 kW - Theoretical','10 kW - Experimental', '5 kW -
Theoretical','5 kW - Experimental'},'Location','northeast', 'FontSize',12);
set(leg1,'Box','off')
```

Appendix C

MATLAB code for the process performance in underwater fibre laser cutting:

```
%%% MODEL FOR UNDERWATER LASER CUTTING FOR THE CUTTING TRIALS IN A 1M^3
TANK %%%
%%% Power must be balanced such that POWER ON THE LEFT=POWER ON THE
RIGHT %%%
%%% OBJECTIVE IS TO PLOT CUT THICKNESS AT DIFFERENT CUTTING SPEEDS %%%

%%-----------------------------------CLEAR EVERYTHING--------------------------------------%%

close all
clear variables
clc

%%-----------------------------------ALL VARIABLES--------------------------------------%%

syms d positive;          %%Defining unknown variable of maximum cut thickness d  (m)

b_c=0.00175;                     %%The average measured cut kerf width (m)
v_c=[50/60000:50/60000:1000/60000];    %%The cutting velocity (m/s)
ro_density=7850;         %%Density of C-Mn steel (kg/m^3)
c_p=500;                 %%Specific heat capacity of C-Mn steel(490-510)(J/kgK)
T_p=2000;                %%The process temperature of mild steel(K)
T_infinity=293;          %%The ambient temperature (K)
H_m =250000;             %%The specific enthalpy of fusion of C-Mn steel(205-281) (J/kg)
T_m=1780;                %%Melting temperature of C-Mn steel(1537-1780) (K)
K=40;                    %%Thermal conductivity of C-Mn steel (36-54 depending on carbon
content)(W/mK)
k=8e-6;                  %%thermal diffusivity of C-Mn steel (m^2/s)   [k=K/(c_p*ro_density)]
H_feo=4800000*0.209;     %%The reaction enthalpy of mild steel for oxygen (J/kg)

n_d=0.0035;         %% Nozzle diameter (m)
u=583.1;                 %% Air flow speed (Mach 1.7) at 8 bar simulations in numerical
model (m/s)
T_l=T_p;            %%Inclination temperature (K)

%%%CHANGE POWER TO PLOT GRAPH%%%

A=0.8;              %%Absorption
P_l=10000;               %%Laser Power at 10 KW (W)
P_l_1=8000;              %%Laser Power at 8 KW (W)
P_l_2=6000;              %%Laser Power at 6 KW (W)
P_l_3=4000;              %%Laser Power at 4 KW (W)

%%Velocities and Peclet numbers%%
```

```matlab
v_diff=0.0078;                          %%Diffussion velocity of mild steel
Pe_diff=v_diff/((2*k)/b_c);             %%Peclet number at diffusion velocity
Pe_min=2*(((H_feo-H_m)/((T_m-T_infinity)*c_p))-1)^(-1.5625);    %%Minimum
Peclet number
v_c_min=((2*k)/b_c)*Pe_min;             %%Minimum autogen cutting
speed


%%Burn off - the mass ratio of iron reacting in the kerf
X_abbr_diff=0.57;       %%Burn off of P_abs + diffusion-limited combustion capacity
P_r
X_abbr_max=1;           %%%Maximum burn-off of 100%
% X_abbr=(c_p/H_feo)*((T_p-T_infinity)+(H_m/c_p)+((T_m-T_infinity).*(Pe(i)/2).^(-
0.64)));    %%%Burn off


%%% Underwater conduction variables
d_sp=0.0015;            %% Beam spot diameter at the back of the workpiece
calculated from the beam profile (see Experimental data)
n=60000;                %% Constant term which depends on the temperature
distribution in the radial direction


%%% Underwater forced convection variables (values of different thermo-physical
properties of water found at
https://onlinelibrary.wiley.com/doi/pdf/10.1002/9781118534892.app2 )


K_w=0.5861;     %%% Thermal conductivity of water at 20 degrees (W/m K)
Pr_w=7.152;     %%% Prandtl number of water at 20 degrees
d_v=0.001002;   %%% dynamic viscosity of water at 20 degrees (Pa s)
p_w=998.2;      %%% the density of water at 20 degrees (kg/m3)
Re_w=(p_w*u*n_d)/d_v;       %%% Reynolds number of air/water mixture



%%--------------------Calculate velocity in power balance equation-------------------%%


for i = 1:length(v_c)

Pe(i)=(v_c(i)*b_c)/(2*k);      %%Peclet number
%%-----------------------------------------RIGHT HAND SIDE-------------------------------------
%%
%%%POWER FOR HEATING THE LIQUID MATERIAL TO SURFACE TEMPERATURE,
MELTING AND CONDUCTION
P_MW(i)=2*K*d*(T_p-T_infinity+(H_m/c_p)).*Pe(i);       %%%Melting and heating
power expressed in terms of the peclet number (W) reduced by 40% underwater

P_hl(i)=4*K.*d*((T_m-T_infinity).*(Pe(i)/2).^0.36);     %%%Thermal leakage
power/Conduction (W) reduced by 30% underwater
```

```matlab
Th_diff=2*sqrt ((K*d_sp)./(ro_density*c_p.*v_c(i)));     %%% A function of laser
interaction time
q_s=(K*(T_m-T_infinity))./(n*Th_diff);               %%% Rate of conduction loss to the
base of the material

H_c=0.797*1e-8*(K_w/b_c)*Re_w^0.5*Pr_w^0.33;          %%%Forced convection
heat transfer and the convective heat transfer coefficient
q_w=H_c*(T_l-T_infinity);               %%%The rate of convective heat loss from the
surface of molten layer

% P_right(i)=0.8*4*K.*d*((T_p-T_infinity+(H_m/c_p)).*(Pe(i)/2)+ (T_m-
T_infinity).*(Pe(i)/2).^0.36);     %%%Total power on the right hand side (W)
P_right(i)=P_MW(i)+P_hl(i)+q_s+q_w;
disp('TOTAL POWER ON THE RIGHT HAND SIDE AT 10 KW')
disp(vpa(P_right(i)));               %%% Display velocity expression of POWER ON
THE RIGHT

%%-------------------------------------------LEFT HAND SIDE------------------------------------
%%
%%%POWER DUE TO ABSORPTION OF LASER BEAM AND REACTION ENERGY BY
EXOTHEMAL OXIDATION

%P_r=ro_density*b_c*d*v_c_max*H_feo*X_abbr;  %%Power arising from the iron
combustion
%P_r=2.*Pe*(K/c_p)*d*H_feo.*X_abbr;        %%Power arising from the iron
combustion at diffusion-limited combustion capacity (W)
P_r = @(d) (2*Pe(i)*(K/c_p).*d*H_feo*X_abbr_max).*(d>0 &
d<0.02)+(0.21*ro_density*b_c.*d*v_diff*H_feo*X_abbr_max).*(d>0.02 & d<0.05);
%%Power arising from iron combustion at diffusion-limited combustion capacity
from AIR with 21%oxygen) (W)

P_abs=A*P_l;                %%Absorbed power (W)

P_left(i)=P_abs+P_r(i);         %%Velocity expression of power on the left (W)

disp('TOTAL POWER ON THE LEFT HAND SIDE')
disp(vpa(P_left(i)));           %% Display velocity expression of POWER ON THE RIGHT

%%-----------------------------POWER BALANCE EQUATION----------------------------%%

POWER_BALANCE(i)=P_left(i)-P_right(i)==0;          %%% POWER BALANCE
EQUATION (W)

disp('TOTAL POWER BALANCE EQUATION')
disp(vpa(POWER_BALANCE(i)));               %%% Display velocity expression of
POWER ON THE RIGHT
```

```matlab
%%-------------CALCULATE VELOCITY FROM POWER BALANCE EQUATION-------------%%

Thickness(i) = vpasolve(POWER_BALANCE(i), d);          %%% Calculate velocity from
power balance equation

disp('Thickness in (mm) is')
disp(vpa(Thickness(i)));                %%% Display velocity VALUE in (m/min)

end

%%--------------EXPERIMENT MAX CUT THICKNESS VS CUTTING SPEED----------------%%

v_exp=[125 150 200 400 600 800 1000];
d_exp=[50 48.54 39.22 26.84 20.91 17.73 15.43];

%%---------------------PLOT MAX CUT THICKNESS VS CUTTING SPEED----------------%%

figure;
p1=plot(v_c*60000,Thickness*1000,'color','k');

xlim([0 1000])
ylim([0 50])

hold on

p2=plot(v_exp,d_exp, 'o', 'MarkerFaceColor','b');

grid on
xlabel('Maximum cutting speed [mm/min]')
ylabel('Maximum cut thickness [mm]')
%title('Maximum cut thickness with the corresponding cutting speed')

hold off

leg1=legend([p1 p2],{'Theoretical','Experimental'},'Location','northeast',
'FontSize',14);
set(leg1,'Box','off')
```

Appendix D

MATLAB code for the kerf width generated in underwater fibre laser cutting:

```
%%% MODEL FOR UNDERWATER LASER CUTTING FOR THE PRELIMINARY CUTTING
TRIALS %%%
%%% Power must be balanced such that POWER ON THE LEFT=POWER ON THE
RIGHT %%%
%%% OBJECTIVE IS TO PLOT CUT THICKNESS AT DIFFERENT CUTTING SPEEDS %%%

%%-----------------------------------CLEAR EVERYTHING--------------------------------------%%

close all
clear variables
clc

%%----------------------------------ALL VARIABLES----------------------------------------%%

syms b_c positive;              %%Defining unknown variable of maximum cut
thickness b_c  (m)

d=0.01;                  %% Thickness (m)
v_c=[125/60000:25/60000:1000/60000];    %%The cutting velocity (m/s)
ro_density=7850;         %%Density of C-Mn steel (kg/m^3)
c_p=510;                 %%Specific heat capacity of C-Mn steel(490-510)(J/kgK)
T_p=2000;                %%The process temperature of mild steel(K)
T_infinity=293;          %%The ambient temperature (K)
H_m =280000;             %%The specific enthalpy of fusion of C-Mn steel (205-281)
(J/kg)
T_m=1780;                %%Melting temperature of C-Mn steel(1537-1780) (K)
K=54;                    %%Thermal conductivity of C-Mn steel (36-54 depending on carbon
content)(W/mK)
k=8e-6;                  %%thermal diffusivity of C-Mn steel (m^2/s)
[k=K/(c_p*ro_density)]
H_feo=4800000*0.209;     %%The reaction enthalpy of mild steel for oxygen (J/kg)

n_d=0.0035;              %% Nozzle diameter (m)
u=583.1;                 %% Air flow speed (Mach 1.7) at 8 bar simulations in numerical
model (m/s)
T_l=T_p;                 %%Inclination temperature (K)
A=0.3;                   %%Absoption
%%%CHANGE POWER TO PLOT GRAPH%%%
P_l=10000;               %%Laser Power at 10 KW (W)

%%Velocities and Peclet numbers%%
v_diff=0.0078;                              %%Diffussion velocity of mild steel
Pe_diff=v_diff/((2*k)/b_c);                 %%Peclet number at diffusion
velocity
```

```matlab
Pe_min=2*(((H_feo-H_m)/((T_m-T_infinity)*c_p))-1)^(-1.5625);        %%Minimum
Pe clet number
v_c_min=((2*k)/b_c)*Pe_min;                              %%Minimum autogen cutting
speed

%%Burn off - the mass ratio of iron reacting in the kerf
X_abbr_diff=0.57;        %%Burn off of P_abs + diffusion-limited combustion capacity
P_r
X_abbr_max=1;           %%%Maximum burn-off of 100%
% X_abbr=(c_p/H_feo)*((T_p-T_infinity)+(H_m/c_p)+((T_m-T_infinity).*(Pe(i)/2).^(-
0.64)));     %%%Burn off

%%% Underwater conduction variables
d_sp=0.0013;            %% Beam spot diameter calculated from the beam profile (see
Experimental data) (beam waist diameter at a thickness of 6 mm)
n=60000;                %% Constant term which depends on the temperature
distrubution in the radial direction


%%% Underwater forced convection variables (values of different thermo-physical
properties of water found at
https://onlinelibrary.wiley.com/doi/pdf/10.1002/9781118534892.app2 )

K_w=0.5861;       %%% Thermal conductivity of water at 20 degrees (W/m K)
Pr_w=7.152;       %%% Prandtl number of water at 20 degrees
d_v=0.001002;     %%% dynamic viscosity of water at 20 degrees (Pa s)
p_w=998.2;        %%% the density of water at 20 degrees (kg/m3)
Re_w=(p_w*u*n_d)/d_v;         %%% Reynolds number of air/water mixture


%%--------------------Calculate velocity in power balance equation-------------------%%

for i = 1:length(v_c)

Pe(i)=(v_c(i)*b_c)/(2*k);       %%Peclet number

%%----------------------------------------RIGHT HAND SIDE------------------------------------%%

%%%POWER FOR HEATING THE LIQUID MATERIAL TO SURFACE TEMPERATURE,
MELTING AND CONDUCTION
P_MW(i)=2*K*d*(T_p-T_infinity+(H_m/c_p)).*Pe(i);        %%%Melting and heating
power expressed in terms of the peclet number (W) reduced by 40% underwater

P_hl(i)=4*K.*d*((T_m-T_infinity).*(Pe(i)/2).^0.36);       %%%Thermal leakage
power/Conduction (W) reduced by 30% underwater
```

```matlab
Th_diff=2*sqrt ((K*d_sp)./(ro_density*c_p.*v_c(i)));     %%% A function of laser
interaction time
q_s=(K*(T_m-T_infinity))./(n*Th_diff);               %%% Rate of conduction loss to the
base of the material

H_c=0.797*1e-8*(K_w/b_c)*Re_w^0.5*Pr_w^0.33;         %%%Forced convection
heat transfer and the convective heat transfer coefficient
q_w=H_c*(T_l-T_infinity);             %%%The rate of convective heat loss from the
surface of molten layer

% P_right(i)=0.8*4*K.*d*((T_p-T_infinity+(H_m/c_p)).*(Pe(i)/2)+ (T_m-
T_infinity).*(Pe(i)/2).^0.36);     %%%Total power on the right hand side (W)
P_right(i)=P_MW(i)+P_hl(i)+q_s+q_w;
disp('TOTAL POWER ON THE RIGHT HAND SIDE AT 10 KW')
disp(vpa(P_right(i)));               %%% Display velocity expression of POWER ON
THE RIGHT

%%---------------------------------LEFT HAND SIDE-----------------------------------%%
%%%POWER DUE TO ABSORPTION OF LASER BEAM AND REACTION ENERGY BY
EXOTHEMAL OXIDATION

%P_r=ro_density*b_c*d*v_c_max*H_feo*X_abbr;   %%Power arising from the iron
combustion
%P_r=2.*Pe*(K/c_p)*d*H_feo.*X_abbr;         %%Power arising from the iron
combustion at diffusion-limited combustion capacity (W)
P_r = @(b_c) (2*Pe(i)*(K/c_p).*d*H_feo*X_abbr_max).*(b_c>0 &
b_c<0.001)+(0.21*ro_density*b_c.*d*v_diff*H_feo*X_abbr_max).*(b_c>0.001 &
b_c<0.0025); %%Power arising from iron combustion at diffusion-limited combustion
capacity from AIR with 21%oxygen) (W)

P_abs=A*P_l;                   %%Absorbed power (W)

P_left(i)=P_abs+P_r(i);           %%Velocity expression of power on the left (W)

disp('TOTAL POWER ON THE LEFT HAND SIDE')
disp(vpa(P_left(i)));               %% Display velocity expression of POWER ON THE
RIGHT

%%---------------------------POWER BALANCE EQUATION----------------------------%%

POWER_BALANCE(i)=P_left(i)-P_right(i)==0;           %%% POWER BALANCE
EQUATION (W)

disp('TOTAL POWER BALANCE EQUATION')
disp(vpa(POWER_BALANCE(i)));               %%% Display velocity expression of
POWER ON THE RIGHT
```

```matlab
%%----------CALCULATE KERF WIDTH FROM POWER BALANCE EQUATION-------%%

Kerf_width(i) = vpasolve(POWER_BALANCE(i), b_c);          %%% Calculate kerf
width from power balance equation

Kerf_width(Kerf_width<d_sp)=d_sp;        %%Limit kerf width by beam diameter on
the material surface

disp('Kerf width in (mm) is')
disp(vpa(Kerf_width(i)));                    %%% %%% Display kerf width VALUE in (m)

end

%%----------------EXPERIMENT MAX CUT THICKNESS VS CUTTING SPEED-------------%%

v_exp=[125 150 200 400 600 800 1000];
b_c_exp=[1.875 1.605 1.555 1.545 1.465 1.56 1.456];        %% Average thickness

b_c_6_exp=[1.66 1.6 1.74 1.78 1.46 1.67 1.47];            %% Kerf width at 6 mm
thickness

%%--------------------PLOT MAX CUT THICKNESS VS CUTTING SPEED-----------------%%

figure;
p1=plot(v_c*60000,Kerf_width*1000,'color','k');

xlim([0 1000])
ylim([0 5])

hold on

p2=plot(v_exp,b_c_exp,'o', 'MarkerFaceColor','b');

grid on
xlabel('Maximum cutting speed [mm/min]')
ylabel('Kerf width [mm]')
%title('Maximum cut thickness with the corresponding cutting speed')

hold off

leg1=legend([p1 p2],{'Theoretical','Experimental'},'Location','northeast',
'FontSize',14);
set(leg1,'Box','off')
```

Appendix E

Figure 105 and Figure 106 indicate the definition of a line at the centreline of the nozzle and velocity plot of the 3D model for a flow time of approximately 1.45 s at an inlet pressure of 8 bar, respectively:
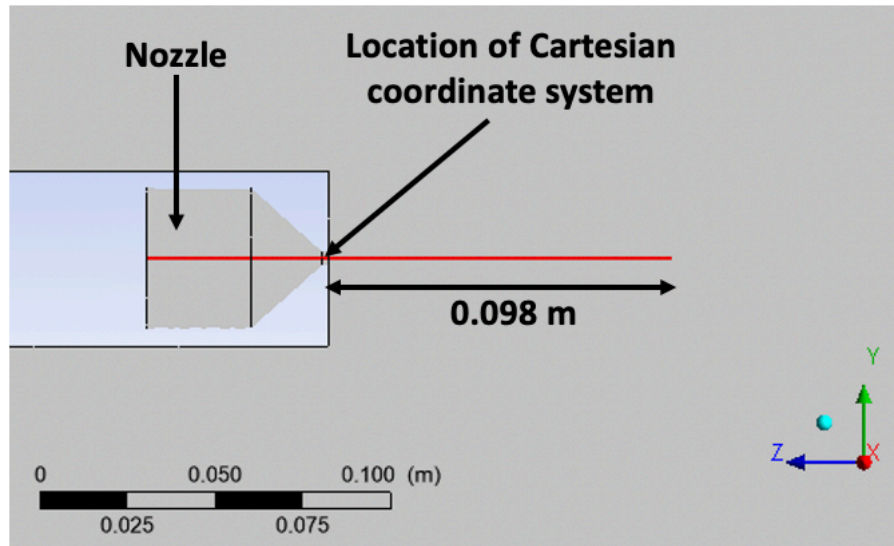
Figure 105: Definition of a line at the centreline of the nozzle
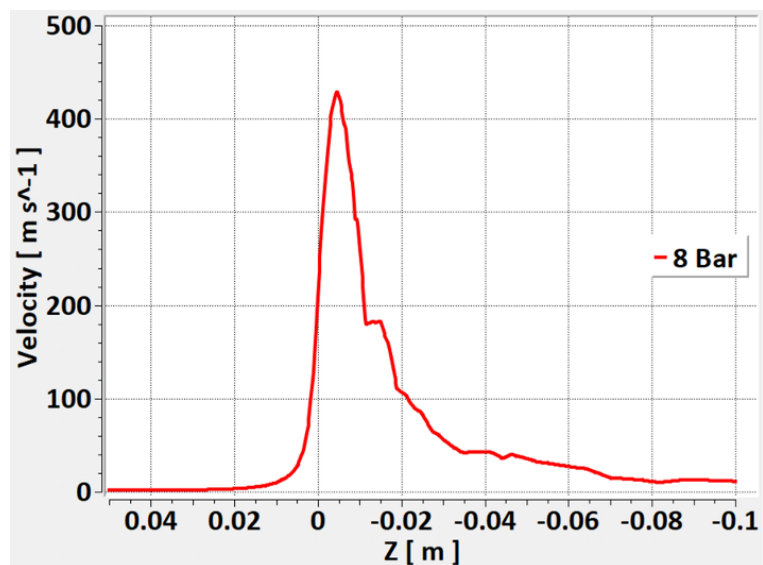
Figure 106: Velocity plot for a flow time of approximately 1.45 s at an inlet pressure of 8 bar